Electrical-field sensitive $YBa_2Cu_3O_{7-x}$ detectors for real-time monitoring of picosecond THz pulses

Zur Erlangung des akademischen Grades eines

DOKTOR-INGENIEURS

von der Fakultät für
Elektrotechnik und Informationstechnik
des Karlsruher Instituts für Technologie (KIT)
genehmigte

DISSERTATION

von

Dipl.-Phys. Juliane Raasch
geboren in Erfurt

Tag der mündlichen Prüfung: 01. August 2017
Hauptreferent: Prof. Dr. Michael Siegel
Korreferent: Prof. Dr. Marc Weber

Vorwort

Diese Arbeit entstand während meiner Zeit als wissenschaftliche Mitarbeiterin am Institut für Mikro- und Nanoelektronische Systeme (IMS) am Karlsruher Institut für Technologie unter der Leitung von Prof. Siegel. Für die Übernahme des Hauptreferats möchte ich mich bei meinem Doktorvater, Herrn Prof. Dr. Michael Siegel, der das Thema der Arbeit angeregt hat, vielmals bedanken. Insbesondere gilt ihm mein Dank für die Förderung meiner wissenschaftlichen Weiterentwicklung und für das Ermöglichen meiner Teilnahme an zahlreichen Konferenzen und Messkampagnen an Teilchenbeschleunigern. Ebenso möchte ich für die Übernahme des Korreferats und das bereits viele Jahre anhaltende Interesse an meiner Arbeit Prof. Dr. Marc Weber meinen Dank aussprechen.

Ich möchte meinem Betreuer, Dr. Konstantin Il'in, für seine Unterstützung bei der Durchführung dieser Arbeit danken. Ich sage danke für die unzähligen Ideen und Lösungsvorschläge bei Problemen in der Technologie und dafür, dass er in jeder Situation Zeit für mich und meine Anliegen gefunden hat.

Den Kollegen in der Arbeitsgruppe, ohne die diese Arbeit nicht das geworden wäre, was sie ist, gilt mein besonderer Dank. Ich danke Alexander Schmid und Artem Kuzmin für die hervorragende Zusammenarbeit bei der Entwicklung der Detektionssysteme und die vielen anstrengenden aber auch schönen Tag- und Nachtschichten an diversen Synchrotronen. Lieber Alex, mit Deiner ruhigen und besonnenen Art hast Du mich auch in den verzwicktesten Situationen davor bewahrt, den Kopf zu verlieren. Bei Matthias Arndt möchte ich mich nicht nur für den Stromquellensupport bedanken, sondern vor allem für die wertvolle Unterstützung an der PLD und natürlich dafür, dass er mir nie die Milch weggetrunken hat. Ich danke den Jungs im Büro, Ilya Charaev, Ekkehart Schmidt und Michael Merker, für die gemeinsame Zeit, egal ob in der Technologie oder im Büro, egal an welchem Wochentag und um welche Tageszeit. Und schließlich gilt mein herzlicher Dank für fachliche und moralische Unterstützung Dr. Stefan Wünsch. Lieber Stefan, ohne Dein offenes Ohr und Deine aufmunternden Worte, wenn es mal nicht wie geplant lief, wäre die Zeit am IMS nur halb so schön gewesen.

Zwar hat sie mich nur in meinen Anfängen begleitet, dennoch gilt mein Dank auch Petra Thoma, die mich während meine Diplomarbeit für die Entwicklung der YBCO-Detektoren gewann. Außerdem danke ich unseren Technikern Alexander Stassen und Karlheinz Gutbrod für den technischen Support und die vielen Momente, in denen ich ihre Hilfe ganz spontan in Anspruch nehmen kon-

nte. Ebenfalls bedanken möchte ich mich bei Doris Duffner, Steffen Dörner, Frank Ruhnau, Erich Crocoll, Philipp Trojan, Max Meckbach und Matthias Hofherr für die schönen Jahre am IMS.
Schließlich möchte ich "meinen" Studenten ein Dankeschön aussprechen. Lisa Neusel, Steffen Koch, Martin Krämer, Philipp Sedlmeier, Jakob Gantenbein, Emanuel Knehr und Jan Feßler: Ihr habt mich immer wieder gefordert und durch Euer Interesse und Eure Nachfragen zum Weiterdenken angeregt.
Miriam Brosi und Johannes Steinmann möchte ich für gemeinsame Messzeiten an ANKA und anderen Beschleunigern, für fröhliche Stunden bei Konferenzen und Seminaren und für zahlreiche spannende Diskussionen danken. Ebenso gilt mein Dank Erik Bründermann für die Vermittlung des Kontakts nach Dresden, für das Teilen seiner umfassenden Expertise und für das Schreiben seines wunderbaren Grundlagenbuches. Für den tollen Strahl während unsere Messzeiten an ANKA danke ich Nigel Smale und Edmund Blomley, außerdem gilt mein Dank Yves-Laurent Mathis und Michael Süpfle für den technischen Support während unserer Messkampagnen. Nicht zuletzt möchte ich mich bei Frau Prof. Dr. Anke-Susanne Müller für das Interesse an unserem Projekt und die fachlichen Hilfestellungen im Bereich der Beschleunigerphysik bedanken.
Während meiner Promotion hatte ich das Glück, an vielen Teilchenbeschleunigern für Messkampagnen willkommen zu sein. Überall dort waren hilfsbereite Menschen der Schlüssel zum Erfolg der Experimente. Deswegen danke ich den Wissenschaftlern und Technikern an UVSOR-III, Diamond, DELTA, TELBE, FELBE, an der SwissFEL Injektor Testanlage und an SOLEIL für ihren Beitrag zum Gelingen dieser Arbeit. Insbesondere danke ich auch Serge Bielawski, Eleonore Roussel, Christophe Szwaj und deren Kollegen von der Universität Lille für die ausgezeichnete Zusammenarbeit in Okazaki und Dortmund.
Den Kollegen am Campus Nord, namentlich Marco Langer, Sandra Kauffmann-Weiß, Jens Hänisch und Prof. Dr. Bernhard Holzapfel, möchte ich für die Unterstützung bei der Optimierung der Dünnfilme, die hilfreichen Diskussionen und Hinweise auf interessante Fachliteratur, die XRD-Analyse unserer Proben und die Bereitstellung des AFM danken.
Schließlich gilt mein Dank meiner Familie, meinen Freunden und meinem Partner. Ich danke meinen Eltern und Großeltern für den unerschütterlichen Glauben an meinen Erfolg und für das von Kindesbeinen an geschürte Interesse für die Mikroelektronik. Mein besonderer Dank gilt meinem Opa. Und natürlich danke ich Dir, Robert. Danke, dass Du an mich glaubst, egal was kommt. Danke, dass Du ein unendlicher Quell von Motivation bist. Und danke, dass Du Du bist.

Karlsruhe, im Juni 2017 Juliane Raasch

Kurzfassung

In der vorliegenden Arbeit wurden aus Dünnfilmen des Hochtemperatursupraleiters $YBa_2Cu_3O_{7-x}$ (YBCO) THz-Direktdetektoren mit sub-µm-Abmessungen entwickelt und hinsichtlich ihres Verhaltens unter gepulster Bestrahlung abhängig von Temperatur und Frequenz untersucht. Minimale YBCO-Schichtdicken von 11,7 nm und laterale Dimensionen des Detektorelements von 150 nm × 800 nm wurden realisiert. Besonderes Augenmerk lag auf der Untersuchung des Detektorverhaltens ohne angelegten Biasstrom. In diesem Betriebsmodus ermöglicht die Sensitivität des Detektors hinsichtlich der Phase des eingestrahlten elektrischen Feldes die detaillierte Analyse oszillierender THz-Signale an Teilchenbeschleunigern.

Das Einsatzgebiet der entwickelten Detektoren ist die Messung kohärenter Synchrotronstrahlung an Linear- und Zirkularbeschleunigern. Diese wird von ultra-kurzen Elektronenpaketen emittiert, deren longitudinale Ausdehnung kürzer als die abgestrahlte Wellenlänge ist. Entsprechend der Elektronenpaketlängen von hunderten Mikrometern bis zu wenigen Millimetern liegen die emittierten Frequenzen im Bereich einiger Gigahertz bis Terahertz. Beschleuniger, als gepulste Strahlungsquellen, zeichnen sich durch ihre hohe Brillanz aus und sind daher für zahlreiche Anwendungen, u.a. im Bereich der medizinischen Bildgebung, THz-Spektroskopie und Festkörperphysik, geeignet.

Aufgrund der Dimensionen der Elektronenpakete ergeben sich Impulslängen im Bereich weniger Pikosekunden, so dass intrinsisch ultra-schnelle Materialsysteme als Detektoren in Kombination mit breitbandiger Ausleseelektronik benötigt werden, um die THz-Signale aufzulösen. Darüber hinaus treten an Synchrotron im sogenannten low-α_c-Betriebsmodus Instabilitäten auf, die dazu führen, dass die zeitliche und spektrale Form des THz-Impulses von Umlauf zu Umlauf variiert. Die Substruktur, mit der der THz-Impuls dadurch moduliert wird, erreicht Zeitskalen von unter einer Pikosekunde.

Halbleitende Bolometer und Raumtemperatursensoren, die auf thermischen oder pyroelektrischen Effekten beruhen, liegen mit ihren Antwortzeiten mehrere Größenordnungen oberhalb der geforderten Auflösung. Daher kommen ultra-schnelle supraleitende Sensoren zum Einsatz. Insbesondere das Materialsystem YBCO zeichnet sich durch seine intrinsischen Relaxationszeiten im Pikosekunden-Bereich aus. Durch Einbettung eines YBCO-THz-Detektors in eine breitbandige Echtzeit-Ausleseelektronik wurden in früheren Arbeiten minimale Antwortzeiten von 16 ps demonstriert und am Teilchenbeschleuniger ANKA in Einzelpulsmessungen die Gesamtlänge des

Impulses und damit die longitudinale Ausdehnung des Elektronenpaketes bestimmt.
Um die zeitliche Limitierung bei der direkten Auslese der THz-Signale zu umgehen und über die Elektronenpaketlänge hinaus auch die Substrukturen im Elektronenpaket aufzulösen, wird ein neuartiger Ansatz verfolgt. Dabei soll mittels eines Arrays aus schmalbandigen THz-Antennen und eingebetteten YBCO-Detektoren das Spektrum des einzelnen THz-Impulses mit Pikosekunden-Auflösung gemessen werden. Dieses System kann auch an Linearbeschleunigern zum Einsatz kommen, wo die Gesamtimpulslängen wesentlich kürzer als an Synchrotronen sind. Die Selektion einzelner Frequenzbänder aus dem breitbandigen THz-Spektrum am Zirkularbeschleuniger erfordert eine Steigerung der intrinsischen Detektorsensitivität um etwa eine Größenordnung.

Aufgrund seines intrinsisch schnellen Antwortverhaltens wurde in dieser Arbeit YBCO als Detektormaterial gewählt. Antwortzeiten im (Sub)-Pikosekunden-Bereich bei Bestrahlung oberhalb der supraleitenden Energielücke können der Elektronen-Elektronen- und Elektronen-Phononen-Wechselwirkung zugeschrieben werden. Die Detektion von Strahlung im optischen Frequenzbereich beruht auf dem Modell des Heiße-Elektronen-Bolometers.
Bei der Detektion von kohärenter THz-Strahlung wurden schließlich Charakteristika beobachtet, die nicht auf Basis des Zwei-Temperaturen-Modells erklärt werden konnten. Insbesondere eine nanosekundenskalige Detektorantwort, die der Relaxation der Phononen ins Substrat entspricht, wurde nicht beobachtet. Zur Erklärung des gemessenen Verhaltens wurde ein Detektionsmechanismus, der auf der verlustbehafteten Bewegung von Flusschläuchen beruht, vorgeschlagen.
Eine weitere Besonderheit bei der Detektion von THz-Strahlung mit YBCO-Detektoren ist das Auftreten eines Detektorsignals ohne Anlegen eines Biasstroms. Von einem klassischen Bolometer wird dieses Verhalten nicht erwartet. Die Analyse der Eigenschaften dieser stromlosen Detektorantwort kann daher Aufschluss geben über die Mechanismen, die die Detektion von Strahlung unterhalb der Energielücke von YBCO bedingen. Da das Detektorsignal im stromlosen Zustand im Vergleich zum Betrieb mit Biasstrom merklich abnimmt, erfordert auch die detaillierte Analyse des Betriebsmodus ohne Biasstrom eine Verbesserung der Detektorsensitivität.

Auf der Grundlage dieser Motivation wurden für die vorliegende Arbeit zwei Ziele formuliert: die Entwicklung eines Herstellungsprozesses für sub-µm-YBCO-Detektoren zur Erhöhung der intrinsischen Detektorsensitivität und die detaillierte Untersuchung des Detektorverhaltens bei Bestrahlung mit gepulsten THz-Signalen, insbesondere im Betriebsmodus ohne angelegten Biasstrom. Die Arbeit gliedert sich in drei Teile: Das physikalische und technische Hintergrundwissen, das die Arbeit motiviert, wird in den Kapiteln 2 und 3 behandelt. Kapitel 4 und 5 befassen sich mit der Dünnfilmabscheidung und -strukturierung und in den Kapiteln 6 und 7 werden die Untersuchungen zum Detektorverhalten bei Bestrahlung mit THz-Signalen im stromlosen beziehungsweise im DC-stromführenden Betrieb zusammengefasst.

Zur Entwicklung sensitiver YBCO-Detektoren und der dazu benötigten Reduktion des Volumens des aktiven Detektorelements wurde die Laserablation ultra-dünner YBCO-Schichten optimiert. Die oszillierende Ablenkung des Laserstrahls auf dem Target ermöglicht hierbei die Abscheidung von Dünnfilmen mit hoher Schichtdickenhomogenität. Für die Abscheidung der YBCO-Schicht und ihrer Puffer- und Schutzschichten wurde die Intervall-Laserablation als Verfahren zur gezielten Monolagenabscheidung eingeführt. Dadurch konnte eine Reduktion des beobachteten Inselwachstums erreicht und die Schichtrauigkeit minimiert werden. Zehn Monolagen YBCO auf einer zweilagigen Pufferschicht aus acht Monolagen $PrBa_2Cu_3O_{7-x}$ und 9,5 nm CeO_2 weisen eine kritische Temperatur von 75,3 K auf. Die Rauigkeit des gesamten Schichtsystem beträgt 3,6 nm. Für die Herstellung der Detektoren wurden Schichtdicken von $20-30$ nm mit $T_c \approx 87$ K verwendet.
Als Metallisierung für die verlustarme Übertragung des THz-Signals von der Antenne zum Detektorelement wurde eine Goldschicht mit einer Dicke von 200 nm gewählt. Hierbei ist die Schichtdickenhomogenität von besonderer Bedeutung, da schon geringe Fluktuationen der Golddicke ein gleichmäßiges Ätzen der sub-µm-Strukturen verhindern. Zur Abscheidung von Gold wurde daher eine Kombination aus der Laserablation einer sehr dünnen Goldhaftschicht und einer dicken gesputterten Goldschicht gewählt. Die beiden Prozesse vereinen die Vorteile niedriger Kontaktwiderstände und hoher Schichtdickenhomogenität bei gleichzeitigem Schutz der darunter liegenden oxidischen Materialien.
Aus der Untersuchung verschiedener Ätzverfahren zum Strukturieren des Detektorschlitzes, der die Länge des Detektionselementes vorgibt, ergab sich das Ionenstrahlätzen in einem reinen Argonplasma als am besten geeignet. Durch die Kombination mit einer Elektronenstrahllithographie konnten minimale Dimensionen von 150 nm verwirklicht werden. Minimale Breiten der Detektorelemente von 800 nm wurden ebenfalls mittels Elektronenstrahllithographie und Argon-Ionenstrahlätzen realisiert. Gegenüber den unstrukturierten Schichten trat nur eine leichte Degradation der supraleitenden Eigenschaften auf ($T_c \approx 83-85$ K). Intrinsische Sensitivitäten für gepulste Anregungen von bis zu 1 V/pJ wurden mit den so hergestellten Detektoren gemessen.

Die Untersuchungen der Detektorantwort für gepulste THz-Anregungen wurden an verschiedenen Beschleunigern durchgeführt. Diese emittieren schmalbandige und breitbandige Strahlung im Bereich einiger Gigahertz bis ca. 6 THz, was nahe der supraleitenden Energielücke von YBCO liegt. Das Verhalten im stromlosen Zustand und im Betrieb mit Biasstrom wurde hinsichtlich der Badtemperatur, der Frequenz der absorbierten THz-Strahlung und der eingekoppelten Strahlungsleistung analysiert.
Ein linearer Zusammenhang zwischen Detektorantwort und eingekoppelter Strahlungsleistung deutet dabei auf die Bewegung von Flussschläuchen im Supraleiter hin, da die Strahlungsleistung proportional zum Quadrat des elektrischen THz-Feldes und damit zum von der Antenne induzierten

Mikrowellen-Strom ist. Dieses Verhalten wurde sowohl im Betrieb ohne als auch mit einem Biasstrom beobachtet. Gleichzeitig konnte kein quadratischer Zusammenhang bei der Abhängigkeit der Detektorantwort vom Biasstrom nachgewiesen werden, so dass angenommen wird, dass die beiden Ströme unterschiedlichen Einfluss auf das Verhalten des Supraleiters haben. Im Bias-Betrieb wurde anhand verschiedener Messgrößen eine Übereinstimmung der Detektorantwort mit den Charakteristika eines Bolometers gefunden. Dazu gehören der Zusammenhang zwischen Sensitivität und Detektorvolumen, sowie die Abhängigkeit des Detektorsignals von der Badtemperatur und die gemessenen Impulsantwortzeiten. Dies gilt auch für Anregungsfrequenzen weit unterhalb der Energielücke von YBCO.
Der stromlose Detektorbetrieb ist gekennzeichnet durch die Sensitivität des Detektors zur Phase des elektrischen Feldes im kompletten untersuchten Temperaturbereich ($T \geq 0{,}7\ T_\mathrm{c}$). Dies unterscheidet den YBCO-Detektor grundlegend von bolometrischen Detektoren, die durch das Anlegen eines Biasstroms sensitiv zur Leistung der THz-Strahlung sind und keine Information hinsichtlich der Phase liefern können. Auf Basis dieser Messergebnisse kann angenommen werden, dass der Detektionsmechanismus nahe T_c und bei tieferen Temperaturen auf dem gleichen Wirkprinzip beruht. Eine nanosekundenskalige Antwortzeit, die der Relaxation von Phononen ins Substrat entsprechen würde, wurde in diesem Betriebsmodus nicht beobachtet.

Die Sensitivität zur Phase des elektrischen Feldes im Betriebsmodus ohne angelegten Biasstrom wurde ausgenutzt, um die Langzeitentwicklung oszillierender Singale im Bereich um 30 GHz am Synchrotron UVSOR-III in Japan zu untersuchen. Hierbei ändert die THz-Strahlung aufgrund von Instabilitäten ihre Phase. Derartige Untersuchungen werden ausschließlich von Detektoren mit Antwortzeiten im Pikosekundenbreich und einer Sensitivität zum elektrischen Feld ermöglicht. Direktdetektoren, die auf YBCO basieren, sind daher derzeit die einzigen Systeme, die für diese Messung verwendet werden können. Durch die Einbettung von sub-µm-Detektoren in ein 4-Pixel-Array aus schmalbandigen Antennen konnte zudem die erste simultane Echzeitauflösung mehrerer Frequenzbänder von kohärenter THz-Strahlung an den Synchrotronen ANKA und der Diamond Light Source (DLS) realisiert werden.

Contents

Vorwort **i**

Kurzfassung **iii**

1 Introduction **1**

2 Ultra-fast direct detection of THz radiation pulses **5**

2.1 Pulsed THz radiation sources 5

2.1.1 Synchrotron storage rings in short-bunch operation 6

2.1.2 Coherent Harmonic Generation 9

2.1.3 Spontaneous CSR 11

2.1.4 Brilliant THz radiation from linear accelerators 12

2.1.5 Photoconductive antennas 13

2.2 Detectors for pulsed THz radiation 14

2.2.1 Room-temperature detectors 14

2.2.2 Bolometric direct radiation sensors 16

2.2.3 Zero-biased Schottky diode detectors 21

2.3 Basics of THz optics 23

2.4 Conclusions of chapter 2 24

3 The detector material YBCO **27**

3.1 Properties of the high-temperature superconductor YBCO 27

3.1.1 Crystalline structure of YBCO 27

3.1.2 Anisotropy of the superconducting properties in YBCO 28

3.1.3 Structure and magnitude of the energy gap in YBCO 29

3.1.4 Vortices in cuprates 30

3.1.5 Properties of thin YBCO films 31

3.2 YBCO technology: thin-film growth and patterning 32

3.2.1 Basics of thin-film growth 32

3.2.2 Physical aspects of pulsed-laser deposition 35

3.2.3 Ultra-thin YBCO films: state of the art 39

3.2.4 Surface degradation of cuprate superconductors 39
3.2.5 Submicrometer patterning: state of the art 40
3.3 Light detection in YBCO thin films 41
3.3.1 Above-gap excitations: optical through infrared radiation 41
3.3.2 Sub-gap excitations in the microwave and FIR region 44
3.4 Direct YBCO THz detector 46
3.4.1 Detector design 46
3.4.2 Technological requirements 51
3.5 Conclusions of chapter 3 52

4 Epitaxy of thin YBCO films 53
4.1 Automation of the PLD system 53
4.1.1 Laser-ablation setup 53
4.1.2 Description of the deposition process 55
4.1.3 Semi-automated control of thin-film growth with LabVIEW 56
4.2 Optimum parameters for the deposition of YBCO thin films 58
4.2.1 The thin-film multi-layer stack 58
4.2.2 Optimization of the thickness homogeneity of laser ablated thin films 60
4.2.3 Smooth CeO_2 buffer layers 62
4.2.4 Interval deposition of PBCO 65
4.2.5 Growth of thin YBCO films 68
4.2.6 Investigation of ablated and sputtered gold films 70
4.3 Conclusions of chapter 4 74

5 Fabrication process for YBCO nanobridges 77
5.1 Definition of the length of the detecting element 77
5.1.1 Etching techniques 77
5.1.2 Comparison of etching techniques 82
5.2 YBCO detector fabrication 85
5.2.1 Detector patterning 85
5.2.2 DC characterization of sub-micron sized YBCO detectors 88
5.3 Conclusions of chapter 5 89

6 Zero-bias response of the YBCO detector to pulsed THz excitations 91
6.1 Detection system 91
6.1.1 Cryogenics for high-temperature superconductors 92
6.1.2 RF readout electronics and DC biasing 93

6.1.3 Coupling of radiation 96
6.2 Operation-point dependent zero-bias response 98
6.2.1 Temperature dependence of the zero-bias response 99
6.2.2 Dependence of the detector response on coupled THz power 101
6.3 Real-time detection in zero-bias operation mode 104
6.4 Sensitivity of the detector response to the phase of the electrical field 108
6.5 Conclusions of chapter 6 111

7 Frequency- and power-dependent behavior in the biased regime 113
7.1 Dependence of the detector response on applied bias current 113
7.2 Influence of the power level 117
7.3 Frequency dependence in biased operation mode 119
7.3.1 Pulsed narrowband THz signals 119
7.3.2 Continuous-wave excitations 120
7.4 Measured pulse shape depending on the operation point of the detector . . 123
7.5 Sensitive YBCO detector arrays for single-shot THz spectroscopy 126
7.6 Conclusions of chapter 7 128

8 Summary and outlook 129

List of Figures 133

List of Tables 137

Nomenclature 139

Bibliography 145

Own publications 165

Supervised student theses 169

International conferences and workshops 171

1 Introduction

In the past, due to the lack of brilliant sources of radiation and efficient detector technologies, the THz frequency range was often referred to as the final unexplored area of the electromagnetic spectrum. Yet, a broad range of applications is found in this region of the spectrum. Amongst them are THz spectroscopy of molecules [1], studies of electronic interactions in condensed-matter physics [2], security applications [3] and bio-medical imaging [4]. With the discovery of brilliant Coherent Synchrotron Radiation (CSR) from short, relativistic electron packages, the THz gap in the source region was finally closed. Linear or circular accelerators accommodating electron packages, called bunches, emit coherent radiation at wavelengths longer than the bunch length in particular operation modes [5]. In general, with longitudinal bunch lengths in the (sub-)mm region, the emission of CSR ranges from a few GHz up to several THz. On Earth, accelerator-based THz emitters are the sources of highest brilliance [6].
Short THz pulse lengths, originating from the overall bunch lengths, combined with high repetition rates require fast direct detector technologies with picosecond response times. This prerequisite prevents the use of most room-temperature THz detectors and semiconducting bolometers [7]. As compared to that, superconducting hot-electron bolometers (HEB) offer fast intrinsic response times combined with high detector responsivities. First bunch-by-bunch resolution in a multi-bunch environment with a pulse repetition rate of 500 MHz was demonstrated at the ANKA storage ring by the use of a NbN HEB. The detection system had a response time of 165 ps full width at half maximum (FWHM) [8]. Real-time detection of THz pulses and the first direct resolution of the overall pulse width with pulse lengths ranging from 15 ps to 25 ps (FWHM) was achieved experimentally with ultra-fast THz detectors based on the high-temperature superconductor (HTSC) $YBa_2Cu_3O_{7-x}$ (YBCO) [9].
The investigation of the micro-bunching phenomenon, an instability leading to (sub-)picosecond-sized substructures on the bunch, requires even faster response times [10]. At the same time, sub-picosecond pulse lengths occur also at linear accelerators that emerge as a new technology for the generation of CSR with even higher intensities [11]. State-of-the-art direct readout electronics for THz detectors do not offer response times below approximately 15 ps [9], such that a single-shot spectroscopic detection scheme was introduced recently [SRK$^+$16]. Herein, the implementation of a new detector technology, designed for the narrowband resolution of CSR signals, entails the need for ever-growing detector sensitivities.

In this work, YBCO was selected as detector material due to its fast intrinsic relaxation times that were found via pump-probe experiments in the optical frequency range [12]. Models explaining the behavior of the YBCO detector for above-gap excitations are based on electron- and phonon-heating effects and the kinetic inductance of the superconductor [13]. Herein, the (sub-)picosecond electron-electron and electron-phonon interaction times enable the ultra-fast operation of the detector.
Lately, the detection at sub-gap frequencies, namely in the the THz frequency range, has been investigated at accelerator-based THz sources [14, 15]. Due to the large superconducting gap of the cuprates, a breaking of Cooper pairs at frequencies up to a few THz is unlikely. The study of the detector response to pulsed, broadband THz excitations revealed distinct characteristics that distinguish the THz region from above-gap excitations. In particular, the bolometric behavior of the detector response is not observed.
In this context, the appearance of a zero-bias response is the most intriguing phenomenon of the detector operation at THz frequencies. The nature of the zero-bias mode herein needs further analysis. This objective reinforces the demand for an ultra-sensitive detector technology, as the detector output decreases in zero-bias operation mode.

This work aims at the coverage of two main goals: The first one is to provide a fabrication technology for sub-µm-sized direct YBCO THz detectors, thereby enabling ultimate sensitivity along with picosecond response times. This task is split in the optimization of the deposition process to reduce the thickness of the detecting element and the actual patterning process that defines the lateral dimensions. The second objective of this thesis is an in-depth investigation of the characteristics of the YBCO detector response to pulsed THz excitations below the superconducting gap. Herein, the zero-bias operation mode as a peculiarity in the detection of THz radiation pulses is of special interest.

As the research presented in this work was carried out at numerous accelerator sources, the different types of circular and linear accelerators and their principles of generation of THz radiation are introduced in section 2.1. Based on the characteristics of the individual THz sources, specific requirements for direct radiation detectors arise. The second part of chapter 2 therefore reviews the range of available THz detector technologies and thereby directly motivates the need for an ultra-fast and highly sensitive THz detector that is operational over a broad frequency range from several GHz up to more than 6 THz. To conclude the introduction to the aspects concerning the generation and detection of THz radiation, the principles of Gaussian beam optics are discussed in the last section of chapter 2.
Chapter 3 presents the theoretical basis needed in regard to the high-temperature superconductor YBCO. The material system is introduced along with the technological background for deposition

and patterning with special attention to the distinctive features of YBCO in sections 3.1 and 3.2. Section 3.3 gives a summary of the current state of research for above- and sub-gap excitations of thin-film YBCO detectors. The chapter concludes with an overview of the YBCO detector design and the formulation of the technological requirements for the detector fabrication that is described in the following chapters.

Chapters 4 and 5 are devoted to the first main goal of this work, namely exploiting the limits of dimensions in the deposition and patterning of YBCO thin films. Section 4.1 gives a complete overview of the deposition system. The optimization of the YBCO thin film and the enveloping buffer and protection layers is discussed in section 4.2. To tackle the requirement for ultra-thin and flat films, the method of interval pulsed-laser deposition is established. Following the deposition, the patterning to sub-µm-sized detecting elements aims for ultimate detector sensitivities. Section 5.1 deals with the most crucial step during fabrication of the YBCO detector: the removal of gold in the area of the detecting element. Moreover, the complete patterning process implemented for the fabrication of sensitive YBCO THz detectors is summarized in the second part of chapter 5.

The response of the as-deposited and patterned YBCO detectors to pulsed THz excitations of different power levels and frequency range is investigated depending on the operation point of the detector. In chapter 6, the detection system with broadband readout for real-time resolution of picosecond THz pulses is introduced. The zero-bias operation, the most intriguing feature of the direct YBCO THz detector, is examined in section 6.2. Real-time resolution of oscillating CSR signals was demonstrated in zero-bias mode (see section 6.3). In the unbiased regime, a temperature-independent sensitivity of the detector response to the phase of the electrical field is observed (see section 6.4).

The biased regime of the sub-µm-sized YBCO detector is highlighted in chapter 7. From the dependence of the detector response on bias current, the study is extended to the influence of the power level and the interplay of both parameters in section 7.2. To complete the picture of the biased response at different THz frequencies, the results are contrasted with the detector response to continuous-wave (CW) excitations (section 7.3). At last, the dependence of the detector pulse shape is investigated with respect to the operation point.

2 Ultra-fast direct detection of THz radiation pulses

The Terahertz (THz) frequency band bridges the gap between the microwave spectrum and infrared radiation [7]. It is also referred to as far-infrared radiation (FIR) and, in this work, will be considered as the frequency range from 0.3 up to 10 THz, corresponding to wavelengths in between 30 µm and 1 mm.

This chapter reviews the range of pulsed THz radiation sources available for the characterization of the investigated detector material YBCO. In the second part, existing direct THz detectors that are commonly in use at THz beamlines are introduced. Herein, the different detection techniques are presented in order of decreasing response time. Finally, the principles of Gaussian THz optics are outlined briefly.

2.1 Pulsed THz radiation sources

Most dielectric materials, such as clothing and paper, are transparent to THz radiation. Along with the high absorption coefficient in water and the reflection from metal surfaces, this allows for the use of THz radiation in numerous experiments, including spectroscopy, medical sciences and security services as well as solid-state physics research [7]. The discovery of intense THz radiation being emitted from synchrotron storage rings paved the way to many of those applications by closing the THz gap in the field of available sources [16].

Charged particles, moving close to the speed of light, emit synchrotron radiation when experiencing a transverse acceleration, usually induced by a (bending) magnet. In a synchrotron storage ring, electrons are accelerated in bunches with typical longitudinal dimensions of several tens of mm. The emitted synchrotron radiation therefore is seen as a short pulse (hundreds of ps) by an observer. Fourier transformation of the time domain signal thus leads to a broad frequency spectrum [17].

An in-phase emission of synchrotron radiation is called Coherent Synchrotron Radiation (CSR). This happens when the emitted wavelengths are longer than or in the range of the emitting structure, which can be either the longitudinal bunch length itself or a substructure on the bunch. The intensity of the emitted CSR is proportional to the square number of electrons in the bunch as opposed to the case of an incoherent emission, where the intensity depends linearly on the number of electrons. The part of the radiation field emitted at wavelengths below the bunch length is incoherent.

With the number of electrons in a bunch being on the order of 10^{10}, CSR intensities are magnitudes of order higher than those of incoherent radiation. Therefore, accelerators emitting CSR in the THz frequency band are to date the sources of highest achievable brilliance on Earth [6].

The emitted THz power P at a given wavelength λ depends on the power P_e emitted by a single electron and the number of electrons N_e in the bunch [17]:

$$\frac{\mathrm{d}P}{\mathrm{d}\lambda} = (N_\mathrm{e} + N_\mathrm{e}(N_\mathrm{e}-1)f_\lambda)\frac{\mathrm{d}P_\mathrm{e}}{\mathrm{d}\lambda} \tag{2.1}$$

The quadratic term in N_e describes the coherent emission and the linear term represents the incoherent emission. The form factor f_λ defines the degree of coherence and depends on the longitudinal charge density distribution inside the bunch. For a Gaussian charge distribution, the form factor f_λ vanishes at wavelengths smaller than the root mean square (rms) bunch length σ and equation (2.1) yields an incoherent emission. In turn, for wavelengths longer than or equal to the longitudinal bunch length, the coherent term becomes dominant. Even small modifications to the bunch profile are amplified by the large number of electrons and therefore lead to a visible change in emitted THz radiation, making CSR also a powerful tool for monitoring electron beam conditions [6].

Different concepts of generating CSR at accelerators each offer individual properties of the THz radiation and are therefore suited to investigate varying aspects of the behavior of the YBCO detector. At the same time, those accelerators entail specific requirements regarding the characteristic detector properties, such as sensitivity, spectral range and response time.

Mechanisms to excite ultra-short THz pulses at accelerator-based sources are introduced in the following, along with the actual facilities where the studies for the results presented in chapters 6 and 7 were conducted. Accelerators providing particle beams that lead to the emission of CSR can be either linear or circular ones.

2.1.1 Synchrotron storage rings in short-bunch operation

CSR can be emitted from electron bunches with very short overall lengths down to sub-mm longitudinal dimensions corresponding to pulse durations of only a few picoseconds. Figure 2.1 shows in green the simulated spectra radiated from Gaussian shaped bunches with rms lengths of 5 ps and 10 ps [SBB+16a]. Since the electron beam inside a storage ring travels in a vacuum chamber, a low-frequency cut-off for the propagation of THz radiation can be seen [18]. In case of radiation emitted from a bending magnet, this cut-off is given by $\lambda_\mathrm{min} = 2h\sqrt{h/\rho}$, with the height h of the vacuum chamber and the bending radius ρ [6]. For the given vacuum chamber dimensions in Fig. 2.1, the cut-off is situated at around 60 GHz. The high-frequency cut-off of CSR is determined

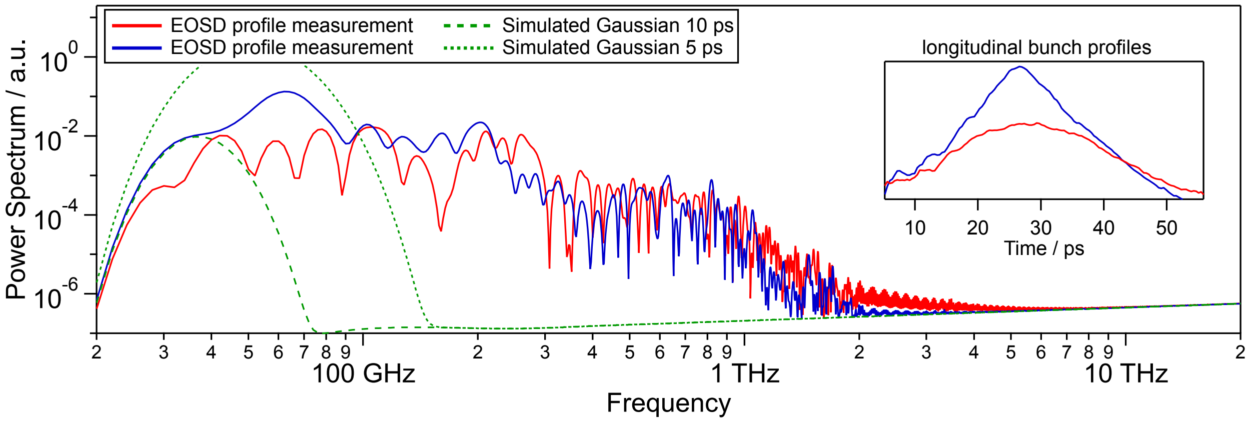

Fig. 2.1: Spectrum of CSR from low-α_c optics. Green lines: simulated spectra of perfectly Gaussian shaped charge distributions, blue and red lines: spectra calculated from single-shot electro-optical spectral decoding (EOSD) measurements. The corresponding longitudinal temporal shape of the bunches, extracted from the EOSD measurements, are shown in the inset [SBB$^+$16a].

by the rms bunch length. The incoherent spectrum of the bunch extends to higher frequencies at lower power levels (see Fig. 2.1).

The ultra-short bunch lengths required for the generation of broadband CSR can be achieved through the use of special magnetic lattices, referred to as low-α_c optics. Herein, α_c denotes the momentum compaction factor and describes the orbit variation with beam energy:

$$\frac{\Delta L}{L_0} = \alpha_c \frac{\Delta p}{p_0} \tag{2.2}$$

with $\Delta L/L_0$ being the difference in orbit length and $\Delta p/p_0$ being the momentum (energy) deviation [19]. This means that electrons with varying energies will propagate on different paths through the bending magnet, thereby changing their position inside the bunch and ultimately increasing the bunch length. Low-α_c optics are designed to reduce those orbit length variations, thus reducing the bunch length. CSR from low-α_c optics was first observed at the BESSY II synchrotron light source [5, 16].

The temporal shape of the electrical field resulting from the charge distribution inside the electron bunch is a single-cycle pulse, corresponding to one full oscillation of the electrical field. Herein, the integral over the time axis vanishes. Yet, it is possible to obtain THz pulse forms where the negative part is stretched in time and thus small in magnitude as compared to the positive pulse. The electrical field of what is called a half-cycle pulse is shown in Fig. 2.2. Half- or single-cycle pulses are a unique characteristic of very broadband sources. Narrowband sources emit oscillating THz signals [6].

Above a certain current threshold, the bunch starts to interact with itself and its own CSR, causing micro-bunching. Thereby, beam instabilities leading to a bursting of the THz radiation occur [10].

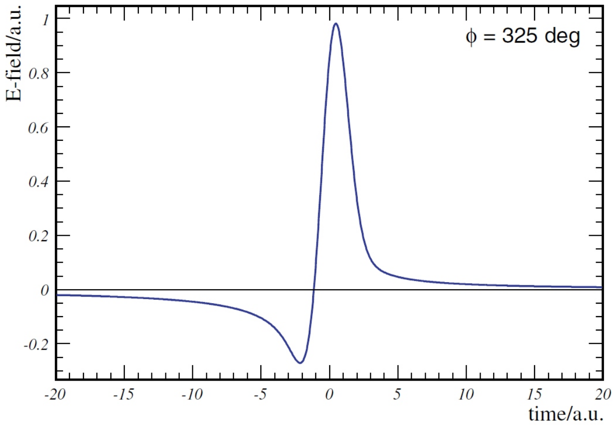

Fig. 2.2: Simulation of the electrical field emitted from a short electron bunch; from [6]. The half-cycle pulse form is visible.

Micro-bunches emit CSR at lower wavelengths and, due to a higher form factor f_λ, at increased power levels. Examples of the resulting electron bunch profiles and their calculated spectra can be seen in Fig. 2.1 in blue and red. Profiles of a single bunch in bursting mode were measured at ANKA using single-shot electro-optical spectral decoding (EOSD) for different revolutions inside the storage ring [20]. The bursting radiation extends its spectrum to higher frequencies and shows an unstable behavior, thus changing its temporal and spectral form from revolution to revolution.

Inside a storage ring, many bunches can circulate. The maximum number of bunches depends on the RF frequency, typically 500 MHz, that defines the spacing between two consecutive electron packages, and the circumference of the storage ring, directly linked to the revolution frequency. Experiments with YBCO detectors were performed at the Ångström Source Karlsruhe (ANKA) at KIT and the Diamond Light Source (DLS) at the Harwell Science and Innovation Campus in Oxford. ANKA fits a maximum of 184 bunches, corresponding to a revolution frequency of 2.71 MHz [21]. At DLS, the revolution frequency is 0.53 MHz and 936 bunches can be stored [22]. The sequence of bunches circulating in a synchrotron is called filling pattern. Single- and multi-bunch filling patterns are carried out. Typical rms bunch lengths are $\sigma \approx 7$ ps at ANKA and $\sigma = 3.5$ ps at DLS [22–24].

Synchrotron storage rings operating in short bunch mode offer intense broadband radiation from a few GHz, limited by the vacuum chamber cut-off, up to presently about 2 THz [25]. Due to the bursting behavior, they require ultra-fast direct THz detectors that can resolve the individual pulse intensity in a single-shot regime and on a turn-by-turn basis. The substructures occurring during micro-bunching reach sub-picosecond time scales while direct detectors are limited by readout electronics to response times of about 16 ps so far. Therefore, it is not possible to resolve micro-bunches with direct detectors [9]. Hence, a second approach is considered: An array of several ultra-fast THz detectors embedded in narrowband antennas is used to measure the spectrum of the

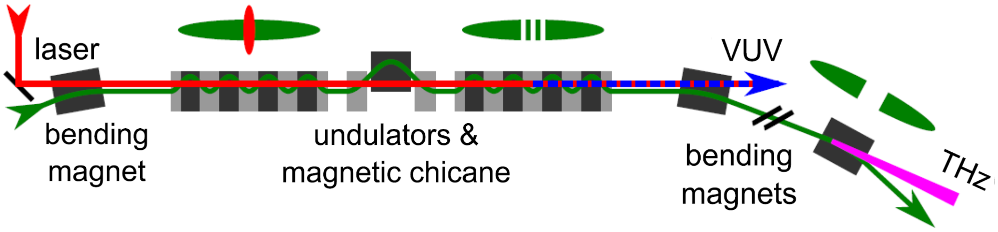

Fig. 2.3: Schematic of the process of Coherent Harmonic Generation (CHG). The trajectory of the electron bunch is depicted in green, the optical path of the laser in red. The top view of the electron bunch (green ellipse) depicts the charge density modulation [UMB+14].

bursting CSR in a single-shot regime. Both concepts will be presented in section 3.4.

2.1.2 Coherent Harmonic Generation

During interaction with an electron bunch, a laser pulse can generate a dip in the longitudinal structure, leading to the emission of CSR at wavelengths above the dimension of the substructure. Using femtosecond (fs) laser pulses, even shorter dimensions than with low-α_c optics are realized. Figure 2.3 shows the principle of Coherent Harmonic Generation (CHG) as employed at the synchrotron DELTA at the Technical University of Dortmund. The laser pulse interacts with the electron bunch inside a first undulator, called modulator, which is tuned to the wavelength of the laser. An undulator is a periodic sequence of dipole magnets with alternating polarity. Thereby the electrons experience a sinusoidal energy modulation depending on their longitudinal position in the bunch. In the following magnetic chicane, electrons with higher energies will move further ahead, while lower-energy electrons move rearwards in the bunch. As a result, micro-bunches appear in the longitudinal charge distribution. With the laser-pulse energy being in the mJ range, the modulation of the longitudinal charge density is typically below 1% [26]. Coherent vacuum-UV radiation is emitted at harmonics of the laser wavelength in the second undulator, called radiator.

In subsequent bending magnets, electrons with different energies travel on dispersive orbits. Thus, off-energy electrons move forwards or backwards in the bunch, leaving a dip in charge density on the sub-mm scale at the position where the laser light has interacted with the electron bunch. This density modulation emits coherent THz radiation when again passing through a bending magnet [27], [UMB+14].

Simulations of typical spectra of the emitted power are depicted in Fig. 2.4(a) along with the simulation of the dip for the bunch first passing by the THz beamline (see Fig. 2.4(b)). Herein, the revolutions of the bunch inside the storage ring after the laser-electron interaction are called "turns", starting with "turn 0" when the bunch passes through the bending magnet of the THz beamline for the first time. The sub-mm dip in the electron bunch generates a THz signal with a broadband spectrum. The subsequent broadening of the dip structure is caused by diffusion and damping. Again, electrons with different energies move on trajectories of various path lengths and

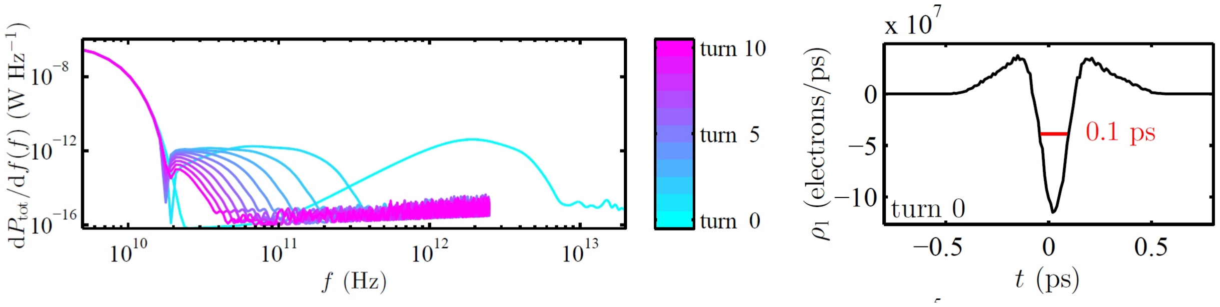

(a) (b)

Fig. 2.4: (a) Spectral power density of the emitted THz signal from Coherent Harmonic Generation (CHG) for the first 11 revolutions of the bunch inside the synchrotron [27, p. 57]. The maximum at low frequencies corresponds to the coherent emission of the overall bunch length, which is not transmitted through the beamline. (b) Electron density modulation on the bunch for "turn 0" [27, p. 55].

thereby change their position inside the bunch which, in turn, leads to different accelerating RF fields. As a result, the peak emission frequency decreases from turn to turn. The "turn 0" signal, in this case, ranges up to a few THz, while "turn 1" is already below 1 THz [27].

Using chirped-pulse beating, a method for intensity modulation of a laser beam, narrowband coherent THz radiation can be generated. Herein, a chirped laser pulse is sent through a Michelson interferometer and, upon interference with itself at variable delays, results in an oscillating signal with adjustable period. As a consequence, multi-cycle, narrowband THz radiation is emitted. The center frequency of the CSR can be selected by adjusting the delay in the Michelson interferometer [27, 28].

CHG is used at DELTA where the beam energy amounts to 1.5 GeV. The laser operates at a wavelength of 800 nm and with pulse lengths of 40 fs (FWHM). CHG is performed with a single bunch filling pattern, where the bunch charge amounts to approximately 10 nC and the overall bunch length is about 100 ps (FWHM) [27].
At UVSOR-III (Ultra-Violet Synchrotron Orbital Radiation) at the Institute of Molecular Science in Japan, a similar laser-induced scheme is employed to generate CSR. UVSOR-III also operates in single bunch mode with a beam energy of 0.75 GeV and a maximum bunch charge of 7 nC at a length of about 300 ps (FWHM) [29, 30]. The laser has a wavelength of 800 nm with a pulse length of 100 – 200 fs [31].
For the detection of CSR from CHG, detectors with a broad frequency range are required, operating from tens of GHz up to several THz. In the case of DELTA, the upper frequency limit is about 7 THz. Additionally, as the amplitude of the emitted THz radiation extends over several orders of magnitude (see Fig. 2.4(a)) the dynamic range has to extend to several tens of dB. With the THz pulse length being linked to the spectral bandwidth, the "turn 0" signal corresponds to a sub-

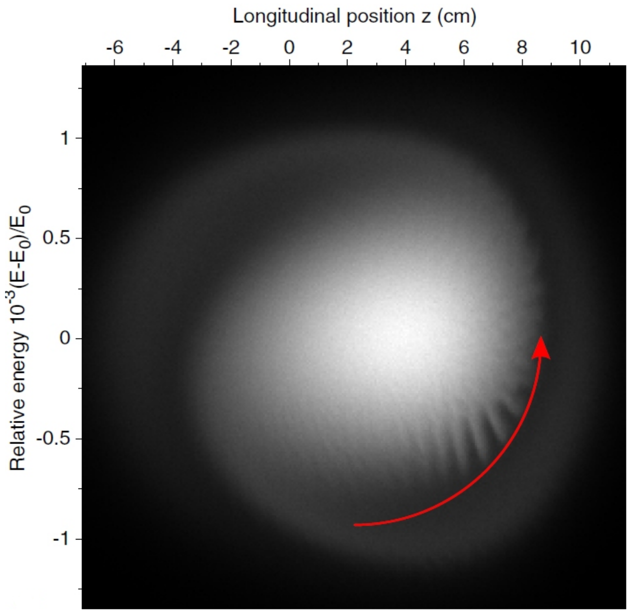

Fig. 2.5: Simulation of the distribution of electrons in the longitudinal phase space at a given time [RES$^+$14a]. The substructure rotates in the direction of the arrow with the synchrotron frequency.

picosecond pulse, which cannot be resolved directly in time. Therefore, the use of a single-shot spectroscopy system would offer the possibility to resolve the structure of the THz pulse in the frequency range.

2.1.3 Spontaneous CSR

Micro-bunching instabilities can also be seen with rather long bunches when a certain current threshold is exceeded. As a result, spontaneous CSR is emitted. Again, an initial random density fluctuation radiates CSR, which then interacts with the bunch itself and thereby amplifies the effect of micro-bunching. As opposed to the case of low-α_c operation, the CSR coming from the overall bunch length is cut off by the vacuum chamber and only the micro-bunching signal is transmitted [32].

Figure 2.5 shows a simulation of the distribution of electrons in the longitudinal phase space at a given time for the UVSOR-III storage ring. The projection of this distribution on the longitudinal coordinate gives the electron density of the bunch. Modulations of the charge density lead to the emission of CSR. The corresponding simulation of the electrical field of emitted CSR is shown in Fig. 2.6. The substructures rotate in phase space as depicted in Fig. 2.5 with the synchrotron frequency (here $\approx$ 23 kHz) and lead to a periodic outburst of THz radiation [RES$^+$14a].

As mentioned before, the overall bunch length amounts to about 300 ps. In single-bunch operation mode, spontaneous CSR is observed above a beam current threshold of approximately 60 mA. The substructures on the bunch are in the mm range and emit CSR with a wavelength of $\lambda \approx 9$ mm, corresponding to about 33 GHz (see Fig. 2.6) [RES$^+$14a]. This frequency can be resolved directly

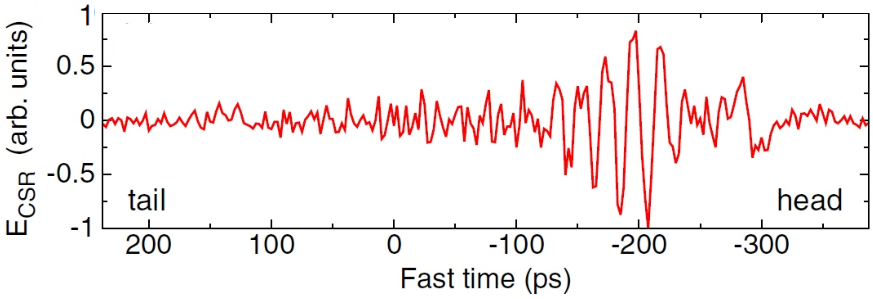

Fig. 2.6: Electrical field of the emitted spontaneous CSR at the point of emission inside the UVSOR-III storage ring [RES$^+$14a]

in the time domain when combining ultra-fast detectors with broadband RF readout. A necessary prerequisite to the detection of the oscillating signal without loosing information on its phase is an electrical-field sensitivity of the detector, the unique quality of the YBCO detector that will be discussed in detail in chapter 6.

2.1.4 Brilliant THz radiation from linear accelerators

Bunch lengths in a linear accelerator (linac) can be up to three orders of magnitude shorter (about 100 fs) than in a circular accelerator with much higher peak powers at the same time. Therefore, THz radiation of even higher brilliance is generated.

At a free-electron laser (FEL), an electron beam, coming from the linac, is passing through a long undulator. The sinusoidal movement of the electron bunch inside the undulator causes the emission of incoherent radiation at a wavelength that depends on the beam energy and the field strength of the undulator. This radiation acts back on the electron bunch leading to a micro-bunching effect which, in turn, causes the emission of CSR. Herein, each bunch only passes once through the undulator [17, 26].

FELs with high repetition rates, such as FELBE as introduced in the following, work with undulators that are embedded in an optical cavity. By adjusting the dimensions of the cavity to the repetition rate of the FEL, the radiation from one bunch is interfering with the next bunch inside the undulator. CSR from the first bunch then feeds back on the bunch and reinforces the micro-bunching.

Ultra-short electron bunches from a linac can also generate coherent transition radiation (CTR), e.g. by passing through a thin metal screen, coherent diffraction radiation (CDR) or bending magnet radiation, much as in a synchrotron. In this case, broadband radiation up to a few THz is emitted [17, 27].

At FELBE, the FEL at the accelerator ELBE in Dresden-Rossendorf, the repetition rate is 13 MHz. With the undulator U100, a frequency range of 1.3 to 15 THz can be accessed with pulse energies of up to 3 μJ. The number of periods of the undulator is 38 [33].

TELBE is the high-field high repetition-rate THz facility, also situated at the accelerator ELBE. Undulator radiation with eight cycles and maximum pulse energies of 100 µJ in the frequency range of 100 GHz up to 3 THz is generated at a repetition rate of 100 kHz [34]. Moreover, broadband CTR and CDR with frequencies up to 3 THz are available at TELBE [11].

Undulator radiation from FELs is multi-cycle and narrowband, thereby suited to probe frequency-dependent characteristics of materials and devices. The repetition rate is much lower than for synchrotron storage rings and usually less than 1 kHz. At the same time, THz pulse energies are magnitudes of order higher. In the particular case of zero-biased electrical-field sensitive detectors, direct detection does not work, as the overall electrical field integrates to zero. This will be explained in more detail in section 6.3.

THz detectors for FELs have to work within a broad frequency and radiation input power range. Due to the time constants that exceed the readout bandwidth of the available electronics, a direct temporal resolution of the THz pulse shape is not feasible. To understand the principles of the lasing mechanism from compressed electron bunches, however, a single-shot resolution of the longitudinal bunch shape is required [35]. Therefore, a spectroscopic detection scheme as proposed for the four-pixel array of YBCO detectors in section 3.4 could be used to monitor the THz spectrum of the emitted CSR. As every bunch only passes once through the beamline, instability phenomena as seen with the bursting CSR at synchrotron storage rings are not occurring at linear accelerators.

2.1.5 Photoconductive antennas

Other than from accelerators, pulsed THz radiation is emitted by photoconductive antennas (PCAs). The operation principle of PCAs relies on the generation of a picosecond current pulse. This excitation is generated by a biased semiconductor when radiated onto with a femtosecond laser pulse above the bandgap. The current pulse contains frequency components in the THz frequency range and can be radiated, when the photoconductor is embedded into an antenna [7, 36].

Typically, two parallel, biased metal stripes, forming a double dipole antenna, are placed on a semiconductor substrate. A laser beam, focused to the center of the antenna arms, generates free carriers when its wavelength exceeds the bandgap of the semiconductor. Those carriers are accelerated between the strip lines by the bias voltage and create a ps current pulse. The carrier life time, i.e. the recombination time of electrons and holes in the photoconductive substrate, determines the decay time of the current pulse, which is directly linked to the radiated frequencies [37].

Low-temperature grown GaAs is a commonly used material for PCAs that offers carrier life times of below 1 ps [38–40].

2.2 Detectors for pulsed THz radiation

The above introduced THz radiation sources impose numerous requirements on detector technologies, not all of them being realizable simultaneously. Firstly, response times are required to satisfy the repetition rate of the electron bunches. At linear accelerators repetition rates as low as a few Hz are possible while they go up to 500 MHz at storage rings. Secondly, when resolving the pulse shape, the time constants have to undercut the bunch length or even that of the substructure, which lie in the (sub-)picosecond region. At the same time, conventional electronics are limited to a resolution of a few ps, when it comes to direct readout. The fastest direct detection system demonstrated so far in the THz frequency range is limited to 16 ps (FWHM) temporal resolution [9]. At even shorter times, single-shot spectral resolution has to be realized in order to deduce the longitudinal (micro-)bunch shape.

The emitted frequencies depend on the mechanism of generation of the THz radiation and the length of the emitting structure. They range from a few GHz up to several THz and may therefore require different radiation coupling concepts. Moreover, varying electron charge levels and a frequency-dependent transmission of THz radiation in free space impose conditions on the dynamic range (DR) of the THz detector. Ultra-high sensitivity can not always be combined with large dynamic ranges, as e.g. smaller detector volumes lead to saturation at relatively low radiation power levels.

In the following, several detector characteristics will be used to assess the advantages of the different detector types. In relation to the real-time analysis of CSR the most important ones are:

(1) Response time, τ

(2) Sensitivity, S
In literature also referred to as responsivity R, it defines the electrical output per optical input of a detection system (in V/W) .

(3) Noise-equivalent power, NEP
The input power required to generate an output signal with a signal-to-noise ratio (SNR) of 1 in a bandwidth of 1 Hz is called the NEP of a detector (in $\mathrm{W}/\sqrt{\mathrm{Hz}}$).

The properties defining the performance of the individual detectors discussed within this section are summarized at the end of the chapter in Tab. 2.1.

2.2.1 Room-temperature detectors

Absolute power measurements can be performed with power meters. One common type of realization is based on the photoacoustic effect. A metal film that is sealed within a gas chamber

changes its temperature and thereby the pressure inside the gas cell upon irradiation. By chopping the THz signal, the resulting modulation of the pressure is detected with a pressure transducer. Furthermore, the use of a Lock-in amplifier (LIA) for readout of the microphone enhances the SNR. Calibration is done by ohmic heating of the metal film [17, 41]. The gas chamber is equipped with THz windows made from a transparent polymer (TPX) for coupling of the radiation [42]. Transmission measurements of TPX can be found in [41, p. 46].
Commercially available power meters with air-filled gas cells reach moderate NEP values of $5\ \mu\mathrm{W}/\sqrt{\mathrm{Hz}}$. The system used in this work is calibrated for the frequency range between 30 GHz and 3 THz. The power meter works with a modulation frequency of about 25 Hz and the integration time amounts to about 1 s [43]. The device is therefore suitable for an integrated measurement of the absolute THz power emitted by a source.

Optoacoustic detection in Golay cells is faster ($\tau_{\mathrm{rise}} \approx 25$ ms) [44]. In a Golay cell a gas volume with a metal film, as described above for the photoacoustic power meter, is combined with a movable mirror as one of the limitation walls of the cell. When the pressure inside the gas cell changes upon absorption of radiation in the metal foil, the mirror moves, thereby distorting an optical signal that is used to detect the movement of the mirror [17]. Golay cells offer low NEP ($\sim 10\ \mathrm{nW}/\sqrt{\mathrm{Hz}}$) and high sensitivities [44].

Pyroelectric sensors work with materials that have a temperature-dependent polarization. The crystal lattice contains bound ions that change their position upon heating, resulting in a polarization. By embedding such a material into two electrodes perpendicular to the direction of polarization, charge is generated during a change of polarization. The sensor thus is a small capacitor, delivering a current upon heating. Herein, the temperature change can be initiated by the absorption of radiation power [7, 45].
The pyroelectric effect itself, meaning the rearrangement of the crystal lattice, is intrinsically very fast and response times on the ps scale would be possible [46]. However, the thermal conductance, that needs to be low in order to enable high sensitivities, makes the detector slow. Also the embedding electronics affect the response time. Since the pyroelectric sensor only produces an output signal during a change of polarization, the incoming radiation signal needs to be modulated, e.g. by the use of an optical chopper.
Commercially available pyroelectric sensors offer response times in the 200 ms range while achieving NEP values of $0.4\ \mathrm{nW}/\sqrt{\mathrm{Hz}}$ [47]. Those detectors can be used to measure even small THz signals (down to 50 nW). However, the response times are far beyond the repetition rates of storage rings.

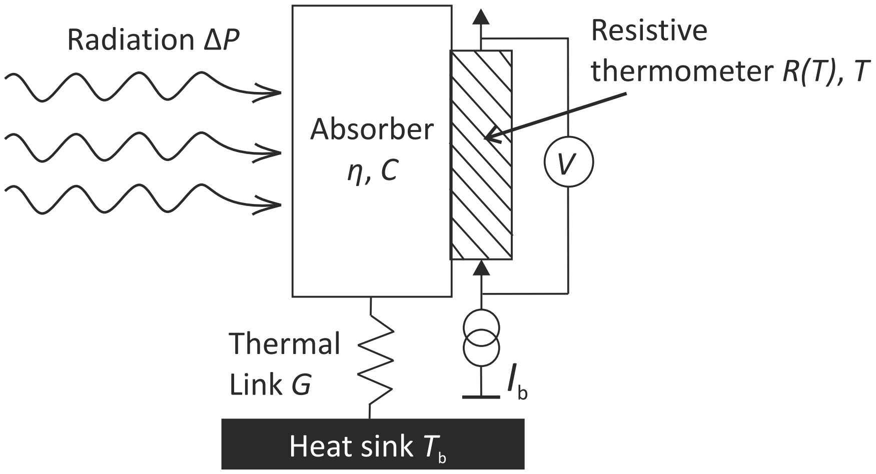

Fig. 2.7: Operation principle of a bolometric detector in composite design with current bias, adapted from [48].

2.2.2 Bolometric direct radiation sensors

As the room-temperature THz detectors presented above are only suitable to integrated power measurements and lack single-turn or even single-bunch resolution, faster detectors are needed to investigate CSR signals. Cooled bolometers therefore are the technology of choice at most THz beamlines.

Theory of the bolometer

Bolometers are resistive thermometers: a change in temperature is translated into a temperature-dependent ohmic resistance, that can be read out via a bias signal. The operation principle of a bolometric detector is depicted in Fig. 2.7. Incident radiation with power variation ΔP is absorbed with an absorptivity of η. The temperature change of the absorber with heat capacity C depends on the incoming radiation power and the heat transfer to the thermal sink at the bath temperature T_b via the thermal link with conductance G. Here, the heat capacitance $C = c_\mathrm{S} \cdot V$ defines the amount of energy that can be stored in the absorber at a given change of temperature ΔT. C depends on the specific heat c_S and the volume of the absorber. The resistive thermometer is biased, in the case of Fig. 2.7 with a current, and the change of resistance is read out as a change in voltage [48]. The special interest in semiconducting and superconducting materials when designing bolometers is explained by the steep temperature dependence of their electrical resistance in distinct temperature ranges.

The absorber and the thermometer can be either realized as the same element (monolithic bolometer) or with a separate thermometer attached to the absorber (composite bolometer). Microbolometers, bolometric detectors embedded in THz antennas, are a special form of bolometers used for THz frequencies. As the dimensions of the detecting volume usually are smaller than the THz wavelengths, the antenna is used to pick up the signal and then couple it to the thermally absorbing detecting element [48].

The temporal evolution of the temperature response can be calculated from the heat flow equation as in [49]:

$$C\frac{\mathrm{d}T}{\mathrm{d}t} + G(T - T_\mathrm{b}) \;=\; \eta \Delta P(t) + RI^2. \tag{2.3}$$

Incoming radiation power and electrical power equal to the energy that is stored in the absorber and the part that is transferred to the thermal sink. The term RI^2 describes Joule heating of the thermometer. With the first-order expansion of the resistance $R = R_0 + (\mathrm{d}R/\mathrm{d}T)\Delta T$, equation 2.3 can be transformed into a time-dependent evaluation of the temperature changes $\Delta T = T(t) - T_b$ by eliminating the time-independent terms:

$$C\frac{\mathrm{d}(\Delta T)}{\mathrm{d}t} + \underbrace{\left(G - I^2\frac{\mathrm{d}R}{\mathrm{d}T}\right)}_{G_\mathrm{eff}}\Delta T \;=\; \eta \Delta P(t). \tag{2.4}$$

Solving this differential equation with the ansatz $\Delta P(t) = P_0 e^{i\omega t}$, with the modulation frequency of ω the radiation, the sensitivity as defined before yields:

$$S_\mathrm{opt} \;=\; \frac{\Delta U}{\Delta P} \;=\; \frac{I(\mathrm{d}R/\mathrm{d}T)\Delta T}{\Delta P} \;=\; \frac{\eta \alpha R I}{\sqrt{G_\mathrm{eff}^2 + \omega^2 C^2}} \;=\; \frac{\eta \alpha R I}{G_\mathrm{eff}\sqrt{1 + \omega^2\tau^2}}, \tag{2.5}$$

with the temperature coefficient $\alpha = (\mathrm{d}R/\mathrm{d}T)R^{-1}$ and the thermal time constant $\tau = C/G_\mathrm{eff}$ [17, 50]. The factor $i\omega$ comes from the derivative of the temperature change ΔT in equation 2.4.

The optical sensitivity S_opt, given in equation 2.5, is the magnitude of the detector voltage per radiated power. As compared to that, the electrical sensitivity S_el takes into account the actual absorbed power with $S_\mathrm{opt} = \eta S_\mathrm{el}$. Thereby, S_el is an intrinsic property of the detector. The values of the sensitivity given in Tab. 2.1 for the different THz detectors refer to the optical sensitivity of the complete detection systems.

G_eff, as defined in equation 2.4, denotes the effective thermal conductivity. Joule heating causes an electro-thermal feedback that effectively changes G. For superconductors the resistance increases with increasing temperature, giving rise to higher Joule heat. Thereby, the effective thermal conductance G_eff decreases. At the same time, the time constant ($\tau = C/G_\mathrm{eff}$) increases [51].

The heat capacitance depends on the volume V of the absorbing material and the thermal conductance for planar structures on a substrate, acting as a heat sink, is proportional to the surface A of the detector. Thereby, the time constant of thin-film bolometers varies with the thickness of the absorber [52, 53].

For a high sensitivity, the detector should have an absorption coefficient close to 1. Moreover, the geometry influences the sensitivity. Depending on the type of incoming radiation, two cases can be distinguished:

(1) Continuous-wave (CW) radiation with the chopping frequency $f = \omega/2\pi$: $\omega\tau \ll 1$
Neglecting the term $\omega\tau$ transforms equation 2.5 into

$$S_{\mathrm{opt}} \approx \frac{\eta\alpha RI}{G_{\mathrm{eff}}} = \frac{\eta\alpha RI}{G - I^2 \mathrm{d}R/\mathrm{d}T}. \tag{2.6}$$

Small thermal conductance G increases sensitivity, however this is at the expense of an increased time constant τ [54].

(2) Large modulation frequencies, pulsed operation: $\omega\tau \gg 1$
In the high-frequency limit thermal conductance drops out of equation 2.5 and small heat capacitances entail large sensitivity:

$$S_{\mathrm{opt}} \approx \frac{\eta\alpha RI}{\omega C} \tag{2.7}$$

The sensitivity is frequency independent at low modulation frequencies and rolls off at high frequencies with the 3 dB value at $\omega\tau = 1$ [55].
The NEP can be determined experimentally from the sensitivity and from V_{n}, the noise voltage divided by the square root of the detection bandwidth [54]:

$$\mathrm{NEP} = \frac{V_{\mathrm{n}}}{S} \tag{2.8}$$

Semiconducting bolometers

Bolometers often operate at low temperatures, thereby decreasing the heat capacitance while keeping the absorption constant. Moreover, for semiconductors, the temperature coefficient of resistance is increased at low temperatures, leading to higher sensitivities, while the thermal noise is reduced.
Composite systems, based on heavily doped Si or Ge thermometers combined with sapphire or diamond absorbers painted in black, are a common type of bolometer [56, 57]. Here, the resistances are strongly decreased by the doping level, since the resistances of intrinsic semiconductors are too high to allow for coupling to a low-noise amplifier at low temperatures. Conduction is based on a hopping process of electrons from one dopant atom to another, yielding an exponential temperature dependence of the resistance [50].
Coupling of radiation to the bolometer is usually done with a cone, e.g. of Winston type. Semi-

conducting bolometers offer high sensitivities, while being relatively fast, as compared to room-temperature detectors, with response times in the µs range [17]. Specific numbers can be found for a composite Si bolometer in Tab. 2.1. Si bolometers are widely used at beamlines and often serve as detectors for Fourier transform infrared (FTIR) spectrometers. Their NEP can be optimized to less than 1 $\mathrm{fW}/\sqrt{\mathrm{Hz}}$, however this is at the expense of response time, as discussed before [58]. In any case, the time constants of semiconducting bolometers are beyond the repetition rate of the synchrotron radiation pulses.

InSb hot-electron bolometers

If photons are absorbed directly by the electron system rather than warming the whole atomic lattice, the detector is no longer a classical bolometer. At very low temperatures in semiconductors radiation can be absorbed by free carriers, causing intraband transitions. Hot electrons which are at thermal equilibrium above the lattice temperature are thereby generated. This change in electron temperature initiates a change of the electron mobility, which results in the bolometric effect of temperature-dependent resistance. Such detectors are called hot-electron bolometers (HEB) [59].
The hot-electron effect in semiconductors requires weak coupling between the carriers and the lattice. In high carrier mobility materials, such as *n*-doped InSb, the effect can therefore be seen at low temperatures (~ 4.2 K), where the electron-electron interaction time τ_{ee} is orders of magnitude smaller than the electron-phonon interaction time $\tau_{\mathrm{ep}} \approx 300$ ns [60]. InSb HEBs offer response times of hundreds of ns and low NEP (see Tab. 2.1) [61]. However, their operation is limited to below 1 THz as the absorption rapidly falls off at higher frequencies [17].

Superconducting HEBs: the two-temperature model

Due to their steep transition from the normal state to superconductivity, superconductors offer large temperature coefficients of resistance and are therefore at the base of ultra-sensitive bolometers. By exploiting the hot-electron effect in superconductors, sensitive and fast sensors can be built from thin-film superconducting microbridges on dielectric substrates.
The operation principle of a superconducting HEB is depicted in Fig 2.8 in accordance with the two-temperature (2T) model, that was first introduced by Kaganov *et al.* for hot electrons in metals [13]. The 2T model assumes the HEB to be near its critical temperature T_{c}, such that the Cooper pair density is small and the quasiparticles can be regarded as normal electrons. In this case, their heat capacitance C_{e} is assumed to be temperature independent in the vicinity of T_{c}. Three subsystems are then distinguished: the electron and phonon system of the thin film and phonons in the substrate [62]. Thermalization within the electron and phonon subsystem is assumed to be instantaneous and uniform.

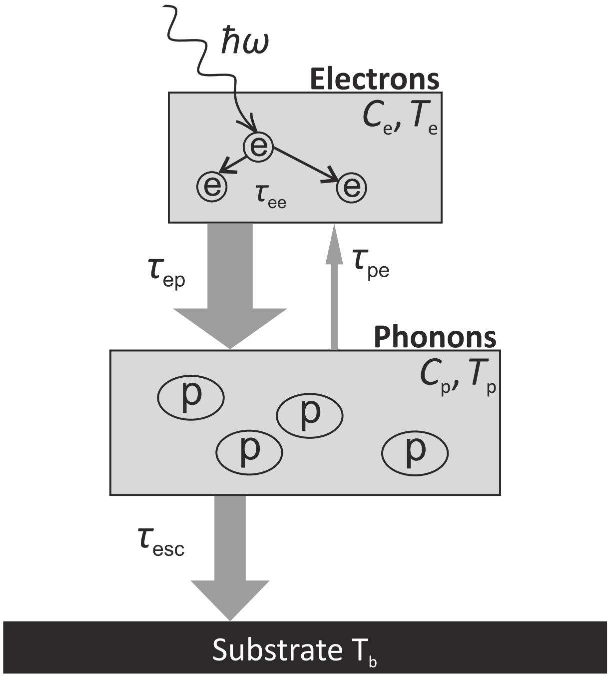

Fig. 2.8: Schematic of a phonon cooled hot-electron bolometer, adapted from [13].

For small deviations from T_c, the heat balance equations simplify to two coupled linear differential equations:

$$\frac{\mathrm{d}T_e}{\mathrm{d}t} = -\frac{T_e - T_p}{\tau_{ep}} + \frac{1}{C_e}\Delta P, \tag{2.9a}$$

$$\frac{\mathrm{d}T_p}{\mathrm{d}t} = \frac{T_e - T_p}{\tau_{pe}} - \frac{T_p - T_b}{\tau_{esc}} = \frac{C_e}{C_p}\frac{T_e - T_p}{\tau_{ep}} - \frac{T_p - T_b}{\tau_{esc}}. \tag{2.9b}$$

Radiation power ΔP in the form of incoming photons is directly absorbed by the electron system, leading to a rise of the temperature T_e within the thermalization time τ_{ee}. Hot electrons then transfer their energy to the phonons with the time constant τ_{ep}, thereby increasing the phonon temperature T_p. Those two processes are described in equation 2.9a. Subsequently, phonons relax to the substrate (T_b) at a rate defined by their escape time τ_{esc} [7, 13]. Moreover, energy backflow from the phonon system to the electron system can occur, where the ratio of the heat capacitances C_p/C_e determines the extent of this effect. The characteristic phonon-electron interaction time τ_{pe} can be replaced by τ_{ep} via [13]:

$$\frac{\tau_{pe}}{\tau_{ep}} = \frac{C_p}{C_e} \tag{2.10}$$

The above-described process refers to the principle of a phonon-cooled HEB. A second possible mechanism is cooling by diffusion of hot electrons to the metal contacts that connect the detector to an external readout. Diffusion cooling requires the electron-diffusion time to be smaller than the electron-phonon interaction time [7, 63]. High electron-diffusion constants and ultra-short lengths of the superconducting microbridge are therefore prerequisites for a diffusion-cooled HEB. This cooling mechanism is mainly observed in Nb HEBs due to their relatively large electron-phonon interaction time of $\tau_{ep} \approx 1$ ns at 4.2 K [7, 13].

Superconducting NbN HEBs

For 3.5 nm thick NbN films and 100 fs long optical pulses, response times of $\tau_{ee} = 6.5$ ps, $\tau_{ep} = 10$ ps and $\tau_{esc} = 38$ ps were found. With $C_p/C_e = 6.5$ the energy backflow to the electron system amounts to 15% and the response time of the HEB is determined by the average electron cooling time [13]. Commercially available NbN HEBs operate at 4.2 K and offer response times of 50 ps combined with high sensitivity [64]. By the use of a NbN HEB it was first possible to resolve single bunches in a multi-bunch environment with a direct THz detector [8]. The response time still does not allow for the observation of the pulse shape of the CSR coming from the single bunches.
The high-temperature superconductor $YBa_2Cu_3O_{7-x}$ (YBCO) can be employed to design HEBs with even faster intrinsic response times. This will be discussed in more detail in section 3.3.1.

2.2.3 Zero-biased Schottky diode detectors

A Schottky-barrier diode (SBD) in its simplest layout is a metal-semiconductor junction with an *n*-doped semiconductor. A potential barrier and depletion region are formed upon contacting of the two materials. The SBD is a majority-carrier device, where in the case of an *n*-doped material thermally excited electrons in the conduction band overcome the barrier or tunnel through it in forward direction [65]. SBDs offer ultra-fast intrinsic response times in the sub-picosecond range as no slow recombination processes are involved in the conduction. The response time is limited by the junction capacitance and its differential resistance. Response times of complete detection systems will be discussed below.
Common SBDs are based on a platinum-GaAs (*n*-doped) contact [66]. Roll-off frequencies between 2 and 10 THz have been reported [67]. However, these systems have differential resistances of several Teraohms at zero bias and therefore need to be biased in forward direction. This adds additional shot noise to the readout and increases the NEP of the detector.

For the detection of CSR, special planar InGaAs/InP SBDs are employed. Due to their low barrier height they allow for the zero-bias operation of the Schottky contact. The roll-off frequency was determined to be about 1 THz [73]. Planar diodes from ACST GmbH are flip-chip mounted and bonded by thermocompression to a logarithmic spiral antenna, ensuring broadband operation of the detection system. Below 1 THz, the optical sensitivity of the system amounts to 250 V/W. As the dynamic range is limited to about 25 dB, the sensitivity falls off to 120 V/W at input powers greater than 20 µW [70, 71]. Response times of 20 ps (FWHM) have been demonstrated with a

Detector type	***f*** **(THz)**	***S*** **(V/W)**	**NEP** **($W/\sqrt{Hz}$)**	**τ** **(s)**	***T*** **(K)**
Absolute power meter	$0.03-3$	-	$5 \cdot 10^{-6}$	1.0	300
Pyroelectric sensor	$0.01-30$	$1.4 \cdot 10^{5}$	$4 \cdot 10^{-10}$	0.2	300
Golay cell	$0.1-20$	$\sim 10^{4}$	$\sim 10^{-8}$	$25 \cdot 10^{-3}$	300
Composite Si bolometer	$0.15-20$	$2.4 \cdot 10^{5}$ *	$1.2 \cdot 10^{-13}$	10^{-3}	4.2
InSb HEB	$0.06-0.5$	$3.5 \cdot 10^{3}$	$7.5 \cdot 10^{-13}$	$300 \cdot 10^{-9}$	4.2
NbN HEB	$0.1-6$	-	$3 \cdot 10^{-13}$	$50 \cdot 10^{-12}$	4.2
Zero-biased SBD (ACST)	$0.05-1$	250	$5 \cdot 10^{-10}$	$20 \cdot 10^{-12}$	300
Zero-biased SBD (VDI)	$0.22-0.33$	$1.5 \cdot 10^{3}$	$4 \cdot 10^{-12}$	$25 \cdot 10^{-12}$	300

Table 2.1: Overview of direct detector technologies that are commonly in use at THz beamlines and performance numbers from commercial providers [17, 41, 43, 44, 47, 61, 64, 68–72]. f denotes the frequency range, S the optical voltage sensitivity (except for values marked with a *, where only electrical sensitivity was specified), DR the dynamic range and T the operation temperature of the detector.

detection system with a readout bandwidth of 18 GHz. The intrinsic response time was estimated to be less than 6 ps [74].

Narrowband detection in the THz frequency range is offered by waveguide-coupled SBDs from Virginia diodes [75]. Those detectors achieve higher responsivities and lower NEP while maintaining fast response times. One example of such a detector is listed with its characteristics in Tab. 2.1. Other configurations are possible, when combining the zero-biased SBD with different waveguides [72].

The highly nonlinear behavior of the current-voltage ($I(V)$) characteristic of SBDs serves for the detection of THz radiation. At the same time, the $I(V)$ characteristic also shows the rectifying behavior of the SBD. Therefore, when operated without bias, only forward directed pulses of the electrical field of THz radiation can be detected.

Table 2.1 summarizes the commercially available direct THz detectors that are in use at THz beamlines. The detectors introduced in this section, except the zero-biased SBDs, have in common that they are sensitive to the intensity of radiation rather than to the electrical field. Thereby, the information on the phase of the THz signal is lost. Schottky diodes offer the fastest response times of the detectors discussed here. However, the minimum time constants of 20 ps are not sufficient to resolve the substructure on the bunches during bursting in short-bunch operation. Adding to that, due to its diode behavior the SBD is rectifying and will only detect oscillations of the electrical field in forward direction. This is fundamentally different for the YBCO detector, as will be discussed in chapter 6.

2.3 Basics of THz optics

THz optics are referred to as quasi-optics because the dimensions of the collimated beam are only a few times larger than the propagating wavelength. In this case, the wavelengths are not negligible as compared to the dimensions of the optical components and diffraction effects have to be taken into account. Gaussian beam optics describe best the process of THz wave propagation in free space [76]. THz radiation can also be transmitted via waveguides as in radio technology. However, losses in waveguides and cables rise with higher frequencies and propagation in electrical components becomes increasingly difficult. Planar antenna structures and horns are therefore employed to couple guided waves to free space [17].

Gaussian beams have Gaussian intensity distributions with radial symmetry in the most simple case. Focusing or defocusing of the beam does not change the Gaussian nature but only the size of the distribution. Herein, the beam waist radius, the distance from the optical axis where the intensity drops to $(1/e)^2$, is defined as:

$$w(z) = w_0 \sqrt{1 + \left(\frac{z}{z_\mathrm{R}}\right)^2} \tag{2.11}$$

with the direction of propagation z and the Rayleigh range z_R. In equation 2.11, w_0 is the minimum of the beam waist at the position at which the phase front is planar. The Rayleigh range, also called confocal distance, describes the length scale at which the beam propagation changes from a near-field to a far-field dominated region:

$$z_\mathrm{R} = \pi \frac{w_0^2}{\lambda}. \tag{2.12}$$

Beyond z_R, beam divergence becomes significant while below the confocal distance, the beam is essentially collimated. Apertures with dimensions smaller than 4.6 w can cause disturbances such as far-field ripples. Therefore, optical components, e.g. mirrors, have to be large with respect to w. By designing the optical components at least 4 times larger than the beam waist, diffraction effects can be avoided and 99.97% of the radiation power is confined within the aperture [17, 76].

An important effect observed in Gaussian beam optics is the Gouy phase shift [78]. When evolving through its focus from $-\infty$ to $+\infty$, the beam acquires an additional phase shift of π as compared

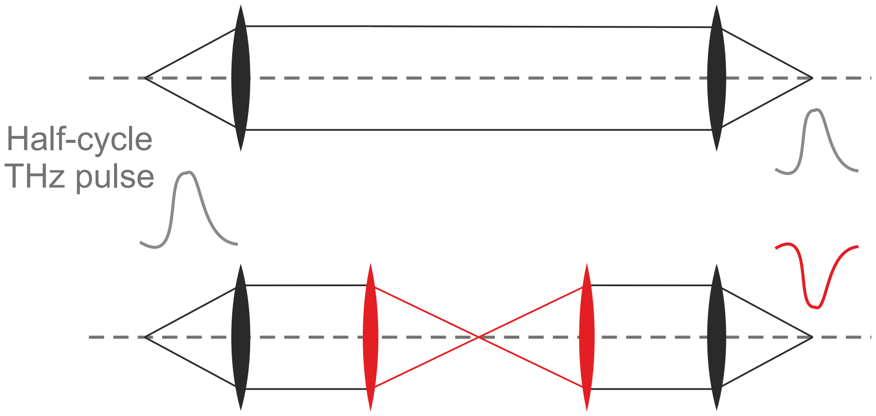

Fig. 2.9: Experimental setup for the observation of the Gouy phase shift, adapted from [77].

to a plane wave. Here, the Gouy phase shift arises from the superposition of plane waves with an angular spread, forming the Gaussian beam. The transverse constituents of the wave vector reduce the magnitude of the axial component, resulting in a phase shift. For any distance z, the Gouy phase shift Φ_G can be calculated as follows [79]:

$$\Phi_\mathrm{G} = -\arctan\left(\frac{z}{z_\mathrm{R}}\right). \tag{2.13}$$

As a direct consequence, a single or half-cycle THz pulse experiences a polarity reversal when evolving through its focal point. The infinity dimension can be projected to experimentally accessible conditions by generating a collimated beam and then introducing a focal point, as depicted in Fig. 2.9 [77]. The Gouy phase shift will be exploited in chapter 6 in order to test the electrical field sensitivity of the YBCO detector.

2.4 Conclusions of chapter 2

Circular and linear accelerators in dedicated operation modes emit brilliant THz radiation that can be used to probe the operation of direct THz detectors. Depending on the scheme of radiation generation, narrowband multi-cycle and broadband single-cycle THz pulses from a few GHz up to several THz with pulse lengths in the (sub-)picosecond range are provided.

At the same time, the understanding of micro-bunching instabilities at synchrotron storage rings and the striving for ever shorter compressed bunches in FELs demand for the single-shot resolution of the THz pulses emitted by these sources. Existing direct detector technologies that are commonly in use at THz beamlines are operable over a broad frequency range and offer moderate to high sensitivities. Amongst them are room-temperature detectors, such as Golay cells and Pyroelectric sensors, cooled semiconducting bolometers and HEBs based on superconducting materials. Zero-biased rectifying SBDs offer the fastest response times of all these detection systems.

Yet, none of them exhibits the (sub-)picosecond response times required for the analysis of CSR. This motivates the use of an intrinsically fast material system in combination with broadband state-of-the-art readout electronics or a spectroscopy system with single-shot resolution based on a fast detector. Therefore, in the following chapter, the material system $YBa_2Cu_3O_{7-x}$ (YBCO) will be introduced as a promising candidate for the real-time detection of picosecond THz pulses.

3 The detector material YBCO

Due to its high critical temperature and its relative simplicity in composition, $YBa_2Cu_3O_{7-x}$ (YBCO) is the most commonly used and the best-probed material amongst the cuprate high-temperature superconductors. In recent years, the material system has been used as ultra-fast radiation detector for optical wavelengths and the mechanisms of the detection have been studied extensively.

This chapter introduces the superconducting material system and its specific features when deposited as thin film. The technological background for chapters 4 and 5 is reviewed as well as the theoretical basis needed to analyze and understand the results discussed in chapters 6 and 7. In particular, section 3.3 contains a summary of the current state of research for optical and THz excitations of thin-film YBCO detectors. The chapter concludes with an overview of the YBCO detector-chip design.

3.1 Properties of the high-temperature superconductor YBCO

YBCO was discovered in 1987 by Wu *et al.*, after the high-temperature superconductivity in cuprates had been found by Bednorz *et al.* in the $La_{0.85}Ba_{0.15}CuO_{3-y}$ system one year earlier [80, 81]. With a transition temperature of 92 K, it was the first superconducting material that could be cooled with liquid nitrogen.

3.1.1 Crystalline structure of YBCO

The $YBa_2Cu_3O_{7-x}$ (YBCO) unit cell with its two limiting cases ($x = 0$ and 1) is depicted in Fig. 3.1. The superconducting $YBa_2Cu_3O_7$ phase has an orthorhombic lattice with the lattice parameters $a = 3.82$ Å, $b = 3.89$ Å and $c = 11.68$ Å [82]. The Y atom is sandwiched between two CuO_2 planes. The unit cell is terminated by CuO planes that contain the one-dimensional CuO chains in b-direction. Two BaO planes are in between the CuO_2 planes and the planes containing the CuO chains. YBCO thus has a distorted, oxygen-deficient perovskite-like structure (ABO_3) which is tripled along the c-axis with yttrium and barium as the central cations [83].

Upon removal of the oxygen atoms in the CuO chains, the crystal lattice transits to a tetragonal structure with $a = b = 3.86$ Å and a prolonged c-axis, $c = 11.82$ Å (see Fig. 3.1(b)) [82]. $YBa_2Cu_3O_6$ is an antiferromagnetic insulator.

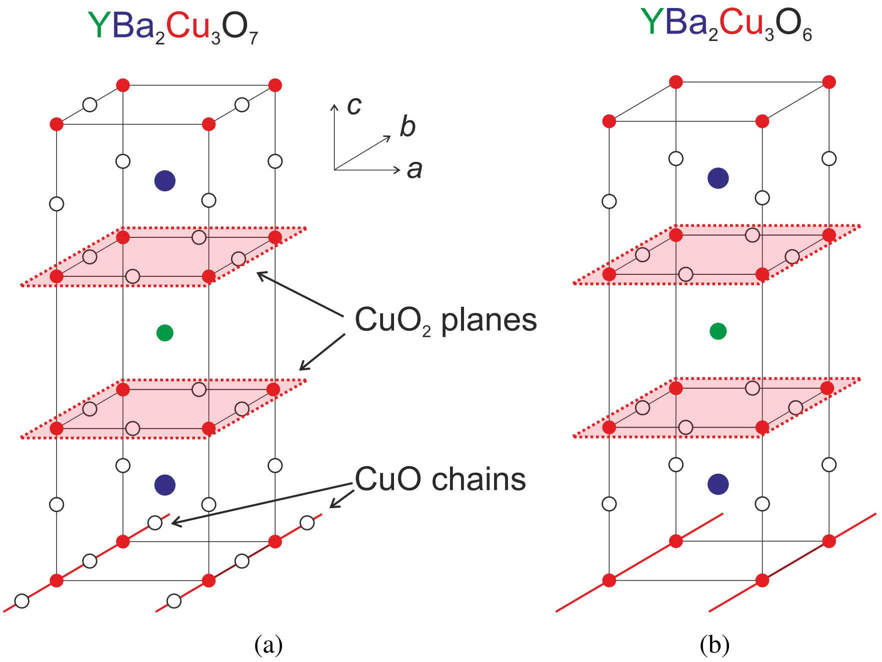

Fig. 3.1: YBCO unit cell: (a) orthorhombic $YBa_2Cu_3O_7$ phase and (b) tetragonal $YBa_2Cu_3O_6$ phase.

Accordingly, the critical temperature in YBCO depends strongly on the oxygen depletion x, this phenomenon is depicted in Fig. 3.2(a) [82]. For small depletion values $0 < x < 0.2$, the critical temperature is almost constant and at its maximum value of about 90 K. A second plateau is seen at ≈ 60 K for $0.3 < x < 0.5$. In between these two plateaus, T_c decreases and above $x = 0.5$ the critical temperature drops sharply to zero. This coincides with the orthorhombic to tetragonal transition at $x \approx 0.65$.

Superconductivity is therefore assumed to occur in the two-dimensional CuO_2 planes with the CuO_x chains acting as a charge reservoir for holes. It has been verified experimentally that the bond length between the Cu atoms in the CuO_x chains and the O atoms in the BaO planes reduces upon removal of oxygen atoms from the CuO_x chains. This process is causing the removal of charge carriers from the conducting CuO_2 planes [82].

Figure 3.2(b) shows the phase diagram of YBCO. During deposition at high temperatures, YBCO grows in the tetragonal phase and has a transition to the orthorhombic phase during annealing at around 600 °C [84]. A typical pulsed-laser deposition process, as used in this work, is indicated by the line in the oxygen pressure vs. temperature diagram.

3.1.2 Anisotropy of the superconducting properties in YBCO

YBCO belongs to the group of type-II superconductors, characterized by a Meissner and a mixed state with critical magnetic fields B_{c1} and B_{c2}. Due to the large anisotropy in the crystal structure ($c \gg a, b$), a high level of anisotropy is also found in the superconducting parameters. The

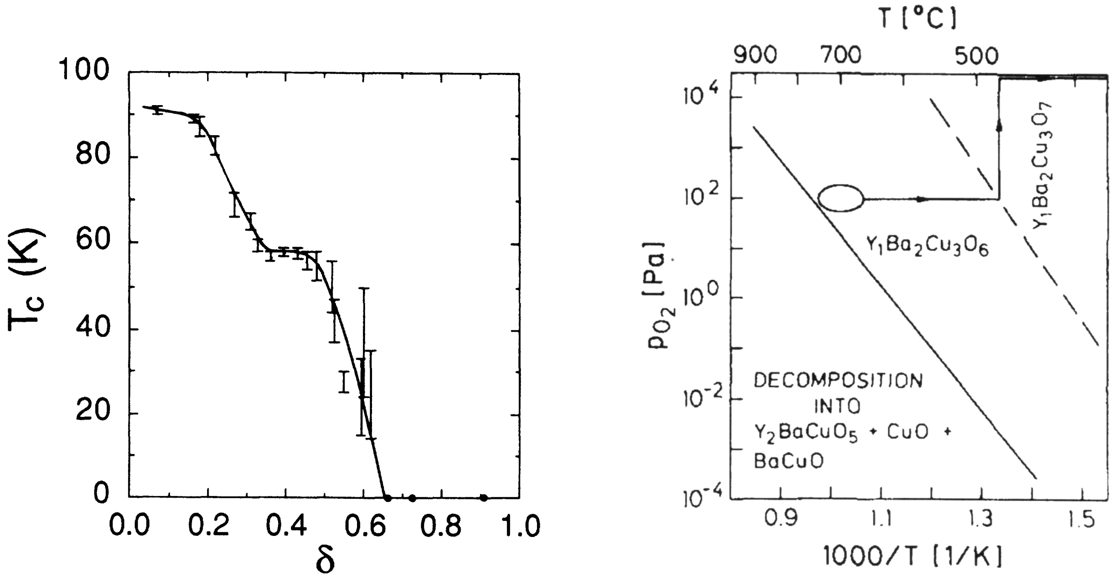

(a)

(b)

Fig. 3.2: (a) Dependence of the critical temperature on the oxygen depletion in YBCO [82], (b) phase diagram of the tetragonal and orthorhombic YBCO phases [84].

anisotropy is described by the ratio of the effective masses along the crystal dimensions: $\gamma = (m_c/m_{ab})^{1/2}$, with $\gamma \approx 7$ for YBCO [85].

With the BCS coherence length ξ being proportional to the Fermi velocity and anti-proportional to T_c, the cuprates are characterized by extremely short coherence lengths. For YBCO, $\xi_{ab}(0) \approx 15$ Å and $\xi_c(0) \approx 2$ Å were found. Thereby, the upper critical fields amount to about 150 T parallel to the *a*-*b*-plane and $B_{c2}||c \approx 40$ T. As a consequence of the short coherence lengths, YBCO thin films are especially susceptible to defects in the crystal lattice.

The magnetic penetration depth depends inversely on the superfluid density $\lambda^2 \propto 1/n_S$, which is small in YBCO compared to the low-temperature superconductors. Thus, large values of $\lambda_{ab}(0) = 150$ nm and $\lambda_c(0) = 600$ nm in YBCO were found experimentally. The first critical magnetic fields that can be derived from λ are $B_{c,1} \perp c \approx 9$ mT and $B_{c,1}||c \approx 50$ mT [83, 85–87].

As the coherence lengths in YBCO are very short, the dirty limit approximation cannot be used when describing the behavior of the *c*-axis oriented YBCO films. The electron mean free path l_0 decreases from $l_0 \approx 2500$ Å at 15 K to about 90 Å at 90 K [88]. YBCO thin films, therefore, always are in the clean limit ($\xi \ll l_0$) [89]. Moreover, the film thickness is always larger than the Ginzburg-Landau coherence length as the height of the unit cell exceeds ξ_c.

3.1.3 Structure and magnitude of the energy gap in YBCO

The energy gap of the high-temperature superconductors has been the matter of numerous investigations. As with the conventional superconductors, far-infrared absorption and reflectance measurements were undertaken to find the gap. However, in a clean superconductor the gap frequency is not seen as a sharp feature in the optical conductivity, therefore Δ cannot be extracted from those measurements. It was shown that the absorption onset seen around 140 $\mathrm{cm}^{-1} \mathrel{\widehat{=}} 4.2$ THz and the peak around 500 $\mathrm{cm}^{-1} \mathrel{\widehat{=}} 15.0$ THz are also visible above T_c and therefore do not mark the gap [89, 90]. The latter one was later identified with the pseudogap from which the energy gap evolves below T_c. As a direct consequence, in the cuprates $\Delta(T)$ does not go to zero at T_c [91].

By measurements of the phase of the superconducting order parameter in YBCO, the energy gap was found to vary in k-space as $\Delta(\vec{k}) = \Delta_0 \left[\cos(k_\mathrm{x}a) - \cos(k_\mathrm{y}a)\right]$, with Δ_0 being the maximal gap value and a the in-plane lattice parameter. Thereby, the order parameter in YBCO has d-wave symmetry [92]. In particular, the gap has nodes in the $[110]$ directions of the $\mathrm{CuO_2}$ planes and maxima in the orthogonal (a- and b-) directions of the $\mathrm{Cu-O}$ bonds [93]. From the d-wave symmetry, it becomes evident that the gap value depends on the direction of the excitation relative to the crystal lattice. In this work, the current flows in the a-b-plane parallel to the a- or b-axis, such that the maximal gap value is assumed to apply.

Measurements of the gap by scanning tunneling microscopy yielded a maximum gap value of $\Delta = 28$ meV $\mathrel{\widehat{=}}$ 6.8 THz [94]. A range of $20-25$ meV (corresponding to $4.8-6.0$ THz) was found for the gap from Andreev-Saint-James reflection measurements [95].

As compared to the low-temperature superconductors, for which the gap value is typically below 1 meV, the gap in YBCO is fairly high. Thus, the absorption of radiation in the THz region (1 THz $\mathrel{\widehat{=}}$ 4.1 meV) corresponds to a sub-gap excitation.

The temperature dependence of the gap was measured by Polturak *et al.* They found a dependence that is similar to the behavior of conventional BCS superconductors, such that the gap is nearly constant at low temperatures and varies as

$$\frac{\Delta_0(T)}{\Delta_0(0)} = 1.74(1-t)^{1/2}, \tag{3.1}$$

with the reduced temperature $t = T/T_\mathrm{c}$, near T_c [85, 96].

Recent studies on single-electron transistors made from YBCO revealed a full gap in nanoscaled under-doped YBCO islands that points towards an order parameter of the type $d_{x^2-y^2} + is$ or $d_{x^2-y^2} + id_{xy}$. However, the additional gap is three orders of magnitude smaller than the maximum value of the d-wave gap ($\Delta_\mathrm{s} = 10$ µeV @ 73 mK) [97].

3.1.4 Vortices in cuprates

According to the Lawrence-Doniach model, YBCO transits from a continuum model at higher temperatures and thus higher coherence lengths in c-direction to 2D superconductivity in the $\mathrm{CuO_2}$

planes coupled by Josephson tunneling far below T_c. The transition temperature is about 78 K in bulk YBCO [85]. In layered cuprate superconductors, the supercurrents of vortices are confined to the CuO_2 planes, and thus called pancake vortices. Magnetic field in c-direction penetrates as a stack of pancake vortices [98].

When considering the movement of vortices in superconducting thin films, three cases can be distinguished: The case of phase-slip centers resulting from Cooper-pair breaking in one-dimensional films with widths substantially smaller than the coherence length ($w \ll \xi$). In YBCO this case can be safely neglected as the coherence lengths are in the range of a few nanometers, even at temperatures above absolute zero. For dimensions $w \gg \lambda_{\mathrm{eff}}$, with the Pearl length $\lambda_{\mathrm{eff}} = \lambda^2/t$ describing the effective magnetic penetration depth in thin films ($t < \lambda$), resistivity stems from Pearl vortices moving due to the presence of a transport current. The velocity of the moving vortices is determined by the Lorentz force due to the applied current and by the viscous force. In the intermediate case ($\xi < w < \lambda_{\mathrm{eff}}$), the sample has 2D geometry but is too small for a Pearl vortex to be placed in the sample. Phase-slip lines then are causing the resistive state [99].

In phase-slip lines with nonuniform order parameter, the propagating waves carrying the order parameter singularity are termed kinematic vortices. It is important to note that a kinematic vortex does not have a critical velocity as opposed to Abrikosov (Pearl) vortices, and can move with any velocity up to infinity. The more uniform the current is distributed in the sample, the faster kinematic (anti-)vortices move. The speed of the kinematic vortices increases also with decreasing bridge width. In this model, kinematic vortices with infinite velocity are conventional phase-slip lines [100].

Abrikosov or Pearl vortices exhibit a critical velocity v_c, where the viscous damping force becomes maximum with the viscous damping coefficient:

$$\eta(v) = \frac{\eta(0)}{1+(v/v_c)^2}. \tag{3.2}$$

In YBCO $v_c \approx 10^3$ m/s [101].

Vodolazov and Peeters developed a model that predicted the rearrangement of a triangular Abrikosov (Pearl) vortex lattice into quasiphase-slip lines at vortex velocities larger than v_c. The transformation results from the modified shape of the vortex cores to an elongated form due to finite inelastic electron scattering time τ_{in}. This process leads to the acceleration of the vortices and the formation of vortex lines [102].

3.1.5 Properties of thin YBCO films

It was observed experimentally that when growing ultra-thin YBCO layers, the monolayers (ML) always consist of a full unit cell in height [103]. The reason to this is that the atomic layer containing the CuO chains is the one with the lowest surface energy and thus the thermodynamically preferred crystal termination. This explains also why c-axis growth is thermodynamically favorable. However, c-axis growth requires a large amount of surface diffusion. In turn, a-axis growth is kinetically favorable, since active crystal growth sites then are available all over the surface of the film. Therefore, lower substrate temperatures (below 600 °C) or high supersaturation values favor a-axis growth. In this work, purely c-axis oriented YBCO films were aimed for during deposition. The c lattice parameter in thin films differs from the bulk value $c_{\mathrm{bulk}} = 11.68$ Å. It was discussed earlier (see section 3.1.1) that the c-axis expands with increasing oxygen deficiency x. However, in thin films the minimum value of c is not reached, even for optimum oxygen concentration. Ye *et al.* found a minimum c-axis length of 11.74 Å for 150 nm thick YBCO films on MgO substrates. The expansion of the c-axis was accounted for defects introduced by the lattice mismatch or deposition faults [104].

With the coherence length in c-direction being smaller than the distance between two adjacent CuO planes, the question arises whether an isolated single unit-cell layer exhibits superconductivity. Superlattices from YBCO and $\mathrm{PrBa_2Cu_3O_{7-x}}$ (PBCO) were deposited to investigate the behavior of ultra-thin YBCO films and a reduced, yet non-vanishing critical temperature of zero resistance $T_{\mathrm{c,0}}$ was found for isolated YBCO thin films [105–107]. Only for YBCO thicknesses smaller than unit-cell height the films showed semiconducting behavior. The reduction of critical temperature was accounted for by the Kosterlitz Thouless transition. This is also supported by the fact that T_{c} increases with decreasing thickness of the PBCO interlayers, meaning that the high T_{c} is to a certain extent due to the coupling between adjacent YBCO unit cells [105].
Li *et al.* found a zero-resistance critical temperature of $T_{\mathrm{c,0}} \approx 70$ K for four unit-cell thick, isolated YBCO films ($t_{\mathrm{YBCO}} = 48$ Å). The single ML of YBCO has a critical temperature of $T_{\mathrm{c,0}} \approx 10$ K for nine MLs of isolating PBCO [105].

3.2 YBCO technology: thin-film growth and patterning

3.2.1 Basics of thin-film growth

Depending on the conditions during the deposition of ultra-thin films, different epitaxial growth modes can be realized, as shown in Fig. 3.3 [108]. The average diffusion length l_{D} of adatoms, meaning atoms from the vapor that were adsorbed on the surface of the substrate, depends on the diffusion coefficient [109]

$$D_{\mathrm{S}} = D_0 \exp\{-\varepsilon_{\mathrm{D}}/kT_{\mathrm{Sub}}\} \tag{3.3}$$

being determined by the substrate temperature T_{Sub} and the activation energy for diffusion ε_{D}. The diffusion length and thus the diffusion coefficient have to be high enough to ensure that adatoms

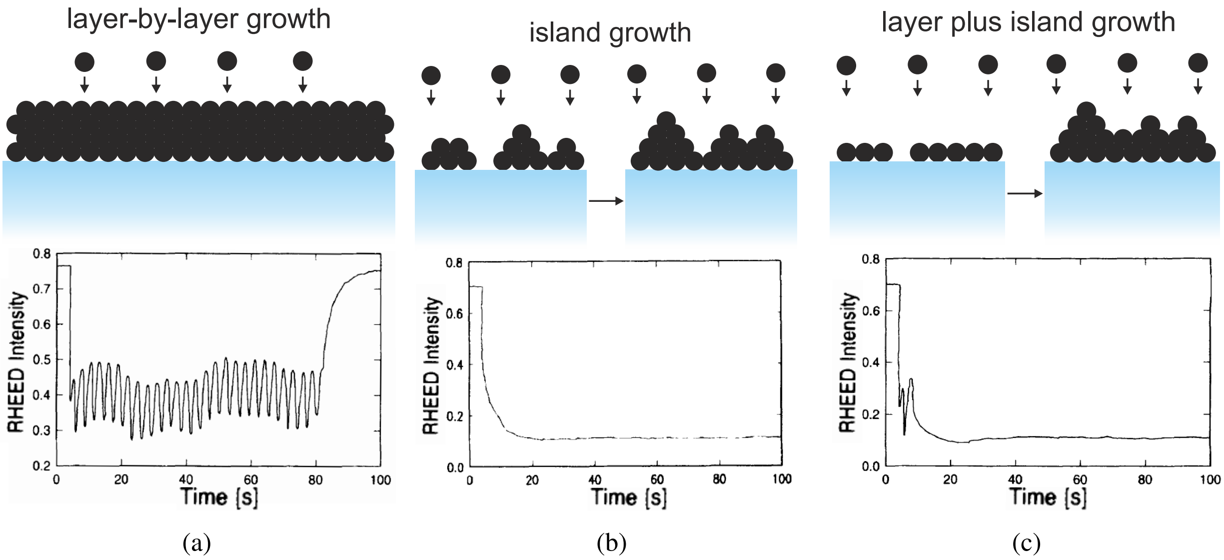

Fig. 3.3: Growth modes of thin films, adapted from [108]. (a) Layer-by-layer (Frank-van der Merwe) growth leading to oscillations of the reflective high-energy electron diffraction (RHEED) intensity, (b) island (Volmer-Weber) growth with a sharp drop in RHEED intensity, (c) layer-by-layer plus island (Stranski-Krastanov) growth characterized by few RHEED oscillations.

can diffuse to thermodynamically favorable sites, such as step edges, defects and islands. The supersaturation

$$m = kT_{\mathrm{Sub}} \ln\left\{r_{\mathrm{dep}}/r_{\mathrm{e}}\right\} \tag{3.4}$$

in turn depends also on T_{Sub} as well as on the deposition rate r_{dep} in relation to the deposition rate at thermal equilibrium r_{e} [110]. Supersaturation describes the deposition vapor pressure as compared to its equilibrium value. High supersaturation can be achieved through low substrate temperatures, high particle fluxes and high background pressures [108].

A common method to monitor the film growth mode during deposition is the concept of reflection high-energy electron diffraction (RHEED). A high-energy beam of electrons (typically a few eV) is directed onto the surface of the growing film under a small angle (below 3°) [111]. From the diffraction pattern of the reflected electrons, the crystal lattice parameters are extracted. When monitoring the temporal evolution of the diffraction peaks, the growth mode can be deduced. The operation of a RHEED measurement setup requires ultra-high vacuum (UHV) conditions.

For the fabrication of ultra-thin films, layer-by-layer growth (Frank-van der Merwe growth) as schematically depicted in Fig. 3.3(a) is the desired growth mechanism. When the surface adhesive force is larger than the cohesive force in between the adatoms, 2D islands coalesce to full monolayers before the growth of the next monolayer is initiated [112]. This occurs in a cyclic process. The RHEED intensity oscillates as the density of steps on the surface changes continuously [113]. During the nucleation of the islands, the RHEED signal decreases due to increased surface roughness, and when the islands coalesce to a monolayer, the RHEED signal increases again. Thus, the number of monolayers grown can be concluded from counting the oscillations. Layer-by-layer growth requires low supersaturation and high diffusion rates. However, for the heteroepitaxial growth of thin films on mismatched substrates, a critical supersaturation has to be achieved [114]. This motivates the deposition of buffer layers that decrease the mismatch between film and substrate.

High supersaturation, low diffusion rates and misfit strain favor 3D island growth (Volmer-Weber growth) of thin films by causing a large number of nucleation sites that can also develop on uncompleted monolayers (see Fig. 3.3(b)) [108, 114]. Volmer-Weber growth corresponds to the case of adatoms being more strongly bound to each other than to the substrate surface. The RHEED intensity shows a sharp drop at the onset of the deposition process as the nonperiodical variation of step density leads to diffuse scattering of the electrons.

When the growth conditions change after the deposition of a wetting layer of few ML thickness, layer-by-layer growth followed by island growth (Stranski-Krastanov growth) can be observed (see Fig. 3.3(c)). Herein, strain is built up during the growth of the initial MLs and then released through the formation of 3D islands. Deposition rate and diffusion constants influence on this transition. The RHEED intensity of Stranski-Krastanov growth is characterized by very few oscillations followed by a decreased signal which does not recover after completing the deposition process.

For non-perfect substrates with edges, a fourth growth mode is possible when the diffusion length l_D is much longer than the distance in between two steps l_T (terrace width). Then, the adatoms will stick to the surface steps rather than to 2D nucleation sites. This growth mode is called step-flow growth [103]. The maintained surface morphology gives rise to a constant RHEED intensity [108].

The above-described models for thin-film growth are based on the assumption the the underlying substrate is a perfect crystal. Schlom *et al.* found that for YBCO thin-films grown on $\mathrm{SrTiO_3}$ classical layer-by-layer or island growth is not observed due to surface defects [115]. They supply low-energy sites for nucleation regardless of the growth mode. The screw dislocation mediated growth describes the process of the addition of adatoms to the surface steps of the spiral-shaped growth terraces that develop from screw dislocations. Screw dislocations, in turn, result from the incoherent meeting of growth fronts during the coalescence of islands [116]. An advancing growth front that divides due to an obstacle, such as an impurity, and then reunites, forms a screw dislocation when the two growth fronts meet at different heights. As a consequence of this mechanism the growth of pyramids is observed leading to a roughening of the thin film.

Moreover, the relief of misfit strain can lead to the nucleation of dislocation half loops and subsequent formation of screw dislocations [103]. Therefore, ultra-thin films of only a few unit cells height of YBCO can grow strained and dislocation free. Above a critical thickness h_c, strain is relaxed through the formation of misfit dislocations leading to the typical pyramid growth. The

growth mode then changes from 2D nucleation to 3D film growth. For YBCO thin films on $SrTiO_3$, Frey *et al.* found a critical thickness of 14 to 16 unit cells of YBCO [108].
The density of screw dislocations can be influenced by several deposition parameters: Increased growth rates entail an increased screw dislocation density while increased temperatures and substrate misorientation can reduce the number of screw dislocations [115].

3.2.2 Physical aspects of pulsed-laser deposition

Among the physical vapor deposition (PVD) processes, pulsed-laser deposition (PLD) offers unique growth conditions. An intense laser pulse impinging on a target generates a plasma plume that then propagates perpendicularly to the target surface in a vacuum [117]. The PLD process can be divided into three phases, the first two of them taking place within the laser pulse duration:

(1) Laser-target interaction
Absorbed laser radiation is converted into electronic excitations and then transferred to the lattice, leading to heating and subsequent evaporation of the target material on a timescale of tens of ps [109, 118]. This process depends on the characteristics of the laser pulse as well as on the properties of the solid. Typical pulse durations are in the range of a few ns for excimer lasers. The energy density has to exceed a threshold value in order to stoichiometrically evaporate the target material. For YBCO, a minimum energy density of $w_\mathrm{L} = 1\ \mathrm{J/cm^2}$ was found [119]. Shorter wavelengths lead to higher absorption coefficients and thus thinner evaporated layers of the target material. As a consequence, a hotter plasma is formed which deposits as smoother and denser thin films [120]. Reflectivity and absorption coefficient as well as thermal properties (heat capacitance, thermal conductance) define the energy deposit in the target.

(2) Laser-plasma interaction and isothermal expansion
The evaporated plasma plume interacts with the laser light by absorption of photons through the effect of inverse bremsstrahlung. This causes the plasma to raise its temperature and its degree of ionization. Dyer *et al.* found an ionization fraction of $1.4\ldots4\%$ in plasmas from YBCO targets when irradiated with KrF excimer laser pulses [121]. As the absorption coefficient decreases with increasing plasma temperature, a balanced state is established leading to an isothermal expansion of the plasma. Plasma temperatures for the ablation of 1:2:3 targets typically lie in the order of 10000 K. Herein, the wavelength of the laser has to be small enough to exceed the plasma frequency, otherwise the laser light will be reflected by the plasma [122].

As the plasma extends at very high velocities, the density decreases rapidly, making the plasma transparent to laser light at some distance from the target. Therefore, absorption occurs mainly near the target surface where the density of charged particles is high due to constant adding of evaporated species from the target.

(3) Adiabatic expansion of the plasma
Due to the pulsed configuration of the PLD process, no further material is evaporated in between two laser pulses, and the plasma does not absorb energy any longer. This leads to the adiabatic expansion of the plasma. The forward directed nature of deposition is caused by the anisotropy of the expansion. It results from the pressure gradient and the initial dimensions of the plasma after step (2). Herein, the acceleration of the species in the plasma is assumed to depend inversely on the dimensions of the plasma. With expansion velocities of about $10^5 - 10^6$ cm/s in phase (2), the perpendicular dimensions of the plasma amount to about $10^{-2} - 10^{-1}$ mm whereas the in-plane dimensions lie in the range of several mm [122]. The anisotropy also determines the spatial composition and thickness variation of thin film. Thickness variations of the deposited film show a $(\cos\theta)^{8-12}$ dependence [122]. Upon expansion, the plasma plume is rapidly cooled and thermal energy is transformed into kinetic energy. During the whole process, the plume is strongly luminescent due to excited species in the plasma.

The model described above does not consider the presence of a background gas, namely oxygen, during the deposition of cuprate thin films. An oxygen partial pressure reduces the fraction of ions in the plasma as well as their average kinetic energy. For multi-component targets, different behavior occurs during collision with background gas atoms. Light species are scattered more strongly than heavy ones.

The main parameters influencing the quality of PLD grown cuprate films are the substrate temperature T_{Sub}, the deposition rate r_{dep} and the oxygen partial pressure p_{O2} [108]. Too low substrate temperature restrains the diffusion of adatoms on the surface. Too high substrate temperatures, in turn, cause film-substrate interactions and interdiffusion. The evaporation rate depends linearly on the laser energy density for energy-independent material parameters of the target [122]. However, since the reflectivity of the target is dependent on the energy density, usually a nonlinear behavior is observed, especially at high energy densities. Dam *et al.* found a linear increase of the target ablation rate in the energy density interval of $1 - 2$ J/cm^2 for YBCO [119]. At very high deposition and/or laser repetition rates, the time for rearrangement on the substrate may not be sufficient for the atomic species to diffuse to energetically favorable positions. Lower deposition rates, achieved through decreased laser energy densities or increased target-to-substrate distances, also entail a more uniform deposit [122].

The shockwave velocity of the particles arriving at the substrate is determined by the interplay of the oxygen partial pressure and the target-to-substrate distance [123]. Higher oxygen pressures

Parameter	Effect
Laser energy density, w_{L}	Stoichiometry Kinetic energy of ejected species Deposition rate
Laser spot area, A_{L}	Dimensions & opening angle of plasma plume Thickness distribution across substrate
Laser repetition rate, f_{L}	Rearrangement time on substrate Deposition rate
Oxygen partial pressure, p_{O2}	Dimensions of plasma plume Oxygen content of thin film
Substrate temperature, T_{Sub}	Mobility of adatoms
Target-to-substrate distance, d_{TS}	Position of Substrate relative to plume Deposition rate
Deposition time, t_{dep}	Film thickness t
Annealing oxygen pressure, p_{ann}	Oxygen content of ceramic layers

Table 3.1: Laser-deposition parameters and their influence on the thin-film quality.

induce smaller kinetic energies, while an increase of the target-to-substrate distance also increases the number of collisions with the background gas. With these parameters, the balance between substrate damage due to too high particle velocities and sufficient mobility of the adatoms on the surface has to be established.
An overview of PLD parameters and their effect on film growth is listed in Tab. 3.1.

PLD offers manifold advantages, amongst them the high versatility of the technique, mainly due to the decoupling of the laser-target interaction from other deposition parameters, with the energy source being located outside the vacuum chamber. The deposition rates are several orders of magnitude higher than those of other PVD and chemical vapor deposition processes and can be controlled precisely through the number of laser pulses. Particles arrive with high kinetic energies at the substrate, allowing for lower substrate temperatures [109, 124]. Multiple targets can be mounted in PLD systems, thus enabling the *in-situ* growth of multi-layer structures. Moreover, under ideal conditions the stoichiometry of the laser plume and the target coincide, which is beneficial when growing complex chemical compounds such as high-T_{c} superconductors. Additionally, PLD systems can be operated at elevated background pressures up to more than 1 mbar. Thereby, high oxygen partial pressures for the oxidation of the grown thin films can be realized.
On the other hand, the high pressure prevents the use of conventional *in-situ* monitoring processes, such as RHEED. The homogeneity of PLD films is limited to small sample dimensions due to the plume size, defined by the laser spot size on the target. Moreover, exfoliation of the target surface,

Parameter	**Effect**
Pulses per interval, n_P	Amount of material deposited per ML
Number of intervals, n_I	Film thickness in MLs
Idle time between two intervals, t_idle	Rearrangement time of adatoms on substrate

Table 3.2: Additional parameters of interval PLD.

recoil ejection and subsurface melting lead to the expulsion of melted material from the target that can form droplets upon arrival at the substrate surface. Resputtering of the substrate material and crystallographic defects in the film caused by the high particle velocities are effects seen with PLD [109]. Finally, the thin-film properties when depositing complex materials can fluctuate due to the wide range of PLD parameters and the difficulty of exact reproduction.

Typical PLD deposition rates are linked to supersaturation values that are orders of magnitude higher than with other deposition techniques. Usually, atomic or ionic species arrive at the substrate one by one. In contrast to that, laser ablation produces a (super-)saturated plasma that impinges on the substrate at once. As described above, high supersaturation favors 3D island growth. However, at very high supersaturation levels, the nucleating islands on the substrate surface are small and of unit-cell height. By using the unique pulsed deposition characteristic of PLD, this effect can be employed to grow ultra-flat YBCO thin films.

Blank *et al.* proposed the method of pulsed-laser interval deposition and showed the feasibility of depositing 90 unit cell thick flat $SrTiO_3$ films on $SrTiO_3$ substrates [125]. By the use of a high-pressure RHEED system, the oscillations in RHEED intensity associated with layer-by-layer growth could be observed. The principle of interval PLD is based on the fast deposition of the exact amount of material needed to complete one ML of the deposited material. Subsequently, a deposition pause, of at least the time interval that is needed for the adatoms to rearrange on the substrate, is realized. By adjusting the pause to a higher value than the diffusion time of adatoms on the substrate, the next layer will be deposited to a passive substrate. This operation principle permits layer-by-layer growth even for deposition parameters, such as substrate temperature and oxygen pressure defined through the stability of the grown phase, where 3D island growth would dominate in a continuous deposition.

A similar scheme was proposed by Frey *et al.* [108]. Growth interruptions were suggested for self smoothing of the grown thin film. Li *et al.* achieved layer-by-layer growth of 10 MLs of YBCO on a $SrTiO_3$ substrate by a comparable method [126]. The additional parameters for interval PLD processes are listed in Tab. 3.2.

3.2.3 Ultra-thin YBCO films: state of the art

Ultra-thin YBCO films were grown by PLD and DC-magnetron sputtering as superlattices from PBCO and YBCO [105–107, 127]. These sandwich structures allow for the fabrication of unit-cell thick YBCO films, as discussed in section 3.1. The critical temperature of the films are $T_{c,0} \approx 75$ K for 4 MLs of YBCO and $T_{c,0} \approx 81$ K for YBCO film thicknesses above eight MLs [105].

Direct deposition of YBCO on lattice matched substrates, such as $SrTiO_3$, always yields lower values of the critical temperature than the above-discussed multi-layer sandwiches. Li *et al.* showed that $T_{c,0} \approx 70$ K for a 4 ML thick YBCO film [105]. Lowndes *et al.* found that there is a transition zone between the thin film and the substrate of about 10 nm where the defect density increases rapidly, thus decreasing the superconducting transition temperature [107]. Lyatti *et al.* used DC-magnetron sputtering to deposit ultra-thin YBCO films on $SrTiO_3$ with an amorphous YBCO cover layer of 15 nm thickness [128]. They achieved a critical temperature of $T_{c,0} \approx 81.5$ K for 3 ML thick YBCO films.

Peroz *et al.* sputtered YBCO thin films on MgO substrates embedded in a sandwich of $2-4$ nm thick PBCO layers and measured critical temperatures of $T_{c,0} \approx 86$ K for 17 nm YBCO film thicknesses. Arpaia introduced a gold capping layer to protect ultra-thin YBCO films grown on MgO by PLD. Critical temperatures of $T_{c,0} \approx 70$ K for 5 nm thick YBCO films and $T_{c,0} \approx 14.5$ K for 3 nm thickness were measured [129]. However, AFM measurements revealed that below 5 nm, the roughness is in the range of the film thickness and islands have not coalesced completely.

YBCO films of 30 nm thickness grown on sapphire substrates with a 15 nm PBCO buffer layer exhibited critical temperatures of up to 86 K [130]. By combining a CeO_2 buffer layer with a PBCO/YBCO/PBCO sandwich, 10 nm of YBCO could be deposited by PLD with a critical temperature of $T_{c,0} \approx 79.4$ K [15].

3.2.4 Surface degradation of cuprate superconductors

During deposition and patterning, numerous influences, such as contact with atmosphere or aqueous solutions, can lead to degradation of the YBCO thin films. Common impacts resulting in deterioration of YBCO are summarized in the following. Due to their isomorphism, the same implications apply to PBCO.

Upon contact with water, two processes are observed. The first few monolayers from the surface collapse to an amorphous layer due to extraction of Ba^{2+} cations [131]. Barium hydroxide then reacts with CO_2, resulting in the growth of $BaCO_3$ precipitates on the surface:

$$\mathrm{Ba(OH)_2 + CO_2 \rightarrow BaCO_3 + H_2O} \tag{3.5}$$

This reaction is especially relevant for thin films, where the degradation of a surface layer is detrimental. Preferable nucleation sites for degradation are grain boundaries and edges.
Additionally, ingress of hydroxyl (OH^-) and exchange with O^{2-} leads to an extension of the *c*-axis and thereby to microcracking of the film. This effect is less pronounced in *c*-axis films, since ingress of OH^- occurs in the *a*-*b*-plane [132].
When exposing YBCO samples to air, a thin reaction layer is formed, where carbonates and hydroxides are formed [133]. As a result, the contact resistance to *ex-situ* deposited metal contacts increases with the exposure time to air t as $e^{\sqrt{t}}$ [134]. The corrosion effect proceeds very slowly. Unpatterned films can therefore be stored without the application of a passivation layer. Similar behavior was found for exposure to a nitrogen atmosphere. No detrimental effects were found for films exposed to oxygen or stored in vacuum.

Ion-beam milling is a widely used patterning technique that allows for the anisotropic etching of sub-μm-sized structures. The bombardment with ions breaks surface bonds and ejects atoms from the surface that is to be etched. Damage can be caused in YBCO even at small ion energies when they knock off the light oxygen atoms from the crystal lattice. Other possible sources of film degradation are lattice damage and heating of the film due to high ion current densities. Schneidewind *et al.* investigated the influence of argon ion bombardment with a beam energy of 500 eV on a bare YBCO surface and found a reduction of 2 K in critical temperature of etched films as compared to as-deposited films of the same thickness ($t_{\mathrm{YBCO}} = 25$ nm) [135].

The above described circumstances imply several rules when it comes to the treatment of YBCO samples: Thin films are to be stored in a dry environment, such as a desiccator, or even in vacuum. Where possible, contact with water is to be avoided. This is especially important after patterning of the YBCO layers, where hydroxyl could ingress from the side walls in the *a*-*b*-planes. Water can be part of wet-etching solutions or when it comes to the chemical reactions during development of lithographic processes. Finally, physical etching, relying on ion bombardment, is only possible in a narrow region of ion energies without impairment of the film. Cooling can be applied during ion milling to avoid overheating of the YBCO sample. Different etching techniques will be discussed in section 5.1.

3.2.5 Submicrometer patterning: state of the art

The patterning of YBCO films is subject to the influences discussed above. Due to the short coherence lengths, the superconducting properties depend delicately on defects in the thin film. Common patterning techniques for nanobridges of cuprates and their impact on the quality of the film are reviewed in the following.
Sub-μm structures were realized using a multilayer hard mask of carbon and titanium by Elsner *et*

al. [136]. The hard mask was defined by reactive-ion etching and the YBCO layers were patterned with a liquid-nitrogen cooled argon-ion milling system. The remainders of the carbon mask were removed in an oxygen plasma. For a 100 nm thick YBCO film on a $SrTiO_3$ substrate, a critical current density of $1 \cdot 10^6$ A/cm^2@77 K was obtained for a 250 nm wide bridge.

A similar patterning scheme was used by Arpaia *et al.* with chromium acting as a mask for the carbon film instead of titanium [129]. 50 nm thick YBCO films on $LaAlO_3$ substrates capped with 50 nm of gold were patterned to nanobridges of 150 nm width and 200 nm length using the carbon hard mask technique. At 4.2 K a critical current density of $\approx 10^8$ A/cm^2 was measured and the critical temperature amounted to ≈ 82 K.

High critical temperatures ($T_c \approx 86$ K) were found by Langheinrich et al. for long bridges ($l = 10$ µm) with widths down to 400 nm. The 150 nm thick YBCO films were deposited on $SrTiO_3$ substrates and patterned with the above described hard-mask technique. Critical current densities amounted to $5 \cdot 10^5$ A/cm^2@77 K [137].

Further patterning procedures include selective epitaxial growth on preprocessed substrates [138], focused ion beam (FIB) and ion-implantation techniques [139]. Curtz *et al.* patterned ultra-thin films of YBCO ($t = 12$ nm) on $SrTiO_3$ with Ga^{3+} FIB milling to submicrometer structures. Here, the pattern is not etched, but the ion irradiation turns the material into an insulating phase by implantation of defects. A 500 nm wide and 15 µm long stripe exhibited a critical temperature of 65 K, whereas the T_c of the unpatterned film was ≈ 80 K [140].

The above-cited work focused on the through-etching of YBCO layers to sub-µm dimensions. For the detectors realized in the present work, the crucial step for detector performance was the etching of the gold film covering the superconducting layer in the area of the detecting element. Upon removal of the protecting gold layer by Ar^+ ion etching in the above cited work by Arpaia *et al.*, the critical temperature of a 50 nm thick YBCO nanowire decreased by 6 K from ≈ 82 K to ≈ 76 K [129]. The effect was attributed to local damaging of the YBCO structure.

A different approach was investigated by Peroz *et al.* [141, 142]. Sputtered PBCO/YBCO(17.5 nm) /PBCO trilayers on MgO substrates were patterned to nanobridges of 600×600 nm^2 by xenon ion-beam milling. The gold layer design was then defined via a lift-off process. A critical temperature of 84 K and a critical current density of $\approx 10^7$A/cm^2 @77 K were found. It has to be pointed out, however, that the application of a lift-off process is at the expense of higher contact resistances.

3.3 Light detection in YBCO thin films

3.3.1 Above-gap excitations: optical through infrared radiation

With the superconducting energy gap in YBCO of $\Delta \approx 20$ meV, radiation in the visible and near-infrared through mid-infrared range lies above the gap. The response of YBCO thin films to

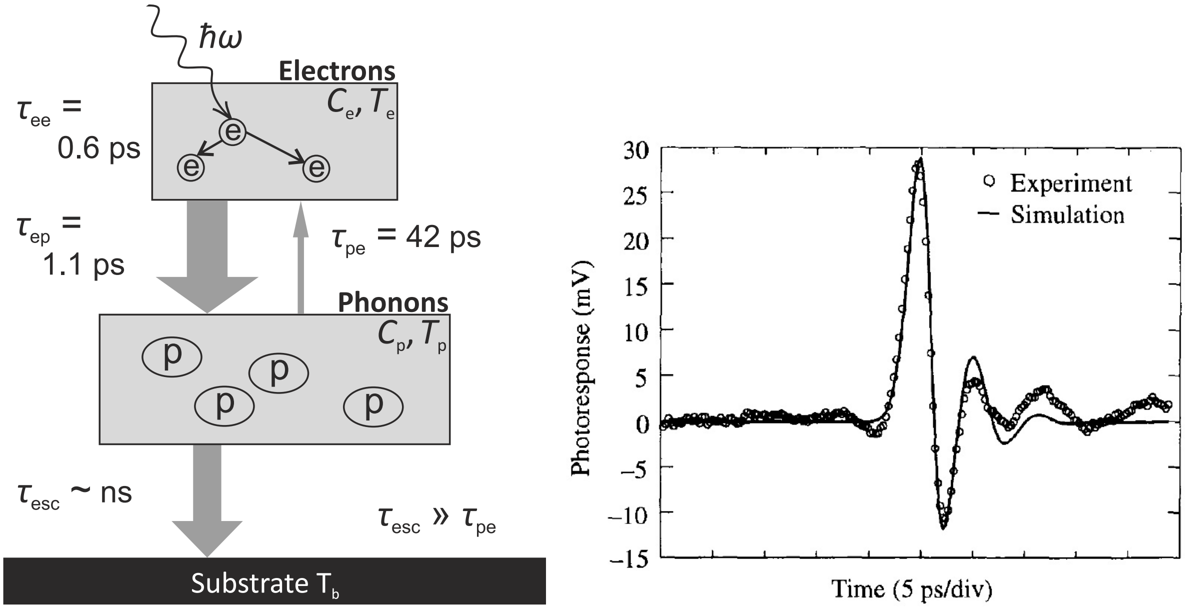

(a) (b)

Fig. 3.4: YBCO detectors at optical wavelengths: (a) Two-temperature model with characteristic time constants for 100 nm thick YBCO film and 100 fs optical pulses ($\lambda = 790$ nm) [12], and (b) kinetic-inductance response followed by oscillations due to energy exchange between phonons and the electron system, from [143]. The YBCO microbridge was operated at 60 K and 0.7 I_c.

photonic excitations can thus be explained by a transient increase of the electron temperature. Near the critical temperature T_c, the two-temperature model of the hot-electron bolometer fits well the experimental results, while a kinetic-inductance model is used to explain the behavior seen in the superconducting state.

YBCO hot-electron bolometer

For photon energies above the superconducting energy gap and operation temperatures near T_c, YBCO works as a hot-electron bolometer. Typically, the YBCO thin film is patterned to microbridges and the optical radiation is focused directly onto the structure.

Due to the intrinsic relaxation times, the detector response to optical and infrared excitations is seen as a picosecond peak followed by a nanosecond-scaled bolometric component. The operation principle of a HEB was introduced in section 2.2.2. Figure 3.4(a) displays the characteristic relaxation times found in YBCO. Electron thermalization and electron-phonon interaction occur on a picosecond timescale. For a 100 fs long optical excitation at 790 nm, $\tau_{ee} = 0.56$ ps and $\tau_{ep} = 1.1$ ps were measured by electro-optical sampling technique at an operation (bath) temperature of 80 K [12]. Lindgren *et al.* found the fast component of the detector response to be essentially independent on temperature and between 1.1 ps and 1.3 ps over the whole temperature range for operation points in the resistive state [144].

With the ratio of the heat capacities $C_p/C_e = 38$, energy backflow from the phonon to the electron system can be neglected ($\tau_{\mathrm{pe}} = 42$ ps) [12]. Consequently, the hot-electron and the phonon contribution to the detector response are decoupled and can be seen as consecutive features in the temporal evolution of the measured signal. The phonon escape time depends, according to equation 2.10, on the YBCO film thickness. For 100 nm thick films on $LaAlO_3$ substrates, Lindgren *et al.* determined $\tau_{\mathrm{esc}} = 3.5$ ns and Probst *et al.* found $\tau_{\mathrm{esc}} = 1.3$ ns for YBCO films of 30 nm thickness on sapphire substrates with PBCO protection layers of 25 nm thickness (effective YBCO thickness: 39 nm) [12, 14].

By adequately adjusting the operation point of the HEB, such that the temperature of the phonon system stays below T_{c} at all times, the YBCO HEB exceeds picosecond response times. The operation of a bolometer requires the provision of a detector bias, such that a change in resistance can be read out as a detector signal.

HTSC HEBS are of the phonon-cooled type, as the diffusion of electrons can be neglected [145]. The electron diffusion length lies in the range $l_d \approx 25$ nm, which is much shorter than realizable dimensions in YBCO nanobridges [146].

Kinetic-inductance response at low temperatures

At temperatures well below T_{c}, the current is carried by Cooper pairs. This state can be described by a kinetic inductance that is inversely proportional to the superfluid density f_{sc}: $L_{\mathrm{kin}}(t) = L_{\mathrm{kin}}(0)/f_{\mathrm{sc}}$. Upon absorption of optical radiation, Cooper pairs are broken and the resulting change in inductance leads to a voltage transient if a constant bias current is applied to the device: $U = I \cdot \mathrm{d}L_{\mathrm{kin}}/\mathrm{d}t$. The nonequilibrium distribution of quasiparticles can be described by the Rothwarf-Taylor equations under the assumption that at low temperatures all quasiparticles have the same energy [13, 147]. The linear dependence of the detector response on bias current, predicted by the above mentioned formula, was found by Lindgren *et al.* for different power levels of the incident optical radiation [144]. Similarly, Semenov *et al.* found linear dependence of the positive signal height on bias current and power level when both parameters are fairly small. With increased power levels or bias currents they found a bolometric component, coinciding with the transition of the detector to the resistive regime [148].

The kinetic-inductance response shows a positive and a subsequent negative picosecond-scaled response corresponding to the breakup of Cooper pairs and their recombination, respectively. A measured voltage transient for a 100 nm thick YBCO film excited with a 100 fs optical pulse is depicted in Fig. 3.4(b) [143]. The characteristic time scale for electron thermalization in the superconducting state was found to be temperature independent and $\tau_{\mathrm{ee}} \approx 0.9$ ps for a 100 nm thick film on $LaAlO_3$ substrate [144].

3.3.2 Sub-gap excitations in the microwave and FIR region

For excitations below the gap, namely in the millimeter and micrometer wavelength range, no concluding picture of the detection of radiation in YBCO has been found so far. From the discussion of the gap in YBCO in section 3.1.3, a frequency of about 10 THz is extracted as the gap energy at low temperatures (1 THz $\widehat{=}$ 4.1 meV). According to the BCS formula, $f \approx 5.5$ THz at 0.9 T_c. Adding to that, the situation is different as compared to the detection of optical wavelengths in that the radiation is in most cases not absorbed directly by the electron system of the superconductor, but by an antenna, and then coupled as an RF current to the superconducting detector.

Continuous-wave radiation

Periodic continuous-wave (CW) excitations at sub-gap frequencies were investigated by Ladret *et al.* by the use of the two-temperature model. Simulations revealed the formation of hot spots in sub-µm-sized YBCO constrictions with lateral dimensions of $l = w = 100$ nm and YBCO film thickness of $t_{\mathrm{YBCO}} = 10$ nm, whereas a plateau of increased electron temperature covering almost the full length of the YBCO detector was observed in somewhat larger YBCO constrictions ($l = 600$ nm, $w = 1000$ nm, $t_{\mathrm{YBCO}} = 35$ nm) [149]. Here, the distribution of the coupled RF power across the YBCO detector was assumed to be homogeneous, as the wavelength of the THz radiation is orders of magnitude larger than the dimensions of the detecting element. Upon introduction of a homogeneous RF current distribution, the power dissipation becomes nonuniform and hot spots can be observed at bias currents below the critical current I_c. The operation temperature for the simulations was set to $T/T_c \approx 0.85$ and the RF frequency varied from 250 GHz to 2.5 THz [150].

Ilin *et al.* found that the response of YBCO detectors to CW microwave signals could not be sufficiently explained by the 2T model at operation voltages below the first maximum of differential resistance in the $I(V)$ characteristic. Rather than the formation of dissipative regions by the RF power, they proposed vibrating vortices inside the YBCO detector as a competing detection mechanism in addition to the conventional hot-electron effect. An increased IF bandwidth of YBCO mixers at low bias current and an increase of the bandwidth with increasing operation temperature were found. As the vortex contribution to the detector response in the proposed model is inversely proportional to the local-oscillator frequency, the effect might be negligible for THz frequencies [151].

Pulsed THz excitations

Nebosis *et al.* investigated the YBCO response to pulsed THz excitations from $0.7-7$ THz. At low temperatures ($T < 78$ K) they found a response time of 120 ps, limited by the readout bandwidth

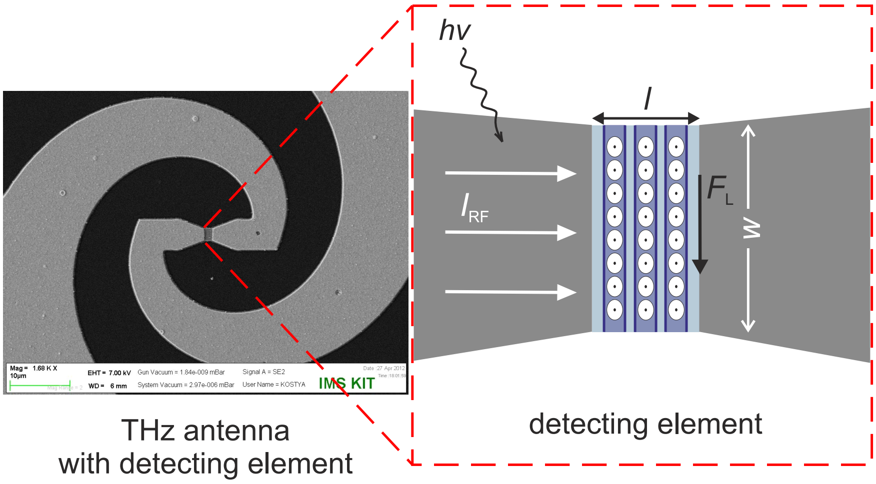

Fig. 3.5: Schematic of the vortex-flow response in YBCO THz detectors.

of the 5 GHz real-time oscilloscope. Moreover, for current densities $j < 0.3\ \mathrm{MA/cm^2}$, a linear dependence of the detector response on bias current was found. At higher temperatures, the response time increased to several nanoseconds, revealing bolometric behavior of the YBCO microbridges [152]. Similarly, picosecond response times were observed by Semenov *et al.* in current-biased YBCO thin films in response to THz radiation pulses. A transition from sub-nanosecond to bolometric, nanosecond-scaled response times was found between 7 and 28 THz [153].
The response of YBCO detectors to pulsed synchrotron radiation of $f \approx 10$ THz was investigated by Carr *et al.* With the pulse length of the infrared radiation of around 1 ns, the fast component of the response could not be seen and as the sample was biased to the resistive state, only a bolometric nanosecond-scaled signal was recorded [52].

Thoma *et al.* found an increase of one order of magnitude in the responsivity of YBCO microbridges as compared to optical wavelengths and the associated hot-electron mechanism for pulsed THz excitations of µm-sized YBCO detectors. The experiments were carried out with CSR from synchrotron storage rings operating in short-bunch mode, thus at frequencies below 1 THz. The nanosecond scaled bolometric behavior was not seen under any operation condition and a linear dependence on bias current and radiation power was observed. As opposed to that, the same YBCO detectors showed nonlinear power and bias dependence and a bolometric response when excited with optical pulses. Lastly, a zero-bias response was observed. These phenomena contradict the characteristics of a hot-electron bolometer and were therefore accounted for the dissipative movement of vortices [14, 15]. In this model, the absorbed THz radiation generates an RF current that is flowing through the YBCO detecting element. This current, when exceeding the critical current for vortex penetration, will generate vortices which then rearrange into a vortex line as discussed in section 3.1.4 (see Fig. 3.5) [102]. Vortices moving with their critical velocity v_c through that channel generate an electrical field that causes a voltage pulse across the YBCO detector. The crit-

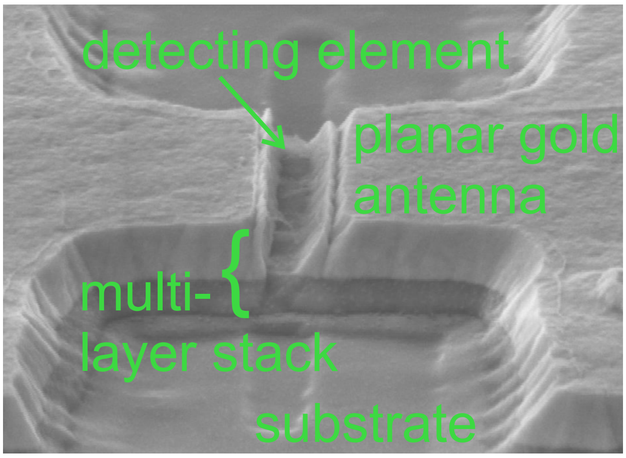

Fig. 3.6: SEM image of the detecting element embedded in a planar gold antenna (side view). The gold metallization is visible in light gray on top of the structure.

ical velocity v_c depends on the inelastic scattering time which corresponds to the electron-phonon interaction. Thus, the response times are in the picosecond range. A detailed analysis of the zero-bias response and its dependence on operation conditions upon excitation with sub-gap photon energies is missing so far. This investigation is within the scope of the present work.

3.4 Direct YBCO THz detector

3.4.1 Detector design

The absorptivity of YBCO goes below 20% at wavelengths $\lambda > 20$ µm and varies greatly when the YBCO film thickness decreases below 100 nm [154]. This makes it impossible to directly absorb THz signals over a broad frequency range in YBCO. Moreover, as shown in section 2.2 small dimensions of the detecting element favor short response time and high sensitivity. With the detecting element being of µm or even sub-µm size, the wavelength of the THz radiation is larger than the detecting element. Therefore, the YBCO detectors in this work were coupled to planar THz antennas made from thin films of gold. The antenna has dimensions comparable to the wavelength. An absorbed THz signal generates an RF current that is coupled electrically from the antenna to the detecting element.

An SEM image of a sub-µm-sized YBCO detecting element embedded in a planar THz antenna is shown in Fig. 3.6. The side view reveals the multi-layer stack consisting of the superconducting film, buffer layers and the gold metallization. The full multi-layer system will be presented in chapter 4. The gold metallization has to be removed in the area of the detecting element, as the surface resistance of gold undercuts that of YBCO at frequencies above 150 GHz [155]. The removal of the gold metallization is the most crucial step during the YBCO detector fabrication and will be discussed in chapter 5.

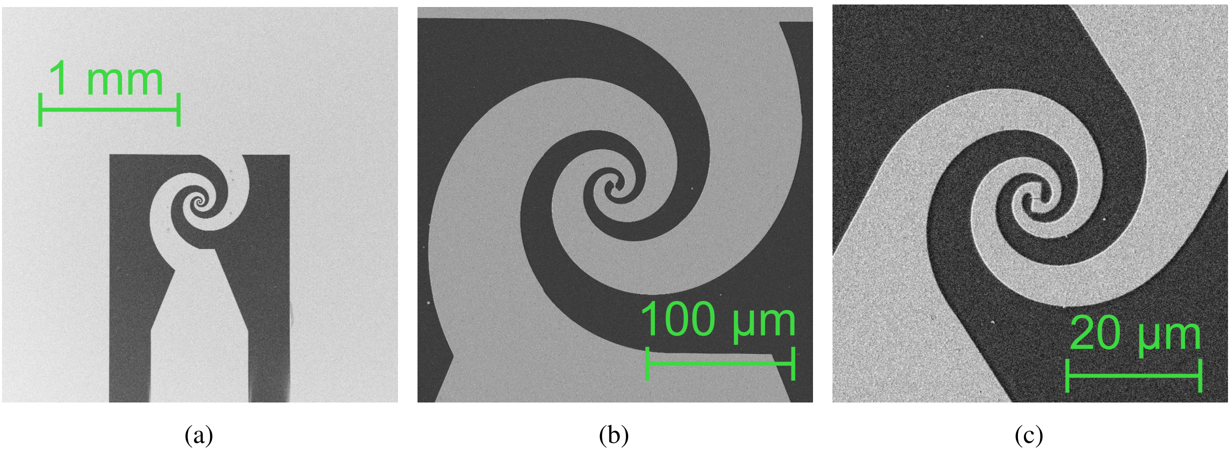

(a) (b) (c)

Fig. 3.7: Broadband logarithmic-spiral antennas designed for different frequency bands: (a) 3×3 mm^2 detector chip with low-frequency antenna and coplanar readout design, (b) dedicated antenna for low-α_c operation mode, and (c) an antenna for frequencies up to 7 THz.

An SEM image of a 3×3 mm^2 detector chip with a broadband antenna and a single YBCO detector situated at the base point of the antenna is depicted in Fig. 3.7(a). The principle design of the detectors consists of an antenna that is embedded in a coplanar waveguide (CPW) for broadband readout of the RF signal. A CPW consists of an inner conductor separated by two slots from the ground planes. The YBCO detecting element, patterned to a (sub-)µm bridge (see Fig. 3.6), is situated at the center of the antenna arms. 3×3 mm^2 detector chips with single or multiple detector pixels were fabricated for various applications and measurement requirements. The different antenna concepts employed within this work are presented in the following. The full layout of the detection system, including readout electronics and cooling design, will be introduced in section 6.1.

Broadband antenna layout

Different requirements to detect CSR from sources of THz radiation were discussed in section 2.1. For the case of broadband radiation sources with pulse durations of several picoseconds, broadband single-pixel detectors are employed to analyze the CSR. Moreover, ultra-broadband detectors can also be employed at narrowband sources over a broad range of emitted frequencies.

Planar logarithmic-spiral antennas for different frequency bands were patterned (see Fig. 3.7). Log-spiral antennas belong to the angle-constant antennas that allow for the design of ultra-broadband antenna structures with homogeneous behavior over the whole frequency range. At IMS, the antenna behavior was investigated and optimized through simulations with CST Microwave Studio® [156, 157].

The antenna bandwidth is defined via the reflection parameter $|\underline{S}_{11}|$ as the region where $|\underline{S}_{11}|$ is below -10 dB corresponding to an absorption of more than 90%. An example of reflection parameters for the narrowband antenna array is depicted below in Fig. 3.9. For the simulation of the reflection parameter, the detector impedance was set to match the antenna impedance, thus avoiding the reflection of the incoming THz signal at the detecting element. In this work, we assume that the real and imaginary part of the detector impedance correspond to the normal state resistance R_n of the YBCO detecting element as it is the case for above-gap excitations of low-temperature superconducting HEBs [14, 158]. For the case of biased operation of the YBCO detectors, this is a valid approach (see the discussion in chapter 7). For zero-bias operation the actual detector impedance is expected to be significantly smaller than R_n.

The upper and the lower frequency limit of the antenna bandwidth can be approximated by the smallest and the largest radius of a circle that is fitted to the log-spiral structure, respectively [159]. Three log-spiral antennas with different frequency operation range were used for this work:

(1) Low-frequency antenna (65 GHz – 1 THz)

An antenna that is ideally suited for very low-frequency signals, as seen at UVSOR-III during the emission of spontaneous CSR [32], was designed [9]. It was also used at ANKA to observe the overall THz pulse length that extends to frequencies below 100 GHz.

To achieve a cut-off frequency of a few GHz while keeping the dimensions of the antenna below the chip size, a low filling factor was realized. With an inner and an outer diameter of 16 µm and 912 µm, respectively, the bandwidth of the antenna extends from 65 GHz up to $\approx$ 1 THz [15, 157]. The antenna impedance is nearly constant over the whole bandwidth with a real part of about 75 Ω and a vanishing imaginary part. For a detector impedance of 50 Ω, which is a reasonable value for µm-sized YBCO detectors as seen in previous works [TRS$^+$13], the reflection parameter $|\underline{S}_{11}|$ of this antenna is below -20 dB over the whole bandwidth, corresponding to reflection losses at the antenna of less than 1%. The dimensions of the antenna are visualized in the SEM image in Fig. 3.7(a).

(2) Broadband THz antenna for short-bunch operation (150 GHz – 2.5 THz)

A dedicated antenna was designed that covers the whole CSR frequency range in short-bunch operation mode at ANKA, where the emitted frequencies during bursting extend to above 1 THz (see Fig. 3.7(b)) [14, 25, 157].

For a detector impedance of 50 Ω, the bandwidth ranges from $\approx$ 150 GHz to $>$ 2.5 THz. Again, the coupling efficiency is greater than 99%. Due to a larger filling factor, the real antenna impedance is somewhat smaller ($\approx$ 60 Ω) and thus better matched to the 50 Ω impedance of the coplanar readout lines. Inner and outer diameter amount to 9.6 µm and 323 µm, respectively.

(3) High-frequency antenna (1 – 7 THz)

A third, much smaller log-spiral antenna was employed for some experiments. Its layout

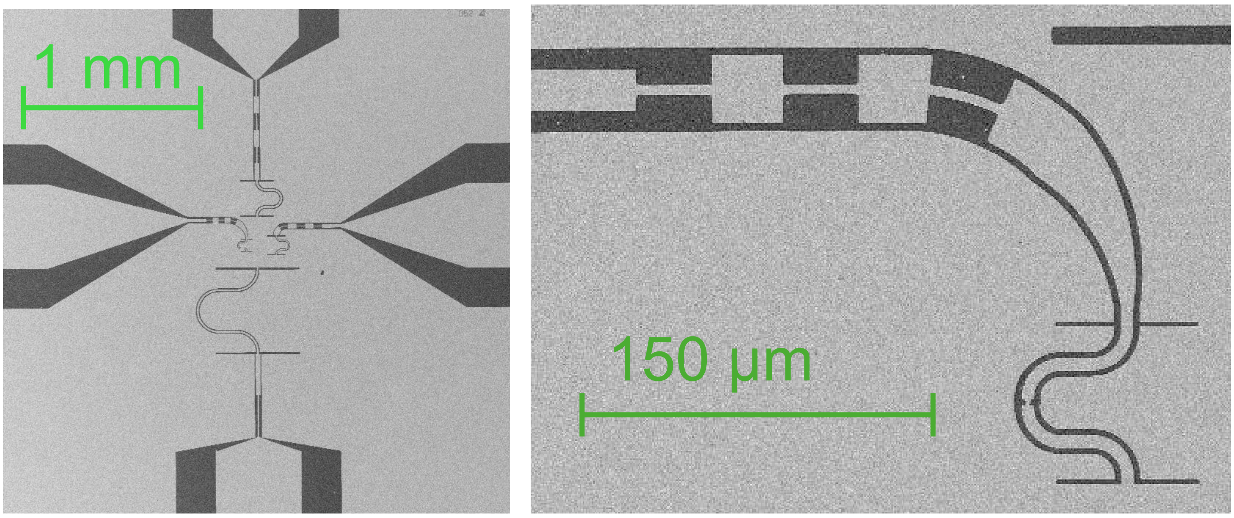

(a) (b)

Fig. 3.8: (a) Narrowband double-slot antenna array with four pixels for the frequencies 140 GHz, 350 GHz, 650 GHz and 1.02 THz. (b) Detailed view of 650 GHz antenna with RF chokes.

is depicted in Fig. 3.7(c). This antenna was needed for THz signals emitted at frequencies above 2 THz as e.g. at DELTA during laser slicing, where the "turn 0" signal extends to about 6 THz [27]. At linear accelerators, such as FELBE, narrowband signals with frequencies of a few THz can be generated [33].

The antenna has an inner diameter of 2.8 µm and an outer one of 48 µm [159]. A corresponding bandwidth of $1.1 - 7$ THz was found by simulations of the reflection parameter with CST Microwave Studio® by A. Schmid. The antenna impedance is frequency dependent and the real part amounts to $\approx 80\ \Omega$ at 2.5 THz. Moreover, the imaginary part cannot be neglected, but stays smaller than the real part up to 6 THz.

Narrowband antenna layout

During bursting in short-bunch operation mode of synchrotron storage rings, CSR at frequencies up to 2 THz is emitted (see section 2.1). The corresponding substructures on the bunch (i.e. microbunching) extend to the (sub-)picosecond region. As these structures cannot be resolved in the time domain with state-of-the-art readout electronics, a different approach was implemented for the turn-by-turn single shot analysis of bursting bunches. An array of YBCO detectors embedded in a set of narrowband antennas was fabricated in order to detect the spectrum of the individual bunches in a single-shot regime [SRK+16, SRK+17]. Additionally, for the experiments on electrical-field sensitivity of the YBCO detector, presented in section 6.4, a single YBCO detector with a narrowband antenna was used during bursting short bunch operation mode. Here, the polarization of the antenna was needed to be linear and frequency independent. This is not the case for the log-spiral antennas presented above.

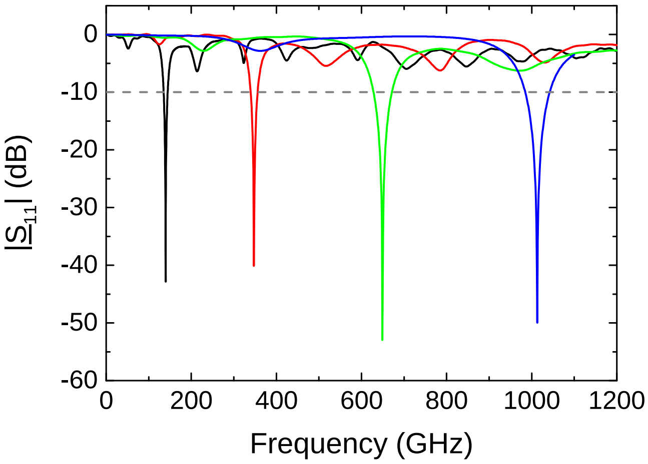

Fig. 3.9: Reflection parameters $|\underline{S}_{11}|$ of the four narrowband double-slot antennas in the array with four pixels [SRK^{+}17].

For the narrowband detectors, a double-slot antenna acts as a resonator for the design frequency. Double-slot antennas, as compared to simple slot antennas, entail a higher directivity and a more symmetrical radiation pattern. In this work, the double-slot antennas were combined with sub-µm YBCO detectors, in order to maximize the detector sensitivity. The small detector dimensions, however, entail large normal resistances of the detector bridge ($\approx 350\ \Omega$). In order to achieve high coupling to the incoming THz radiation, the antenna has to be matched to the detecting element. High slot impedances are achieved with a design with slot lengths of $l = \lambda/2$. The length of the CPW was adjusted to $\lambda/2$, too, in order to preserve the impedance. As the slot distance was found to yield the best directivity results in the farfield for $d \approx \lambda/2$, a design with curved CPWs and the detecting element moved out of the antenna center was implemented (see Fig. 3.8(b)) [160]. The antenna impedances vary from 300 Ω to 350 Ω and good matching for detector impedances between 200 Ω and 450 Ω was found in simulations [SRK^{+}17].

The array of four narrowband antennas with individual YBCO detectors used for the detection of bursting CSR is displayed in Fig. 3.8(a). The four design frequencies are 140 GHz, 350 GHz, 650 GHz and 1.02 THz. Comparison with Fig. 2.1 shows that these frequencies cover the range of bursting CSR at ANKA. Figure 3.8(b) is an enlarged SEM image of the 650 GHz antenna. Isolation between the detector and the readout path at the antenna frequency is obtained through RF chokes. Antenna bandwidths of below 10% are achieved with this design. The reflection parameters $|\underline{S}_{11}|$ of the four narrowband antennas are depicted in Fig. 3.9 for ideal matching between the antenna real impedance and the detector impedance. The geometrical parameters and bandwidths of the individual antennas are listed in Tab. 3.3. A benefit of the small bandwidths is reduced crosstalk between the individual antennas.

	140 GHz	**350 GHz**	**650 GHz**	**1.02 THz**
Arm length, l (µm)	442	177	94	61
Arm width, w (µm)	9	7	5	2
Arm spacing, d (µm)	452	187	100	67
Antenna bandwidth (%)	7.1	7.2	6.8	6.7

Table 3.3: Narrowband-antenna dimensions for the four antennas in the array and corresponding antenna bandwidths for a detector impedance of 350 Ω [SRK$^+$17].

3.4.2 Technological requirements

In summary, several conclusions can be drawn concerning the detector design and fabrication process. The different types of pulsed THz sources, discussed in section 2.1, have in common that they require picosecond response times, ultra-high sensitivity and detection over a broad THz frequency range. Especially in the case of bursting CSR a resolution of the individual pulse shapes is crucial to a further understanding of the source of the instability.

While the available frequency range of the detector and the overall response time of the detection system are determined by antenna and readout design, as discussed in the previous section and in section 6.1, the intrinsic response time and sensitivity depend on the dimensions of the YBCO detecting element. The YBCO film thickness influences the critical current, thus the barrier for vortex entry, as well as the phonon response time of a hot-electron bolometer. In particular, for the investigation of the zero-bias operation mode, YBCO detectors with ultimate sensitivity are required. Therefore, the goal of this work is to realize minimal film thicknesses of $t_{\mathrm{YBCO}} = 10$ nm, while keeping the critical temperature above 77 K. Due to lattice mismatch and chemical reactions, the sapphire substrate has to be buffered. The details will be introduced in section 4.2. It is important to note that the growth of ultra-thin films requires flatness of the superconducting film itself and the underlying buffer layers. High film roughnesses do not allow for the growth of coalesced ultra-thin films of few monolayers thickness.

Similarly, the area of the active detecting element has an impact on the detector sensitivity. The critical current density depends on the width of the detecting element and the sensitivity for pulsed excitations is expected to vary as V^{-1} with the volume V of the detecting element. Therefore, the patterning to sub-µm dimensions is a prerequisite for the sensitive operation of the YBCO detectors. In this context, the layer thickness homogeneity of the gold metallization films and the exact knowledge of their etching rate becomes important to avoid overetching and the associated degradation of the superconducting detecting element. For the operation of the YBCO detector array with narrowband antennas, a reduction of the detecting element dimensions and the related increase in sensitivity is required as the antenna only absorbs part of the THz spectrum emitted by the synchrotron.

3.5 Conclusions of chapter 3

The high-temperature superconductor $YBa_2Cu_3O_{7-x}$ (YBCO) is characterized by a unit cell with intrinsic anisotropy causing a strong dependence of the superconducting properties on the crystal direction. Furthermore, the oxygen content of the CuO chains is detrimental to the occurrence of superconductivity and thus, the adherence to the ideal oxygen stoichiometry is one of the most crucial requirements for the deposition of YBCO thin films. YBCO is characterized by a d-wave energy gap of large amplitude as compared to the low-temperature superconductors. The temperature dependence of the energy gap was found in the literature to be comparable to that of BCS superconductors.

In the second part of this chapter, PLD as a suitable method to deposit ultra-thin YBCO films was introduced. In particular, the method of interval PLD, that combines high supersaturation of the plume impinging on the substrate with long enough pauses for diffusion of the adatoms and full coalescence of the monolayers, is a suitable technique for the deposition of few-ML thick YBCO films by layer-by-layer growth. Herein, the minimal growth unit for c-axis orientation of the deposited films is one unit cell in height, as the CuO planes are the ones with the lowest surface energies.

The current status of understanding of the detection of light in YBCO was summarized in section 3.3. For above-gap excitations, the behavior is well understood and can be explained by the generation of hot electrons in the resistive state and a change of the kinetic inductance in the superconducting state. Likewise, for continuous-wave radiation in the low THz frequency range and operation points above the first maximum in differential resistance, the detection mechanism is of bolometric nature. The response of µm-sized YBCO detectors to pulsed THz radiation was found to deviated from the response at optical frequencies. As the photon energy is too small to break Cooper pairs at THz frequencies, a detection mechanism based on the dissipative movement of magnetic vortices was reported. Herein, the occurrence of a detector response at zero bias current is particularly interesting and should be further investigated. This will be carried out in chapter 6.

Finally, the layout of the YBCO detectors was introduced. Single-pixel and multi-pixel detector arrays with YBCO elements embedded in narrowband and broadband antennas comply with the different requirements of the individual accelerator-based THz sources.

4 Epitaxy of thin YBCO films

High-quality thin films of the superconducting detector material YBCO are the prerequisite for the fabrication of sensitive detectors. Extending the achievable range of film thicknesses towards a few monolayers only opens up the path for even higher detector sensitivities and also for new applications, such as superconducting nanowire single-photon detectors.

In the following, the existing PLD setup at IMS along with the deposited multi-layer stack for YBCO THz detectors is presented. The individual layers were optimized towards minimum roughness to enable the deposition of ultra-thin fully coalesced YBCO films. At the same time, optimum superconducting properties of the YBCO film are necessary for high detector efficiencies at liquid-nitrogen operation temperatures. The film quality was evaluated through SEM, XRD and AFM analysis as well as the measurement of the critical temperature T_c.

4.1 Automation of the PLD system

The PLD setup at IMS is depicted in Fig. 4.1. The system consists of three main components: a laser, an optical path that focuses the laser light onto the target, and the vacuum chamber where the deposition process takes place.

4.1.1 Laser-ablation setup

The laser source is a KrF excimer laser radiating at a wavelength of 248 nm with a maximum output power of 7 W and a maximum repetition rate of 10 Hz (model COMPexPro 201, Coherent). The pulse length is 25 ns. Directly behind the exit window of the laser, the signal is shaped to a rectangular form by an aperture with the dimensions $h = 15$ mm, $w = 8$ mm. Moreover, two plates of fused silica act as absorbers, each of them with an attenuation of about 8%. The absorbers extend the range of minimum energy densities to lower values, as the laser itself is limited to an operating high voltage interval of 18 to 27 kV corresponding to about 200 to 700 mJ pulse energy. Subsequently, the laser beam is guided to the window of the deposition chamber via two mirrors, one of them being equipped with a piezoelectric motor that enables the vibration of the mirror. That way, the laser beam is oscillating over the surface of the target in horizontal direction. A lens focuses the laser beam with the focal point being situated several millimeters in front of the target surface. Thereby, an ablation area of $A = 1.5 \ \times 2.5\ \text{mm}^2$ is achieved. The energy density can then

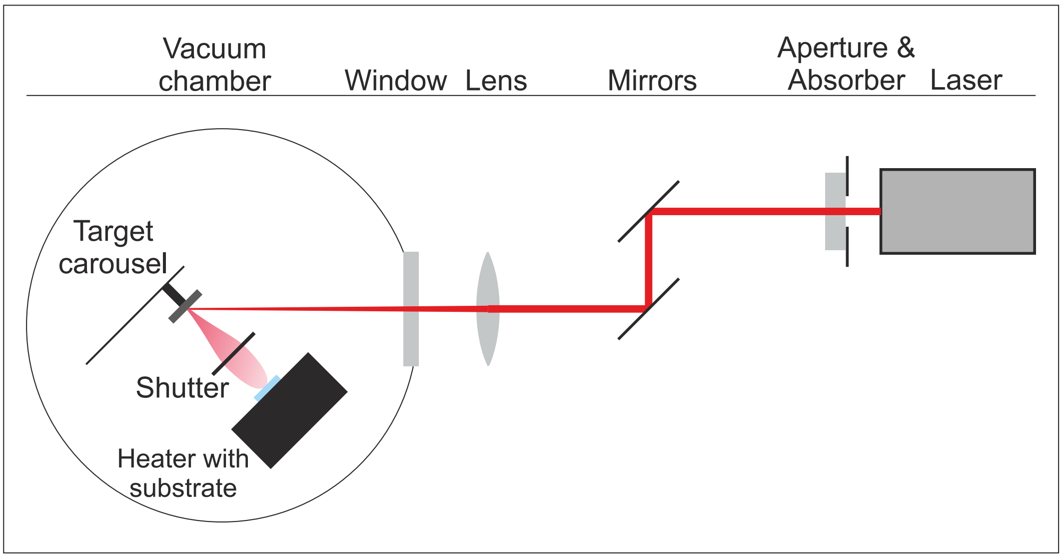

(a)

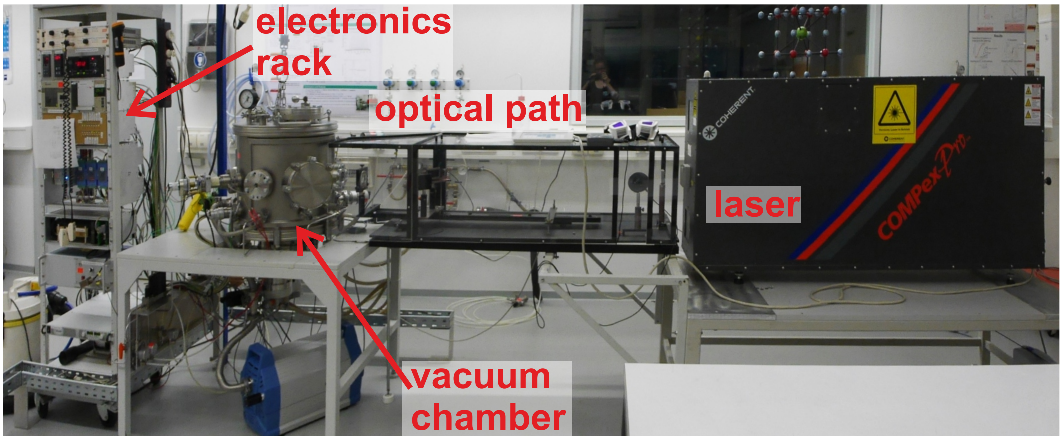

(b)

Fig. 4.1: The PLD system at IMS consisting of a laser, an optical path, the vacuum chamber and the electronics rack. (a) Schematic layout of the optical path of the PLD system. (b) Photograph of the existing setup.

be determined from the laser pulse energy: $w_{\mathrm{L}} = E_{\mathrm{L}}/A$. The losses in the optical path depend on the usage of the absorbers and the aperture and are measured every time before a deposition process is started with a pyroelectric sensor. The average transmission value measured as the coefficient of laser power behind the window of the vacuum chamber and behind the aperture amounts to $\approx 58\%$.

The deposition chamber has a volume of about 80 l and can be opened from the top. It is equipped with a fused silica window with an anti-reflective coating for 248 nm on both sides, through which the laser beam arrives (see Fig 4.2(a)). On a target carousel, up to six different targets can be mounted. An external DC motor is used to position the target needed for deposition at the point of laser incidence. Currently four 1 inch targets are installed: a YBCO target, a $\mathrm{PrBa_2Cu_3O_{7-x}}$

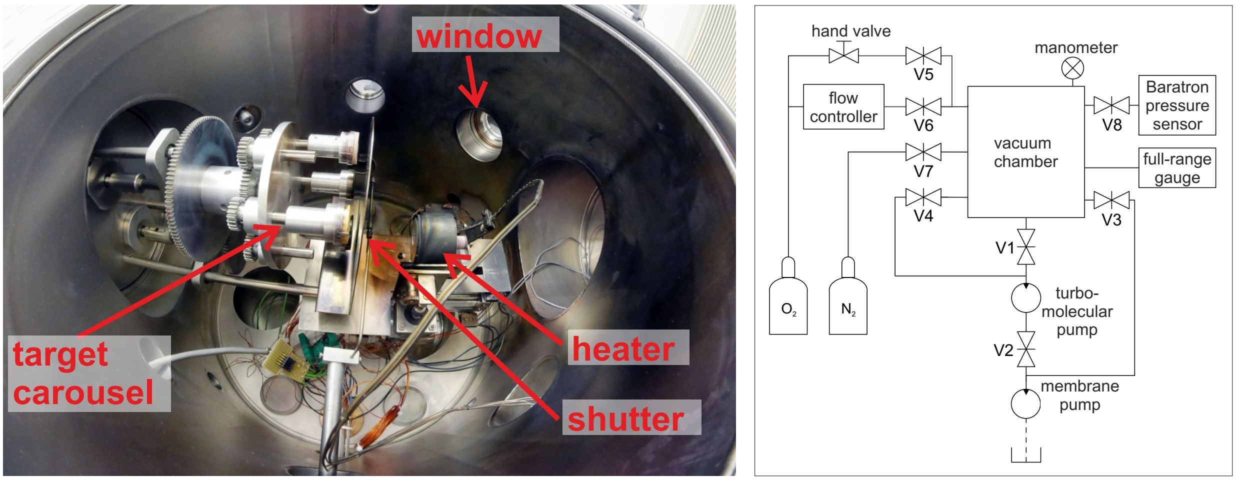

(a) (b)

Fig. 4.2: (a) Inside view of the vacuum chamber. (b) Scheme of the PLD vacuum components.

(PBCO) target, a CeO_2 target and a gold target. During deposition, the targets are rotated around their own axis.

The heater is placed on a stage and can be moved in forward and backward direction to change the target-to-substrate distance. Moreover, tilts in horizontal and vertical direction are possible through the use of stepper motors. A shutter can be placed in between the heater and the ablated target to start and stop the deposition process. It is operated via an externally mounted DC motor.

Figure 4.2(b) shows the vacuum configuration of the deposition chamber along with the different inlets for the process gases. The forepump of the system is a membrane pump since the deposition of YBCO is not compatible with oil pumps. The turbomolecular pump can be connected to the process chamber via a gate valve and via a small bypass valve. During evacuation and heating of the system, the turbomolecular pump operates at a high throughput with the gate valve being open. During deposition the oxygen partial pressure is in the range of 1 mbar and the cross section is reduced by connecting the turbomolecular pump via the bypass valve. Oxygen can enter the chamber via two different valves that are needed for the different pressure ranges during deposition and annealing. The oxygen partial pressure during deposition is adjusted via a flow controller and a PID controller.

4.1.2 Description of the deposition process

Before starting a deposition process, the substrates are glued onto the heater with silver paste. This ensures good thermal contact during the deposition. The silver paste is heated to 150 °C to harden the glue. Also, the ceramic targets are polished to avoid exfoliation of the target and the formation of droplets during ablation. Subsequently, the chamber is pumped to a base pressure of $5 \cdot 10^{-5}$ mbar.

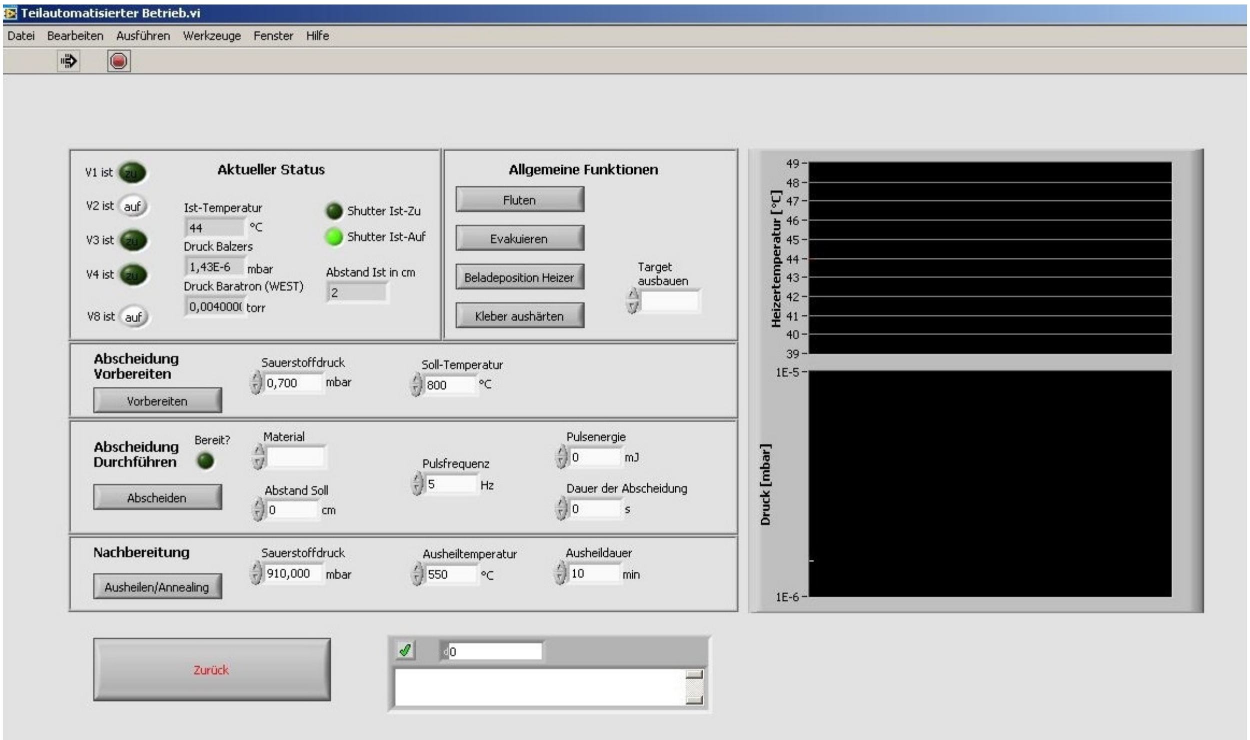

V1 ist zu
V2 ist auf
V3 ist zu
V4 ist zu
V8 ist auf
Ist-Temperatur 44 °C
Druck Balzers 1,43E-6 mbar
Druck Baratron (WEST) 0,004000(torr
Abstand Ist in cm 2
Sauerstoffdruck 0,700 mbar
Soll-Temperatur 800 °C
Abstand Soll 0 cm
Pulsfrequenz 5 Hz
Pulsenergie 0 mJ
Dauer der Abscheidung 0 s
Sauerstoffdruck 910,000 mbar
Ausheiltemperatur 550 °C
Ausheildauer 10 min
d0

Fig. 4.3: LabVIEW workspace for the semi-automated deposition process.

The substrate is heated up with a rate of 700 K/hour to the deposition temperature which is in the range of 800 °C. Deposition parameters for the buffer layers and the superconducting YBCO layer are the laser energy density w_{L}, the repetition rate f_{L}, the substrate temperature T_{Sub}, the target-to-substrate distance d_{TS} and the oxygen partial pressure p_{O2}. The choice of the adequate deposition parameters for the individual layers will be presented in the following section.

After the deposition of the ceramic layers, the vacuum chamber is filled with oxygen up to a pressure of 910 mbar. The temperature is reduced to 550 °C with a cooling rate of 600 K/hour, held at this temperature for 10 minutes and then further decreased to 400 °C. At 400 °C, the heater is completely turned off, such that the temperature decreases exponentially. The annealing process that corrects for oxygen deficiencies in the as-grown ceramic layers takes place between 600 °C and 400 °C [161]. Moreover, the YBCO phase transits from tetragonal to orthorhombic at around 600 °C, as already discussed in section 3.1 [84].

Finally, the vacuum chamber is evacuated to $5 \cdot 10^{-5}$ mbar and a thin layer of gold is deposited *in-situ*.

4.1.3 Semi-automated control of thin-film growth with LabVIEW

An automated deposition process offers the benefit of better reproducibility of the deposition parameters and lowers the risk of errors caused by the experimenter. Therefore, a LabVIEW software controls the deposition process from a computer that is connected to the electronics via serial in-

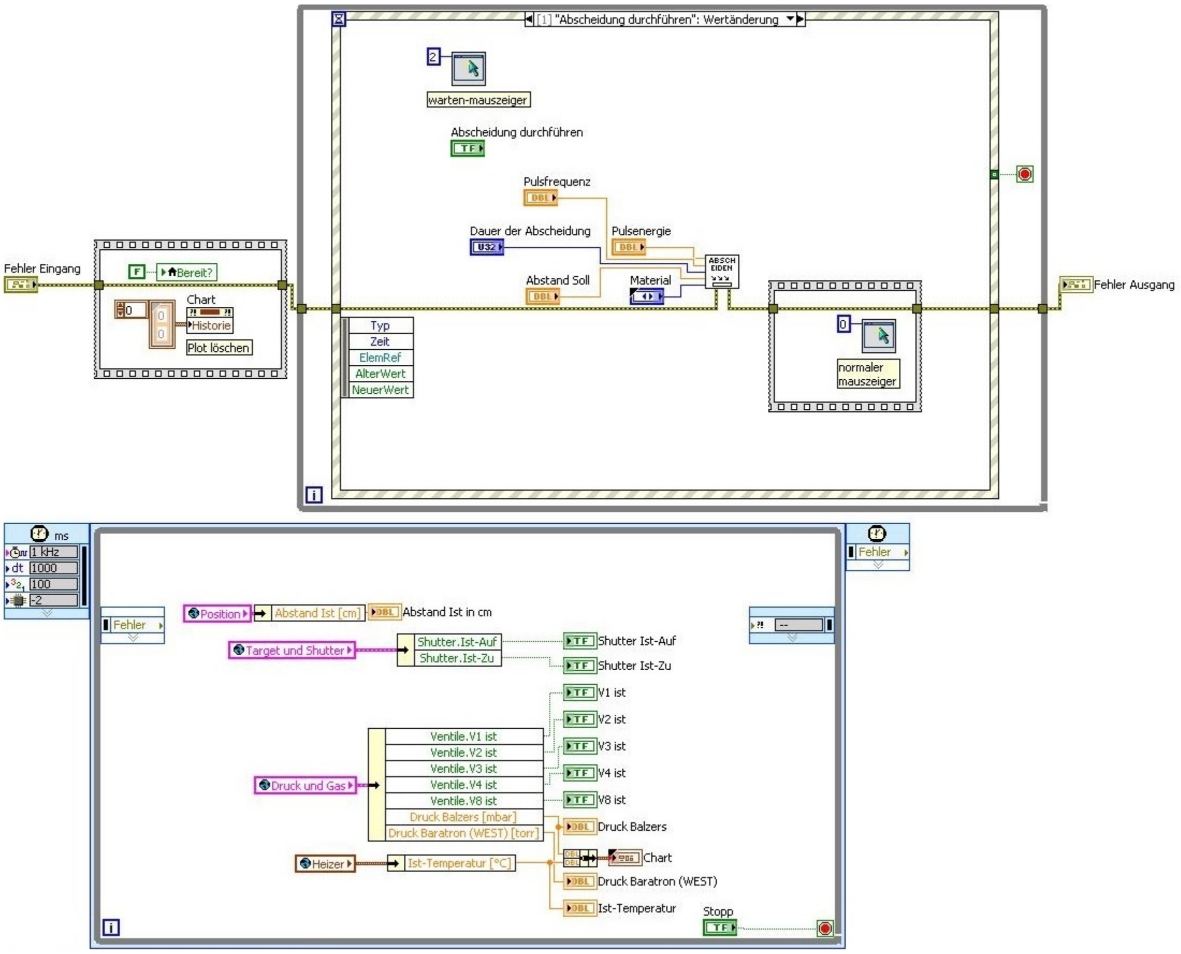

Fig. 4.4: LabVIEW block diagram. The laser ablation step within the semi-automated process is shown.

terfaces. The rack with the electronics in Fig. 4.1(b) contains the control units for the different components of the PLD system. Data acquisition modules are used for readout and input of signals.

The LabVIEW software is arranged in two main structures. The first one continuously retrieves and saves system parameters, such as the heater temperature and the pressure. The second one registers user input and sends commands to the control units of the electronics. The program window for the deposition process is depicted in Fig 4.3. The workspace is divided in several areas: At the upper left, the current status of the system is displayed, to the right some general functions are accessible, such as flooding and evacuation of the vacuum chamber or the hardening of the silver paste. The lower part is divided into the three main phases of the deposition process: heating of the substrate, laser ablation and annealing of the as-deposited film. The diagrams on the right hand side display temperature and pressure evolution. This program is referred to as a semi-automated deposition process since the individual steps of the process are carried out automatically, meaning that the software controls all the necessary parameters such as temperature, pressure, laser operation, heater movement and valve positions. Exemplarily, Fig. 4.4 shows the corresponding block diagram for the process step of the actual laser ablation. The lower part of the diagram is the program code for the monitoring of the system status, while the upper part retrieves the parameters of the PLD process and communicates them to the VI "Abscheiden" (German for "deposition"). Since the individual automated tasks are time-controlled, only one task at a time can be executed, therefore the program shows an hourglass cursor during deposition and switches back to the normal cursor afterwards.

The LabVIEW environment contains also two manual operation modes. The first one allows for the autonomous adjustment of settings and is only accessible via a password request, while the second one considers dependencies of process parameters and only allows operations that cannot cause damage at the deposition system. This applies for example to the control of the valves and the turbomolecular pump but also to the maximum temperature range of the heater and the prevention of collisions between the heater and the shutter.
The semi-automated and manual LabVIEW programs accesses different VIs that can read parameters and send commands to the control units using the individual device drivers. The communication is realized RS-485 or RS-232 interfaces. A complete description of the electronics and the communication with the LabVIEW software can be found in [162].

4.2 Optimum parameters for the deposition of YBCO thin films

4.2.1 The thin-film multi-layer stack

The basis of the YBCO THz detector is an R-plane sapphire (Al_2O_3) substrate. The R-plane has a pseudo-rectangular surface structure with lattice parameters $a_r = 4.76$ Å and $b_r = 5.12$ Å [163]. The lattice mismatch to c-axis grown YBCO amounts to 6% and 12%, respectively. In principle, other substrates such as $LaAlO_3$ and $SrTiO_3$ are a better fit to the epitaxial growth of YBCO due to smaller lattice mismatch (2.0% and 1.4% respectively) [84]. However, for the microwave design and the absorption of a THz signal, the dielectric losses of the substrate as well as the impedance of the microwave structures are of crucial importance. With a loss tangent of $\tan\delta = 8.4 \cdot 10^{-6}$ @ 77 K and 10 GHz and a relative permittivity of $\varepsilon_r = 10.06$, sapphire is well suited to be used as a microwave substrate [164]. As compared to that, the relative permittivity of $SrTiO_3$ increases greatly at low temperatures. Also, $SrTiO_3$ and $LaAlO_3$ exhibit high dielectric losses at microwave frequencies [165]. Moreover, sapphire transmits THz radiation up to a few THz which is a prerequisite for the back-side illumination of the YBCO detectors [17, pp. 58-60]. From the crystallographic point of view, an ideal substrate should not only match the lattice structure of the deposited material but also exhibit chemical stability and a similar thermal expansion coefficient. When depositing YBCO directly on sapphire Al, Ba and Cu diffuse in a 30 nm thick uncontrolled interfacial region that was found to consist of $BaAl_2O_4$ [166].

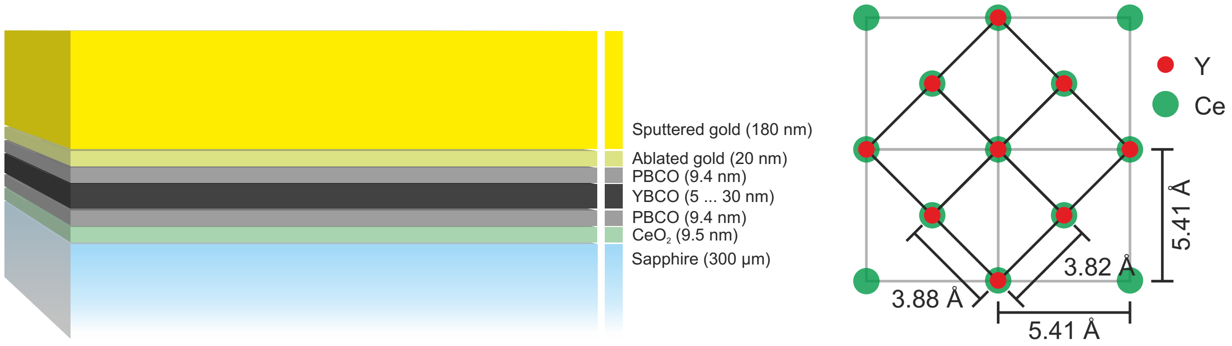

(a)

(b)

Fig. 4.5: (a) Multi-layer stack for the detector fabrication. The YBCO thin film is grown on a buffered sapphire substrate. The CeO_2 and PBCO buffer layers act as chemical barrier and compensate for the lattice mismatch. A second PBCO layer protects the ultra-thin YBCO film and a gold metallization layer is grown in two steps. The optimal thicknesses were found during the optimization process as explained in the following subsections. (b) YBCO grows tilted by 45° in the *a*-*b*-plane of CeO_2.

To avoid inter-diffusion, a buffer layer is needed. CeO_2 can be used for lattice matching and as a chemical barrier at the same time. An ultra-thin CeO_2 diffusion barrier of 20 nm thickness prevents diffusion of Al into the thin film. An interface layer between sapphire and CeO_2 of 5.5 nm thickness was found [167]. The lattice mismatch between CeO_2 and sapphire amounts to 5.7% in *a*-direction and 12% in *b*-direction [165]. YBCO then grows with the [100] direction parallel to the [110] direction of CeO_2 which results in a lattice mismatch of below 2% [168]. The 45° tilt of the YBCO lattice in the *a*-*b*-plane as compared to CeO_2 is depicted in Fig. 4.5(b).

PBCO was used as second buffer material. It is a room-temperature semiconductor and has an orthorhombic structure with the lattice constants $a = 3.87$ Å, $b = 3.93$ Å and $c = 11.73$ Å. The lattice mismatch to YBCO is less than 1.5% in the *a*-*b*-plane, allowing for epitaxial growth of YBCO on top of PBCO. Moreover, oxygen diffuses through PBCO such that it can be deposited *in-situ* with YBCO [107]. For ultra-thin YBCO films with thicknesses below 30 nm, the additional buffer layer is necessary since otherwise lattice mismatch from the substrate dominates over the whole film thickness and leads to oxygen deficiencies that entail a reduced critical temperature T_c [151]. PBCO also prevents inter-diffusion from CeO_2. The interface layer thickness between YBCO and CeO_2 was found to amount to about 9.4 nm [167]. Since PBCO and YBCO are chemically compatible, they form a sharp interface [130]. The lattice mismatch between the [110] direction of PBCO and the [100] and [010] directions of CeO_2 amounts to 1.02% and 2.67%, respectively [Feß16].

To protect ultra-thin YBCO layers against out-diffusion of oxygen, a second passivating PBCO layer is deposited on top. Too thick PBCO layers, however, hamper the annealing process of the full multi-layer system as they prevent the oxygen through-diffusion over the complete thickness of the PBCO and YBCO layers.

Material	**in-plane lattice parameters**	**thermal expansion coefficient** (10^{-6} K^{-1})	**misfit to YBCO** (%)
Sapphire, Al_2O_3, hexagonal	$a_\mathrm{r} = 4.76$ Å $b_\mathrm{r} = 5.12$ Å	8.0	6 - 12
CeO_2 cubic	$a = 5.41$ Å	9.9	0.16 - 1.7
PBCO orthorhombic	$a = 3.87$ Å $b = 3.93$ Å	11.0	< 1.5
YBCO orthorhombic	$a = 3.82$ Å $b = 3.88$ Å	11.0	-

Table 4.1: Overview of materials used in the multi-layer system with their crystallographic parameters [82, 107, 163, 168–170].

Finally, gold is deposited for the antenna and RF design, as the surface resistance of YBCO exceeds that of gold at frequencies above approximately 150 GHz [155]. Gold is grown at lower temperatures and does not grow as an epitaxial layer. The gold film of 200 nm thickness is grown in two steps that are explained in section 4.2.6. The deposited multi-layer structure is depicted in Fig. 4.5(a) and the crystallographic parameters of the different layers are summarized in Tab. 4.1.

4.2.2 Optimization of the thickness homogeneity of laser ablated thin films

The decrease of the deposition rate to a steady state value with increasing laser exposure of the target is a well-known phenomenon. Herein, the asymptotic value and the decrease rate depend on the incident laser flux. This behavior was also observed for the YBCO target used in this work (see Fig. 4.6) [Krä14]. Foltyn *et al.* showed that the target surface is modified by the impact of the laser. A closely packed columnar structure evolves and the deposition rate decreases [171]. The target surface can be restored by polishing the target.
Further improvement to the modification of the target surface is achieved through the scanning of a larger area with the laser beam. In particular, when the laser beam impinges at a bigger radius of the rotating target, a circular ring of larger surface is ablated. Therefore, a piezoelectric mirror was installed in the optical path of the PLD setup, as described in section 4.1. The surface of the target is thus scanned in radial and in circular direction. Thereby, nearly the complete uniform areas of the individual targets are exploited.

This results not only in the stabilization of the deposition rate but also increases the homogeneity of the deposited layers. Along with the scanning laser beam, the position of the plume oscillates

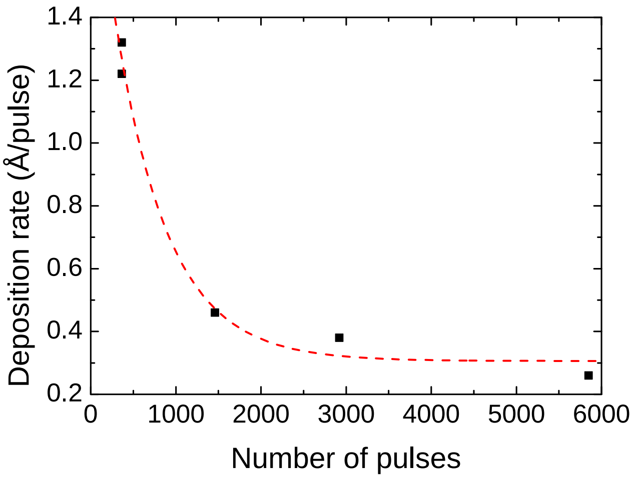

Fig. 4.6: Dependence of the deposition rate on the number of laser pulses. 6000 laser pulses correspond to an approximate YBCO layer thickness of 150 nm. The dashed line is to guide the eye.

repeatedly over the substrate leading to a more homogeneous layer thickness and to an evenly distributed stoichiometry all over the film. Figure 4.7 shows the thickness of YBCO and gold layers deposited while the plume was oscillating. On an area of 10×10 mm^2, the layer thickness deviates by $\pm 4\%$ for YBCO and $\pm 6\%$ for the ablation of gold. This corresponds to an absolute variation of ± 0.8 nm and ± 1.2 nm, respectively, for a thin film of 20 nm thickness. The combination of increased thickness homogeneity and constant stochiometric distribution gives an even more homogeneous result for the critical temperature that is plotted in Fig. 4.8 as a function of the position on the heater. The optimal center position of the 10×10 mm^2 substrate was determined as $x = 20$ mm, $y = 18$ mm (see Fig. 4.7) in accordance with the measured layer thicknesses.

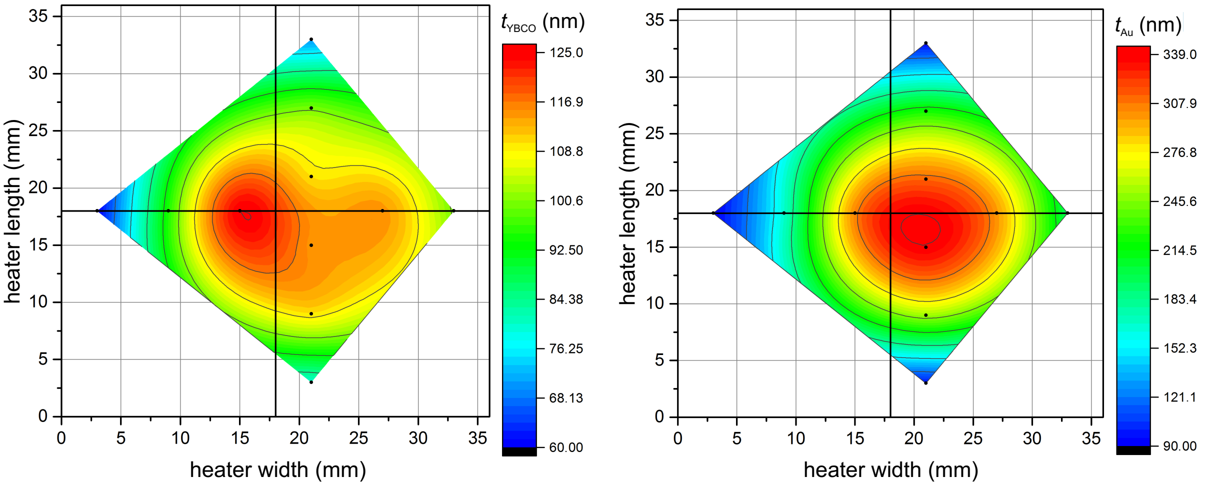

(a)

(b)

Fig. 4.7: Layer thickness homogeneity achieved with oscillating piezoelectric mirror [Gan15]. Film thickness in the x-y-plane of the heater for (a) a YBCO film, and (b) a gold film. The black dots correspond to the measurement points.

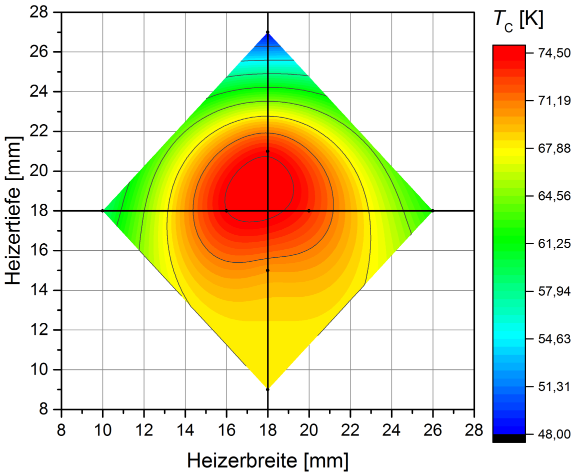

Fig. 4.8: Dependence of the critical temperature on the position of the substrate on the heater [Gan15]. The black dots correspond to the measurement points.

4.2.3 Smooth CeO_2 buffer layers

The flatness of the CeO_2 buffer layer and its epitaxial growth are equally important for the deposition of ultra-thin YBCO films. Lee *et al.* could deposit YBCO films with smooth surfaces on sapphire substrates by implementing a post-annealed CeO_2 buffer layer [172]. A surface roughness of 6.5 Å was measured for 140 nm thick YBCO films. Nie *et al.* showed a significantly improved flatness of post-annealed CeO_2 films as compared to as-grown PLD films [173]. However, at thicknesses below 10 nm, the post annealing leads to the rearrangement of the layer into large two-dimensionally ordered islands of about 25 nm height. Therefore, the post-annealing process cannot be used for samples thinner than 10 nm.

In this work, we used a CeO_2 target from Kurt J. Lesker Ltd. that replaced the target from Adelwitz Technologiezentrum GmbH from previous works. Therefore, all deposition parameters had to be readjusted to the new target. Figure 4.9 shows the critical temperature and transition width for a 20 nm thick YBCO film directly grown on CeO_2 buffer layers of different thicknesses. The critical temperature increases with decreasing CeO_2 thickness and optimum conditions were found for a thickness of 9.5 nm which is in good agreement with earlier works [15]. Increased layer thickness leads to increased surface roughness due to the island growth of CeO_2. Superconductivity in thin YBCO films, herein, is influenced profoundly by a rough underground. At lower CeO_2 buffer thicknesses on the other hand, the lattice mismatch cannot be fully corrected by the thin buffer layer, leading to a strain-induced reduced critical temperature.

Based on the before mentioned results on post-annealed CeO_2 films, the deposition temperature was raised from 800 °C to 820 °C and the oxygen partial pressure during deposition of CeO_2 was increased to 1.2 mbar. Thereby an increase in critical temperature of about 4.5 K was reached: $T_c = 74.5$ K for a 20 nm thick YBCO film as compared to $T_c = 69.9$ K for $p_{O2} = 0.93$ mbar. The

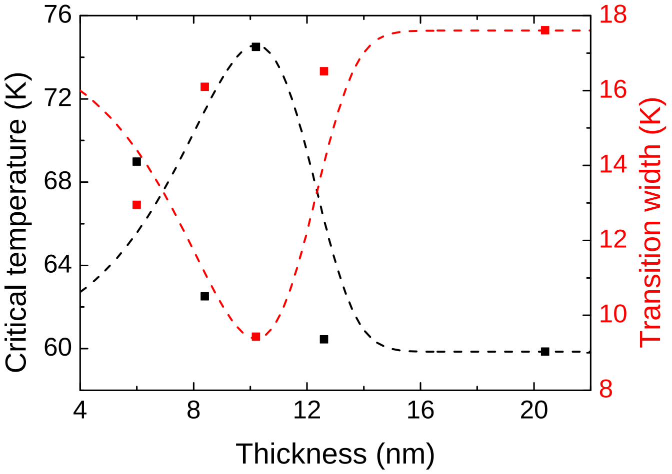

Fig. 4.9: Critical temperature and transition width vs. thickness of the CeO_2 buffer layer for a 20 nm thick YBCO film. T_c in black and ΔT in red with lines to guide the eye.

target-to-substrate distance is directly linked to the oxygen partial pressure as the size of the plume is influenced by the background gas pressure [123]. Optimum deposition conditions are reached when the edge of the plasma plume touches the surface of the substrate [174]. Here, the target-to-substrate distance was adjusted to $d_{\mathrm{TS}} = 62$ mm. The optimum energy density and repetition rate of the laser were found to be $w_{\mathrm{L}} = 2.82\ \mathrm{J/cm^2}$ and $f_{\mathrm{L}} = 5$ Hz.

The roughness of CeO_2 films of different thicknesses, deposited with the above-stated parameters, was investigated with an AFM [Kne15]. Figure 4.10 shows the measurement of the film with a thickness of 9.5 nm. The rms roughness amounts to $R_q = 350$ pm on an area of 0.5 $\mu\mathrm{m}^2$. With the lattice parameter of cubic CeO_2, $a = 5.41\ \text{Å} = 541$ pm, the roughness is less than one ML. Height profiles measured on films of different thickness are depicted in Fig. 4.11. For thicker films, the

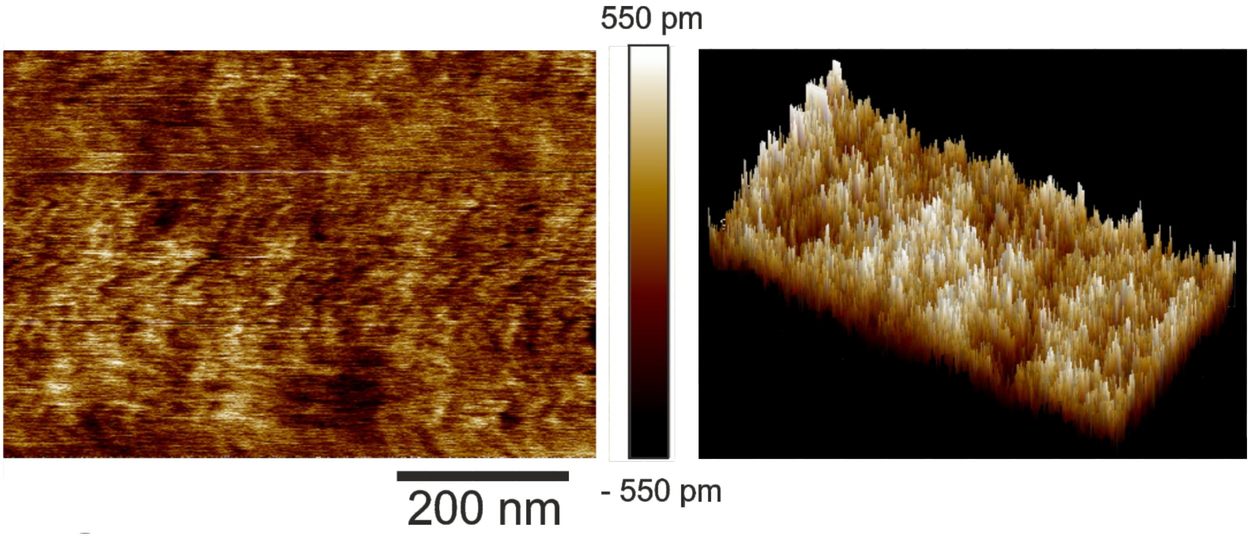

Fig. 4.10: 2D and 3D AFM images of the 9.5 nm thick CeO_2 buffer layer.

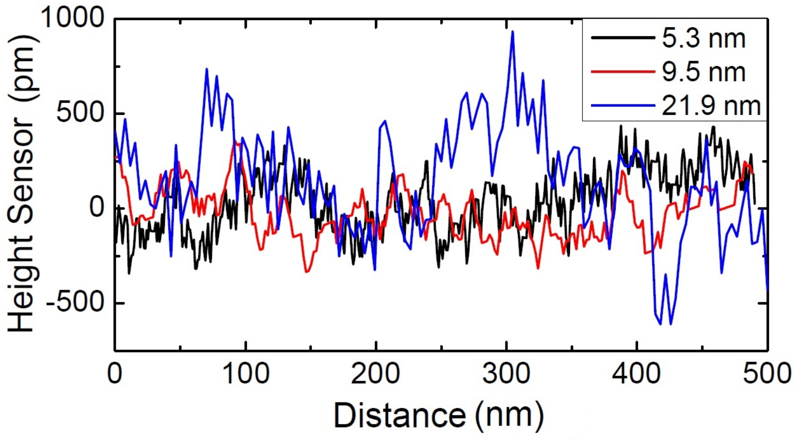

Fig. 4.11: AFM line scans for different CeO_2 film thicknesses.

roughness increases to about $R_q = 550$ pm for a 22 nm thick CeO_2 layer. Very thin films also show a slightly increased roughness, here $R_q = 470$ pm for a 5.3 nm CeO_2 layer. The reason to that may be the lack of full coalescence of the growing islands.

Finally, the epitaxial growth of the CeO_2 buffer layer was investigated by XRD measurements. A θ-2θ scan of a bare 20 nm thick CeO_2 film deposited at optimum conditions is depicted in Fig. 4.12(a). The $(00l)$ peaks are seen as expected, however they are not very pronounced due to the small thickness of the film. Moreover, a (111) peak is visible, indicating a small portion of an undesired growth direction. Figure 4.12(b) shows a texture measurement of the (103) plane of a thin YBCO film grown directly on top of a 9.5 nm CeO_2 buffer [Kne15]. The reflexes occur at the same azimuthal angle as seen in a texture measurement of the (222) plane of the CeO_2 film, indicating the expected 45° twist between the *a*-*b*-planes of CeO_2 and YBCO.

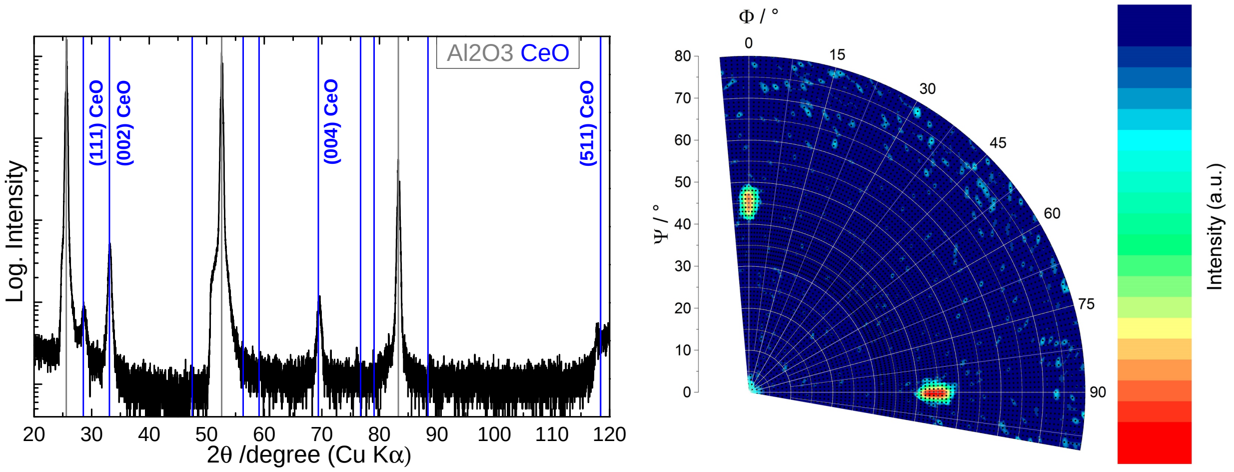

(a)

(b)

Fig. 4.12: XRD characterization of the CeO_2 buffer layer. (a) θ-2θ scan of a 20 nm CeO_2 film on sapphire substrate. (b) texture of the (103) plane of a YBCO film grown on a CeO_2 buffer.

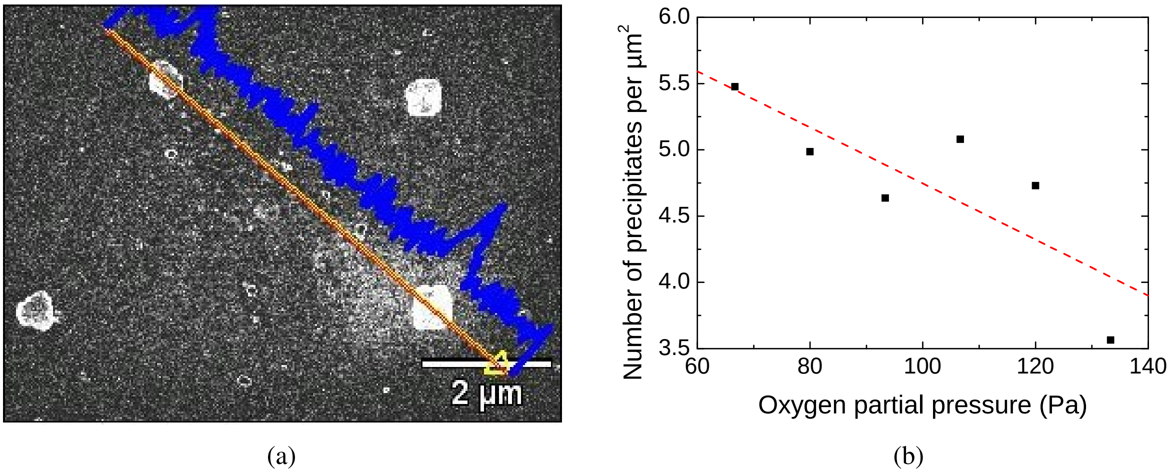

(a) (b)

Fig. 4.13: Occurrence of CuO precipitates during the growth of PBCO and YBCO. (a) EDX analysis of Cu content on a CeO_2(8 nm)/YBCO(30 nm) sandwich, (b) Dependence of the precipitate density measured in an area of 22 µm^2 on the oxygen partial pressure [Kne15]. The line is to guide the eye.

4.2.4 Interval deposition of PBCO

With PBCO being a room-temperature semiconductor, as compared to isolating CeO_2, the additional possibility arises to characterize the samples with SEM. Herein, the film surface is assessed with regard to the size of the grown grains, the density of islands and the size and number of precipitates. Precipitates are secondary phases, such as CuO outgrowths or Y_2O_3 inclusions, that can appear during the growth of YBCO and PBCO films [175]. The occurrence of precipitates is likely as the film deposition parameters (i.e. oxygen partial pressure and substrate temperature) are near the decomposition line of PBCO and YBCO [176]. In this work, the EDX analysis of the secondary phases revealed CuO outgrowths (see Fig. 4.13(a)). A new PBCO target from the Leibniz Institute for Solid State and Materials Research in Dresden was used.

Precipitates do not influence the superconducting properties of the overall film negatively. Contrarily, Gong *et al.* showed that films with a higher density of precipitates have less defects in the stochiometric 1:2:3 compound [177]. They explained their results as the segregation into secondary phases of off-stochiometric elements arriving at the film surface. However, when their position coincides with that of the detecting element, the effective volume of the detector is modified. Also, patterning of sub-µm structures is challenged by the presence of precipitates on the surface of the film.

Increased oxygen partial pressure leads to stronger scattering of the light elements in the plume, thus the Cu content decreases as compared to Pr and Ba. Therefore, the density of CuO precipitates decreases with augmenting oxygen pressure during the deposition of PBCO or YBCO. The number of precipitates was measured in an area of 22 µm^2 on a PBCO thin film [Kne15]. The

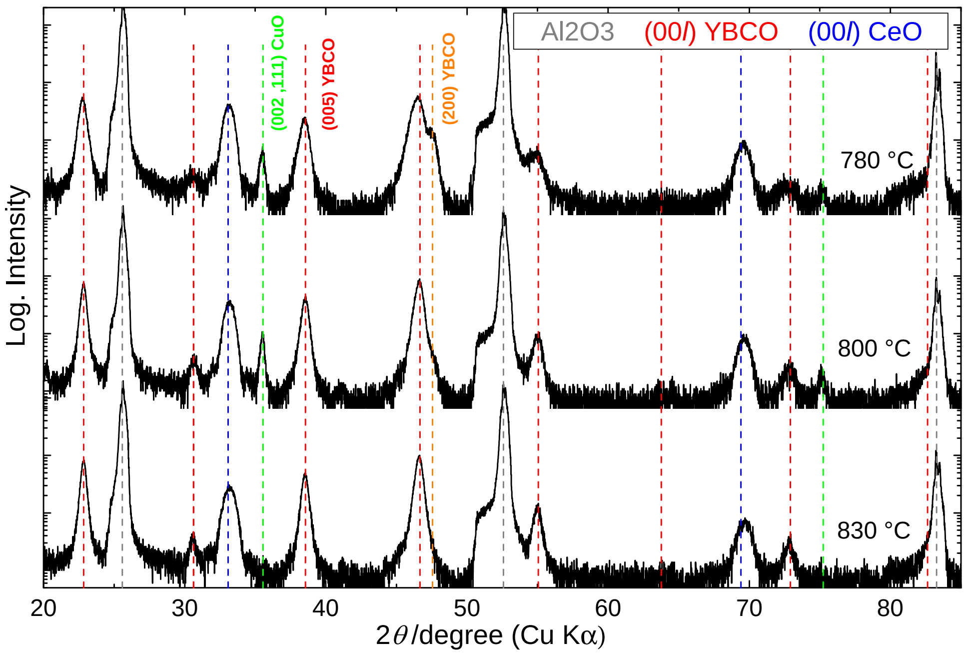

Fig. 4.14: θ-2θ scans of CeO_2(9.5 nm)/PBCO(31.5 nm)/YBCO(20 nm) multi-layer stacks for different growth temperatures of PBCO. The green lines indicate (111) or (002) CuO phases (precipitates) and the orange line (200) YBCO, thus *a*-axis growth [Kne15].

resulting precipitate density vs. the oxygen partial pressure is plotted in Fig. 4.13(b).

Han *et al.* found that the number of CuO particles can additionally be reduced by increasing the substrate temperature and by a decrease in deposition rate [178]. These results suggest that a higher temperature of the heater is preferable. This is backed by the fact that also the crystalline growth of PBCO and YBCO is improved by increased substrate temperatures (see Fig. 4.14). At lower substrate temperatures ($T_{\text{Sub}} = 780$ °C), incipient *a*-axis growth is observed. The $(00l)$ peaks, indicating *c*-axis growth of PBCO and YBCO, show enhanced intensity with increasing substrate temperature. Additionally, the ω scans reveal decreasing width from 1.4° (FWHM) at $T_{\text{Sub}} = 780$ °C to 1.2° at $T_{\text{Sub}} = 830$ °C, meaning that the spread in the *c*-axis tilt declines. Moreover, as expected, the portion of secondary CuO phases grows when the temperature is reduced. This can also be seen in Fig. 4.15 where SEM pictures of the CeO_2 (9.5 nm)/PBCO(31.5 nm)/YBCO(20 nm) multi layer system maintained at different heater temperatures during the deposition of PBCO are depicted [Kne15].

The optimal parameters found for the continuous deposition of PBCO are: $E_{\text{L}} = 2.4$ J/cm^2, $f_{\text{L}} = 10$ Hz, $d_{\text{TS}} = 52$ mm, $p_{\text{O2}} = 0.8$ mbar and $T_{\text{Sub}} = 815$ °C with a deposition rate of $r_{\text{dep}} = 0.8\ \text{nm/s} \mathrel{\hat{=}} 0.8\ \text{Å/pulse}$. For a thickness of the PBCO buffer layer of 4.8 nm a critical temperature of $T_{\text{c}} = 78.3$ K and a transition width of $\Delta T = 8.9$ K were found for a 20 nm thick YBCO film. The rms roughness of the PBCO film deposited on top of the CeO_2 buffer layer amounts to $R_{\text{q}} \approx 1$ nm

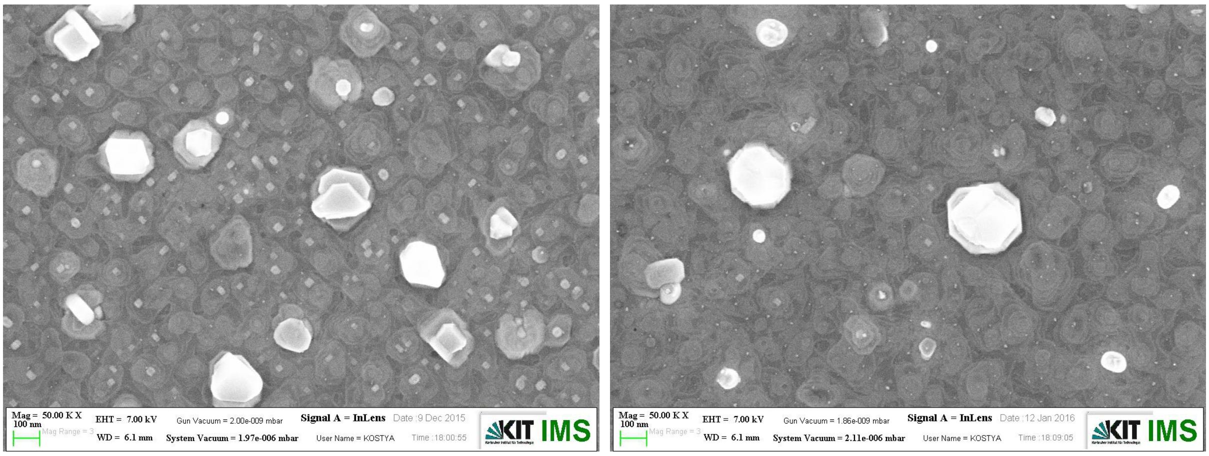

(a)

(b)

Fig. 4.15: SEM pictures of a CeO_2(9.5 nm)/PBCO(31.5 nm)/YBCO(20 nm) multi-layer stack for different substrate temperatures during the growth of PBCO. (a) $T_{\mathrm{Sub}} = 800$ °C, (b) $T_{\mathrm{Sub}} = 830$ °C [Kne15].

on an area of 0.75 μm^2, which is less than one ML of PBCO. When increasing the PBCO thickness to 31.5 nm a higher critical temperature of 86.5 K is achieved. However, the island growth of PBCO then leads to increased roughness of the film, $R_q \approx 6.7$ nm on an area of 1 μm^2. This prevents for the growth of closed ultra-thin YBCO layers. Moreover, as discussed in section 3.2.1, layer-by-layer growth can only occur up to a critical thickness h_C of several ML for YBCO and the isomorphic PBCO. Therefore, the PBCO buffer layer thickness needs to be kept as small as possible.

A method to further improve the flatness of the deposited buffer layer is the interval PLD which was introduced in section 3.2.2 [108, 125, 126]. The number of pulses needed to deposit exactly the material for one ML was calculated from the deposition rate and equals $n_P = 14.6$. As this result is subject to variations of the laser energy and the transmission of the optical path as well as measurement errors when determining the layer thickness, samples with $n_P = 14$ and $n_P = 15$ pulses per ML were produced. SEM images of the two samples are displayed in Fig. 4.16. The sample deposited with 14 pulses per ML shows holes and a high density of precipitates. This is the result of insufficient deposition of material per ML leading to the formation of preferential nucleation sites for precipitates. As compared to that, 15 pulses per ML give a very smooth film with a closed surface and only few and small precipitates. The typical terraced surface structure of PBCO and YBCO films is not visible, indicating actual layer-by-layer growth. Small 2D islands of the next ML of PBCO are growing on the surface, which is a sign for $n_P = 15$ slightly too much material for one ML is deposited.

The optimal idle time between two consecutive MLs was determined as $t_{\mathrm{idle}} = 12$ s. Similar pause times were found by other groups [125]. The PBCO buffer layer thickness was increased to eight MLs in order to allow for better matching of the substrate to the lattice constants of YBCO. The

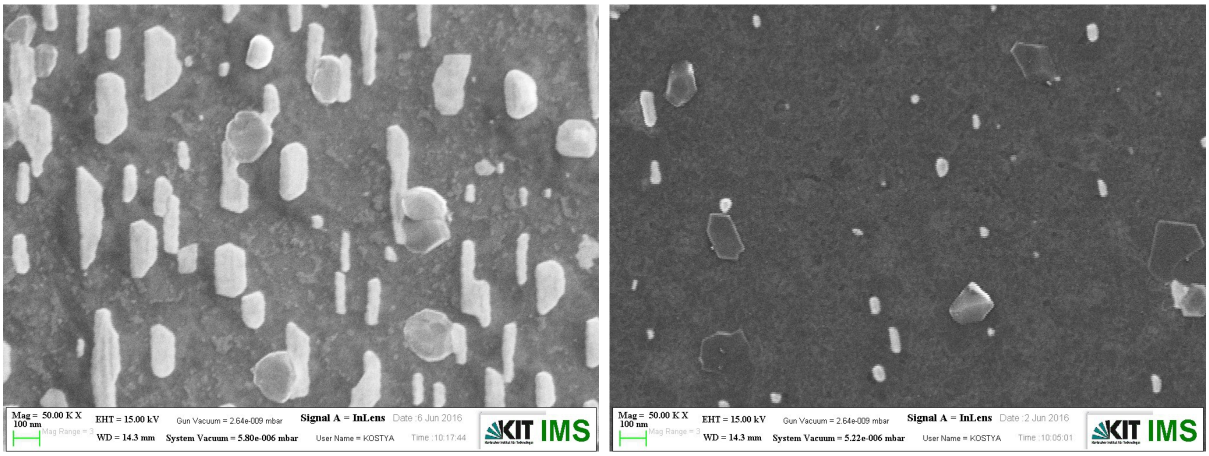

(a) (b)

Fig. 4.16: SEM pictures of interval-deposited PBCO: (a) $n_\mathrm{P} = 14$ pulses per ML, (b) $n_\mathrm{P} = 15$ pulses per ML [Feß16]. The layer thickness is four MLs.

rms roughness of the PBCO buffer layer was measured as $R_\mathrm{q} = 1.9$ nm on an area of 4.6 $\mu\mathrm{m}^2$. According to Guan *et al.* the roughness of the film could be further decreased by working at higher laser repetition rates and thereby reducing the ripening time of a nucleating island [179]. As a consequence, more and smaller islands are formed on the surface. Ideally, the island height corresponds to one ML and layer-by-layer growth is observed. In our case, $f_\mathrm{L} = 10$ Hz is the highest repetition rate at which the laser can operate. The time needed for complete diffusion of the adatoms on the target surface, according to the literature, amounts to $\tau \approx 0.5$ s [125, 126]. Therefore, laser repetition rates that are much larger than 2 Hz are appropriate for interval PLD.

The critical temperature of a 20 nm thick YBCO film deposited on top is comparable to the results achieved with the four ML thick buffer layer: $T_\mathrm{c} = 78.8$ K. The transition width ($\Delta T = 7.6$ K) and the normal state resistances are smaller [Feß16]. Therefore, a smaller number of defects is expected to be incorporated in the YBCO film grown on top of the eight ML thick PBCO buffer layer.

4.2.5 Growth of thin YBCO films

For the deposition of the superconducting layer, the old target from Jupiter Technologies was replaced by a target from Forschungszentrum Jülich that had been stored in the desiccator since 2008. The goal of this optimization step was to deposit of a completely coalesced YBCO film of a few MLs thickness. To this end, as with PBCO, the continuous deposition parameters were investigated at first and then transferred to interval PLD.

One of the most crucial parameters for high-quality thin films is the laser flux. Its optimal value was determined to be $E_\mathrm{L} = 2.4\ \mathrm{J/cm^2}$. As it was seen already during the optimization of the PBCO layer, a reduced target-to-substrate distance ($d_\mathrm{TS} = 52$ mm) leads to a lower density of

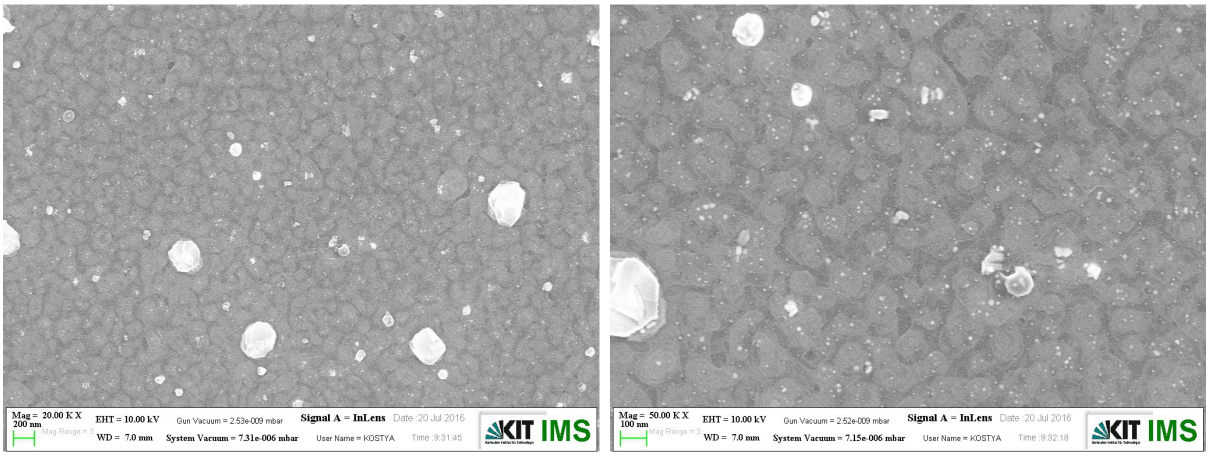

(a) (b)

Fig. 4.17: SEM pictures of continuously deposited YBCO: (a) 20.000 fold magnification, (b) 50.000 fold magnification [Feß16].

precipitates. Similarly, the oxygen partial pressure had to be reduced ($p_{O2} = 0.8$ mbar). The highest critical temperatures were found for YBCO films deposited at substrate temperatures below 800 °C. With decreasing temperature, the density of precipitates increases while the individual segregations become smaller. This can be attributed to a reduced diffusion length of the adatoms. Too low substrate temperatures yield films with holes in the YBCO layer and the optimal point was found at $T_{Sub} = 780$ °C [Feß16].
With a laser frequency of 5 Hz, the deposition rate amounts to $r_{dep} = 0.51$ nm/s $\widehat{=}$ 0.1 nm/pulse. SEM images with different magnification factors of the optimized YBCO film are depicted in Fig. 4.17. For a YBCO film, thickness of 30.6 nm the critical temperature was found as 87.8 K with a transition width of 3.3 K. Decreasing the YBCO film thickness by 5 nm yields comparable results ($T_c = 87.2$ K, $\Delta T = 3.2$ K) [Feß16].

From the above mentioned deposition rate for continuous ablation of YBCO, the number of pulses for one ML was calculated as $n_P = 11.5$. Laser repetition rates of 5 Hz and 10 Hz were tested. According to Blank *et al.*, a higher repetition is preferable because of the increased supersaturation [125]. However, in this work an increase of the critical temperature by nearly 10 K was found for 20 ML thick YBCO films upon decrease of the repetition rate to 5 Hz as compared to $f_L = 10$ Hz. Two MLs were deposited per interval and the range of $2n_P = 23$ - 25 was investigated for YBCO films of 10 MLs thickness (see Fig. 4.18). The deposition of two MLs during one interval enables a more exact determination of the optimum number of pulses per ML since half pulses cannot be realized for a single ML deposition. Optimum T_c values were found for $2n_P = 25$ ($T_c = 75.3$ K, $\Delta T = 8.6$ K). The deviation from the calculated value could be due to measurement errors during thickness determination of the samples, as the surface roughness deteriorates the exactness of the measured values.

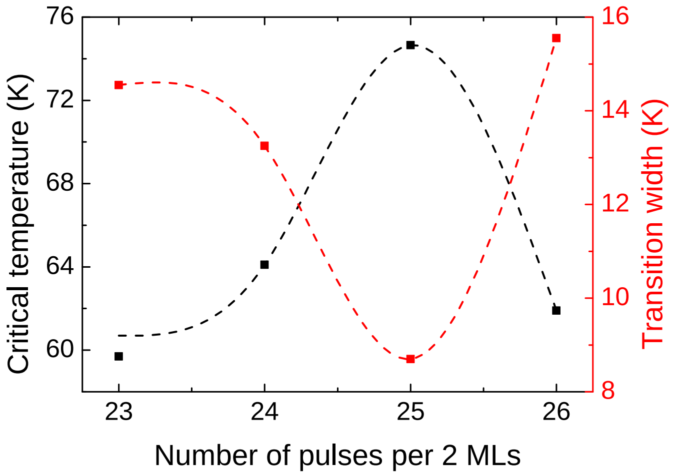

Fig. 4.18: Dependence of the critical temperature T_c and the transition width ΔT on the number of pulses per two MLs [Feß16].

The rms roughness was determined to amount to 3.6 nm on an area of 1 μm^2 measured on a YBCO film of 10 MLs thickness. Seen that the underlying PBCO buffer layer already introduced a roughness of 1.9 nm (see section 4.2.4), this corresponds to an additional roughening of < 2 nm. In particular, this result indicates that the growth of fully coalesced continuous YBCO films on top of the buffer layers used in this work is possible down to 4 or 5 MLs thickness of the superconducting thin film.

PBCO passivation layer

A passivating PBCO layer must be deposited on top of the few ML thick YBCO in order to prevent the oxygen from out-diffusion. Without the passivation layer, these films are not superconducting when measured directly after the deposition. Generally, the use of a passivation layer prevents thin YBCO films (< 30 nm) from degradation during the patterning process or due to humidity.

The passivation layer was deposited with interval PLD using the same parameters as for the PBCO buffer layer. Only the substrate temperature was adjusted to the deposition of YBCO ($T_{\mathrm{Sub}} = 780$ °C) as an increase of the substrate temperature when keeping the oxygen partial pressure constant would result in an out-diffusion of oxygen from the as-deposited YBCO film. The thickness was also kept at eight MLs, corresponding to 9.4 nm. Herein, the thickness becomes critical when the oxygen can not fully diffuse through the layer during annealing of the multi-layer structure. It was shown that thicknesses up to 25 nm are possible [15].

4.2.6 Investigation of ablated and sputtered gold films

For the YBCO detectors, a gold film of 200 nm thickness is deposited. Herein, the film thickness corresponds to the skin depth at a frequency of 140 GHz and room temperature [180]. Two

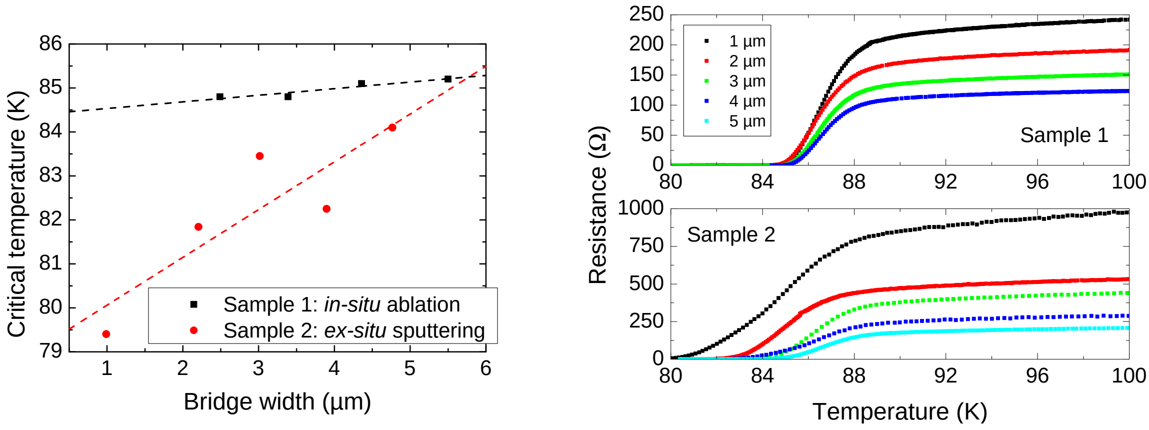

(a) (b)

Fig. 4.19: (a) Dependence of the critical temperature on the bridge width for *in-situ* ablated and *ex-situ* sputtered gold films deposited on top of a CeO_2/PBCO/YBCO/PBCO multi stack, with lines to guide the eye, and (b) corresponding $R(T)$ curves.

possibilities for the gold deposition were considered: *in-situ* ablation of PLD gold and *ex-situ* DC-magnetron sputtering combined with a pre-cleaning treatment.

In-situ deposited gold contacts offer the advantage of low contact resistances. Du *et al.* found contact resistivities of $\rho_C < 1 \cdot 10^{-8}$ µΩcm^2 at 77 K for gold that was evaporated in-situ on YBCO films from Theva GmbH [181]. Similarly low contact resistivities from *ex-situ* gold deposition can only be achieved through post-annealing of the layers. However, this treatment implicates agglomeration of the metal and diffusion of Au atoms into the YBCO and PBCO layers [182]. For *ex-situ* gold deposition on a pre-cleaned YBCO surface, contact resistivities of $10^{-6} \ldots 10^{-7}$ µΩcm^2 were reported [181]. Therefore, at least partial *in-situ* deposition of the gold film is required.

Moreover, the pre-cleaning of the bare PBCO passivation layer surface harms the film. In this work, before the *ex-situ* sputtering of gold, the surface was pre-cleaned with a DC plasma source. The effect of degradation due to the pre-cleaning is depicted in Fig. 4.19. Two identical chips were deposited and patterned into several µm-sized bridges, one of them with an *in-situ* PLD gold layer and the second one with a DC-magnetron sputtered gold film on top of the passivating PBCO layer. Generally, the critical temperatures of the first sample are higher. An overall tendency of decreasing T_c with decreasing width of the bridges is visible and can be explained by the degradation from the sides during etching of the µm-sized structure. However, this effect is clearly more pronounced for the second sample, which is attributed to the degradation during the pre-cleaning of the PBCO surface. This is backed by the fact that the normal-state resistances R_n are increased for Sample 2 as compared to Sample 1. Further details on the configuration of the pre-cleaning process and the patterning of (sub-)µm structures can be found in chapter 5.

There are two aspects that favor a DC-magnetron sputtered gold film as compared to the ablated

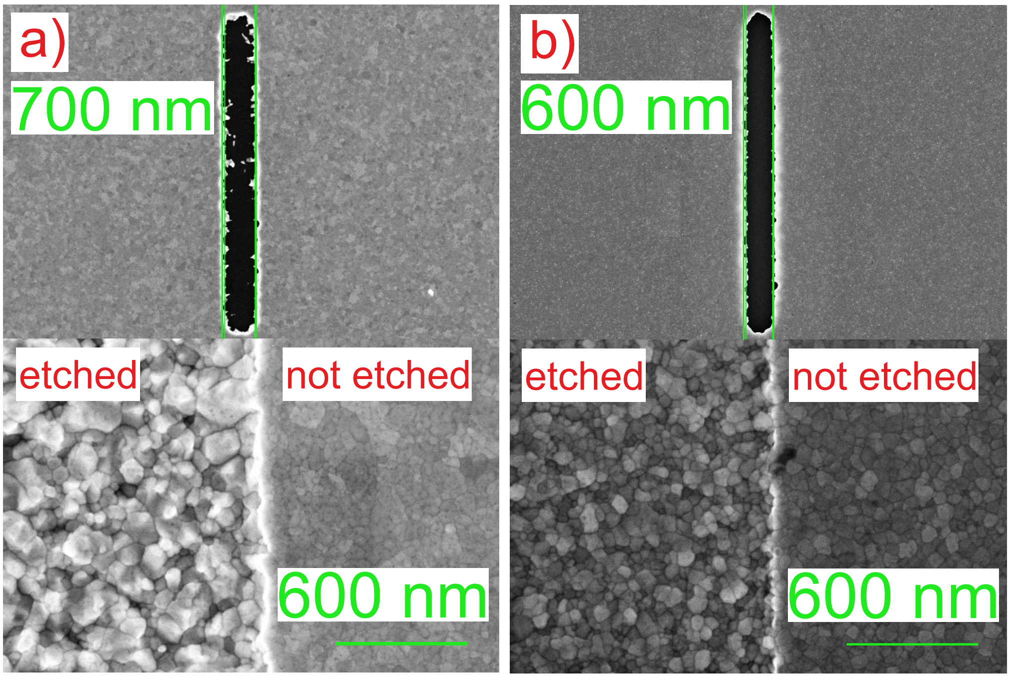

(a) (b)

Fig. 4.20: SEM pictures of the granular structure and wet-etching behavior for (a) laser ablated gold films and (b) DC-magnetron sputtered gold films.

films. As already discussed in section 4.2.2, the thickness of laser-ablated gold films deviates by ±6% on an area of $10 \times 10\,\mathrm{mm}^2$. For a 200 nm thick PLD gold film, a thickness variation of 24 nm on the chip area would restrain the etching process of the layer. As compared to that, the *ex-situ* sputtered gold films exhibit good thickness homogeneity as the size of the substrate ($10 \times 10\,\mathrm{mm}^2$) is much smaller than the diameter of the target (2 inches).
Also, the granular structure of PLD gold is larger than the grains from DC-magnetron sputtering. For this reason, the ablated gold behaves unreproducibly during wet-chemical etching and rough edges are formed (see Fig. 4.20). Moreover, the etching rate is nonuniform, leading to holes in the etched areas. The sputtered gold films offer higher homogeneity and reproducible etching behavior as well as stable etching rates.

In summary, not the full gold layer can be deposited by PLD and only the first 20 nm of the gold film are ablated *in-situ* to assure good contact resistance and protection of the underlying YBCO layer. The resulting thickness variation of the PLD gold films of roughly 1 nm is within the limit of reproducibility of the overall film thickness. Subsequently, the remaining 180 nm are deposited *ex-situ* by DC-magnetron sputtering after a pre-cleaning treatment of the PLD thin-film stack. That way, thickness homogeneity and reproducible etching behavior of the gold film are ensured.

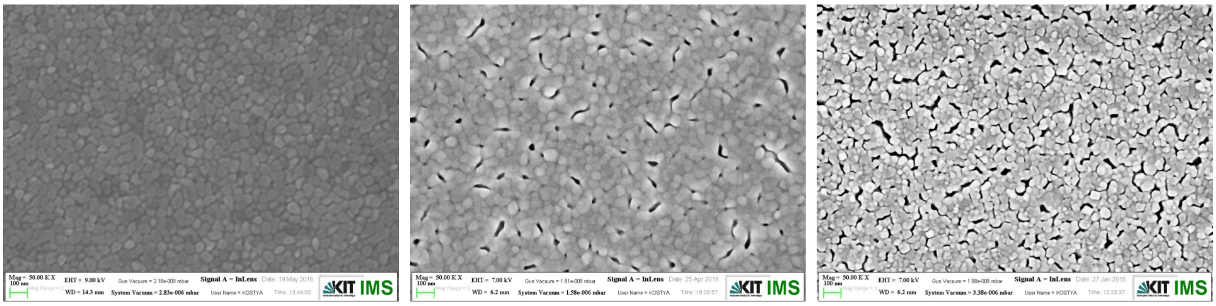

(a) (b) (c)

Fig. 4.21: SEM images (50.000 fold magnification) of the granular structure for DC-magnetron sputtered gold films: (a) $I_{\mathrm{dep}} = 10$ mA and $p_{\mathrm{Ar}} = 2 \cdot 10^{-2}$ mbar, (b) $I_{\mathrm{dep}} = 10$ mA and $p_{\mathrm{Ar}} = 4 \cdot 10^{-2}$ mbar, and (c) $I_{\mathrm{dep}} = 150$ mA and $p_{\mathrm{Ar}} = 0.1$ mbar.

Optimization of DC-magnetron sputtered gold films

Ablated gold has another advantage that arises from the larger grains and correspondingly fewer grain boundaries. The resistivities of the thin films are very low and even comparable to the literature values for bulk gold: $\rho_{\mathrm{PLD}} = 2.58$ µΩcm at 300 K for a film thickness of 150 nm and $\rho_{\mathrm{Literature}} = 2.21$ µΩcm [183, p. 12-41]. Lower resistivities entail lower surface resistances and thus less RF losses in the antenna and the readout lines [184]. As compared to that the resistivity of 200 nm thick sputtered gold amounts to $\rho_{\mathrm{Sputter}} = 3.98$ µΩcm at room temperature for the standard deposition parameters ($p_{\mathrm{Ar}} = 5 \times 10^{-3}$ mbar and $I_{\mathrm{dep}} = 150$ mA).

An optimization of the quality of the sputtered gold films was therefore necessary. By decreasing the deposition rate, the growth of the gold film becomes more homogeneous leading to lower resistivities. Smaller growth rates can be realized through the lowering of the deposition current I_{dep} or by increasing the argon pressure p_{Ar}. Higher argon pressures correspond to a larger number of argon ions near the magnetron. Thereby, the resistance of the plasma decreases and with it the power density ($P = RI_{\mathrm{dep}}^2$). Likewise, lower deposition currents entail a decrease in power density, which in turn is proportional to the deposition rate [185].

To minimize the deposition rate, the deposition current I_{dep} was lowered to the minimum value that is needed to maintain a stable plasma. This value was found to be $I_{\mathrm{dep}} = 10$ mA. Subsequently, the optimum argon pressure was determined. An increase of the argon pressure decreases the mean free path of the sputtered gold atoms and causes the growth of an inhomogeneous film with holes in between the gold grains. This film structure leads to increased resistivities (see Fig. 4.21). At lower argon pressures, in turn, the deposition rate increases, resulting in an increase of the resistivity, too. The optimum pressure was found to be $p_{\mathrm{Ar}} = 2 \cdot 10^{-2}$ mbar (see Fig. 4.22). The corresponding gold deposition rate is $r_{\mathrm{dep}} = 0.74$ Å/s. A room temperature resistivity of $\rho_{\mathrm{Sputter}} = 2.49$ µΩcm is achieved, which is smaller than the resistivity of PLD gold.

During thin-film optimization, the gold layer thicknesses fluctuated between 160 nm and 260 nm.

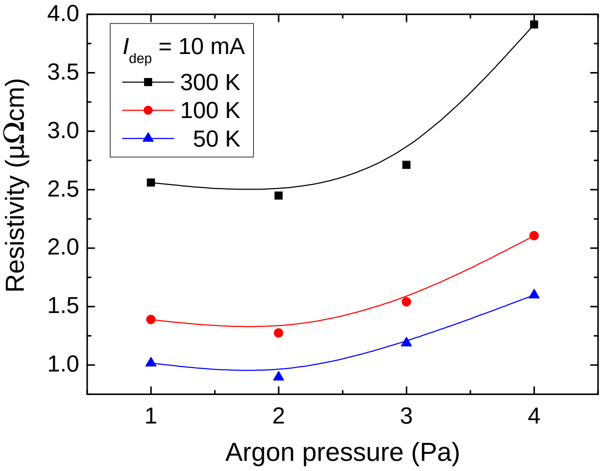

Fig. 4.22: Resistivity of DC-magnetron sputtered gold films depending on the argon pressure p_{Ar} measured at different temperatures. The optimum result was achieved for $p_{\mathrm{Ar}} = 2 \cdot 10^{-2}$ mbar and is comparable to the literature value. The lines are to guide the eye.

The influence of the layer thickness on resistivity can, however, be neglected above film thicknesses of 100 nm for gold [186, 187].

4.3 Conclusions of chapter 4

In this chapter, the deposition process of the multi-layer system for the fabrication of YBCO THz detectors was introduced. PLD was used to deposit the superconducting thin films, exploiting the high background pressures to ensure stochiometric oxygen content within the individual layers. The laser ablation of thin films was realized with a semi-automated deposition process, controlled by LabVIEW, thereby enabling reproducible deposition conditions. The requirements for film thickness homogeneity were met by the implementation of a piezoelectric mirror that scans the laser beam along the target surface. Finally, the concept of interval PLD was introduced to minimize the overall film roughness and to allow for the deposition of single MLs of PBCO and YBCO. To minimize RF losses, a gold film was deposited on top of the multi-layer stack. Laser ablation of the first 20 nm of gold protects the underlying PBCO and ensures low contact resistance. Subsequent pre-cleaning of the surface and DC-magnetron sputtering of further 180 nm of gold results in stable etching behavior, reproducible layer thicknesses and overall resistivities that are comparable with the literature value. The optimal solution to the deposition of stable and low resistive gold films with low contact resistance and sticking coefficient to the underlying layers would be the *in-situ* sputtering of gold films. Therefore, a DC magnetron should be integrated into the vacuum chamber of the PLD system.

The individual layers were optimized towards maximum critical temperature T_c and crystalline homogeneity of the YBCO film, minimum film roughness to enable the deposition of ultra-thin

YBCO and minimum resistivity of the gold film. The full set of optimal parameters, found for the deposition of the multi-layer system, is summarized below:

CeO_2 buffer layer, $t = 9.5$ nm
$w_{\mathrm{L}} = 2.82\ \mathrm{J/cm^2}$, $d_{\mathrm{TS}} = 62$ mm, $p_{\mathrm{O2}} = 1.2$ mbar, $T_{\mathrm{Sub}} = 820$ °C, $f_{\mathrm{L}} = 5$ Hz, $t_{\mathrm{dep}} = 17$ s

PBCO buffer layer, $t = 9.4\ \mathrm{nm} \mathrel{\widehat{=}} 8$ ML
$w_{\mathrm{L}} = 2.4\ \mathrm{J/cm^2}$, $d_{\mathrm{TS}} = 52$ mm, $p_{\mathrm{O2}} = 0.8$ mbar, $T_{\mathrm{Sub}} = 815$ °C, $f_{\mathrm{L}} = 10$ Hz, $n_{\mathrm{P}} = 15$, $n_{\mathrm{I}} = 8$, $t_{\mathrm{idle}} = 12$ s

YBCO thin film, 25 pulses/2 ML
$w_{\mathrm{L}} = 2.4\ \mathrm{J/cm^2}$, $d_{\mathrm{TS}} = 52$ mm, $p_{\mathrm{O2}} = 0.8$ mbar, $T_{\mathrm{Sub}} = 780$ °C, $f_{\mathrm{L}} = 5$ Hz, $n_{\mathrm{P}} = 25$, $t_{\mathrm{idle}} = 12$ s

PBCO passivation layer, $t = 9.4\ \mathrm{nm} \mathrel{\widehat{=}} 8$ ML
$w_{\mathrm{L}} = 2.4\ \mathrm{J/cm^2}$, $d_{\mathrm{TS}} = 52$ mm, $p_{\mathrm{O2}} = 0.8$ mbar, $T_{\mathrm{Sub}} = 780$ °C, $f_{\mathrm{L}} = 10$ Hz, $n_{\mathrm{P}} = 15$, $n_{\mathrm{I}} = 8$, $t_{\mathrm{idle}} = 12$ s

***In-situ* gold film**, $t = 20$ nm
$w_{\mathrm{L}} = 9.08\ \mathrm{J/cm^2}$, $d_{\mathrm{TS}} = 42$ mm, $p = 5 \times 10^{-5}$ mbar, $T_{\mathrm{Sub}} \approx 80$ °C, $f_{\mathrm{L}} = 10$ Hz, $t_{\mathrm{dep}} =$ s

***Ex-situ* sputtered gold film**, $t = 180$ nm
$I_{\mathrm{dep}} = 10$ mA, $p_{\mathrm{Ar}} = 2 \cdot 10^{-2}$ mbar, $t_{\mathrm{dep}} = 2432$ s

For the thinnest deposited film ($t_{\mathrm{YBCO}} = 11.7\ \mathrm{nm} \mathrel{\widehat{=}} 10$ ML) a maximum critical temperature of $T_{\mathrm{c}} = 75.3$ K was found. The rms roughness measured on a stack of CeO_2(9.5 nm)/PBCO(8 ML)/YBCO(10 ML) adds up to 3.6 nm. The resistivities for ablated and sputtered gold films at room temperature amount to $\rho_{\mathrm{PLD}} = 2.58\ \mu\Omega\mathrm{cm}$ and $\rho_{\mathrm{Sputter}} = 2.49\ \mu\Omega\mathrm{cm}$, respectively.

As the final YBCO detector chips have to be operable at liquid-nitrogen temperature and moreover are required to offer long-term stability, YBCO films with thicknesses between 20 nm and 30 nm were deposited for the multi-layer system used for detector fabrication. For a film thickness of $t_{\mathrm{YBCO}} = 25$ nm and a continuous deposition of the YBCO film, the critical temperature is well above the boiling temperature of liquid nitrogen ($T_{\mathrm{c}} = 87.2$ K, $\Delta T = 3.2$ K).

5 Fabrication process for YBCO nanobridges

In order to increase the sensitivity while keeping the response times of the YBCO detectors in the picosecond range, the thin films are patterned to sub-µm-sized detecting elements. This chapter deals with the most crucial step during fabrication of the YBCO detector: the removal of gold in the area of the detecting element. The optimization of the fabrication process aimed for the patterning of minimal detector lengths of 100 nm. The second part of the chapter introduces the complete patterning process implemented for the fabrication of sensitive YBCO THz detectors and summarizes their superconducting properties.

5.1 Definition of the length of the detecting element

As mentioned before (see section 4.2.1), the surface resistance of YBCO exceeds that of gold at frequencies above about 150 GHz [155]. Therefore, the gold metallization has to be removed in the area of the detecting element to ensure that the THz signal propagates through the YBCO detecting element. The design of the YBCO detecting element was introduced in section 3.4, see Fig. 3.6. An elegant way to pattern the metal contacts and antenna is a lift-off process. As described in section 3.2.5 this is what is usually found in literature, when it comes to the patterning of YBCO THz detectors. However, as discussed in section 4.2.6, the *ex-situ* deposition of gold entails high contact resistances. Also, the preparation and cleaning of the PBCO passivation layer surface is complicated and often associated with surface degradation. Especially for very thin films, this can lead to a degradation of the entire multi-layer stack. As the thin-film quality and the protection of the YBCO layer are essential for the superconducting properties of the detector, the more complicated procedure of *in-situ* deposition and subsequent removal of the gold was implemented in this work. Therefore, a thin slit is etched into the gold film, wherein the width of the slit defines the length of the actual detecting element, see dotted line in Fig. 5.1. The different possibilities for gold etching which were considered are discussed in the following.

5.1.1 Etching techniques

Wet-chemical etching solutions

Wet etching has the advantage of high selectivity. Thereby, only the gold layer is etched and the underlying ceramic layers remain unharmed. Essentially, wet etching is an electrochemical

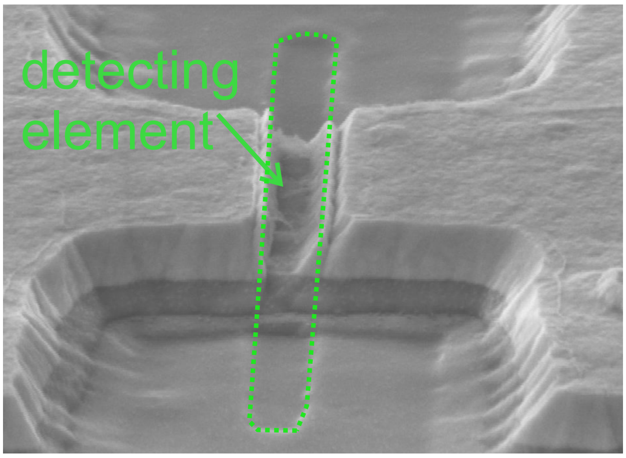

Fig. 5.1: SEM image depicting the definition of the length of the detecting element. The slit that is etched into the gold metallization is marked by the dotted green line.

process, where the gold atoms are oxidized to Au^+ in the anodic reaction, forming a complex with the ligand L^-. The electrons generated during this process are consumed in the cathodic process during the reduction of the oxidant [188]. A wet etchant that has shown to have no detrimental effect on YBCO is potassium iodide ($I_2(KI)_5$). It is usually applied in an aqueous solution. The I_3^-/I^- system is used as oxidizing agent of gold:

$$\mathrm{Au^+ + 2\,I^- \rightarrow Au\,I_2^- + e^-} \tag{5.1}$$

$$\mathrm{I_3^- + 2\,e^- \rightarrow 3\,I} \tag{5.2}$$

A reduction of the critical current density of about 25% was found in YBCO films of 250 nm thickness by Eidelloth et al. [189]. The observed diminishment was attributed to the degradation of the YBCO surface during rinsing of the sample in deionized water.

In this work, the YBCO surface is protected by the PBCO passivation layer. We used a solution of 1:5:40 of iodine (I_2), potassium iodide (KI) and deionized water. The solution was dissolved 1:3 in deionized water. After etching, the sample was rinsed in deionized water for $10-20$ s. Etching rates for ablated and sputtered gold amount to 2 nm/s and 1 nm/s, respectively.

Figure 5.2 (red squares) displays the influence of the etching procedure on the critical temperature of unpatterned YBCO films [Rot16]. Here, unprotected films of YBCO on a CeO_2 buffer layer were suspended to the etchant in order to simulate the effect of over-etching. Relating to the above mentioned etch rates, over-etching with the potassium iodide solution should not exceed 30 s. Degradation of the sample due to the contact with deionized water can be observed as expected from [189]. Here, the critical temperature of the sample is reduced by ≈ 3 K.

Another disadvantage of wet-chemical etching is the isotropic behavior of the etchant that entails strong underetching and undercutting of the mask. With the potassium iodide etchant in a 1:6

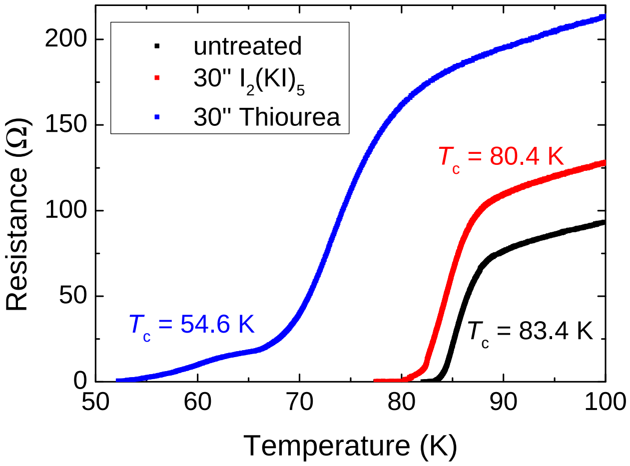

Fig. 5.2: Influence of the etchant on the critical temperature of an unpatterned film for potassium iodide in 1:3 aqueous solution (red squares) and for thiourea, diluted 1:10 in deionized water (blue squares).

dilution typical underetching dimensions of 1000 nm/min were found [190]. Those values exceed the underetching expected from the measured etching rates. However, the resist mask can be partially detached from the gold surface during etching, leading to enhanced lateral etching rates [188]. Therefore, a composite etching procedure was previously used, in which the first 180 nm of the gold layer were removed by argon-ion milling and only the final 30 nm were etched wet chemically [TRS$^+$13]. Thereby, the underetching could be reduced to about 80 nm and slits with minimum widths of about 300 nm could be produced. For the patterning of even smaller slits with dimensions of down to 100 nm the use of a wet-etching solution is not preferable. Adding to that, the wet-chemical etching procedure involves the formation of rough edges (see Fig. 4.20 and Fig. 5.4(c)).

A second wet etchant based on thiourea was tested because of the low etching rates (< 10 nm/min) and the corresponding low underetching [188]. The solution consists of the etchant thiourea (CH_4N_2S), the oxidant potassium ferricyanide ($K_3[Fe(CN_6)]$) and a stabilizer based on sodium sulfite ($Na_2SO_3 \cdot 5H_2O$), all of them diluted in water at the ratio of 1:10 [191, 192]. However, the application of the solution led to severe degradation of the YBCO samples (see Fig. 5.2), and could therefore not be employed as a replacement for the potassium-iodide solution.

Physical etching: argon-ion milling

Due to its high degree of anisotropy, ion-beam etching (IBE) with Ar^+ ions allows for the patterning of sub-µm structures. Physical etching processes offer no selectivity between the different layers of a multi-layer stack other than different etching rates. With gold having a relatively high sputtering yield, due to its electronic structure [193], gold etch rates are substantially higher than

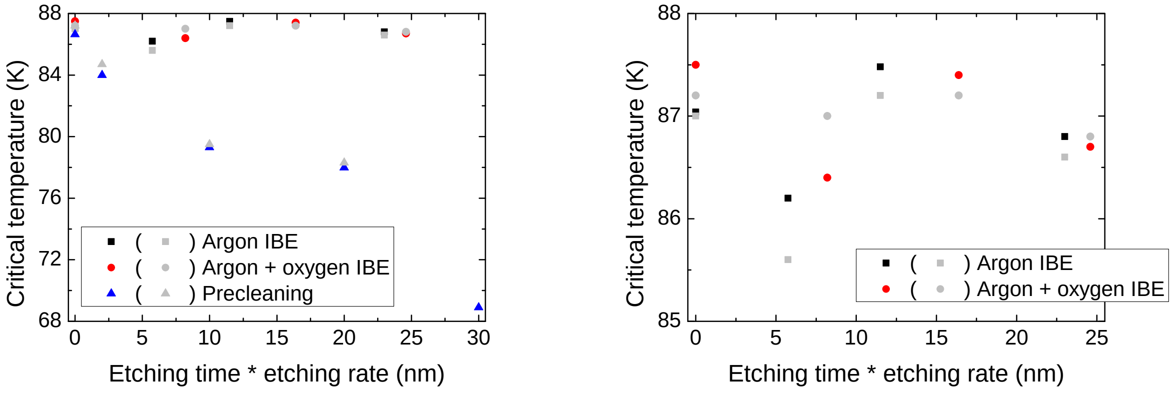

(a) (b)

Fig. 5.3: Influence of argon-ion bombardment on the critical temperature for samples processed with the three different systems. The measured values of the critical temperature directly after treatment and after one month of storing in a desiccator are displayed as a function of the over-etching. The over-etching is displayed as the equivalent gold thickness that would be etched during the etching time (etching rate * etching time). Over-etching of up to 25 nm of gold was tested. (a) Comparison of all three etching techniques, (b) detailed view of the results achieved with the IBE system with pure argon-ion milling and with oxygen-assisted argon-ion milling.

those of the cuprates. Thereby, overetching can be effectively avoided by working with adequate beam energies and etching times.

Two argon-ion sources were considered for etching of the gold thin film: an argon-ion milling system with the possibility to cool the sample stage to -10° C, referred to in the following as the IBE system, and a second argon-ion source, which is operated with a low-energy ion beam and used for pre-cleaning in a sputtering system. The pre-cleaning system is equipped with a neutralizer.

In the IBE system, the sample holder is inclined by 10° in respect to the argon ion beam. As the etching yield per ion depends on the incidence angle this configuration allows for higher etching rates at constant beam energy. Thereby, defects due to sample heating can be reduced [135]. Rotation of the sample holder during etching ensures the straight transfer of the resist pattern to the etched layers. During gold etching the argon flow was set to $F_{\mathrm{Ar}} = 6.90$ sccm, corresponding to an argon pressure of $p_{\mathrm{Ar}} = 2.5 \cdot 10^{-4}$ mbar. The ion-beam energy was defined through the potential at the positive grid ($V_+ = 200$ V). At the extractor grid a negative voltage of $V_- = -270$ V was applied. Moreover, the RF power used to generate the Ar^+ plasma was set to $P_{\mathrm{RF}} \approx 120$ W and continuously adjusted, such that the current at the positive grid remained at a constant value of $I_+ = 65$ mA.

The sample holder was cooled to -10° C and an etching procedure consisting of repeated etching for 30 s and subsequent pausing of the etch procedure for 30 s was carried out. Both measures aim towards the minimization of temperature increase at the sample.

Gold etch rates were determined to amount to 11.5 nm/min and 12.0 nm/min for ablated and sputtered gold, respectively. Overetching of up to two minutes was therefore simulated on unpatterned YBCO films, as described before for the wet-chemical etching procedure. The results are depicted in Fig. 5.3. Fluctuations of the critical temperature are independent of the etching time and are attributed to the limits of reproducibility of the laser-ablation process. To determine the long-term stability of the process, the samples were characterized again after one month. A slight degradation of the samples ($\Delta T_c < 0.5$ K) was observed and attributed to harming of the surface during etching which led to minor out-diffusion of oxygen from the film. Based on these results, argon-ion milling with the IBE system to define the length of the detecting element is considered as a viable process step.

The pre-cleaning argon-ion source was operated with a beam voltage of 150 V and a beam current of 20 mA. The argon flow was set to $F_{\mathrm{Ar}} = 5$ sccm, corresponding to a pressure of $p_{\mathrm{Ar}} = 1.3 \cdot 10^{-3}$ mbar. After acceleration by the negative grid, the argon ions pass a neutralizer which emits charge-balancing electrons and thereby prevents the charging of the sample. In order to ensure charge balance, the neutralizer had to be adjusted to an emission current that equals the beam current. The sample holder was rotated during etching of the sample.
An impairment of the sample during pre-cleaning was already discussed in section 4.2.6. The influence on the critical temperature of unpatterned films is depicted in Fig. 5.3(a). As the gold etching rates are in the range of $2-3$ nm/min, overetching of up to 15 minutes was simulated. A drastic decrease of the critical temperature was observed ($\Delta T_c = 17.7$ K). This outcome is attributed to the heat generated by the neutralizer and consequential degradation of the YBCO film. The pre-cleaning system can therefore not be used to etch slits into the gold metallization.

Oxygen-plasma assisted argon-ion milling

The RF-plasma source of the IBE system has an additional inlet for oxygen gas, such that a plasma of argon and oxygen ions can be ignited. The use of oxygen prevents degradation of the ceramic layers. At the one hand, collisions between oxygen and argon ions reduce the kinetic energy of the ions in the plasma such that fewer oxygen atoms are removed from the lattice and damage to the ceramic layers is reduced. At the same time, knocked-off oxygen atoms from the lattice can be replaced by oxygen from the plasma at the same time. The composition of the plasma was investigated in a previous work and an optimal ratio of argon and oxygen flux $F_{\mathrm{Ar}} : F_{\mathrm{O2}} \approx 1:2$ was found [190].
For this etching step, the argon flux was adjusted to $F_{\mathrm{Ar}} = 5.9$ sccm ($p_{\mathrm{Ar}} = 1.9 \cdot 10^{-4}$mbar) and the oxygen flux was set to $F_{\mathrm{O2}} = 11.5$ sccm ($p_{\mathrm{O2}} = 1.05 \cdot 10^{-4}$mbar). The RF power was slightly decreased to $P_{\mathrm{RF}} \approx 100$ W and with an accelerating voltage of $V_+ = 120$ V the current at the positive grid amounted to $I_+ = 42$ mA during etching. The extractor grid was supplied with $V_- = -270$ V

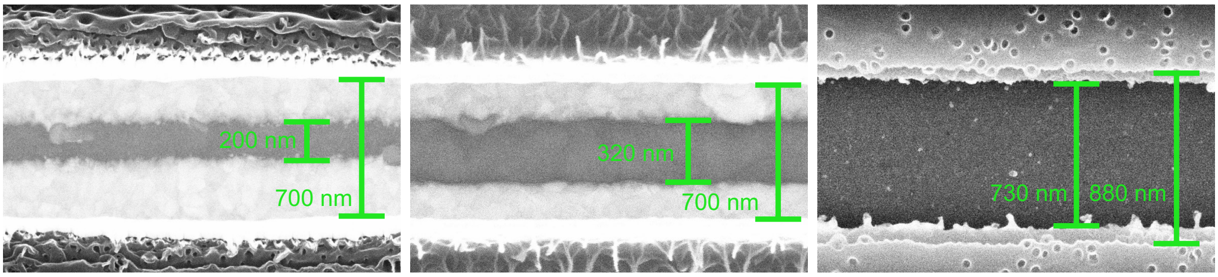

(a) (b) (c)

Fig. 5.4: SEM images of slit dimensions etched with (a) IBE, (b) oxygen-plasma assisted IBE and (c) the $I_2(KI)_5$ solution in 1:3 dilution. The green markers indicate the width of the etched gold slit and of the resist mask, respectively. During wet-chemical etching the resist mask is underetched (see (c)). As the PMMA resist is not stable under electron bombardment, it melts during SEM imaging.

as before.

Due to the lower ion-beam energy the etching rate decreases. 1.64 nm/min and 1.72 nm/min were measured for ablated and sputtered gold, respectively. The high reactivity of oxygen leads to a considerable etching of the resist. For the PMMA 950K 5% resist (diluted in chlorbenzene at a ratio of 3:1 [194]) which was used in this work for positive electron-beam lithography (EBL), the rate amounts to 34.5 nm/min. The overall thickness of the resist after lithography and development is $\approx$ 850 nm, such that the resist can stand oxygen-plasma assisted IBE of up to 25 minutes.

Figure 5.3 displays the degradation of unpatterned YBCO samples when overetched for several minutes in argon and oxygen plasma. In regard to the gold etching rates, overetching of up to 15 minutes was investigated. The measured T_c values after the etching procedure and with a 4 week delay fluctuate on the scale of less than 1 K, which can be attributed to the reproducibility of the PLD procedure and of the $R(T)$ measurement technique. In summary, oxygen-plasma assisted argon-ion milling does not degrade the films and the processed samples show long-term stability. The results are comparable to those achieved with pure argon-ion milling in the IBE system.

5.1.2 Comparison of etching techniques

To select the optimal patterning process for YBCO THz detectors from the etching techniques discussed above, two chips with YBCO microbridges were patterned and compared with regard to their critical temperature and current density. The etching of the slits was performed with pure argon-ion milling and oxygen-plasma assisted IBE, as those procedures showed promising results in the previous section.

For that matter, the full multilayer system as presented in chapter 4 was deposited. The YBCO film thickness was 23 nm. In a first patterning step, the length of detecting element was defined. To this end, slits of $100-1000$ nm width were patterned with EBL in PMMA 950K 5% resist, diluted 3:1 in AR 600-01 thinner [194]. On both chips, the first 180 nm of the gold layer were removed

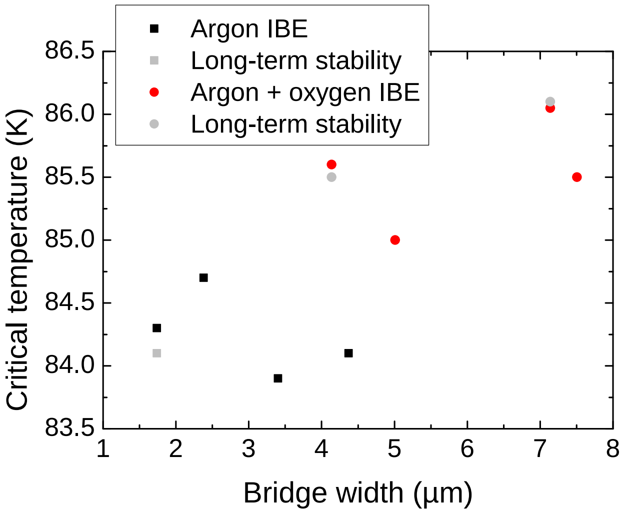

Fig. 5.5: Critical temperature depending on the bridge width for slits etched with IBE and with oxygen-plasma assisted argon-ion milling. Values measured directly after patterning and after one month of storing in a desiccator are displayed.

with pure argon-ion milling in the area of the bridge. With the etching rate of gold (11.5 nm/s, see section 5.1.1) the etching time is $t_{\text{etch}} = 15$ min. The remaining 20 nm of gold were etched by pure argon-ion milling in the IBE system on the first chip (additional 1 min 45 s etching time) and by oxygen-plasma assisted argon-ion milling on the second chip (etching time of ≈ 13 min). The etching parameters corresponded to the ones introduced in section 5.1.

After etching of the slits the dimensions were determined by SEM (see Fig. 5.4). The slits with design widths of 500 nm are shown. The smallest dimensions are achieved for pure argon-ion milling ($w \approx 250$ nm). Etching with a combined oxygen and argon plasma yields slightly larger structures ($w \approx 300$ nm), which might be due to collisions between the individual plasma species and thereby a reduced directivity of the etching process. In both cases, the slits exhibit smooth edges. For comparison, the same slit defined by EBL and etched with the $I_2(KI)_5$ solution in 1:3 dilution in deionized water is shown in Fig. 5.4(c).

Subsequently, µm-wide bridges and a four-probe DC contact design were defined by photolithography with undiluted AZ5214E resist and etched with IBE [195]. The patterning procedure is similar to the fabrication of THz detectors which will be discussed in the following section (see section 5.2.1).

The DC characterization of the samples revealed a constant critical temperature within the individual chips, where the purely argon etched slits exhibit slightly lower T_c values (see Fig. 5.5). The degradation of T_c as compared to the critical temperature of the unpatterned film ($T_c \approx 87$ K, see section 4.2.5) is less than 2 K for the sample, where the slits were etched with the combined argon and oxygen plasma, and < 3 K for the purely IBE etched slits. After one month, no additional degradation is seen. The critical temperature T_c and the normal state resistance R_n were found to

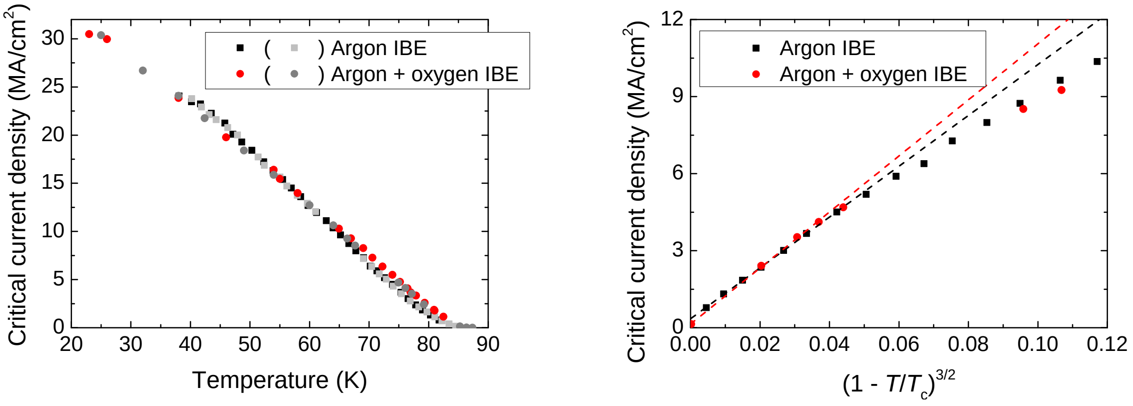

(a) (b)

Fig. 5.6: (a) Critical current density depending on the temperature measured directly after patterning and one month later. Results are depicted for the 1.7 µm wide and 720 nm long slit etched with IBE (black squares) and for a slit which was defined with oxygen and argon-plasma milling ($w = 4.1$ µm, $l =$ 340 nm, red dots). (b) Ginzburg-Landau temperature dependence of the critical current densities for both microbridges. The critical current densities at 77 K are 2.36 MA/cm^2 and 3.34 MA/cm^2 for the purely argon-ion and combined argon and oxygen-plasma etched nanobridges, respectively.

be stable.

The temperature dependence of the critical current density and its long-term stability are displayed for two exemplary bridges in Fig. 5.6(a). Herein, the slit of the first microbridge was etched with argon-ion milling and the second one with oxygen and argon plasma. The critical current is defined as the value where the detector voltage first deviates from zero. As expected from the higher T_c values the oxygen-assisted argon-ion etched structure exhibits the higher absolute critical current density at 77 K. The temperature dependence is similar for both bridges and quasi-linear with a tendency to concave curvature, corresponding to an Ambegaokar-Baratoff behavior at lower temperature. Near T_c a transition to the convex-shaped Ginzburg-Landau dependence is visible. A fit to the Ginzburg-Landau like $(1 - T/T_c)^{3/2}$ temperature dependence is depicted in Fig. 5.6(b). The relatively high temperature, at which the transition from Ginzburg-Landau behavior to the quasi-linear region occurs, indicates optimal oxygen doping of the superconducting thin film [196, 197]. Consequently the bridge with the lower critical temperature transits at lower temperature: $T < 71$ K for the argon-ion milled bridges as compared to $T < 73$ K for the microbridge with the slit etched with oxygen-assisted argon-ion milling. The overall temperature dependence of the critical current densities shows no variation with the width of the microbridge. This is consistent with other results found on µm-sized YBCO structures with widths larger than the effective penetration depth λ_{eff} [15]. With the critical depairing current and the critical current for the onset of flux flow both showing Ginzburg-Landau dependence near T_c, the nature of the voltage drop cannot be extracted from the plots in Figs. 5.6(a) and 5.6(b) [198]. An analysis of the $I(V)$ characteristic will be presented

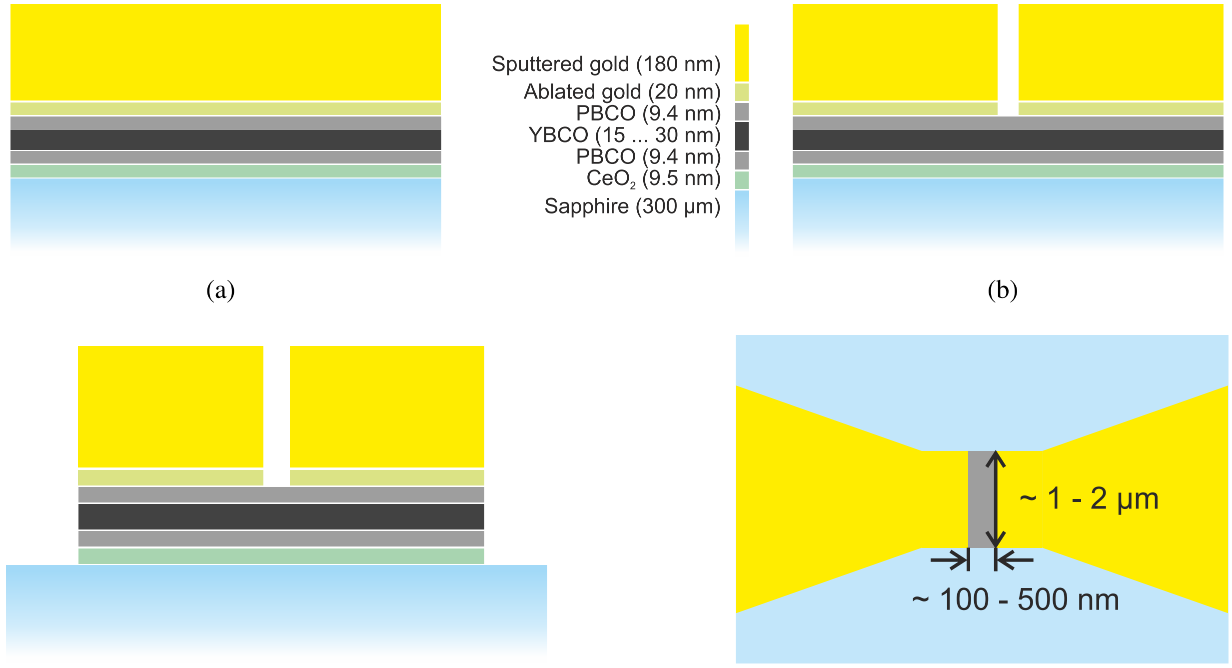

(a) (b) (c) (d)

Fig. 5.7: Patterning process for YBCO THz detectors: (a) schematic of the full multilayer system after deposition, (b) side view of the slit after argon-ion milling, (c) side view after etching of the THz antenna and the coplanar design, and (d) top view of the detecting element embedded in the antenna center.

in section 5.2.2 for a readily fabricated YBCO detector.

Both physical etching procedures were found to be suitable for the patterning of the detecting element. The pure argon-ion milling entails a slight degradation of the film. However, the long-term stability is still assured and the measured critical temperatures are well above the boiling temperature of nitrogen. Moreover, the smallest lengths of the YBCO detectors were achieved with pure argon-ion milling. Therefore, the cooled argon-ion milling process in the IBE system was selected for etching of the detecting element.

5.2 YBCO detector fabrication

5.2.1 Detector patterning

The fabrication process of YBCO THz detectors is schematically shown in Fig. 5.7. The full multi-layer system (see Fig. 5.7(a)) was laser ablated and DC-magnetron sputtered as discussed in chapter 4 with the optimized parameters summarized in section 4.3. On the sample of 10×10 mm^2 area an array of 3×3 detector chips is patterned. After fabrication the substrate is sawn into nine individual chips, each of them accommodating a YBCO detector embedded into a THz antenna or an array of YBCO detectors and antennas.

A PMMA resist for positive EBL was used to write alignment marks and to define the length of the detecting element. First, PMMA 950K 5% resist in 3:1 dilution was spun onto the sapphire substrate with the multilayers at a rotation speed of 9000 rpm for 60 s and the solvent was baked out for $5-10$ min at 150° C [194]. For the EBL, the high voltage was set to 15 kV and the electron beam was truncated by an aperture with 10 µm diameter, such that the beam current amounted to 22 pA. The write field measured 500×500 µm^2 and the beam-step size was set to 8 nm. Since the alignment marks and the slit for the removal of gold in the area of the detecting element itself fit in the same write field, both structures can be written in one lithography step. For the alignment marks a dose of 106 $\mu\mathrm{C}/\mathrm{cm}^2$ was used with the typical dimensions amounting to $1-2$ µm. The dose for the slits varied: For design dimensions of $100-300$ nm a dose of 158 $\mu\mathrm{C}/\mathrm{cm}^2$ was used and for larger slits up to 1 µm the dose was set to 145 $\mu\mathrm{C}/\mathrm{cm}^2$. The different requirements for the exposure dose are a consequence of the proximity effect [199].

After lithography, the chip was slewed in the developer for 30 s and then suspended into an ultrasonic bath for 10 s. The development process was stopped by 30 s of rinsing of the sample in isopropanol and further 10 s in the ultrasonic bath.

The slits and alignment marks are etched with the IBE process and the parameters described in section 5.1.1. The etching time for the full 200 nm of gold was ≈ 17 min. The schematic of the slit after etching is depicted in Fig. 5.7(b) and Fig. 5.8(a) shows an SEM image of a slit etched into the gold layer. The width of the slit corresponds to the length of the detecting element of the readily processed device.

In the second patterning step, consecutive negative EBL and argon-ion milling are used to define the width of the detecting element as well as the planar narrowband antennas and the coplanar design of the detector chip itself. In this process stage, the complete multi-layer stack was etched through to the substrate. To that end, undiluted ARN 7520.18 resist was spun onto the sample [194]. The spinning process took 60 s at a rotation speed of 9000 rpm. Baking for two minutes at 85° C was carried out. The lithography was divided into two parts: lithography of the antenna and detecting element and lithography of the coplanar design. The write field was set to 500×500 µm^2. For the antenna writing the electrons were accelerated with a voltage of 10 kV and sent through a small aperture (10 µm), such that the beam current amounted to 18 pA. The area step size was 8 nm.

Argon-ion milling of the YBCO layers damages the sidewalls of the structures. Due to the increased temperature during etching, dislocations can move from the edges to the center of the bridge. Moreover, temperature-induced oxygen diffusion, preferentially in the *a*-*b*-plane, takes place. Schneidewind *et al.* found a reduction of the critical current density of µm-sized YBCO structures starting at beam voltages of 700 V and 900 V for etching without and with liquid-

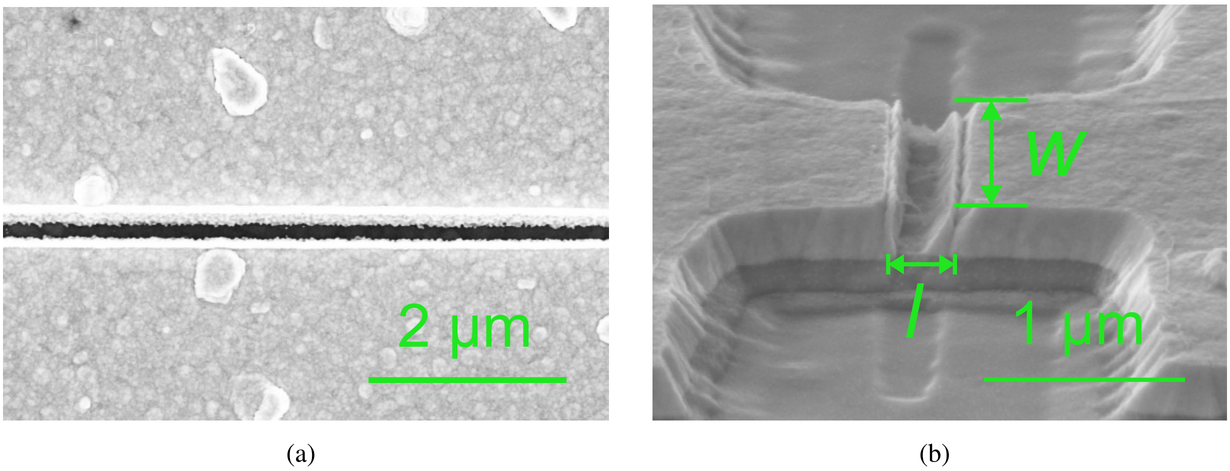

(a) (b)

Fig. 5.8: SEM images of the YBCO THz detector fabrication: (a) slit in the gold metallization after etching with a width of 150 nm and (b) YBCO detecting element in the center of the antenna arms. The lateral dimensions of the detecting element are $l = 180$ nm and $w = 1500$ nm. The gold metallization in light gray can be distinguished from the underlying PLD layers that appear dark gray. The slit area of the gold removal in the first patterning step can be seen in vertical direction as small cavities adjacent on both sides of the detecting element.

nitrogen cooling, respectively [135].

To minimize damage, the edges of the resist have to be steep. Smaller exposure doses entail straighter resist walls due to less exposure of the adjacent regions. Therefore the dose was adjusted to 110 $\mu\mathrm{C/cm}^2$, which is the minimum value needed for complete development of the structure while keeping the resist thickness of the unexposed areas thick enough for the etching procedure.

For the lithography of the readout design the high voltage was increased to 15 kV and the largest aperture of 120 µm diameter was used. The beam current increased by several orders of magnitude to 4.4 nA. The area step size and electron dose were set to 88 nm and 120 $\mu\mathrm{C/cm}^2$, respectively. As a result of the high beam current, the writing speed amounted to about 40 mm/s and the sample with nine detector chips could be processed within 8 hours. Development was carried out in metal-ion free AR 300-47 developer, diluted 4:1 in deionized water, and took 75 s [194]. The development process was stopped in water for only 10 s thereby limiting the contact of the sample to water to a minimum.

The IBE system was used for etching of the samples. Higher acceleration voltages and RF powers were needed as the PBCO and YBCO layer are ceramic-like hard materials. The RF power was set to $P_{\mathrm{RF}} \approx 170$ W and continuously adjusted to ensure a constant current at the positive grid of 65 mA. The argon flux amounted to 4.1 sccm ($p_{\mathrm{Ar}} = 1.1 \cdot 10^{-4}$ mbar) and the voltages at the positive and negative grid were $+250$ V and -270 V, respectively. During etching the sample holder rotated with a tilt angle of 10° and it was cooled to $-10°$ C. The overall etching time of 40 minutes was split into two blocks of 20 minutes with a ten-minute break. Moreover, as for the etching of the slit in the first step, an interval etching procedure with 30 s of exposure to the

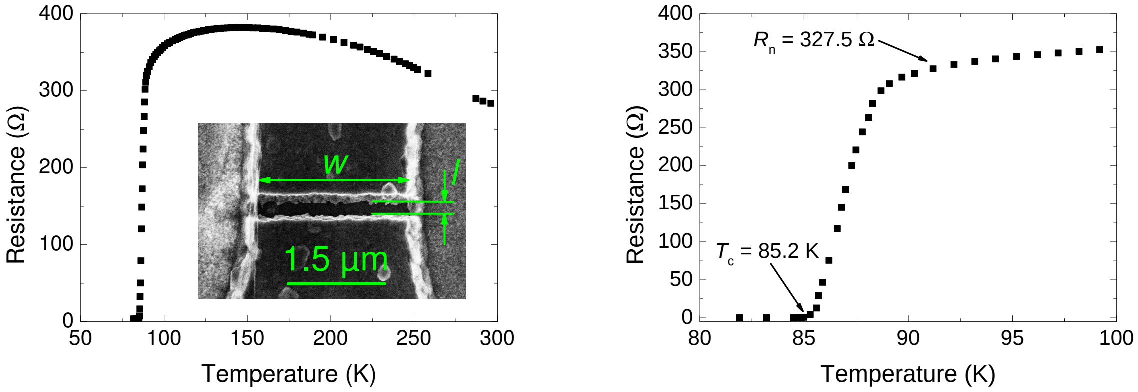

(a) (b)

Fig. 5.9: $R(T)$ characteristic of YBCO THz detector with dimensions $l = 200$ nm, $w = 2.4$ µm and $t_{\mathrm{YBCO}} = 30$ nm. (a) $R(T)$ characteristic starting at room temperature, the inset shows an SEM image of the detecting element. The shunting of the YBCO layer by the lower resistance of the semiconducting PBCO layer is visible at high temperatures. (b) Zoom to the superconducting transition of the detector at $T_c = 85.2$ K.

argon ions followed by a 30 s pause was carried out. The patterning step is schematically shown in Figs. 5.7(c) and 5.7(d) and an SEM image of the patterned YBCO detecting element is depicted in Fig. 5.8(b).

5.2.2 DC characterization of sub-micron sized YBCO detectors

The YBCO detectors were characterized regarding their critical temperature and their temperature-dependent $I(V)$ characteristic by a two-point measurement. In section 6.1 the experimental setup will be introduced. The measured data was corrected for the resistance of the supply wires of 3.5 Ω.

The temperature dependence of the detector resistance is displayed in Fig. 5.9(a) for a sub-µm-sized detector with 30 nm YBCO film thickness. The graph covers the whole temperature range from room temperature to the critical temperature T_c. At higher temperatures, the semiconducting PBCO layer shunts the YBCO layer and the resistance increases with decreasing temperature. The linear decrease of the resistance expected for YBCO is observed at temperatures below 100 K, when the resistance of PBCO exceeds that of the YBCO thin film. T_c is defined as the temperature where the resistance has dropped to 1% of its normal state value R_n. The zoom to the superconducting transition of the $R(T)$ characteristic is shown in Fig. 5.9(b). Here, R_n corresponds to the resistance which first deviates from a linear behavior of the $R(T)$ characteristic. With $R_n = 327.5$ Ω, the critical temperature amounts to 85.2 K. The lateral dimensions of the detecting element were realized such that R_n matches the real part of the antenna impedance ($\approx$ 350 Ω), thus minimizing reflection losses (see section 3.4).

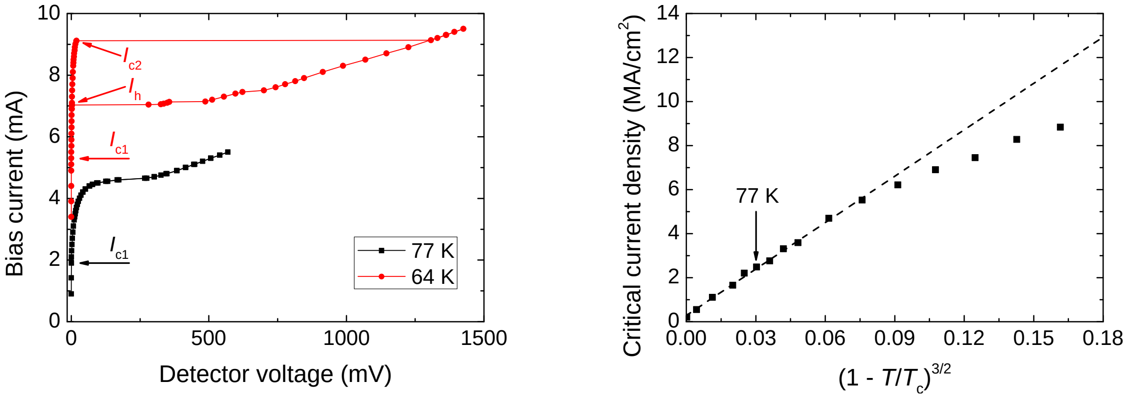

(a)

(b)

Fig. 5.10: (a) $I(V)$ characteristic of the same detector as in Fig. 5.9 at 77 K and 64 K, with I_{c1} and I_{c2} being the critical current density for vortex entry and hot-spot generation, respectively, and the hysteresis current I_h. (b) Dependence of the critical current density j_{c1} on $(1-T/T_c)^{3/2}$.

Current-voltage ($I(V)$) characteristics of the detector measured at temperatures of 77 K and 64 K are displayed in Fig. 5.10(a). In the case of YBCO, the first critical current I_{c1} corresponds to the onset of vortex flow, and the $I(V)$ characteristics are of the flux-flow type. In the following chapters, I_{c1} will be referred to as I_c for simplicity. At low operation temperatures (here $T < 74$ K) a second critical current I_{c2} is observed, where the detector bridge (or part of the detecting element) has a crossover to the normal-conducting state. The discontinuity in the $I(V)$ characteristic is linked to the appearance of a hysteresis. In Fig. 5.10(b) the critical current density for vortex entry is plotted as a function of $(1-T/T_c)^{3/2}$. Ginzburg-Landau like behavior is seen down to 70 K (corresponding to approximately 0.82 T_c).

5.3 Conclusions of chapter 5

The etching techniques, considered for the definition of the length of the detecting element, were reviewed in section 5.1 regarding their influence on the YBCO thin-film quality and the minimal dimensions which could be realized. Wet-chemical etching was discarded because of underetching and the degradation of PBCO and YBCO, due to the water content of the etchant. Similarly, ion-beam etching with the pre-cleaning system was found to degrade the critical temperature of the YBCO thin films. This effect was attributed to the heating of the sample caused by the neutralizer. Samples with high critical temperatures and long-term stable behavior could be obtained with the ion-milling system using a plasma of pure argon or a combined argon and oxygen plasma. Herein, the minimal dimensions were achieved with a pure argon plasma. As the critical temperature of the oxygen-assisted ion-milled samples was only slightly higher (≈ 1 K) than that of the IBE etched samples, pure argon-ion milling was selected to etch the slit and thereby define the length of the detecting element.

In the second part of the chapter, the patterning process for YBCO THz detectors was introduced. Sub-µm-sized detector elements were realized with EBL and the IBE technique. The detector dimensions are only limited by the lithography step. YBCO detectors were patterned into YBCO thin films of thicknesses between 15 nm and 30 nm with typical lateral dimensions of $l = 150 - 500$ nm and $w = 0.8 - 2.5$ µm. With the optimized fabrication process, T_c values as high as ≈ 85 K for 30 nm thick YBCO films and $j_\mathrm{c} \approx 2.5$ MA/cm^2@77 K are achieved. Stable operation of the detectors at liquid-nitrogen temperatures is thus possible.

6 Zero-bias response of the YBCO detector to pulsed THz excitations

The detector response to pulsed broadband and narrowband THz radiation was investigated in a frequency range from a few GHz up to several THz. This chapter discusses the behavior of the unbiased YBCO detector. At first in section 6.1, the detection system and measurement setup for pulsed THz excitations are introduced. The dependence of the unbiased detector response on temperature, frequency range and radiation power is discussed. The most prominent feature of the YBCO THz detector, the sensitivity to the direction of the electrical field, is investigated in section 6.4.

6.1 Detection system

The setup used for experiments with the YBCO detection system at circular and linear accelerators is shown in Fig. 6.1. Here, the emitted THz radiation is assumed to be in a parallel beam configuration, such that the radiation can be focused via a parabolic mirror. Given the focal length of the beam of about 200 cm at the IR2 beamline at ANKA and the distance between the beamline window and the detection system of about 40 cm, this is a reasonable assumption. Different optical paths were used for various experiments, however the setup with the parabolic mirror is the simplest configuration.

The detection system itself consists of a liquid-nitrogen or liquid-free cryostat and the DC bias and

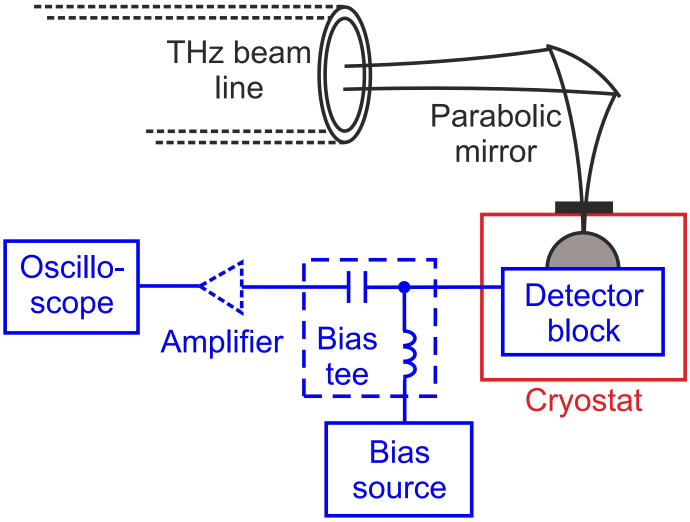

Fig. 6.1: Schematic of the YBCO detection system for pulsed THz excitations consisting of a cryostat (red) and the electronics (blue). The optical path is depicted in black.

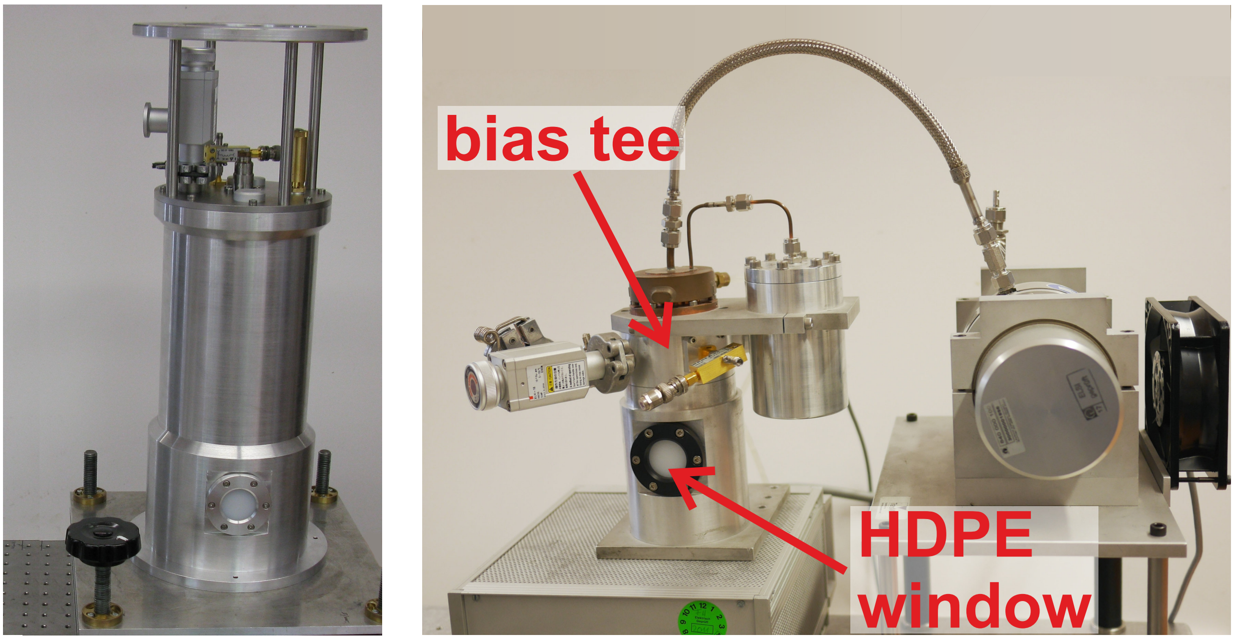

(a) (b)

Fig. 6.2: (a) Liquid-nitrogen bath cryostat with HDPE THz window and readout connectors on the top plate. (b) Pulse-tube cryocooler consisting of a cold finger and a vacuum vessel (left) and the linear compressor that is connected via a flexible transfer tube (right). The HDPE window and the bias-tee are marked.

RF readout electronics. Both components will be presented in the following. At last, the optical radiation coupling is discussed.

6.1.1 Cryogenics for high-temperature superconductors

As discussed in chapters 4 and 5, the thin films and patterning processes were optimized towards high critical temperatures. The typical T_c for sub-µm detectors is approximately 85 K. This allows for cooling with liquid nitrogen and for the use of compact cryogen-free systems. Two cryogenic systems are depicted in Fig. 6.2: a liquid-nitrogen bath cryostat and a pulse-tube cryocooler.

Different bath cryostats with liquid nitrogen as the cooling agent and a filling volume of 0.85 l were used for the experiments [200]. One such system is depicted in Fig. 6.2(a). Top plates with one to four RF connectors were fabricated at IMS. With this configuration, YBCO detector arrays with up to four detectors can be read out simultaneously. With the integration of an additional heat shield, standing times of up to 12 h are achieved, depending on the number of connectors on the top plate. A detailed view of the copper cold plate that is the bottom plate of the liquid-nitrogen reservoir, simultaneously, is depicted in Fig. 6.3(a). The detector block (see Fig. 6.5) is mounted on the cold plate. Copper is used to ensure optimal thermal coupling to the cold plate.

Liquid-nitrogen cryostats are easy to handle and therefore best suited for transportation to synchrotron storage rings. However, the operation temperature of the detector cannot be adjusted

(a) (b)

Fig. 6.3: (a) Copper cold plate with detector block inside the liquid-nitrogen cryostat, and (b) battery-driven bias source for constant-current operation.

below ≈ 77.5 K [200]. Therefore, the experiments presented in this chapter and in chapter 7 were carried out with a coaxial pulse-tube cryocooler for the most part. The TransMIT PT-09b system consists of a separate compressor that is connected to the cold finger and the vacuum vessel via a flexible transfer tube (see Fig. 6.2(b)). The pulse-tube cryocooler works with a helium filling pressure of 28 bar. At the room-temperature side, the cold finger is cooled with a water chiller and an additional fan. The minimal operation temperature is 49 K and at 60 K, a maximum cooling power of 2 W is available. Temperature fluctuations are below 0.1 K. A LabVIEW software and control electronics are used to regulate the temperature of the pulse-tube cryocooler [201]. The vacuum system is equipped with a single RF feed-through, such that only single-pixel YBCO detectors can be read out.

6.1.2 RF readout electronics and DC biasing

The readout bandwidth of the whole detection system was designed for the upper frequency limit of 65 GHz corresponding to the V band. At the room-temperature side, one bias tee that splits the DC biasing and the RF readout path, is connected to the V port on the top plate of the cryostat for every detector channel (see Fig. 6.2(b)). The DC port of the bias tee SHF BT65 is laid-out for a maximum DC voltage input of 16 V and a maximum DC current of 400 mA [202]. A battery-driven low-noise bias source (see Fig. 6.3(b)) that was developed at IMS can be connected [15]. An attachment of the detection system to the line voltage and the affiliated risk of detector damage by voltage peaks and instabilities are thereby avoided. The bias source can be operated in constant-current and constant-voltage mode and is equipped with a short-cut modulator to protect

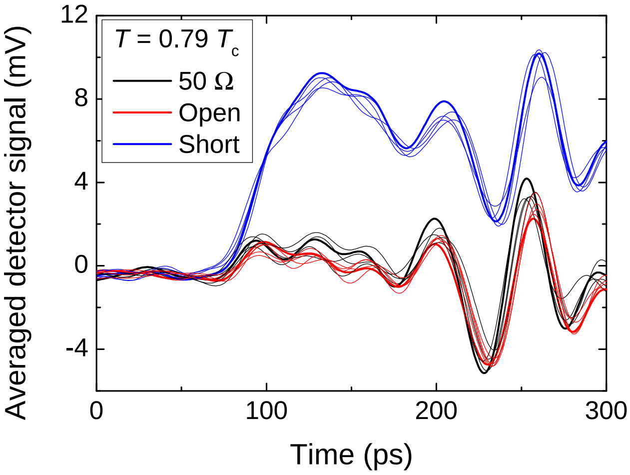

Fig. 6.4: Termination of the DC port for zero-bias operation: comparison of 50 Ω and short-cut termination with an open connector. Several THz signal traces are displayed for each configuration as the bursting signal at the ANKA storage ring changes its temporal shape from revolution to revolution.

the YBCO detector from voltage peaks during turning on of the bias supply. The battery block supplies the source with ±12 V and a maximum output current of ±40 mA is provided.
Zero-bias operation of the detection system is realized by disconnecting the bias source and terminating the DC port of the bias tee with a 50 Ω resistor. In principle, leaving the DC connector open would implement real zero-bias conditions, as only then the flow of loop currents is completely blocked. However, an open port leaves the YBCO detector sensitive to electrical discharge. As the sub-µm-sized detecting elements are especially susceptible to voltage peaks, the open-port configuration is best to be avoided. The measurement of the detector response to pulsed THz excitations revealed similar detector signals for an open connector and a termination of the DC port with a 50 Ω resistor as compared to a short (see Fig. 6.4). Therefore, the 50 Ω resistor was used as termination for the DC port during zero-bias operation.

The cryogenic parts of the readout electronics need to work from DC up to several GHz, as the connecting elements are used for RF readout as well as for DC biasing. To that end, broad- and narrowband antennas are embedded in a coplanar waveguide (CPW) with a bandwidth of DC up to 65 GHz. A CPW consists of an inner conductor that is separated from the two ground planes by slots. By adjusting the width of the slots ($w_{\mathrm{slot}} = 210$ µm), the CPW line impedance can be matched to the 50 Ω impedance of the V band connector. Part of the CPW is patterned directly onto the sapphire substrate. The detector chip is surrounded by a Rogers TMM®10i substrate with both-side copper cladding where the CPW continues [203]. Both substrates are connected via indium wire bonds and mounted in the copper detector block. Depending on the number of detector channels, the detector block is equipped with one to four flange V-band connectors with glass-bead launchers from Anritsu GmbH that link the Rogers substrate to the V-band readout ca-

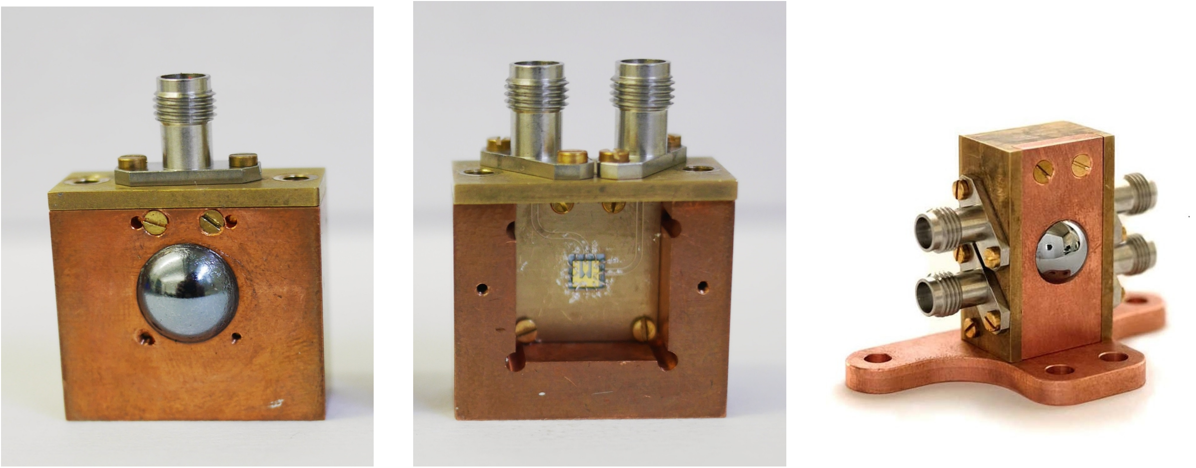

(a) (b) (c)

Fig. 6.5: Copper detector blocks: (a) front view of the single-pixel detector block with silicon lens, (b) two-pixel detector block with opening on the backside that shows the Rogers substrate and the detector chip, and (c) detector block for four channels [SRK+17].

bles. The overall readout bandwidth of the single-pixel detector block, including the Rogers board and the CPW, amounts to 30 GHz [157]. The detector blocks for one to four channels are depicted in Fig. 6.5.

The cryostats are equipped with V-band vacuum feed-throughs from SHF Communication Technologies AG, where the semi-rigid coaxial V cable with a -3 dB roll-off frequency of ≈ 65 GHz coming from the detector block is connected to the room-temperature bias tee. Flexible V cables link the RF port of the bias tee to the oscilloscope. A broadband SHF 804 TL amplifier from SHF Communication Technologies AG, shown as a dotted line in Fig. 6.1, with a voltage gain of 22 dB can be used additionally in the setup. The broad bandwidth of the amplifier (200 kHz to 55 GHz) enables the amplification of picosecond pulses [202]. At room temperature, flexible V-band cables from Totoku Electric Co., Ltd. of 1 to 1.5 m length were used. The transmission and reflection coefficients of the individual components of the readout path can be found in [15].

The detector signal was read out with real-time oscilloscopes from Keysight Technologies Inc. The DSA-X 96204Q oscilloscope has a bandwidth of 63 GHz on two channels and the DSA-X 93204A oscilloscope provides 32 GHz bandwidth on two channels and 16 GHz on four channels [204].

According to [147], the cut-off frequencies of all components of the readout path define the effective readout bandwidth:

$$f_{\text{eff}} = \left[\sum_i \frac{1}{f_i^2} \right]^{-1/2}, \tag{6.1}$$

with f_i being the upper bandwidth limits of the individual components of the readout path. The corresponding minimal temporal resolution (FWHM) is $\tau = 0.35/f_{\text{eff}}$.

For the single-pixel configuration with the fast real-time DSA-X 96204Q oscilloscope, the overall bandwidth amounts to 22 GHz which is equivalent to a minimal Gaussian pulse width of 15.8 ps (FWHM) or an rms width of $\sigma = 6.7$ ps. By adding the SHF amplifier to the readout path, the response time increases to 17.2 ps. Sub-µm sized YBCO detectors with high sensitivities were therefore used for experiments at synchrotron storage rings when ultimate time resolution was required. Thus, the use of the amplifier was not necessary.

Most of the experiments presented in the following were conducted with the DSA-X 93204A oscilloscope. The overall bandwidth of the readout path is 18.9 GHz (18.5 ps FWHM) without the use of the amplifier. By adding the amplifier to the readout path the response time increases to 19.6 ps. For simultaneous readout of all four channels the bandwidth decreases to 13.2 GHz which allows for a temporal resolution of 26.5 ps.

6.1.3 Coupling of radiation

THz radiation is fed to the detector through a high-density polyethylene (HDPE) window that all cryogenic systems used in this work are equipped with (see Fig. 6.2(b)). HDPE transmits THz radiation up to at least 10 THz and absorbs optical and infrared signals. The material is used because of its low refractive index ($n \approx 1.54$). It is strong enough to serve as a vacuum seal at liquid-nitrogen temperatures. The transmission is at least 80% in the relevant frequency range [17].

Inside the detector block, the sapphire substrate is glued to the flat side of a high-resistivity silicon lens, which along with the planar THz antenna acts as a hybrid antenna [159]. The silicon lens is hyperhemispherical with a diameter of 12 mm and a cylindrical extension with a total length of 2.03 mm, resulting from the geometry of the silicon lens and the thickness of the sapphire substrate (330 µm) [157]. The transmission at the surface of the silicon lens was simulated and found to be 68% [157].

The coupling of the incoming Gaussian THz beam to the lens antenna can be calculated as

$$K = \frac{4w_1^2 w_2^2}{(w_1^2 + w_2^2)^2}, \tag{6.2}$$

with the beam waist of the THz radiation w_1 and the equivalent beam waist of the lens pattern at 1 THz: $w_2 = 2.2$ mm [14, 76]. With a typical CSR beam waist of $w_1 \approx 5$ mm as in the experimental conditions at ANKA, the coupling is 54%. Finally, the synchrotron radiation is polarized linearly. The absorption by the narrowband antennas is determined by the angle α between the direction of the electrical THz field and the polarization of the antenna as $\cos(\alpha)$. The polarization loss factor relating to the coupled power is thus $\cos^2(\alpha)$. In the case of the broadband log-spiral antennas, 50% of the radiation field is coupled due to their circular polarization [205].

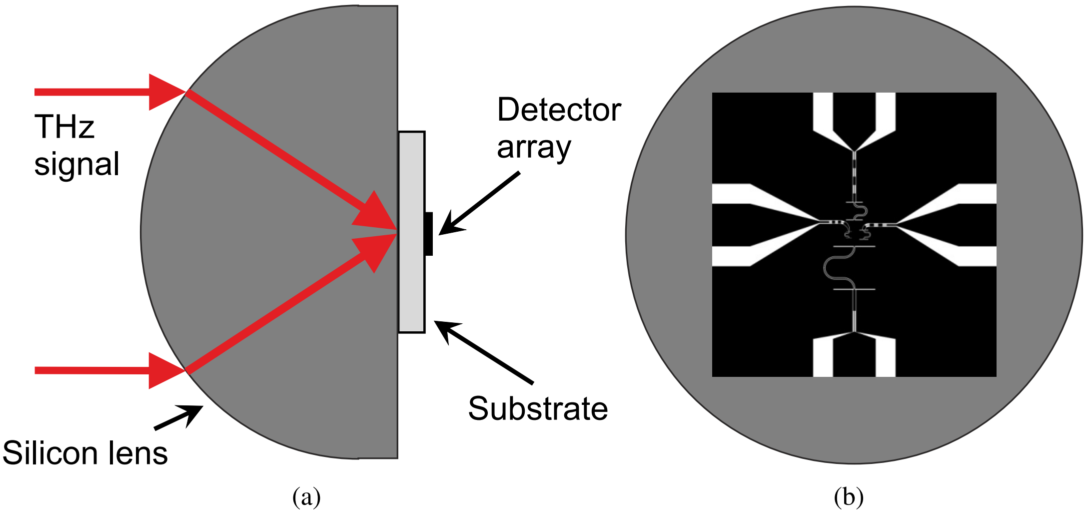

Fig. 6.6: Off-centered antenna elements in the four-pixel detector array: (a) side view of the hyperhemispherical silicon lens with the sapphire substrate glued to the flat side and (b) front view with the detector array placed on the silicon lens. The individual antennas are off-centered. The size of the array and the lens are not to scale.

Mismatched antenna and detector impedances entail a reflection of a part of the absorbed THz field:

$$|\underline{S}_{11}| = \frac{Z_\mathrm{a} - Z_\mathrm{d}^*}{Z_\mathrm{a} + Z_\mathrm{d}^*} \tag{6.3}$$

with the complex antenna and detector impedances Z_a and Z_d, respectively. As discussed in section 3.4 we assume the real and imaginary part of the detector impedance to correspond to the normal state resistance R_n of the YBCO detector. The corresponding coupling efficiency of the THz power is $\eta = 1 - |\underline{S}_{11}|^2$ [205].

Upon absorption of the THz field an RF current, which is directly proportional to the electrical field of the THz radiation, is induced in the antenna: $I_\mathrm{RF} \propto |\vec{E}_\mathrm{THz}|$.

For multi-pixel YBCO detectors, the individual narrowband detecting elements have to be placed off-centered on the sapphire substrate in relation to the lens center as depicted Fig. 6.6. This leads to a tilt of the main lobe in the far field and thereby to reduced coupling efficiencies [206]. At the same time, the crosstalk due to mutual coupling $|\underline{S}_{21}|$ increases when moving the detecting elements further to the lens center and thus closer together. As crosstalk deteriorates the narrowband behavior of the antennas, $|\underline{S}_{21}|$ needs to be smaller than -20 dB . For the 4-pixel array discussed in section 3.4 the minimal spacing between the antennas for 140 GHz and 350 GHz is about 1000 µm and the resulting tilt of the main lobe amounts to 13° for the 140 GHz antenna [SRK$^+$16].

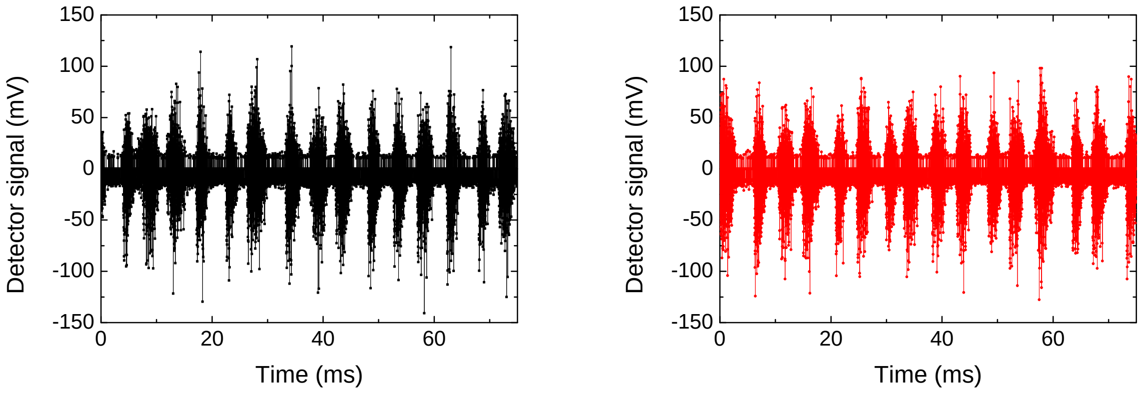

(a)

(b)

Fig. 6.7: Bursting THz signal at ANKA measured in zero-bias operation mode. Two traces recorded with the same detector at different points in time are depicted in (a) and (b).

6.2 Operation-point dependent zero-bias response

YBCO detecting elements embedded into broadband log-spiral and narrowband double-slot antennas were illuminated with broadband THz radiation at the ANKA storage ring. Their zero-bias behavior depending on operation temperature and incoming THz power was investigated.

At ANKA, CSR is generated in the short-bunch mode where the bunch length is reduced by the use of dedicated optics (see section 2.1). Typical bunch lengths are in the range of 15 to 25 ps (FWHM) and can thus be resolved by the aforementioned readout electronics (see section 6.1.2) [207]. As the bursting THz signal changes its temporal and spectral shape with every revolution of the electron bunch inside the synchrotron, the zero-bias signal has to be evaluated in an averaged form to extract information on the detector sensitivity. For a thorough investigation of the YBCO detector response, a single-shot comparison to another direct THz detector type that is able to resolve the CSR pulse shape would be favorable. Due to the lack of such detectors, information on sensitivity of the YBCO detector is extracted from averaged measurements. Moreover, positive and negative pulses are recorded by the detector in zero-bias operation mode. Therefore, the absolute value of the detector response has to be taken into account upon averaging of the detector signal. Typically, sixteen thousand segments of the detector response are recorded with the oscilloscope, corresponding to its maximum memory depth. With a re-arm time of the oscilloscope of 4.5 µs and the revolution frequency of ANKA (2.7 MHz), every thirteenth revolution of the bunch can be resolved and an overall period of roughly 80 ms is recorded. Two recordings of the zero-bias detector response are depicted in Fig. 6.7. It is evident that the temporal period is sufficiently long to eliminate the influences of the bursting THz radiation by averaging the detector signal. The averaged maximum height of the zero-bias detector signal thus gives a measure of the optical sensitivity of the detection system.

Detector	**1**	**2**	**3**	**4**	**5**	**6**
Detecting element length, l (nm)	200	170	300	480	310	370
Detecting element width, w (µm)	2.42	0.85	0.91	1.53	1.31	1.52
YBCO film thickness, t_{YBCO} (nm)	30	20	30	30	30	30
Normal-state resistance, R_{n} (Ω)	330	340	193	218	319	146
Critical temperature, T_{c} (K)	85.2	83.4	82.9	85.6	83.0	84.6
Critical current density, j_{c} @ 77 K $(\mathrm{MA/cm^2})$	0.7	1.2	3.8	2.2	0.5	4.3
Antenna type	nb	bb	bb	bb	bb	bb

Table 6.1: Detector overview: DC characteristics and dimensions, with abbreviations bb - broadband, nb - narrowband. The results presented in chapters 6 and 7 refer to this list of detectors.

Experimental results obtained with different sub-µm sized YBCO detectors will be discussed in the following. The dimensions and DC characteristics of the detectors are summarized in Tab. 6.1. The same detectors will be referenced in chapter 7 for the investigation of the bias-dependent detector response.

6.2.1 Temperature dependence of the zero-bias response

Figure 6.8(a) depicts the averaged absolute detector response in zero-bias operation mode at different temperatures for detector no. 1. The detector response increases with temperature and reaches a maximum at 94% of T_{c}. The overall pulse width is in the range of 80 ps. The broadening of the pulse is due to the averaging of all recorded segments. Herein, the varying arrival times of positive and negative pulses during bursting lead to a widening of the averaged signal. For comparison, a single-shot measurement of a CSR THz pulse recorded in zero-bias mode is depicted in Fig. 6.8(b). The pulse width amounts to $\tau_{\mathrm{FWHM}} = 23.9$ ps which is in good agreement with the expected pulse widths for ANKA in short-bunch operation mode.

Several YBCO detectors were investigated regarding their temperature-dependent zero-bias response. To this end, a Matlab script was used to average the sixteen thousand segments of each individual file and to extract the maximum peak height. In Fig. 6.9(a), the averaged maximum of the absolute detector signal $|U_{\mathrm{max}}|$ is depicted as a function of the reduced temperature T/T_{c} for three exemplary detecting elements. For all investigated samples, the maximum of the detector signal was found in a temperature region of $0.90 - 0.95\ T_{\mathrm{c}}$.

For pulsed THz excitations, the $I(V)$ curve at the operation temperature at which the signal level reaches its maximum does not show a plateau-like behavior with an associated singularity in differ-

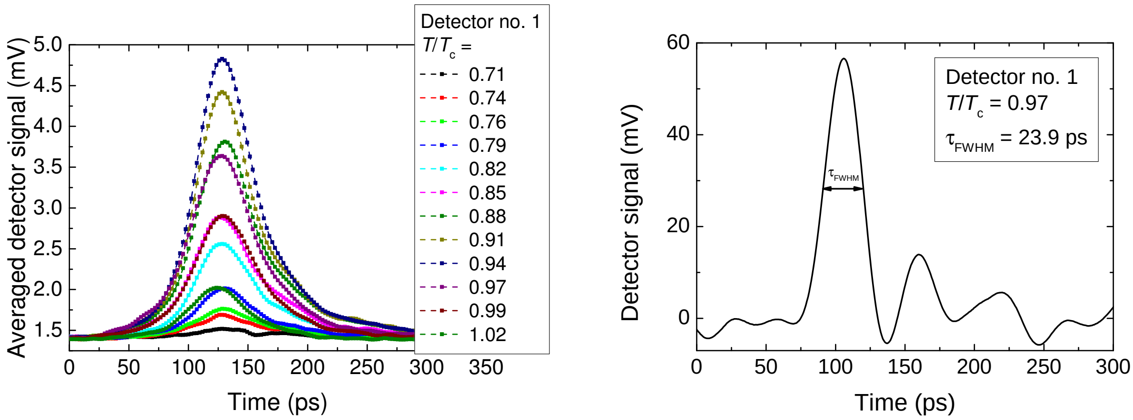

(a) (b)

Fig. 6.8: Zero-bias operation mode of detector no. 1: (a) averaged, absolute detector signal for different temperatures, and (b) single-shot measurement of the detector response at a temperature of $T = 82.7$ K ($T/T_c = 0.97$).

ential resistance. As opposed to that, in the biased regime maximum sensitivity is seen at the exact temperature where the $I(V)$ characteristic exhibits a plateau. This will be discussed in section 7.3. The $I(V)$ characteristics of detectors 1 - 3 corresponding to the temperature at which the highest zero-bias sensitivity is observed, are depicted in Fig. 6.9(b). The lack of a hysteresis or a plateau indicate that the maximum sensitivity in zero-bias mode occurs at higher temperatures than in the biased mode.

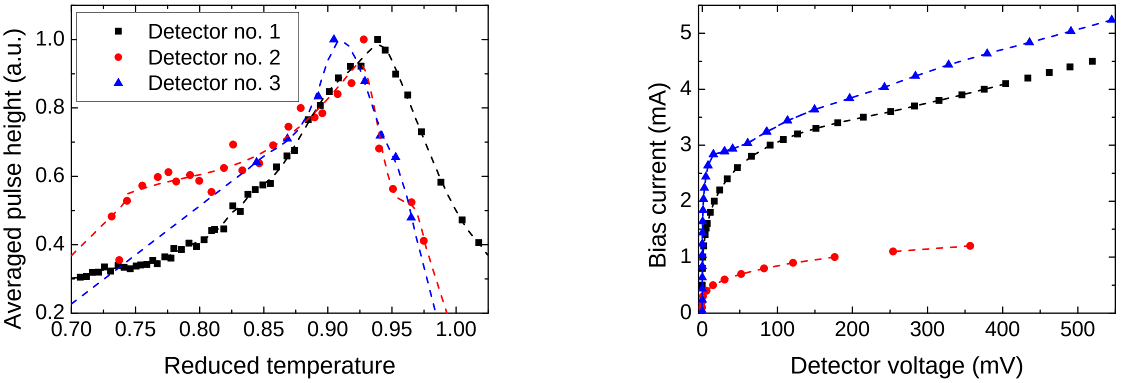

(a) (b)

Fig. 6.9: (a) Dependence of the averaged zero-bias signal height on temperature for detectors no. 1 to 3, and (b) $I(V)$ characteristics corresponding to the temperature at which the largest zero-bias detector signal is measured.

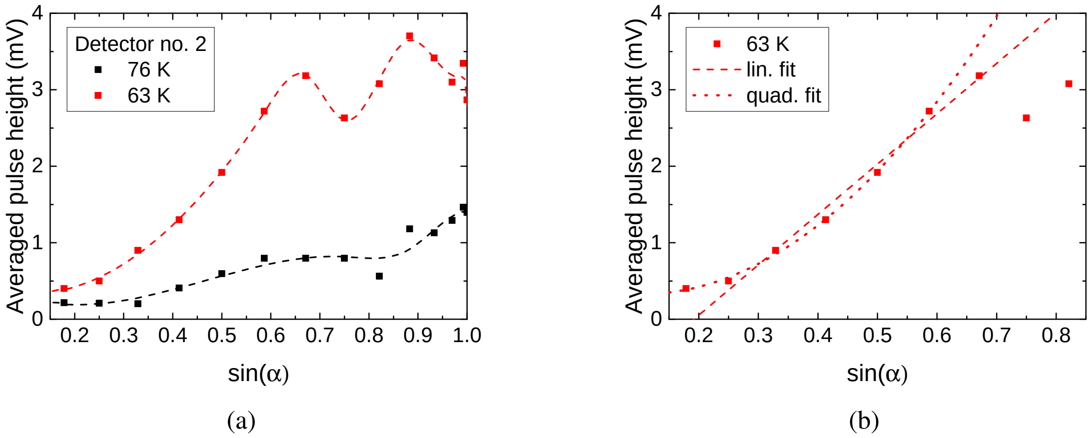

(a) (b)

Fig. 6.10: (a) Dependence of the detector response on electrical field strength ($E_t = E_0 \cdot \sin(\alpha)$) for detector no. 2 at different operation temperatures. (b) Quadratic and linear fit of the power dependence at low THz power levels.

6.2.2 Dependence of the detector response on coupled THz power

To investigate the dependence of the YBCO detector response on coupled THz power, the CSR was attenuated with a wire grid. A wire grid with wire distances much smaller than the wavelength of the THz signal transmits the portion of the electrical field vector that is perpendicular to the wires [76]. The wire grids used in this setup work up to 2.5 THz. The measurement setup consisted of two grids in total: The first one, acting as a polarizer, was aligned horizontally such that only vertically polarized CSR was transmitted. At ANKA, a substantial part of the CSR arrives at the beamline in vertical polarization. The second grid was the actual attenuator and α was adjusted between 0° and 90°. Here, α denotes the angle between the wires of the grid and the electrical field direction of the THz signal.
The electrical field strength transmitted by this arrangement varies as the sine of α: $|\vec{E}_t| = \sin(\alpha)|\vec{E}_0|$. With the polarization of the broadband log-spiral antennas being nearly circular [157], the coupled THz field is assumed to vary also as $\sin(\alpha)$. As opposed to that, double-slot antennas exhibit linear polarization and are mounted in the detector block in vertical configuration. Therefore the coupled THz field depends on α as $|\vec{E}_{\mathrm{coupl}}| = \sin^2(\alpha)|\vec{E}_0|$.

Figure 6.10(a) shows the averaged absolute detector signal depending on $\sin(\alpha)$ and thereby depending on the electrical field strength of the THz radiation for detector no. 2. The observed trend is characteristic for sub-µm YBCO detectors in zero-bias operation mode. For small angles, corresponding to small THz powers, the detector response depends quadratically on electrical field strength (see Fig. 6.10(b)). For comparison, a linear and a quadratic fit are plotted. Due to the small number of points both fits yield plausible results. However, in Fig. 6.13(a) it becomes evident that the averaged detector response is best fit by a linear function when plotted vs. the THz

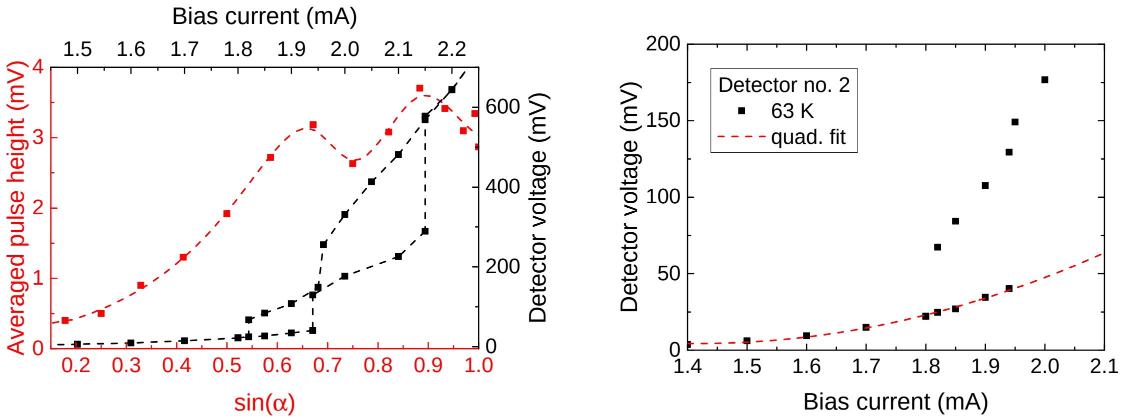

(a) (b)

Fig. 6.11: Dependence of the zero-bias detector response on the $I(V)$ curve for detector no. 2 at 63 K: (a) Comparison of the characteristics of the electrical-field dependence of the detector response with the $I(V)$ curve above the critical current. (b) Quadratic fit of the $I(V)$ characteristic at 63 K for low bias currents in the flux-flow regime.

power P_{THz}. As the THz power is proportional to the intensity of the radiation which in turn depends on the square of the electrical field, the relation $P_{\mathrm{THz}} \propto \left|\vec{E}_{\mathrm{THz}}\right|^2$ applies. In particular, this means that the YBCO detector response does not depend linearly, but rather quadratically, on the electrical field strength.

At higher field strengths, the detector saturates. Similar behavior as depicted for detector no. 2 in Fig. 6.11(a) is seen with several detectors. Here, the power dependence at a temperature of 63 K matches the characteristics of the $I(V)$ curve. Two discontinuous jumps in the detector voltage correspond to two maxima in the electrical field strength dependence of the detector response.

Figure 6.11(b) deals with the question where the quadratic dependence of the detector signal on electrical field strength arises from. As discussed earlier, the absorbed electrical field induces an RF current in the antenna that is directly proportional to the electrical field: $I_{\mathrm{RF}} \propto |\vec{E}_{\mathrm{THz}}|$. In the superconducting phase above the critical current, the $I(V)$ characteristic can be fitted with a quadratic dependence of the detector voltage on bias current. The dependence $U \propto (I_{\mathrm{b}} - I_{\mathrm{c}})^2$ is typical for the flux-flow regime [208]. From the fit, the critical current was found to amount to $I_{\mathrm{c}} = 1.4$ mA.

These results imply that the detector response in zero-bias operation mode depends on the $I(V)$ curve and that the RF current from the absorbed THz signal fed to the YBCO detector acts as a bias current. To probe this assumption the temperature dependence of the first critical current, indicating the onset of vortex flow, was measured for detector no. 1 (see Fig. 6.12(a)). Subsequently, the averaged zero-bias pulse height measured at ANKA (see Fig. 6.9(a)) was correlated with the critical current. The result of this analysis is depicted in Fig. 6.12(b). A fit of the data to $U \propto (I_{\mathrm{b}} - I_{\mathrm{c}})^2$ with $I_{\mathrm{b}} = I_{\mathrm{RF}}$, the RF current induced in the antenna by the absorption of the THz signal, yields good results and an RF current of $I_{\mathrm{RF}} \approx 7$ mA is estimated from the fit. This is in

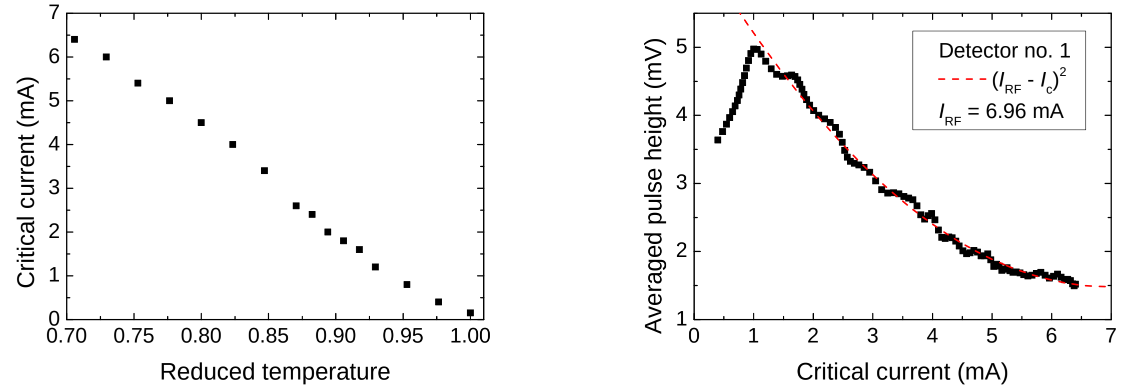

(a) (b)

Fig. 6.12: (a) Temperature dependence of the critical current for detector no. 1. (b) Averaged pulse height measured in zero-bias operation mode with detector no. 1 depending on its critical current. The data can be interpolated by a square-law fit assuming flux flow.

agreement with values found for the induced RF current by Probst *et al.* [14].

Absolute THz power and the dependence of the zero-bias detector response was measured at the IR1 beamline at ANKA. The ring was operated in short-bunch mode at 1.3 GeV and with a multi-bunch filling pattern to satisfy the sensitivity requirements of the calibrated THz power meter with the noise limit around 15 µW [43]. Fig. 6.13(a) shows the measured average detector response depending on the average THz power for detectors no. 4 and 5 at different operation temperatures. The linear dependence on THz power is seen up to $P_{\mathrm{THz}} \approx 200$ µW. At higher power levels, the detectors saturate.

With a repetition rate of $f_{\mathrm{rep}} = 500$ MHz and a filling pattern with 100 occupied bunches out of

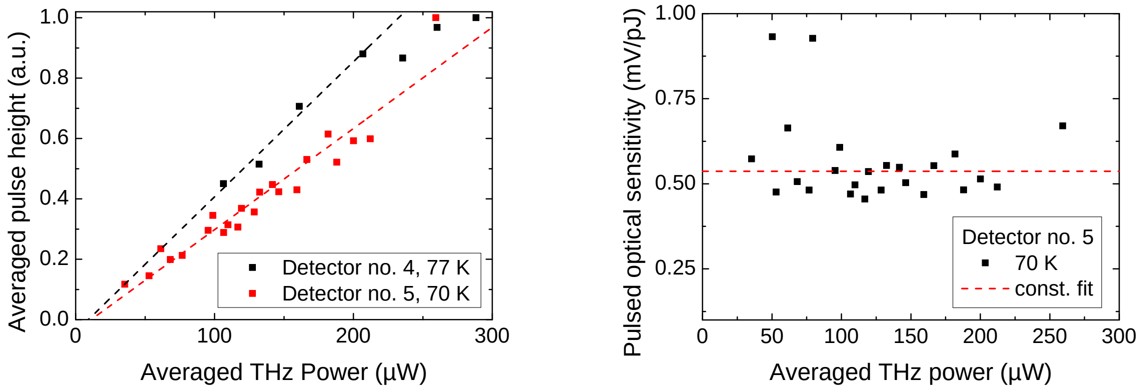

(a) (b)

Fig. 6.13: (a) Linear dependence of the detector response on averaged absolute THz power measured with a calibrated THz power meter for detectors no. 4 and 5. (b) Detector no. 5: constant optical sensitivity vs. absolute THz power.

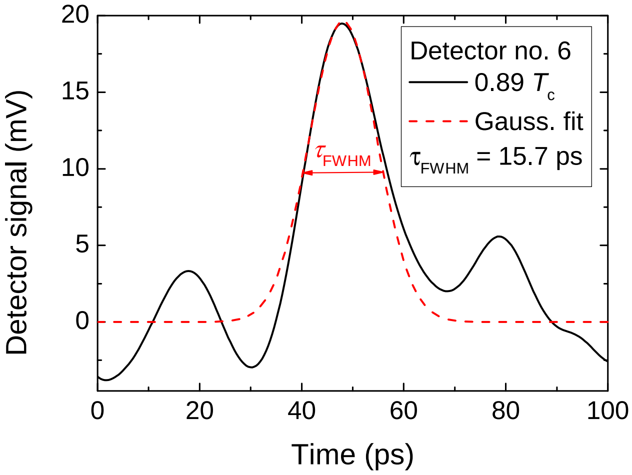

Fig. 6.14: Single-shot zero-bias response of detector no. 6 to a broadband pulsed THz excitation at ANKA, Gaussian fit with $\tau_{\mathrm{FWHM}} = 15.7$ ps ($\sigma = 6.7$ ps) [RIS$^+$14].

187 possible buckets, the averaged pulse energy amounts to $E_{\mathrm{THz}} = P_{\mathrm{THz}}/f_{\mathrm{rep}} \cdot 187/100$ and at a THz power of 100 µW a pulse energy of $E_{\mathrm{THz}} \approx 0.37$ pJ is found. The optical sensitivity per THz pulse power of the detection system in zero-bias operation mode can be determined from the measured absolute average pulse height of the detector response as $S_{\mathrm{opt}} = |U_{\mathrm{max}}|/E_{\mathrm{THz}}$. For detector no. 5, the sensitivity amounts to $S_{\mathrm{opt}} \approx 0.54 \pm 0.10$ mV/pJ and is constant up to 200 µW (see Fig. 6.13(b)).

To determine the intrinsic zero-bias sensitivity of the sub-µm-sized YBCO detector no. 5, the average coupled THz power was estimated as described in section 6.1.3. A coupling efficiency of $\eta = 9.46\%$ was found. This corresponds to a coupled energy of $E_{\mathrm{THz}} \approx 35$ fJ per pulse for an average absolute THz power of 100 µW. An intrinsic sensitivity of $S_{\mathrm{el}} = 5.7$ mV/pJ is estimated from this value. Here, the reflection between the antenna and the detecting element was determined from the normal state resistance $R_{\mathrm{n}} = 320\ \Omega$ and the antenna impedance ($Z_{\mathrm{a}} = 60\ \Omega$). In zero-bias operation, the detector impedance should be substantially lower, such that the reflection should be even higher. However, with 85% of the THz radiation being reflected from the optical components (window, lens & log-spiral antenna), the coupling efficiency cannot be larger than 15%, even for a perfectly matched detector impedance.

6.3 Real-time detection in zero-bias operation mode

With the broadband readout electronics discussed in section 6.1.2 and the 63 GHz real-time oscilloscope, minimal pulse-widths of $\tau_{\mathrm{FWHM}} = 15.8$ ps can be resolved, corresponding to a Gaussian pulse shape with an rms width of $\sigma = 6.7$ ps. As the bunch lengths at ANKA in short-bunch operation mode lie in the range of $\sigma \approx 7$ ps, the detection system is fast enough to resolve the overall

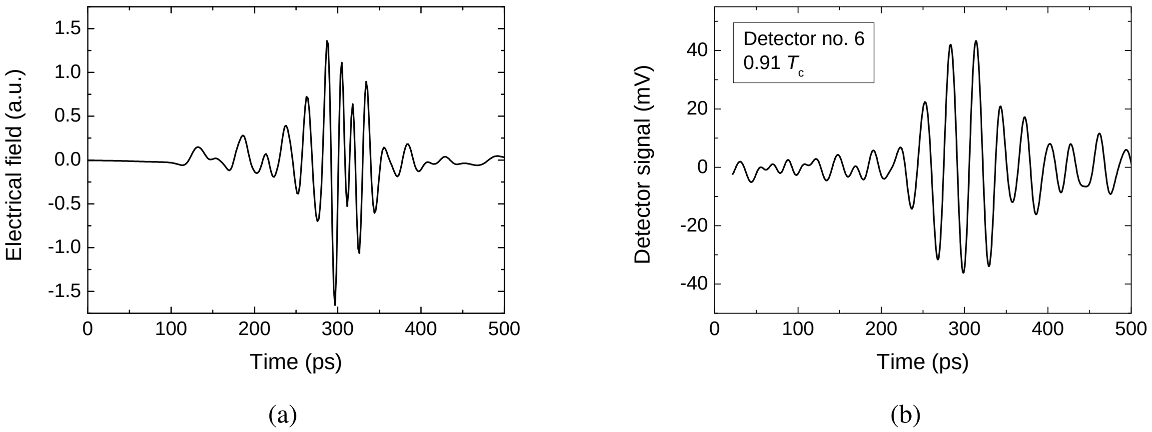

(a) (b)

Fig. 6.15: (a) Simulated electrical field of the spontaneous CSR for a single bunch at the point of emission inside the UVSOR-III storage ring vs. (b) zero-bias detector signal measured with detector no. 6 at liquid-nitrogen temperature. The Fourier transformations result in peak frequencies of 40.3 GHz and 33.7 GHz for the simulation and the measurement, respectively [RES$^+$14a, RKT$^+$15].

pulse shape in single-shot measurements, provided the intrinsic response time of the YBCO detector is small enough [23]. This has been shown for the case of biased YBCO detectors [9], [RKT$^+$15].

The bursting bunch exhibits additional high-frequency components in the spectrum, visible in the time domain as a substructure on the bunch (see spectrum of ANKA in Fig. 2.1). These micro-bunches cannot be resolved with the presented measurement configuration, as the readout bandwidth is not high enough. In the spectrum, the bunch envelope corresponds to a Gaussian with rms width $1/\sigma$, resulting from the Fourier transformation of the time-domain signal. It is important to note, that a single-cycle or half-cycle THz signal, which can be described by one or several Gaussian pulses in the time domain, leads to a broadband spectrum in the frequency domain. The readout electronics act as a lowpass filter with the -3 dB upper bandwidth limit given by equation 6.1.

A single shot of a zero-bias signal, recorded with detector no. 6 at the storage ring ANKA, is depicted in Fig. 6.14 [RIS$^+$14]. The sub-µm-sized detector was operated at liquid-nitrogen temperature. By fitting the detector response to a Gaussian pulse a width of $\tau_{\mathrm{FWHM}} = 15.7$ ps was determined.

The ability of the YBCO detector to detect THz signals of opposite polarity in zero-bias operation mode was investigated at UVSOR-III, where the THz signal oscillates with frequencies in the range of 30 GHz (see section 2.1.3), such that the oscillation can be resolved by the 63 GHz real-time oscilloscope (see section 6.1.2). Spontaneous CSR is emitted from several hundred picoseconds long electron bunches above a given current threshold due to the formation of micro-bunches. A simulation of the electrical field at the point of emission inside the storage ring is shown in Fig. 6.15(a)

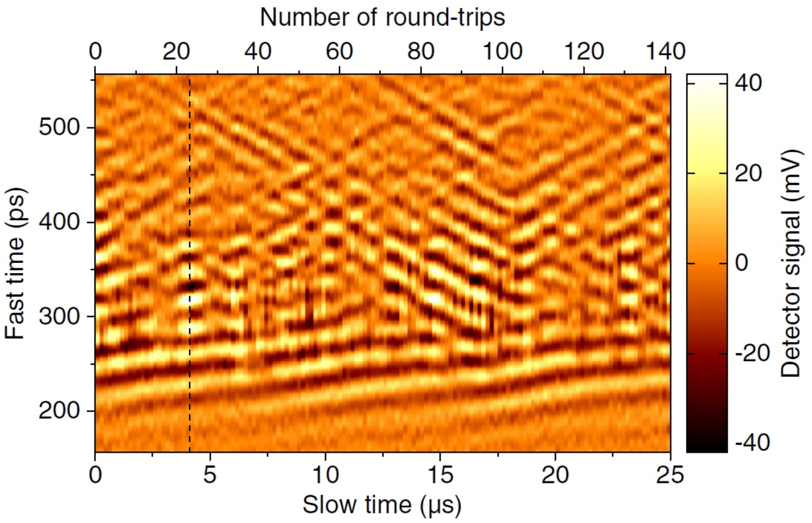

Fig. 6.16: 3D-plot of the long-time evolution of the spontaneous CSR THz signal measured in zero-bias operation mode with detector no. 6. The 500 ps duration of the single-shot signal is plotted on the *y*-axis, while the *x*-axis displays the number of revolutions of the bunch inside the synchrotron. The measured detector signal is color graded [RES$^+$14a].

[RES$^+$14a]. The electrical field oscillates around zero. As the Fourier transform of a sine function corresponds to the delta function, the spectrum reveals a sharp peak around 40.3 GHz with an rms width of 3.6 GHz. In the time domain, the electrical field of narrowband CSR thereby always manifests as a multi-cycle oscillating signal with an envelop that vanishes upon integration.

For the detection of the GHz oscillation a detector with the broadband log-spiral antenna for low THz frequencies was used (see section 3.4). The recorded detector response of detector no. 6 is depicted in Fig. 6.15(b). The FFT of the signal, depicted in Fig. 6.17(a), reveals an oscillation with a center frequency of 33.7 GHz. It is important to note, that a picosecond oscillation around zero cannot be recorded by a classical bolometer, which requires a bias current and acts as a power-sensitive detector, thereby losing the information on the phase of the electrical field. Also, the zero-biased Schottky diode. discussed in section 2.2.3, is a rectifier and can only detect oscillations of the electrical field of one distinct polarity.

The direct detection of the spontaneous CSR enables the observation of the spatiotemporal evolution of the micro-bunch structures upon revolution of the electron bunch inside the storage ring. The behavior is summarized in Fig. 6.16. Two parts of the bunch are observed: a structure at the head of the bunch which drifts towards the tail (< 250 ps) and, in the second part of the bunch, two structures which move in both directions inside the bunch. These drifts can be interpreted from the motion of the electron bunch in phase space. The speed of motion results from the parameters describing the synchrotron, e.g. the resistive and inductive impedances of the storage ring. Deviations of the measured detector response from the simulation results can thus be attributed to faulty assumptions of these model parameters. [RES$^+$14a].

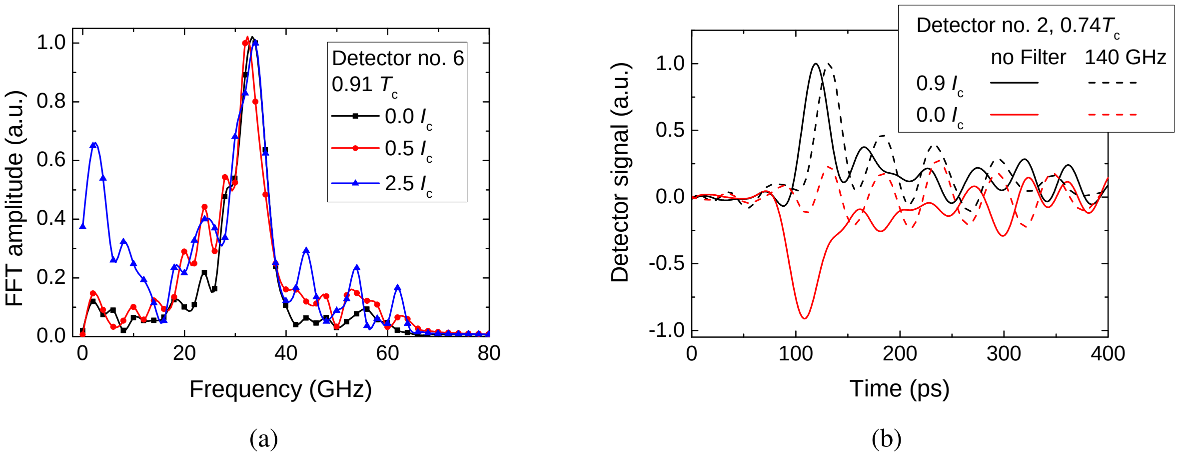

(a)

(b)

Fig. 6.17: (a) FFT of the signal recorded at UVSOR-III with different bias currents at liquid-nitrogen temperature. The oscillation can be resolved by the detection system and an additional low-frequency component, corresponding to the envelop of the oscillating signal, appears with an applied bias current. (b) Broadband signal from PCA with 140 GHz filter. The zero-bias signal disappears upon application of a narrowband filter with a center frequency above the readout bandwidth of the detection system. The signal is normalized to the biased signal height for the cases with and without filter.

By applying an additional positive bias current to the YBCO detector, the measured signal is shifted and the envelop function does not vanish anymore. In the FFT of the time-domain signal this is visible as a peak at low frequency (≈ 2.0 GHz) which increases with increasing bias current (see Fig. 6.17(a)).

For narrowband CSR with oscillation frequencies above the readout bandwidth of the detection setup, the RF readout acts as a lowpass filter and cuts off the signal. Therefore, narrowband radiation at higher frequencies cannot be detected in zero-bias operation mode and the frequency dependence of the zero-bias detector response cannot be investigated via a direct readout detection system. Detector no. 2 showed a zero-bias response at ANKA, when excited with broadband THz radiation (see section 6.2), whereas the same detector did not reveal a zero-bias response at the narrowband undulator source FELBE at frequencies between 1.3 THz and 6 THz. The response measured at FELBE with the biased detector no. 2 will be discussed in section 7.1.
The effect of the vanishing zero-bias signal in direct detection is visualized in Fig. 6.17(b), where detector no. 2 was excited with the broadband signal of a PCA. Upon insertion of a 140 GHz bandpass filter the negative zero-bias detector signal (depicted in red) disappears. As opposed to that, a detector signal is observed with and without the filter in the biased regime (black lines). The bandpass filter used in the setup is based on multi-layer frequency-selective surfaces fabricated by the use of the electroplating technique. The bandwidth of the filter is 20% (FWHM) [SBB$^+$16a], [209].

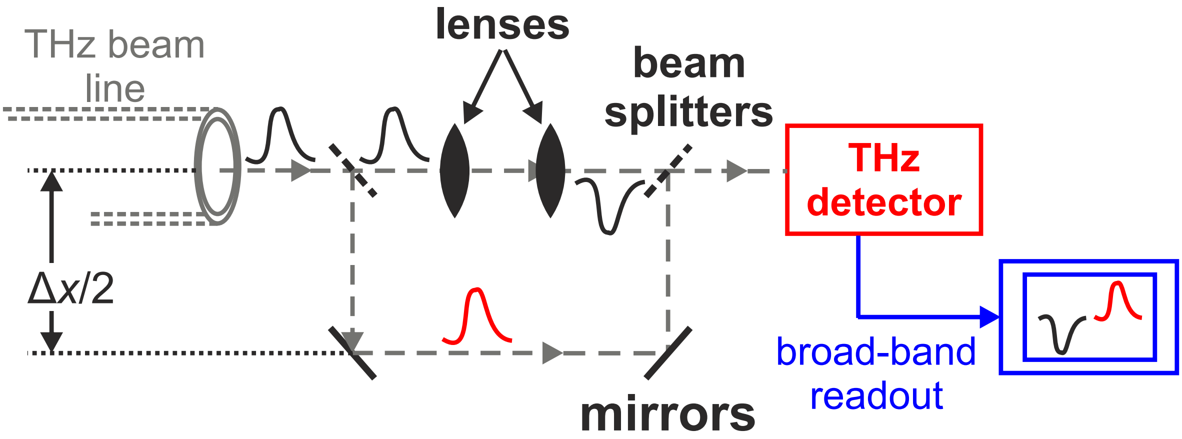

Fig. 6.18: Gouy phase shift setup for bursting CSR: The incoming CSR pulse is split into two identical pulses and then sent through a phase-shifting lens configuration on one of the two optical paths. Both pulses are detected with the same sub-µm-sized YBCO detector (detector no. 1).

6.4 Sensitivity of the detector response to the phase of the electrical field

The detection of oscillating THz signals in zero-bias operation mode, as presented above, can be explained within the model of dissipative vortex motion suggested by Probst *et al.* (see section 3.3.2) [14]. The direction of movement of vortices through the YBCO detector depends on the direction of the RF current, generated by the THz photons. Herein, the polarity of the RF current is directly linked to the phase of the electrical field. Therefore, when operating the detector at zero-bias conditions, a sensitivity to the phase of the electrical field should be observed rather than a sensitivity to the intensity of radiation.

Delay-line setup with Gouy phase shift

At ANKA in bursting mode, the THz radiation changes its spectral and temporal characteristics from revolution to revolution. Changes of the polarity of the THz signal (see signal traces in Figs. 6.19(a) and 6.19(b)) as well as the extinction of the measurable THz signal in between two bursts of THz radiation are observed (see Fig. 6.7). It is evident that averaging leads to a loss of information on the shape of the single THz pulse. While averaged signals are a good measure for the overall detector sensitivity and thus suited for the investigation of the operation-point dependent detector behavior, only single-shot measurements can be used to investigate the electrical-field sensitivity of the YBCO detector. As the pulse shape changes from revolution to revolution the electrical field of a THz pulse has to be compared to its own phase-shifted signal.

The setup used at ANKA is depicted in Fig. 6.18. The THz signal is split in two optical paths at the first beam splitter and recombined at the second one. Subsequently it is fed to the YBCO detector which is read out with the broadband readout electronics. Due to the length distance of

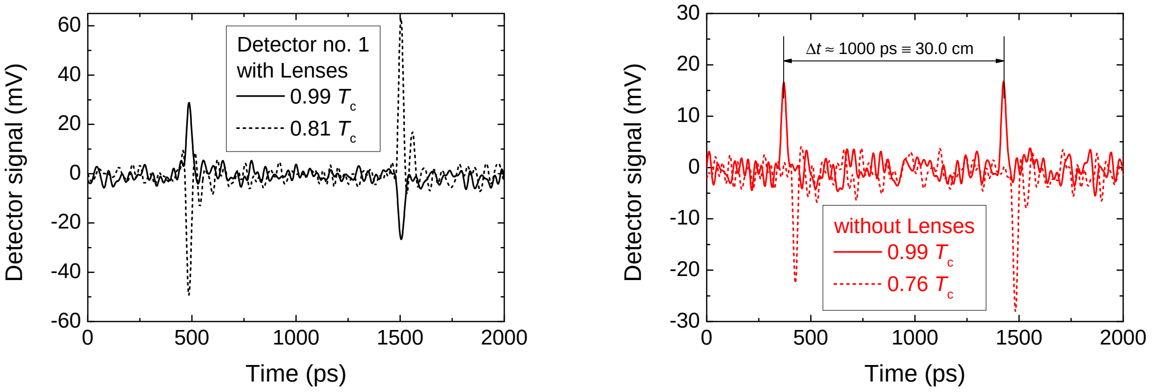

(a) (b)

Fig. 6.19: Signal traces recorded with the Gouy phase-shift setup: (a) two traces with the Gouy phase shift at different temperatures measured with detector no. 1. The polarity of the recorded pulses is reversed. (b) Same measurement without the lenses, thus without a phase shift on the upper optical path in Fig. 6.18. No reversal of the pulse polarity is observed.

$\Delta x \approx 30.0$ cm, the THz signal, traveling with the speed of light, is shifted by about 1 ns on the second beam path, as compared to the THz pulse propagating on the upper optical path. Thus, the setup generates two individual THz pulses originating from the same CSR signal and irradiating one sub-µm-sized YBCO detector with a time delay of 1 ns.

Two lenses with focal lengths of $f = 100$ mm @ 500 GHz were placed at a distance of $2f = 200$ mm in the upper beam path. By exploiting the Gouy phase shift, as discussed in section 2.3, a phase shift of π can be applied to the THz signal. For the picosecond-scaled CSR pulses, this method corresponds to a reversal of the direction of the electrical field. By inserting the two lenses in the setup, a relative switching of the phase of the electrical field of the first THz pulse as compared to the second one is thus achieved. For a detector which exhibits sensitivity to the phase of the electrical field, same-polarity pulses are expected without the lens configuration. On the contrary, reversed polarity should be observed upon application of the Gouy phase shift with the two lenses. Note that the THz beam at ANKA is assumed to be in parallel configuration. Therefore, only two lenses are necessary to implement the phase shift.

Before entering the delay-line setup, the THz signal coming from the beamline port was sent through a horizontally aligned wire grid. Moreover, a sub-µm-sized YBCO detector with a defined linear polarization was used, in order to ensure vertical polarization at all points of the experiment. Detector no. 1 has a narrowband antenna with a center frequency of 140 GHz. The detector was mounted in the cryocooler, such that the antenna exhibited vertical polarization.

Typical signal traces, measured with and without lenses, are shown in Fig. 6.19, where Fig. 6.19(a) depicts two exemplary traces measured with the Gouy phase shift in the upper optical path. As expected, the detector signal consists of two pulses with a temporal spacing of approximately

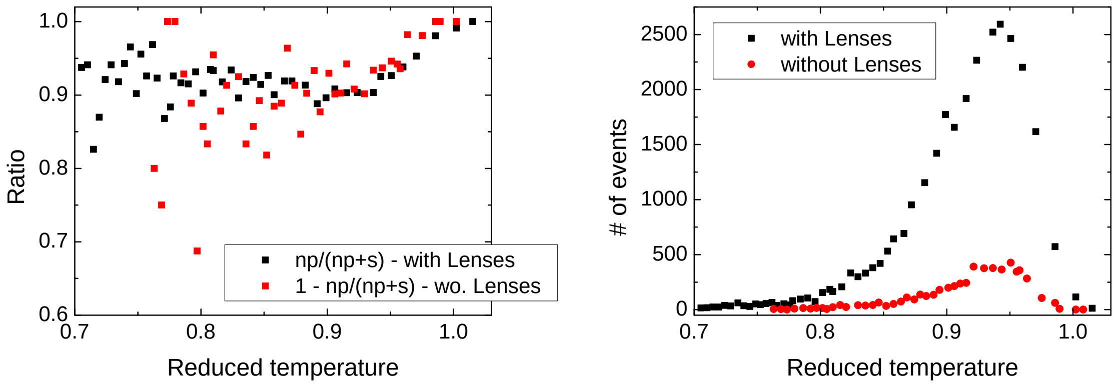

(a) (b)

Fig. 6.20: Analysis of the electrical-field sensitivity depending on temperature for detector no. 3: (a) ratio $\mathrm{np}/(\mathrm{np}+\mathrm{s})$ for the configuration with lenses and $1-\mathrm{np}/(\mathrm{np}+\mathrm{s}) = \mathrm{s}/(\mathrm{np}+\mathrm{s})$ for the setup without lenses. (b) Temperature dependence of the zero-bias response represented by the number of events.

1000 ps. The pulse widths are in the range of $25-30$ ps which is above the temporal resolution of the readout path with the 33 GHz real-time oscilloscope and the SHF amplifier. Independently of the operation temperature and the polarity of the original CSR pulse, a reversal of the second pulse, as compared to the first one, is seen. When switching the setup to the configuration without the lenses, the opposite behavior is observed: A positive pulse is followed by a second positive one and a negative pulse entails a negative one (see Fig. 6.19(b)).

This behavior is evidence for the ability of the YBCO detector to respond to the direction of the electrical field. In order to investigate the temperature dependence of the observed characteristic, a statistical means was introduced: Signal traces with opposite polarity of the two pulses were labeled "np" and those with same polarity were attributed "s". From segmented recordings with sixteen thousand segments the number of "np" and "s" events was extracted via a Matlab script for every operation point. As discussed above, for the detector signals measured with the Gouy phase shift a reversal of the signal is expected, such that the ratio of "np" events to the sum of all events $(\mathrm{np}+\mathrm{s})$ should be 1. Similarly, in the opposite case, the ratio $\mathrm{s}/(\mathrm{np}+\mathrm{s})$ is expected to equal to 1.

The results of the data analysis are presented in Fig. 6.20(a). Sensitivity to the phase of the electrical field is maintained over the whole temperature range. As discussed in section 6.2.1 the detector signal decreases at lower temperatures, such that the range above 0.7 T_c could be investigated. The expected behavior is observed for both lens configurations. Higher fluctuations are observed in the measurement without the lenses. This can be explained by the smaller signal-to-noise ratio of this measurement. As the beam current in the synchrotron decays exponentially, the emission of CSR decreases gradually. Therefore, the signal level in consecutive measurements is different and fewer events are recorded in the configuration without the lenses (see Fig. 6.20(b)). Lower total signal then entails a higher noise of the measurement which results in the fluctuation of the ratio depicted in Fig. 6.20(a).

A direct consequence of the monotony of the measured data over temperature is that the mechanism of radiation detection should be the same near T_c and far below T_c. According to equation 3.1, at 0.7 T_c the in-plane gap in YBCO amounts to approximately 95% of its zero-temperature value. Experimentally, slightly lower values of the temperature-dependent gap, than predicted by the BCS theory, were found ($\Delta(T) \approx 0.78\Delta(0) \approx 31$ meV) [96]. Moreover, for the thin films used in this work, the critical temperature does not reach the bulk value of $T_\mathrm{c} = 92$ K, such that an additional reduction of the gap, as compared to the estimated value, can be expected ($\Delta(T) \approx 25$ meV). Yet, equating the gap value to the energy of a single photon yields 25 meV $\widehat{=}$ 6.1 THz and thus a breaking of Cooper pairs, at the relevant frequencies emitted at ANKA ($f < 1$ THz), is not possible.

On the other hand, electron heating due to the RF current cannot be excluded. In the BCS theory, the density of Cooper pairs depends quadratically on the order parameter, yielding $n_\mathrm{s}(0.7\ T_\mathrm{c}) \approx 0.61\ n_\mathrm{s}(0)$. Measurements of the London penetration depth in YBCO, that can be correlated via $n_\mathrm{s} \propto 1/\lambda_{ab}^2$ to the Cooper-pair density, indicate even lower values ($n_\mathrm{s}(0.7\ T_\mathrm{c}) < 0.5\ n_\mathrm{s}(0)$) [210]. Moreover, reflectance measurements of cuprates in the far- and mid-infrared region imply that merely 20% of the doping-induced carriers contribute to the superfluid [211]. Therefore, a contribution of quasiparticle heating to the detector response and thus a hot-electron effect is a potential detection scheme at all relevant temperatures. In this case, the switch in polarity of the RF current, as a consequence of the Gouy phase shift, would explain the altered polarity of the detector response. However, a nanosecond-scaled phonon escape was not observed in the zero-bias operation mode (see section 7.4).

Similarly, the obtained sensitivity of the YBCO detector to the direction of the electrical field for pulsed-THz excitations can be explained in the frame of the model based on dynamics of self-generated vortices. The fact, that the power and temperature dependence of the zero-biased detector response, as discussed in section 6.2.2, can be fitted to a flux-flow model, clearly supports this assumption.

6.5 Conclusions of chapter 6

In section 6.1, the YBCO detection system, consisting of the cryostat and the broadband readout electronics as well as the DC-bias source, was introduced. Minimal response times of ≈ 16 ps (FWHM) can be realized with sub-µm-sized YBCO detectors, which exhibit high sensitivities and can be operated without additional signal amplification. The zero-bias operation mode was realized with a 50 Ω resistor connected to the DC port of the bias tee.

The dependence of the observed zero-bias response on the operation conditions of the YBCO detector was investigated. A maximum of the zero-bias response is seen in the range of $0.90-0.95\ T_\mathrm{c}$ for all YBCO detectors. The response was found to depend linearly on the THz power and to saturate at high power levels. Specifically, the response can be fitted to the trend of the $I(V)$ characteristic which is governed by flux flow in the relevant region. Absolute optical sensitivities of $S_\mathrm{el} = 5.7\ \mathrm{mV/pJ}$ were found for detector no. 5.

By the use of the Gouy phase shift, which is a distinct feature of Gaussian beams, the sensitivity of the YBCO detector to the phase of the electrical THz field was demonstrated over a broad temperature range ($T \geq 0.7\ T\mathrm{c}$). This result implies a stability of the detection mechanism throughout the temperature interval. The zero-bias operation combined with the sensitivity of the YBCO detector to the phase of the electrical field is a unique characteristic of the YBCO detector amongst the direct THz-detector technologies. Real-time detection of THz signals could be demonstrated at ANKA and the UVSOR-III storage ring. It enables the monitoring and analysis of bursting CSR and oscillating THz signals at circular and linear accelerators.

7 Frequency- and power-dependent behavior in the biased regime

To complete the picture of the YBCO THz detector, the biased regime is investigated in this chapter. First, the dependence of the detector response on bias current is examined. At the ANKA storage ring and at the linear accelerator FELBE, the impact of the THz power level and the frequency of the radiation on the detector response were probed with sub-µm-sized YBCO detectors with different volume. The results are summarized in sections 7.2 and 7.3. For comparison of the results obtained from pulsed THz excitations, the detector signal seen with continuous-wave irradiation at sub-gap frequencies is shown. The discussion of the detector response is completed by an examination of the observed pulse shapes for pulsed THz excitations at different frequencies and power levels in section 7.4.

7.1 Dependence of the detector response on applied bias current

At ANKA, the bursting bunches emit picosecond THz pulses which change their temporal and spectral shape from revolution to revolution. Therefore, as for the temperature dependence of the zero-bias response in section 6.2, the averaged detector signal with an applied bias current was examined at ANKA. At the linear accelerator FELBE, where the bunch shape is periodically modulated by an undulator, the emitted CSR is stable within a few percent (see section 2.1). To exclude small fluctuations of the signal height, the measured detector response was averaged in the same way as at ANKA. The detection setup used was introduced in section 6.1, and the battery-driven bias source was operated in current-bias mode.

Figure 7.1(a) shows the absolute, averaged signal recorded at FELBE with detector no. 2 (see Tab. 6.1) at different temperatures and bias levels. The center frequency of the emitted CSR was 1.3 THz. The measured curves were interpolated with a power-law dependence ($|U_{\text{max}}| = \text{Offset} + (I - I_0)^n$) and the exponents extracted from the fits are given in the plot. As the critical current increases with decreasing temperature, the maximum detector signal is shifted to higher bias currents. The power-law dependence varies with temperature and the exponent decreases with increasing temperature from $n = 2.4$ at 0.7 T_{c} to $n = 1.2$ at 0.95 T_{c}. This effect points to a saturation of the detector response when the temperature is increased.

Data recorded at ANKA at low bias currents support this assumption (see Fig. 7.1(b)). Here, the dependence on bias current coincides for all operation temperatures and exhibits linear behavior

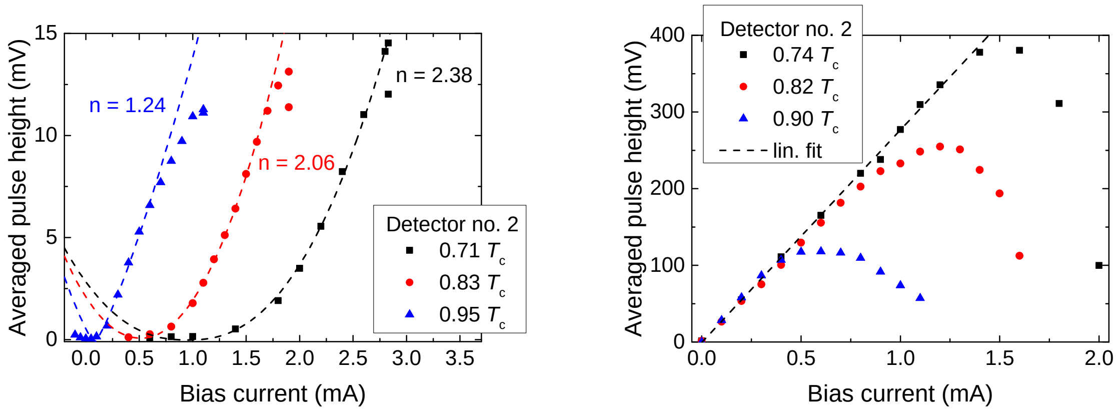

(a) (b)

Fig. 7.1: Dependence of the detector response on bias current for different temperatures for detector no. 2 (a) at 1.3 THz at FELBE and (b) at the IR2 beamline at ANKA. In (a), the dashed lines correspond to power-law fits according to $|U_{\max}| = \text{Offset} + (I - I_0)^n$. The exponents n of the interpolated data sets are given in the plot. The dashed line in (b) is a linear fit for $T = 0.74\ T_c$.

below the critical current ($n = 1.0$). Note that the measured absolute voltage levels of the detector response are increased by more than one order of magnitude, as compared to the results from FELBE, indicating even higher power levels and thereby a saturation of the detector. According to the flux-flow model discussed in section 6.2.2, the absorbed THz signal acts as a bias signal and should add up to the applied bias current, such that the detector output signal should vary as the $I(V)$ characteristics at the same temperatures with a current offset due to the RF current. For comparison, the $I(V)$ characteristics of detector no. 2 are depicted in Fig. 7.2. It is evident that the bias dependence of the detector signal seen in Fig. 7.1(a) cannot be directly correlated with the $I(V)$ characteristics, such that a flux-flow model seems not to explain the detection of radiation

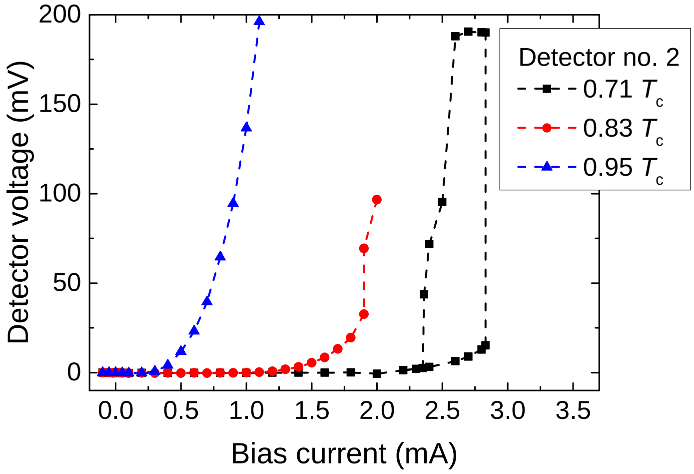

Fig. 7.2: $I(V)$ characteristics of detector no. 2 at the same temperatures as in Fig. 7.1(a). For clarity, the bias current I_b is plotted on the x-axis.

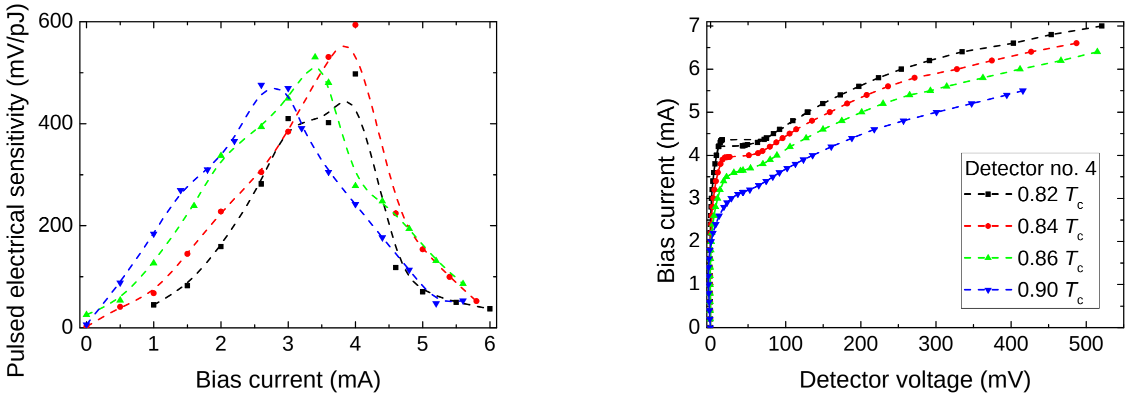

(a)

(b)

Fig. 7.3: (a) Electrical sensitivity of detector no. 4 measured at ANKA at different temperatures, and (b) corresponding $I(V)$ characteristics of detector no. 4 at the same temperatures as in (a).

in the biased regime. Especially at high operation temperatures of the detector ($T/T_c = 0.95$), the almost linear trend of the signal vs. bias current is not reproduced by the $I(V)$ characteristic. However, the maximum signal height, measured for pulsed excitations, coincides with the second critical current, where a discontinuous jump in the $I(V)$ curve is observed at lower temperatures. A nonlinear dependence of the signal height on bias current was also observed by several groups for YBCO detectors operating in a bolometric regime during excitation with optical radiation pulses [15, 212].

As the beam current (e.g. the number of electrons in the bunches) decays exponentially over time at ANKA, the emitted THz power decreases continuously. Therefore, the measured signal height at different temperatures cannot be directly used to extract information on the temperature-dependent sensitivity of the detector. Instead, the sensitivity of the detection system must be determined from signal-height measurements, combined with a simultaneous evaluation of the absolute THz power. The averaged detector response, depending on the absolute THz power, was measured at ANKA in bursting multi-bunch mode by the use of a calibrated THz power meter [43]. Based on antenna properties and the normal-state resistance of detector no. 4 (see Tab. 6.1), a coupling efficiency was estimated, as described in section 6.1.3, and the intrinsic sensitivity S_{el} was extracted. Again, the sensitivity is defined as the averaged detector signal with respect to the average pulse energy rather than the averaged radiation power. This definition is more appropriate to pulsed radiation sources with pulse lengths which are short in comparison to the repetition rate (500 MHz at ANKA).
The sensitivity, depending on bias current, is shown in Fig. 7.3(a) for detector no. 4 along with the corresponding $I(V)$ characteristics in Fig. 7.3(b). The maximum sensitivity is seen at the temperature and bias-current level where the $I(V)$ characteristic exhibits a plateau ($T/T_c = 0.94$, $I_b = 4.0$ mA). This temperature corresponds to the lowest operation temperature where no hystere-

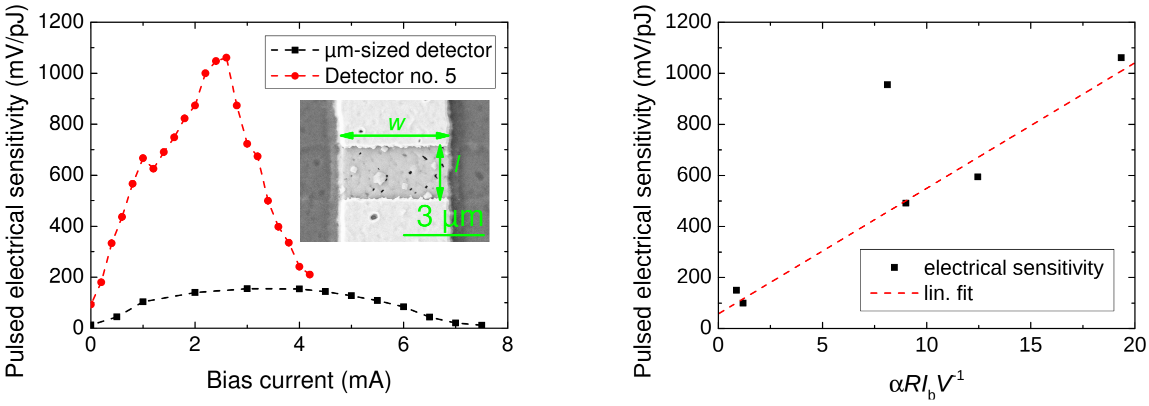

(a) (b)

Fig. 7.4: Dependence of the electrical sensitivity on lateral dimensions of the detecting element: (a) comparison of sub-µm-sized detector no. 5 and a µm-sized detector. An SEM image of the µm-sized detecting element is depicted in the inset. The lateral dimensions of the detector are $w = 4.14$ µm, $l = 1.91$ µm and $t_{\mathrm{YBCO}} = 30$ nm. (b) Dependence of the maximum electrical sensitivity on the factor $\alpha R I_\mathrm{b} \cdot V^{-1}$ for YBCO detectors with different volumes. The dashed line is a linear fit of S_el.

sis in the $I(V)$ curve is seen, yet. The behavior is similar for CW excitations, compare section 7.3.2 and references [15, 190]. Thereby, the temperature dependence of the sensitivity points towards a bolometric nature of the biased detector response. Note that for low bias currents in Fig. 7.3(a), a tendency of decreased exponent is seen with increasing temperature, same as for detector no. 2 in Fig. 7.1(a).

In comparison to these results, the data recorded at ANKA with detector no. 2 (see Fig. 7.1(b)) show maximum detector-signal height at the lowest temperature ($T/T_\mathrm{c} = 0.74$). This is due to the fact that after filling of the synchrotron with electron bunches, the detector response was measured starting from the lowest operation temperature and extending to higher temperatures. Therefore, the emitted THz power was maximal at the lowest temperature, and as the recorded signal was not normalized to the THz power, the signal is maximal at 0.74 T_c.

Likewise, the investigation of the sensitivity depending on detector volume indicates a bolometric nature of the detector response. Figure 7.4(a) shows the sensitivity as a function of the bias current at the temperature with the highest sensitivity for the sub-µm-sized detector no. 5 (see Tab. 6.1), as well as for a µm-sized YBCO detector which is depicted in the inset of the graph. The volume of detector no. 5 is reduced by a factor of about 20 as compared to the larger one. The determination of the intrinsic detector responsivity to pulsed excitations via the coupling efficiency and the averaged measured pulse height yields a maximum value of 160 mV/pJ for the larger YBCO detector. Detector no. 5 shows responsivities of 1.06 V/pJ for optimal operation conditions. Thereby, the patterning of thin-films to sub-µm sized structures provides high responsivities and allows for the detection of small CSR powers [RIS$^+$14].

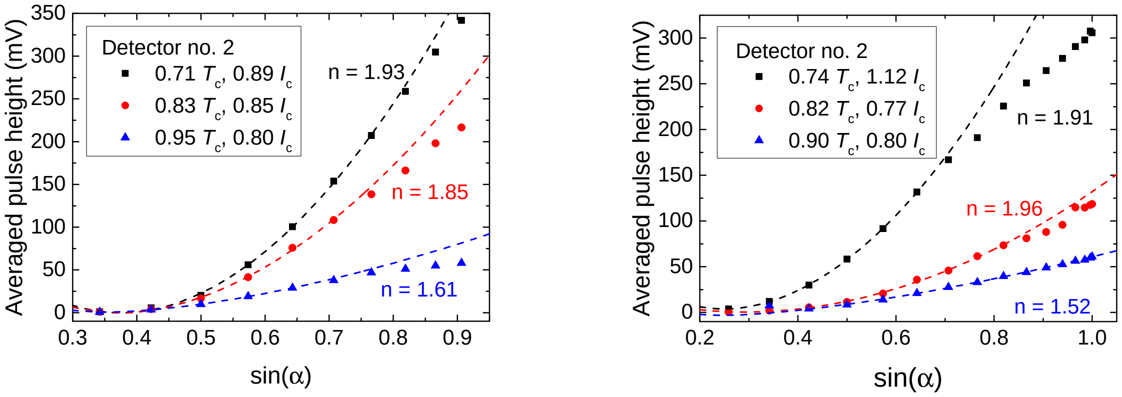

(a) (b)

Fig. 7.5: Dependence of the detector response on coupled electrical field strength ($\sin(\alpha)$) and temperature for detector no. 2 (a) at 1.3 THz at FELBE and (b) at the IR2 beamline at ANKA. The dashed lines correspond to power-law fits as in Fig. 7.1(a) ($|U_{\text{max}}| \propto \sin^n(\alpha)$). The exponents n of the interpolated data sets are given in the plots.

According to equation 2.7, for pulsed excitations the intrinsic sensitivity depends on the operation point as

$$S_{\text{el}} = \frac{\mathrm{d}R/\mathrm{d}T \cdot I_{\text{b}}}{\omega C}. \tag{7.1}$$

At ANKA, the modulation frequency is constant ($\omega = 500$ MHz). Moreover, the specific heat capacitance varies as the volume of the detecting element: $C \propto V$. The maximum intrinsic sensitivity to pulsed excitations S_{el} measured with different YBCO detectors is plotted in Fig. 7.4(b) as a function of the detector-dependent factor in equation 7.1 ($\mathrm{d}R/\mathrm{d}T \cdot I_{\text{b}} \cdot V^{-1}$). The maximum value of $\mathrm{d}R/\mathrm{d}T$ and the bias current at the operation point of highest intrinsic sensitivity were inserted in the formula for every detector. The dashed line is a linear fit to the data. It can be seen that the intrinsic sensitivity fits well the predictions of a bolometric model.

7.2 Influence of the power level

The influence of the power level on the detector response was investigated with detector no. 2 at ANKA and FELBE. To adjust the power level, a wire grid was used. The effect of the wire grid was discussed in section 6.2.2. In short, the electrical field of the transmitted THz field varies as the sine of the angle α in between the direction of the incoming electrical field vector and the wires of the grid. The initial polarization was vertical and defined by a first polarizing grid.

Figures 7.5(a) and 7.5(b) depict the dependence of the averaged, absolute detector signal on $\sin(\alpha)$ recorded at FELBE (1.3 THz) and at the IR2 beamline at ANKA at the same operation temperatures as in Figs. 7.1(a) and 7.1(b). For the experiment, the bias current was adjusted in the vicinity of the critical current at the corresponding operation temperature. The behavior is similar for nar-

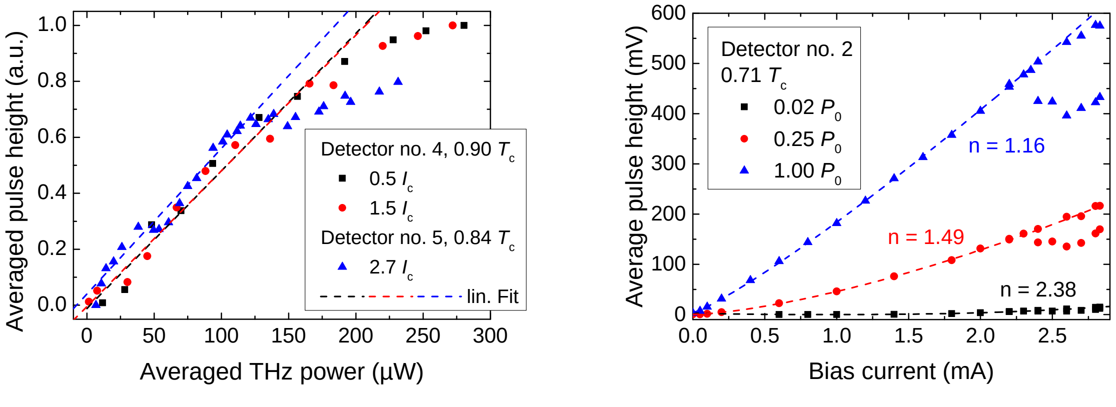

(a)

(b)

Fig. 7.6: (a) Dependence of the detector response on averaged, absolute THz power for detectors no. 4 and 5. (b) Detector signal vs. bias current trend observed for different power levels at FELBE ($f = 1.3$ THz) with detector no. 2 and at a temperature of 0.71 T_c.

rowband excitations at FELBE (1.3 THz) and broadband CSR from ANKA at the IR2 beamline, where the maximum in the emitted THz spectrum lies at around 400 GHz. The characteristics seen at higher frequencies will be discussed in the following section.

From the power-law fits of the measured curves, quadratic dependence ($n \approx 2$) of the detector response on THz field and thereby on induced RF current can be extracted. At higher temperatures, a saturation ($n < 2$) is seen, similarly as for the bias-dependence at high temperatures, as discussed in the previous section. The quadratic dependence on THz field strength implies a linear trend for the averaged detector signal vs. absolute THz power. This relation was observed at the IR1 beamline of ANKA for detectors no. 4 and 5 at moderate temperatures and bias levels (see Fig. 7.6(a) and Tab. 6.1). At higher input powers, the detector response saturates and deviates from the linear trend. Linear dependence of the response on THz power was also found with µm-sized YBCO detecting elements [213]. For those detectors, the dynamic range exceeded 30 dB. The dynamic range and the detector sensitivity can, however, not be maximized at the same time. Small detector volumes entail high sensitivities. At the same time, the dynamic range is scaled down due to the saturation seen in the plot.

Figure 7.6(b) adds to the bias dependence of the detector response that was measured at FELBE with detector no. 2 at a temperature of 0.71 T_c (see Fig. 7.1(a)). The power level during this measurement was rather low and a power-law dependence of the detector signal height on I_b was seen with $n \approx 2.4$. Figure 7.6(b) shows the same quantity recorded at different power levels, where the measurement from Fig. 7.1(b) corresponds to a power level of 0.02 P_0. The exponent n decreases with increasing power level and reaches $n = 1.15$ at the highest power, where the measured signal levels exceed those measured at ANKA in Fig. 7.1(b). This measurement supports the assumption that the detector saturates at high power levels.

Summarizing the influences from the previous two sections, saturation due to THz power, bias current and operation temperature were seen. In a two-temperature model with quasiparticle heating all three parameters influence the electron temperature. A two-temperature model, however, would imply the occurrence of a bolometric nanosecond-scaled response component. In previous works, this bolometric tail was not seen [14]. Pulse shapes recorded at the operation points covered in this section will be discussed in section 7.4.

Moreover, as the THz power depends on the square of the electrical field, a linear dependence of the detector response on the power level implies a square-law dependence on the induced RF current in biased as well as in zero-bias operation mode. This supports the aforementioned hypothesis of a detector response which is caused by flux flow. However, the actual applied bias current did not show this square-law trend, see the discussion in the previous section. The influences of a static bias current and of a pulsed excitation, thus, seem to have different effects on the detector behavior.

7.3 Frequency dependence in biased operation mode

To complement the data on the operation-point dependent behavior in the biased regime, the dependence of the detector response at higher frequencies ($f = 6.5$ THz) was investigated as well as the response of the same YBCO detectors to continuous-wave (CW) radiation.

7.3.1 Pulsed narrowband THz signals

At FELBE, the emitted THz frequency can be adjusted by varying the magnetic field strength of the undulator and the electron-beam energy. The response of detector no. 2 to pulsed narrowband signals was investigated in a frequency range from $1.3 - 6.5$ THz, where the lower frequency limit is imposed by the accelerator and the upper limit arises as the optical components start to absorb the majority of the THz power. In particular, the transmission of a sapphire substrate at a temperature of 77 K, measured with a calibrated THz power meter, amounted to $T \approx 0.1$ at $f = 6.5$ THz.

At 6.5 THz, the measurement of the dependence of the detector response on bias current and temperature, which was conducted at a frequency of 1.3 THz in section 7.1 (see Fig. 7.1(a)), was repeated. The results are depicted in Fig. 7.7(a). The overall signal levels are even lower than in Fig. 7.1(a), indicating lower levels of absorbed THz power. As before, the trend of a decrease of the exponent n of a power-law fit ($|U_{\max}| = \text{Offset} + (I - I_0)^n$) with increasing operation temperature and thus increased electron temperature is seen. However, the absolute values of n are larger at the same temperatures as in section 7.1 for the data recorded at 1.3 THz.

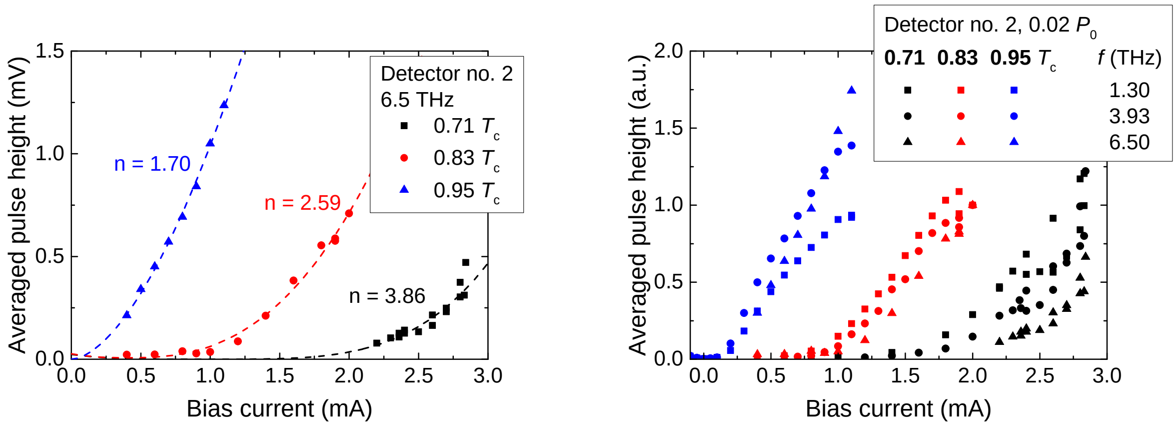

(a)

(b)

Fig. 7.7: Dependence of the biased detector response on THz frequency for pulsed excitations for detector no. 2: (a) response at different temperatures at 6.5 THz fitted with a power-law trend ($|U_{\max}| = \text{Offset} + (I - I_0)^n$) and (b) averaged, absolute detector signal for 1.3 THz, 3.9 THz and 6.5 THz at low THz power levels ($P = 0.02\ P_0$) depending on bias current.

Figure 7.7(b) gives a summary of the detector response depending on operation point (i.e. bias current and temperature) for the frequencies 1.3 THz, 3.93 THz and 6.5 THz at low radiation power levels ($P = 0.02\ P_0$) in order to avoid saturation of the detector. The squares indicate the data recorded at 1.3 THz and the power-law fits can be found in Fig. 7.1(a), whereas the triangles stand for the data measured at 6.5 THz (compare Fig. 7.7(a)). Similar behavior is observed over the whole frequency range, such that the same physical mechanism should be the cause of the detector signal.

According to equation 3.1, the gap at 0.83 T_c amounts to 72% of its zero-temperature value and assuming $\Delta(0) = 40$ meV (see section 3.1.3), this gives a gap frequency of 7 THz. At the lowest temperature of 0.71 T_c, almost the full gap is developed. Even at the highest operation temperature near T_c, the gap amounts to $0.39\ \Delta(0) \mathrel{\widehat{=}} 3.8$ THz. This is, however, clearly below the highest measured frequency response at 6.5 THz. Note that the detector signal considered up to now is the peak signal following the initial rising edge of the detector response. In the two-temperature model, this peak stems from the rise in electron temperature. Seen that, in the BCS theory, the density of Cooper pairs scales with the square of the order parameter, a non-vanishing number of quasiparticles is present at all temperatures considered in this work. A heating of quasiparticles, likewise at radiation frequencies above and below the superconducting gap, can therefore not be excluded as the mechanism of radiation detection.

7.3.2 Continuous-wave excitations

A quasi-optical measurement setup with a backwards-wave oscillator source was used to characterize the detector response to CW radiation. The measurement setup is depicted in Fig. 7.8.

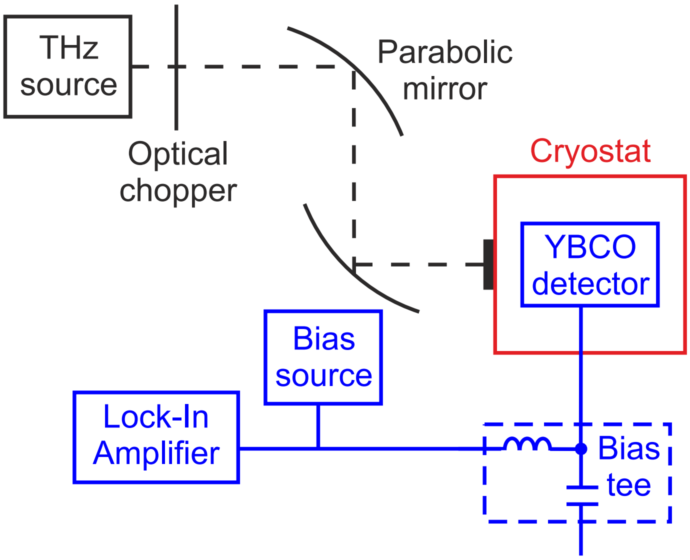

Fig. 7.8: Measurement setup for continuous-wave THz excitations: The optical path and components are depicted in black, the cryostat in red and the electronics in blue.

The source emits radiation at a frequency of 290 GHz, corresponding to a vacuum wavelength of 1034 µm. Via two parabolic mirrors, the signal is focused and fed to the detector which is mounted in the cryostat described in section 6.1.1. An optical chopper modulates the incoming radiation to enable the readout of the detector signal via the DC port of the bias tee with a lock-in amplifier (LIA). Herein, the use of the LIA increases the SNR of the experiment. A deflection of the operation point of the detector due to the absorbed THz signal is measured.

In Fig. 7.9(a), the measured detector response of detector no. 4 to the CW radiation with a frequency of 290 GHz at the same temperatures as in Fig. 7.3(a) is depicted. The corresponding $I(V)$

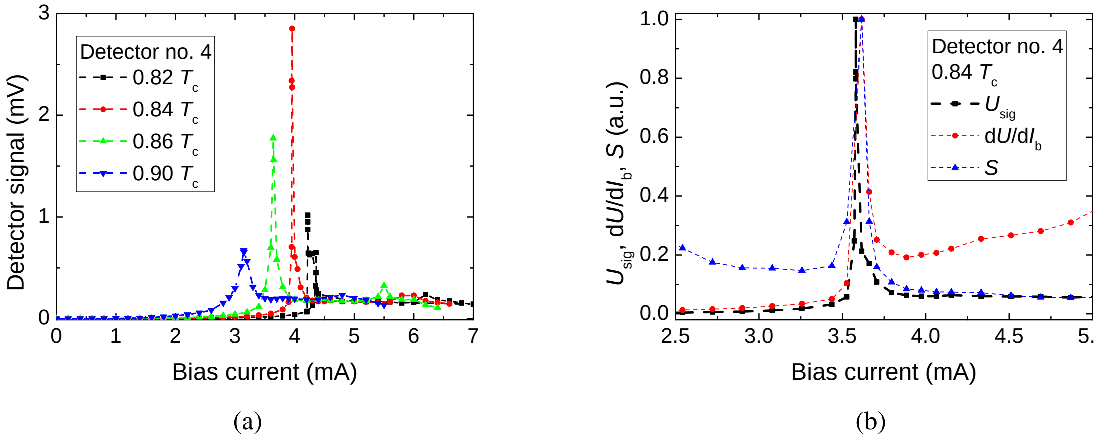

Fig. 7.9: (a) Detector response to continuous-wave excitations at 290 GHz depending on the applied bias current for detector no. 4 and the same temperatures as in Fig. 7.3(b). (b) Detector signal at the operation temperature of maximum detector signal (0.84 T_c) in comparison with the differential resistance and the sensitivity of a bolometer according to [214], all of them depending on bias current.

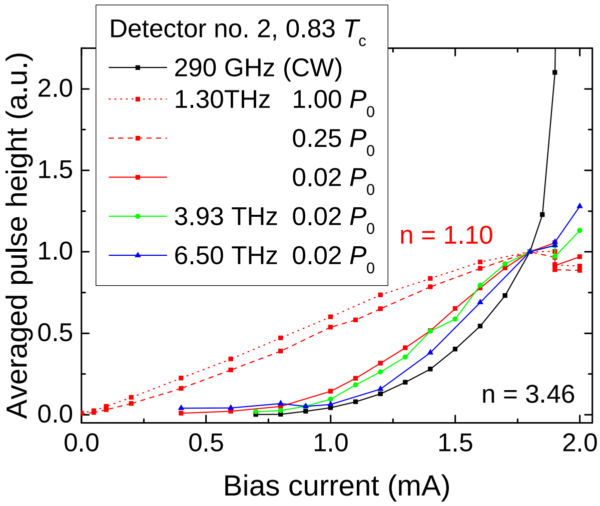

Fig. 7.10: Frequency-dependent detector response vs. bias current (detector no. 2) at the operation temperature of maximum sensitivity (0.83 T_c). The exponents n of the power law fits of the CW data (black line) and the saturated detector data at 1.3 THz (red dotted line) are given in the plot.

characteristics were already shown in Fig. 7.3(b) along with the detector response to pulsed THz excitations. The maximum sensitivity is observed at the temperature where the $I(V)$ characteristic exhibits a plateau and the differential resistances becomes maximal. Accordingly, the measured detector signal could be matched with the dependence of the differential resistance ($Z_\mathrm{d} = \mathrm{d}U/\mathrm{d}I_\mathrm{b}$) on bias current as depicted in Fig. 7.9(b).

The sensitivity of a bolometer can be calculated, using nothing but the $I(V)$ characteristic of the detector, as:

$$S = \frac{Z_\mathrm{d} - R}{2 I_\mathrm{b} R}, \tag{7.2}$$

with the differential resistance Z_d of the detector and the resistance R at each bias current [214]. In Fig. 7.9(b), the obtained sensitivity is plotted in arbitrary units in blue along with the aforementioned detector signal and the differential resistance of the detector. All three curves match well, indicating a bolometric behavior of the detector at bias current levels above the first critical current ($I_\mathrm{c} = 2.0$ mA @ 0.84 T_c). Note that the same relation, thus maximum sensitivity at the plateau of the $I(V)$ characteristic of detector no. 4, was observed experimentally for broadband pulsed THz radiation at ANKA (see section 7.1). A more detailed analysis of the detector response to CW radiation can be found in [15] and [190], where similar behavior was observed over a large range of µm- and sub-µm-sized YBCO detectors at a radiation frequency of 650 GHz.

In the biased regime, the power and bias current dependence of the detector response for pulsed THz excitations below the gap show characteristics which can be explained by bolometric behavior. In particular, the dependence of the sensitivity on detector volume (see Fig. 7.4(b)) is a strong indicator of a bolometric detection mechanism. The detector response to CW excitations, in turn,

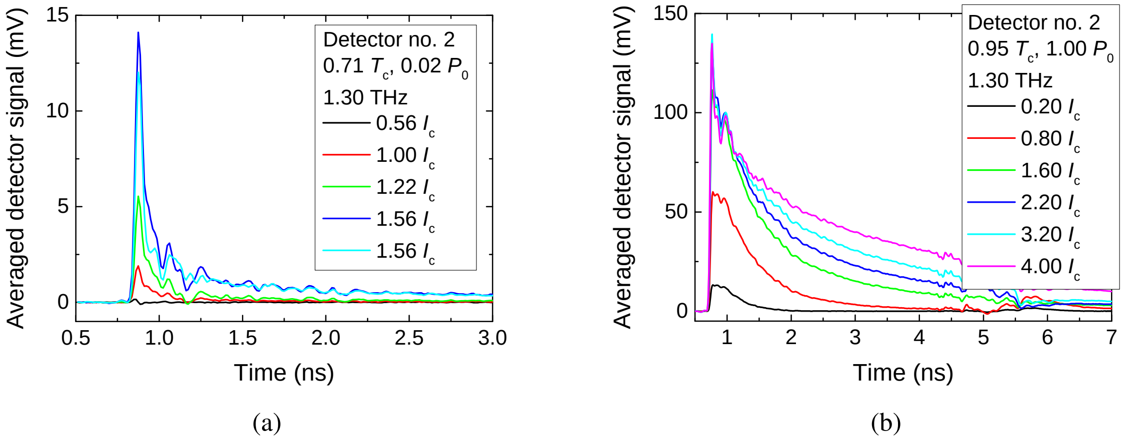

Fig. 7.11: Measured averaged pulse shapes at 1.3 THz under different operation conditions of detector no. 2: (a) at low temperature and power level (0.71 T_c, 0.02 P_0) and (b) in the resistive state ($T = 0.95\ T_c$, $P = P_0$). The pulse shapes at different bias levels are depicted.

can be directly fitted to a bolometer model. Therefore, it is worth comparing the detector signal in both regimes. Figure 7.10 depicts the normalized detector signal measured with detector no. 2 at the temperature with maximum differential resistance (0.83 T_c) at different radiation sources. The signal was normalized to the operation point just before the discontinuous jump in the $I(V)$ characteristic. A trend from power-law dependence with $n \approx 3.5$ to linear dependence on the bias current is observed for increasing power levels of the THz radiation in accordance with the saturation of the detector when the absorbed power increases. Apart from that, the dependencies coincide, reinforcing the finding that the detector response to pulsed excitations in the biased regime is of a bolometric type.

7.4 Measured pulse shape depending on the operation point of the detector

While in zero-bias operation mode picosecond long pulses without bolometric nanosecond-scaled components are observed exclusively, the biased operation mode reveals different pulse forms and widths, depending on the operation point of the detector. The pulse width in the zero-bias mode is either limited by the readout bandwidth or by the overall pulse length of the THz signal itself, which demonstrates that the actual response time of the detector is shorter than ≈ 15 ps in all cases. Up to now, the analysis of the biased regime focused on measured peak heights and their dependence on the operation point. The investigation of the phonon contribution to the detector signal requires the analysis of the pulse shape, including the decay time of the detector response. Figures 7.11(a) and 7.11(b) show averaged pulse forms of data recorded at FELBE at a center frequency of 1.3 THz with detector no. 2. In (a), the detector is operated at a low temperature and low absorbed THz power while in (b), the operation temperature is near T_c and the maximum THz power was

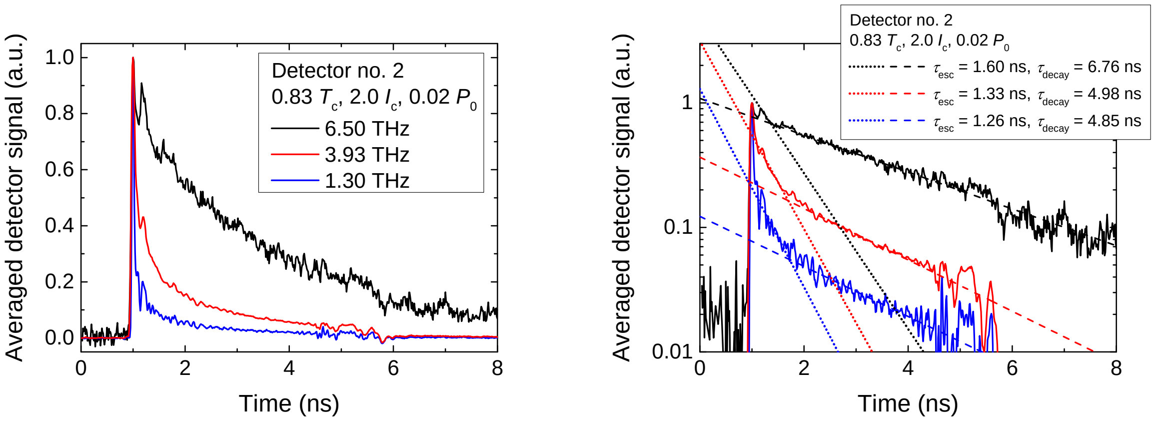

(a) (b)

Fig. 7.12: Dependence of the pulse shape on CSR frequency for detector no. 2: (a) plotted on a linear scale and (b) plotted on a logarithmic scale with the corresponding exponential fits of the data.

radiated onto the detector, such that the detector is saturated. Picosecond pulses were recorded at all operation conditions and Gaussian fits of the rising edge revealed pulse lengths of ≈ 40 ps (FWHM). Depending on the operation point, an additional exponential decay with longer time scales was observed. This pulse shape is comparable to the detector response seen with a YBCO HEB for optical radiation pulses [15]. However, the decay time of this nanosecond-scaled detector response depends on temperature and bias current and increases with increasing saturation of the YBCO detector. This result is not consistent with a detector response caused by phonon escape to the substrate, as τ_{esc} is essentially independent of the temperature and operation point of the detector over a broad range of temperatures [215].

When keeping the operation point of the detector constant at intermediate temperature and bias current and increasing the frequency of the emitted CSR at FELBE, the decay time is seen to increase (see Fig. 7.12(a)). Note that the overall signal height at 6.5 THz is considerably smaller than for the lower frequencies. By plotting the same data in a logarithmic graph, the decay time can be extracted from a linear fit. From Fig. 7.12(b) it becomes evident that the decay of the detector response consists of two superimposed exponential decays with different time scales. The first one is characterized by an operation-point independent decay time, which can be identified as the phonon escape time of the 30 nm thick YBCO film. According to [14], the phonon escape time for the multi-layer system used in the present work amounts to $\tau_{\mathrm{esc}} = 0.036\ \mathrm{ns/nm} \times t_{\mathrm{eff}}$ with the effective film thickness $t_{\mathrm{eff}} = t_{\mathrm{YBCO}}[1 + t_{\mathrm{PBCO}}/(2t_{\mathrm{YBCO}} + t_{\mathrm{PBCO}})]$ and the passivating PBCO layer thickness $t_{\mathrm{PBCO}} = 30$ nm. Inserting the individual film thicknesses and solving for the phonon escape time yields $\tau_{\mathrm{esc}} \approx 1.44$ ns. The values determined for detector no. 2 in Fig. 7.12(b) are in good agreement with this time scale.

The second decay is longer and depends on frequency. At higher frequencies the absorption by

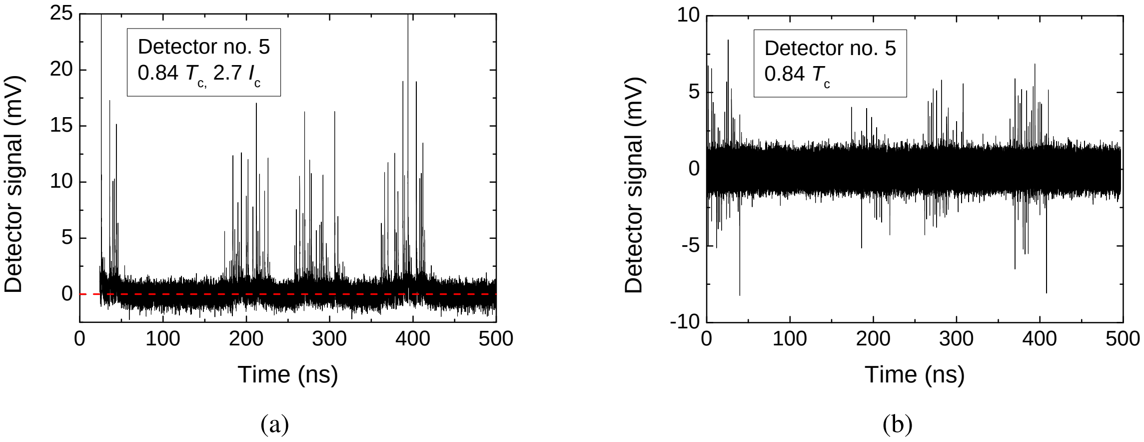

Fig. 7.13: Detector response of detector no. 5 in multi-bunch operation at ANKA. (a) The biased operation reveals a plateau from phonon heating in the detecting element, which is not seen during zero-bias operation, see (b).

the silicon lens and, more importantly, the sapphire substrate increases. Thereby, conventional heating of the substrate itself and an increased substrate (bath) temperature, driving the YBCO detector further in the resistive state, could be the source of the longer decay time. Similar behavior was observed by Nebosis *et al.* for YBCO films on MgO substrates and a radiation frequency of 30 THz [152]. Likewise, Semenov *et al.* found increased response times upon raising the radiation power level at THz frequencies between 0.8 THz and 30 THz [153]. It should be noted that at a frequency of 6.5 THz, the longer nanosecond scaled decay was seen at all operation points, even at low temperatures and small coupled radiation power levels.

The extinction of the nanosecond-scaled bolometric detector response at lower temperatures and bias levels, as well as the non-occurrence of a bolometric signal upon excitation of µm-sized YBCO detectors with pulsed broadband radiation at ANKA ($f < 1$ THz) in previous works [14], can still be explained within the two-temperature model. Assuming that the operation point of the detector is selected such that the phonon temperature does not exceed T_c at any time, the bolometric component is not displayed in the detector response. However at ANKA, where the repetition rate of THz pulses in multi-bunch operation is 500 MHz, the phonon system has not yet relaxed to the ambient bath temperature upon absorption of the subsequent THz signal. Therefore, the temperature of the phonon system is gradually increased from pulse to pulse and at some point exceeds the critical temperature T_c. This effect is depicted in Fig. 7.13(a) for detector no. 5 (see Tab. 6.1) where the detector response in between the individual pulses does not relax back to the zero level (indicated by the dashed line). Similar behavior was observed for µm-sized YBCO detectors with a YBCO film thickness of 15 nm operated at a current level of $I_b \approx 2I_c$ [216]. As opposed to that, the zero-bias response of detector no. 5 in Fig. 7.13(b) does not show the plateau-

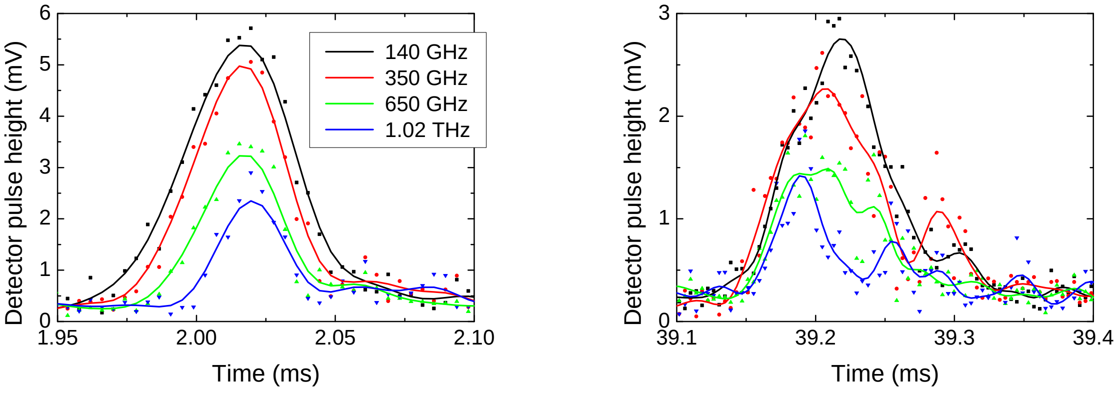

(a) (b)

Fig. 7.14: Bursting CSR at the Diamond Light Source recorded with a four-pixel array of sub-µm-sized YBCO detectors. Different bursting schemes are depicted in (a) and (b). Both bursts were recorded within the same signal trace at a constant operation point of the detector array ($T = 0.93\ T_c$).

like behavior.

The analysis of the biased operation mode of the detectors thus points to a heating of quasiparticles which are present at all relevant operation temperatures. Subsequent relaxation to the phonon system and cooling of the phonon system can be seen under certain operation conditions where the phonon temperature exceeds the critical temperature of the detector.

7.5 Sensitive YBCO detector arrays for single-shot THz spectroscopy

For the sub-µm-sized YBCO detectors, increased sensitivities for pulsed and continuous-wave operation were found. As discussed in section 7.1, the sensitivity to pulsed radiation increased by almost one order of magnitude to approximately 1V/pJ as compared to µm-sized YBCO detectors used in previous works. As the power-dependent sensitivity is a well-established number to characterize detector performance of direct detectors, the sensitivity to continuous-wave excitations was determined with the setup introduced in section 7.3.2. The electrical sensitivity for detector no. 3 (see Tab. 6.1) was found to amount to 710 V/W which is a factor of two higher than the electrical sensitivity of a µm-sized YBCO detector [TRS$^+$13].

Single-shot detection with an array of four YBCO detectors embedded in narrowband antennas was thus first demonstrated by the use of sub-µm-sized detecting elements in biased operation mode at the MIRIAM beamline of the Diamond Light Source (DLS) [RSK$^+$16]. The design of the array was introduced in section 3.4. The YBCO film thickness amounted to $t_{\mathrm{YBCO}} = 30$ nm and the lateral dimensions of the detecting elements were $w \approx 2$ µm and $l = 150 - 170$ nm. For the operation of the array, a liquid-nitrogen bath cryostat was employed corresponding to an operation

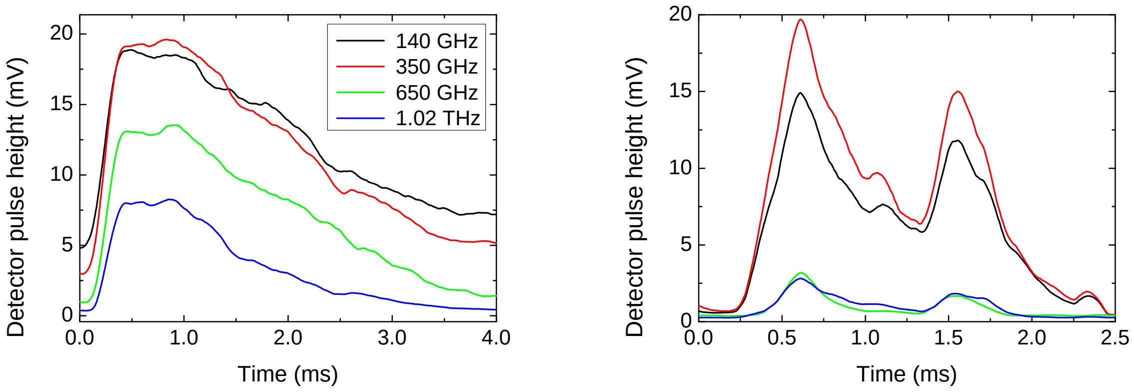

(a) (b)

Fig. 7.15: Bursting CSR at ANKA recorded with the same four-pixel array as in Fig. 7.14. Different bursting schemes are depicted in (a) and (b). Both bursts were recorded within the same signal trace at a constant operation point of the detectors in the array ($T = 0.93\ T_c$).

temperature of 0.93 Tc.

The synchrotron was operated in short-bunch mode with a bunch length of 8.2 ps (FWHM) and a bunch current of 50 µA. For two individual bursts of THz radiation Figs. 7.14(a) and 7.14(b) show the single-shot peak signal recorded with the four detectors simultaneously. The detection system sensitivity S_{opt} is sufficient to detect the CSR signal signal in the frequency range of 140 GHz to 1 THz. In the first burst (Fig. 7.14(a)), the low frequencies appear when the bunch first starts to compress, whereas the higher frequencies start to burst later. This behavior is evident from a model which views the bunch as a repeatedly compressing and decompressing structure. In contrast, in Fig. 7.14(b) a different kind of burst is seen where initially all four frequencies appear simultaneously but the higher frequencies decline first. Moreover, the overall signal height is smaller.

Similar experiments were performed at the IR2 beamline of ANKA with the same detector array. Two different types of bursts are depicted in Figs. 7.15(a) and 7.15(b). Here, the bursts differ from each other not only in temporal evolution but also in frequency content. The higher frequencies are less pronounced in the second burst, which is shown in Fig. 7.15(b). The time scale is different from the bursts seen at DLS. At DLS, the duration of the bursts of ≈ 150 µs corresponds to 75 revolutions of the electron bunch, while at ANKA the burst extends over several milliseconds, which translates into almost 10.000 revolutions of the bunch [21, 22].

The frequency-dependent behavior of the bursts at wavelengths shorter than the overall bunch length is a direct consequence of the micro-bunching phenomenon. From the above-presented measurements, the need for single-shot spectroscopic resolution of bursting CSR in short-bunch mode becomes evident.

7.6 Conclusions of chapter 7

This chapter reviewed the behavior of the YBCO detectors in biased operation mode when excited with pulsed or continuous-wave THz signals, where the first two sections discussed the influence of the operation point on the detector response. The highest sensitivity of the detector was found at the temperature where the current-voltage characteristic exhibits a plateau and the differential resistance of the detector becomes maximum, both for CW and for pulsed signals. This behavior is consistent with a bolometric nature of the detector response. The sensitivity of YBCO detectors with different lateral dimensions can be fitted to the relation given in equation 2.7 for the sensitivity of a bolometer to pulsed excitations.
The bias current did not show the same influence on the detector response as the RF current induced by the absorbed THz signal. For zero-bias operation (see chapter 6), a square-law dependence of the response on induced RF current was observed, indicating flux flow. In biased operation mode, the same linear trend of the detector response vs. THz power was seen. However, the influence of the bias current on the detector response exhibits exponents well above $n = 2$ for power-law fits of the detector-signal height, and the results point towards a bolometric detection scheme. This implies different mechanisms of influence of the RF and DC currents.

Continuous-wave excitation of a sub-µm-sized YBO detector was investigated at different operation temperatures. The dependence of the detector signal on bias current could be explained by a purely bolometric model. Moreover, a comparison of the data recorded at a narrowband pulsed THz source at different power levels with the CW measurements revealed similar behavior of the detector in both regimes. The detector signal vs. bias current shows a power-law dependence with decreasing exponent, when saturating the detector, e.g. by increasing the operation temperature or the power level.
The discussion of the shape of the detector response revealed a picosecond-scaled pulse followed by a bolometric decay which was present at all frequencies above 1.3 THz. A superposition of a phonon escape and a longer time scale of supposedly substrate heating was extracted from exponential fits of the data. At lower frequencies, for broadband THz excitations with a repetition rate of 500 MHz, a plateau in the detector response was found, revealing the bolometric nature of the detector response, even at frequencies far below the superconducting energy gap.

In biased mode, a maximum sensitivity of 1.06 V/pJ was determined from measurements of the absolute THz power at the ANKA IR1 beamline. Sensitive detector arrays based on sub-µm-sized YBCO detecting elements were then used at the synchrotron storage rings ANKA and DLS in short-bunch operation mode for the first successful demonstration of single-shot spectroscopy. Different shapes of bursts, due to the micro-bunching instability, were observed.

8 Summary and outlook

In this work, direct THz detectors based on thin films of the high-temperature superconductor $YBa_2Cu_3O_{7-x}$ were developed and investigated in a wide temperature and THz frequency range regarding their biased and non-biased behavior. Deposition as well as patterning procedures were optimized towards a minimization of the volume of the detecting element reaching film thicknesses of 11.7 nm and lateral dimensions of 150 nm × 800 nm. The response of the detector to pulsed and continuous THz radiation revealed distinct characteristics in the zero-bias and biased operation mode. Herein, the sensitivity of the zero-biased YBCO detector to the direction of the electrical field is a unique quality which enables a comprehensive analysis of Coherent Synchrotron Radiation in bursting mode.

This work was motivated by two major goals:

- In previous studies, the response of µm-sized YBCO detectors to pulsed THz radiation exhibited characteristics that qualitatively and quantitatively deviated from the response at optical frequencies and could not be explained by the two-temperature model. A detection mechanism based on the dissipative movement of vortices was suggested under the assumption that the photon energy of CSR from short-bunch operation was too small to break Cooper pairs. In this work, the zero-bias response of the detector as the most prominent feature seen at THz frequencies was further investigated. The detailed analysis of the zero-bias operation mode herein demanded for high detector sensitivities. Moreover, the picture of the biased response was completed by probing the detectors with narrowband THz radiation that extended to frequencies in the range of the superconducting energy gap of the thin films.

- The ever-growing demand for higher sensitivities and faster response times in the area of direct THz detectors motivates the development of a single-shot spectroscopic detection system to circumvent the readout speed limitations imposed by state-of-the-art electronics. As only a part of the CSR spectrum is absorbed by a narrowband antenna, an increase in sensitivity of the embedded YBCO detecting element by about one order of magnitude, as compared to existing µm-sized YBCO detectors, was required.

The first part of this thesis focused on the development of a fabrication process for ultra-sensitive direct YBCO THz detectors. A pulsed-laser deposition system was automated and equipped with a

scanning mirror, thereby improving the layer thickness homogeneity to $\pm4\%$ for the YBCO films on an area of 10×10 mm^2. The implementation of the interval PLD process enabled the deposition of flat layers, and a combined rms roughness of the buffer layers CeO_2 and PBCO of 1.9 nm was achieved. Subsequent deposition of YBCO films with minimal film thicknesses of 11.7 nm yielded critical temperatures of 75.3 K and a value of 87.2 K for a 25 nm thick unpatterned YBCO film was achieved. Measured on top of the YBCO film, the rms roughness amounted to 3.6 nm.
The prerequisite for patterning of the as-deposited films to sub-µm-sized detecting elements was the deposition of a uniform gold film for the antenna and coplanar design. By combining the *in-situ* deposition of an ultra-thin PLD gold film with *ex-situ* sputtering of the main part of the gold film at very low deposition rates, the advantages of the two methods were exploited. Resistivities of the gold film ($\rho = 2.49$ µΩcm) that are comparable with literature values for bulk gold were realized along with low contact resistances to the underlying layers and the best possible layer thickness homogeneity.
Pure argon-ion etching was found to be the optimum procedure to etch detector slits with lateral dimensions as small as 150 nm while preserving the superconducting properties of the unpatterned YBCO film. Thereby, multiple electron-beam lithographies and ion-beam etching steps are the only processes involved in the actual patterning of the detecting element, making the process highly reproducible. As for the definition of the width of the detecting element, the degradation of the side walls due to ion etching was the main challenge and minimal widths of 800 nm were realized. Typical critical temperatures of the readily processed YBCO detectors amount to $83-85$ K, and for 30 nm thick YBCO films, critical current densities of 2.5 MA/cm^2 @ 77 K were found. The current-voltage characteristics were dominated by flux flow at operation points just above the critical current.

In the zero-bias operation mode of the sub-µm-sized YBCO detectors, as well as with an applied bias current, a linear dependence of the detector response on coupled THz power was found and linked to the quadratic trend of the current-voltage characteristic in the flux-flow regime. At the same time, the dependence of the detector response to pulsed THz excitations on an applied bias current did not exhibit quadratic behavior. The influences of the static bias current and the picosecond RF current pulse, induced by the electrical field of the CSR, are thus found to differ.
The sensitivity of the zero-bias response to the phase of the electrical field which would be expected from a detection mechanism based on flux flow was demonstrated over a broad temperature range ($T \geq 0.7\ T_c$), indicating the stability of the detection mechanism within this range. In regard to the magnitude of the energy gap at the relevant temperatures, a contribution of quasiparticle heating can, however, not be excluded as the dominant mechanism of radiation detection. Yet, heating of the phonon system, linked to a hot-electron detection scheme, was not observed in the

zero-bias operation mode.
Accordance of the measured intrinsic detector sensitivity for pulsed THz excitations with a bolometric model of the electrical sensitivity was found for current-biased YBCO detectors. Likewise, the detector response to continuous-wave THz excitations could be fitted by a purely bolometric model. This suggests that the response of the biased YBCO detector to pulsed THz excitations below the energy gap can be explained by heating of quasiparticles. This is supported by the exponential decay of the detector response at frequencies ranging from below the gap up to the estimated gap value in the a-b-plane of YBCO. The time constant of the decay could be correlated with the phonon escape time of the superconducting thin film.

The zero-bias operation mode of the YBCO detector and the associated sensitivity to the phase of the electrical field allowed for the real-time resolution of oscillating spontaneous CSR signals at the UVSOR-III storage ring. Based on these measurements models describing the evolution of the electron bunch inside the accelerator were assessed. This is a unique ability of the YBCO detector.
Advancement in the investigation of bursting instable CSR was achieved by the first turn-by-turn single-shot spectroscopic study of the THz signals emitted at the beamline. To that end, an array of four narrowband YBCO detectors was operated and read out simultaneously on all four channels.
An increase of the intrinsic detector sensitivity to pulsed THz excitations was the premise to these experiments. The improvement in sensitivity of sub-µm-sized detecting elements by one order of magnitude, as compared to µm-sized YBCO detectors, lead to a maximum intrinsic sensitivity for pulsed THz excitations of 1.06 V/pJ.

Future work on the investigation of the detection mechanism for pulsed sub-gap excitations in YBCO will benefit from the emergence of stable linear accelerator sources for brilliant THz radiation. These will enable the investigation of the operation-point dependent detector response at constant radiation-power output levels [217]. Moreover, pulse lengths much shorter than the 15 ps measured at ANKA are emitted, thereby allowing for a thorough analysis of the detector response time.
At the same time, linear accelerators emit at frequencies above the typical spectra seen at synchrotron storage rings, operating in short-bunch mode. Therefore, they demand for detector technologies which are operable up to more than 10 THz. As the absorption in the sapphire substrate increases considerably at frequencies above ≈ 5 THz, a new substrate needs to be selected and optimized for the interval laser ablation of ultra-thin YBCO films. Silicon absorbs by one order of magnitude less radiation power in the frequency range of $5 - 10$ THz [17, pp. 59 - 60]. Moreover, the possibility of integration with CMOS electronics and waveguide structures opens up the road to new detector technologies, such as nanowire single-photon detectors, that can be implemented on the basis of the sub-µm patterning technology for YBCO thin films.

List of Figures

2.1 Spectrum of CSR from low-α_c optics . . . 7
2.2 Simulation of half-cycle pulse . . . 8
2.3 Schematic of the CHG process . . . 9
2.4 Spectral power density and "turn 0" electron density modulation during CHG . . . 10
2.5 Distribution of electrons in the longitudinal phase space for spontaneous CSR . . . 11
2.6 Emitted electrical field for spontaneous CSR . . . 12
2.7 Operation principle of a bolometric detector . . . 16
2.8 Schematic of a hot-electron bolometer . . . 20
2.9 Experimental setup for the observation of the Gouy phase shift . . . 24

3.1 YBCO unit cell . . . 28
3.2 YBCO orthorhombic and tetragonal phase: oxygen depletion and phase diagram . . 29
3.3 Thin-film growth modes . . . 33
3.4 YBCO detectors at optical wavelengths . . . 42
3.5 Schematic of the vortex-flow response in YBCO THz detectors . . . 45
3.6 Detecting element embedded in planar antenna . . . 46
3.7 Broadband logarithmic-spiral antennas . . . 47
3.8 Narrowband double-slot antennas . . . 49
3.9 Reflection parameters of narrowband double-slot antenna array . . . 50

4.1 PLD system at IMS . . . 54
4.2 PLD vacuum chamber . . . 55
4.3 LabVIEW workspace for semi-automated processes . . . 56
4.4 LabVIEW block diagram . . . 57
4.5 Multi-layer stack for the detector fabrication . . . 59
4.6 Dependence of the deposition rate on the number of laser pulses . . . 61
4.7 Layer thickness homogeneity with oscillating piezoelectric mirror . . . 61
4.8 Dependence of the critical temperature on the position of the substrate . . . 62
4.9 Critical temperature and transition width vs. thickness of the CeO_2 buffer layer . . 63
4.10 AFM images of the CeO_2 buffer layer . . . 63
4.11 AFM line scans for different CeO_2 film thicknesses . . . 64

4.12 XRD characterization of the CeO_2 buffer layer 64
4.13 Occurrence of CuO precipitates during the growth of PBCO and YBCO 65
4.14 θ-2θ scan of CeO_2/PBCO/YBCO multi-layer stack 66
4.15 SEM pictures of CeO_2/PBCO/YBCO multi-layer stack 67
4.16 SEM pictures of interval-deposited PBCO 68
4.17 SEM pictures of continuously deposited YBCO 69
4.18 Dependence of the critical temperature on the number of pulses per two MLs . . . 70
4.19 Dependence of the critical temperature on the bridge width for *in-situ* and *ex-situ* deposition of gold 71
4.20 SEM pictures of the granular structure for laser ablated and sputtered gold films . . 72
4.21 SEM pictures of the granular structure for different sputtered gold films 73
4.22 Resistivity of DC-magnetron sputtered gold films vs. argon pressure 74

5.1 Definition of the length of the detecting element 78
5.2 Influence of wet-chemical etching on the critical temperature 79
5.3 Influence of argon-ion bombardment on the critical temperature 80
5.4 SEM images of slit dimensions etched with different etching techniques 82
5.5 Critical temperature depending on the bridge width 83
5.6 Critical current density depending on the operation temperature 84
5.7 Schematic of the patterning process for YBCO THz detectors 85
5.8 SEM images of the YBCO THz detector fabrication 87
5.9 $R(T)$ characteristic of YBCO THz detector 88
5.10 Critical current density of YBCO THz detector 89

6.1 YBCO detection system for pulsed THz excitations 91
6.2 Cryogenic concepts 92
6.3 Cold plate with detector block and bias source 93
6.4 Termination of the DC port for zero-bias operation 94
6.5 Multi-pixel copper detector blocks 95
6.6 Off-centered antenna elements in the detector array 97
6.7 Bursting THz signal at ANKA 98
6.8 Zero-bias response of detector no. 1 for different operation temperatures 100
6.9 Dependence of the averaged zero-bias pulse height on temperature 100
6.10 Dependence of the detector response on electrical field strength 101
6.11 Dependence of the zero-bias detector response on the $I(V)$ curve 102
6.12 Dependence of the detector response on the critical current 103
6.13 Dependence of the detector response on absolute THz power 103

6.14 Zero-bias response to a broadband pulsed THz excitation 104
6.15 UVSOR-III: simulated electrical field vs. measured detector signal 105
6.16 Measured long-time evolution of the electrical field during spontaneous emission of CSR 106
6.17 Narrowband zero-bias response depending on frequency 107
6.18 Gouy phase shift setup for bursting CSR 108
6.19 Signal traces recorded with the Gouy phase-shift setup 109
6.20 Analysis of the electrical-field sensitivity depending on temperature 110

7.1 Dependence of the detector response on bias current for different temperatures . . . 114
7.2 $I(V)$ characteristics of detector no. 2 114
7.3 Electrical sensitivity of detector no. 4 at different temperatures 115
7.4 Dependence of the electrical sensitivity on detector volume 116
7.5 Dependence of the detector response on coupled electrical field and temperature . . 117
7.6 Dependence of the biased detector response on the power level 118
7.7 Dependence of the detector response on the THz frequency 120
7.8 Measurement setup for continuous-wave THz excitations 121
7.9 Detector response to continuous-wave excitations at 290 GHz 121
7.10 Frequency-dependent response at the operation temperature of maximum sensitivity 122
7.11 Measured pulse shapes at 1.3 THz under different operation conditions 123
7.12 Dependence of the pulse shape on CSR frequency 124
7.13 Detector response in multi-bunch operation mode at ANKA 125
7.14 Bursting CSR at DLS recorded with a four-pixel array 126
7.15 Bursting CSR at ANKA recorded with a four-pixel array 127

List of Tables

2.1 Overview of direct THz detectors 22

3.1 Laser-deposition parameters 37
3.2 Parameters for interval deposition 38
3.3 Narrowband-antenna parameters 51

4.1 Overview of materials for the multi-layer stack 60

6.1 Detector overview: DC characteristics and dimensions 99

Nomenclature

Abbreviations

2T	two-temperature model
AFM	atomic-force microscopy
ANKA	Ångström source Karlsruhe
BCS	Bardeen Cooper Schrieffer (theory)
BESSY	Berliner Elektronenspeicherring-Gesellschaft für Synchrotronstrahlung
CHG	coherent harmonic generation
CDR	coherent diffraction radiation
CPW	coplanar waveguide
CSR	coherent synchrotron radiation
CTR	coherent transmission radiation
CW	continuous wave
DELTA	Dortmunder Elektronenspeicherring-Anlage
DLS	Diamond light source
DR	dynamic range
EBL	electron-beam lithography
EDX	energy dispersive X-ray spectroscopy
ELBE	Elektronen Linearbeschleuniger mit hoher Brillianz und geringer Emittanz
EOSD	electro-optical spectral decoding
FEL	free-electron laser
FELBE	FEL at ELBE
FFT	fast Fourier transform
FIB	focused ion beam
FTIR	Fourier transform infrared spectroscopy
FWHM	full width at half maximum
HDPE	high-density polyethylene
HEB	hot-electron bolometer
HTSC	high-temperature superconductor

IBE	ion-beam etching
IR1/IR2	IR/THz beamlines at ANKA
MIRIAM	B22 multimode infrared imaging and microspectroscopy beamline at DLS
ML	monolayer
LIA	lock-in amplifier
linac	linear particle accelerator
NEP	noise-equivalent power
PBCO	$PrBa_2Cu_3O_{7-x}$, praseodymium barium copper oxide
PCA	photoconductive antenna
PLD	pulsed-laser deposition
PMMA	poly(methyl methacrylate)
PVD	physical vapor deposition
RHEED	reflection high-energy electron diffraction
SEM	scanning electron microscopy
SBD	Schottky-barrier diode
SNR	signal-to-noise ration
TPX	polymethylpentene
UHV	ultra-high vacuum
UVSOR-III	ultra-violet synchrotron orbital radiation
VI	LabVIEW virtual instrument
XRD	X-ray diffraction
YBCO	$YBa_2Cu_3O_{7-x}$, yttrium barium copper oxide

Symbols

a,b,c	lattice parameters
A_L	laser spot area
α	temperature coefficient of resistance, angle between the electrical THz field and the polarization of the antenna
α_c	momentum compaction factor
B_c1	first critical magnetic field
B_c2	second critical magnetic field
c_S	specific heat capacity
C	heat capacity
C_e	electron heat capacity
C_p	phonon heat capacity

d_{TS}	target-to-substrate distance
D_{S}	diffusion coefficient of adatoms
Δ	superconducting energy gap
ΔT	superconducting transition width
E_{L}	laser energy
$\vec{E}_{\mathrm{coupl}}$	coupled electrical field of THz radiation
$\vec{E}_{\mathrm{THz}}$	electrical field of THz radiation
$\vec{E}_{\mathrm{t}}$	electrical field of THz radiation transmitted at wire grid
f	frequency, focal length
f_{eff}	effective readout bandwidth
f_{i}	upper readout bandwidth limits of the individual components in the RF readout path
f_{L}	laser repetition rate
f_{rep}	repetition rate of electron bunches at accelerator sources
f_{sc}	superfluid density
f_{λ}	form factor of electron bunch
F_{Ar}	argon flow
F_{O2}	oxygen flow
G	thermal conductance
G_{eff}	effective thermal conductance
γ	anisotropy parameter
h	height
h_{c}	critical thickness for ML growth
I	current
I_{b}	bias current
I_{c}	critical current
I_{dep}	deposition current
I_{h}	hysteresis current
I_{RF}	RF current
I_{+}	current at the positive grid of the IBE system
j_{c}	critical current density
K	power coupling coefficient of Gaussian beams
l	length of detecting element, length of antenna arms
l_{D}	diffusion length of adatoms
l_{T}	terrace width

l_0	electron mean free path
L_{kin}	kinetic inductance
L_0	orbit length
λ	wavelength
$\lambda_{\mathrm{ab,\,c}}$	magnetic penetration depth in the *ab*-plane or *c*-direction
λ_{eff}	Pearl length
λ_{min}	low-frequency cut-off of vacuum tube
m	supersaturation during PVD
$m_{\mathrm{ab,\,c}}$	effective mass in the *ab*-plane or *c*-direction
n_{I}	number of intervals
n_{P}	pulses per ML
n_{S}	density of Cooper pairs
N_{e}	number of electrons in bunch
η	power coupling efficiency, absorptivity, viscous damping coefficient
p_0	momentum of electron in circular accelerator
p_{ann}	annealing oxygen pressure
p_{Ar}	argon partial pressure
p_{O2}	oxygen partial pressure
P	power
P_{e}	power emitted by a single electron
P_{RF}	RF power
P_{THz}	THz power
Φ_{G}	Gouy phase shift
r_{dep}	deposition rate
r_{e}	deposition rate at thermal equilibrium
R	resistance
R_{n}	normal-state resistance
R_{q}	rms roughness
ρ	resistivity, bending radius of vacuum chamber
S	sensitivity
S_{el}	electrical sensitivity
S_{opt}	optical sensitivity
$\lvert\underline{S}_{11}\rvert$	reflection parameter
$\lvert\underline{S}_{21}\rvert$	crosstalk
σ	rms bunch length

t	time, reduced temperature, film thickness
t_{dep}	deposition time
t_{eff}	effective YBCO film thickness
t_{etch}	etching time
t_{idle}	idle time between two intervals
T	temperature, transmission
T_{b}	operation (bath) temperature
T_{c}	critical temperature
T_{e}	electron temperature
T_{p}	phonon temperature
T_{Sub}	substrate temperature
τ	response or relaxation time, diffusion time
τ_{ee}	electron-electron interaction time
τ_{ep}	electron-phonon interaction time
τ_{esc}	phonon escape time
τ_{FWHM}	pulse width (FWHM)
τ_{in}	inelastic electron scattering time
τ_{pe}	phonon-electron interaction time
τ_{rise}	rise time
U	voltage
$\lvert U_{\mathrm{max}} \rvert$	averaged maximum detector signal
v_{c}	critical velocity
V	volume
V_{+}	potential at the positive grid of the IBE system
V_{+}	potential at the negative grid of the IBE system
V_{n}	noise voltage
w	width of detecting element, width of antenna arm, Gaussian beam waist
w_{L}	laser energy density
w_{slot}	slot width of CPW
ω	modulation frequency of radiation
x, y, z	geometrical coordinates
$\xi_{\mathrm{ab,\,c}}$	coherence length in the *ab*-plane or *c*-direction
Z_{a}	antenna impedance
Z_{d}	detector impedance
z_{R}	Rayleigh range

Bibliography

[1] B. M. Fischer, M. Walther, and P. U. Jepsen. Far-infrared vibrational modes of DNA components studied by terahertz time-domain spectroscopy. *Physics in Medicine and Biology*, 47(21):3807, 2002.

[2] U. Schade, M. Ortolani, and J. Lee. Technical report: THz experiments with Coherent Synchrotron Radiation from BESSY II. *Synchrotron Radiation News*, 20(5):17–24, 2007.

[3] T. May, G. Zieger, S. Anders, V. Zakosarenko, M. Starkloff, H.-G. Meyer, G. Thorwirth, and E. Kreysa. Passive stand-off terahertz imaging with 1 hertz frame rate. In *SPIE Defense and Security Symposium*, pages 69490C–69490C. International Society for Optics and Photonics, 2008.

[4] D. Arnone, C. Ciesla, and M. Pepper. Terahertz imaging comes into view. *Physics World*, 13(4):35, 2000.

[5] M. Abo-Bakr, J. Feikes, K. Holldack, P. Kuske, W. B. Peatman, U. Schade, G. Wüstefeld, and H.-W. Hübers. Brilliant, coherent far-infrared (THz) synchrotron radiation. *Physical Review Letters*, 90(9):094801, 2003.

[6] A.-S. Müller. Accelerator-based sources of infrared and terahertz radiation. *Reviews of Accelerator Science and Technology*, 3(01):165–183, 2010.

[7] A. Rogalski and F. Sizov. Terahertz detectors and focal plane arrays. *Opto-electronics Review*, 19(3):346–404, 2011.

[8] A. D. Semenov, H.-W. Hübers, K. S. Il'in, M. Siegel, V. Judin, and A.-S. Müller. Monitoring coherent THz-synchrotron radiation with superconducting NbN hot-electron detector. In *2009 34th International Conference on Infrared, Millimeter, and Terahertz Waves*, pages 1–2. IEEE, 2009.

[9] P. Thoma, A. Scheuring, M. Hofherr, S. Wünsch, K. Il'in, N. Smale, V. Judin, N. Hiller, A.-S. Müller, A. Semenov, H.-W. Hübers, and M. Siegel. Real-time measurement of picosecond THz pulses by an ultra-fast $YBa_2Cu_3O_{7-d}$ detection system. *Applied Physics Letters*, 101(14):142601, 2012.

[10] G. Stupakov and S. Heifets. Beam instability and microbunching due to coherent synchrotron radiation. *Physical Review Special Topics – Accelerators and Beams*, 5(5):054402, 2002.

[11] M. Gensch. Super-radiant linac-based THz sources in 2013. *Proceedings of the 35th International Free-Electron Laser Conference*, 2013.

[12] M. Lindgren, M. Currie, C. Williams, T. Y. Hsiang, P. M. Fauchet, R. Sobolewski, S. H. Moffat, R. A. Hughes, J. S. Preston, and F. A. Hegmann. Intrinsic picosecond response times of Y–Ba–Cu–O superconducting photodetectors. *Applied Physics Letters*, 74(6):853–855, 1999.

[13] A. D. Semenov, G. N. Gol'tsman, and R. Sobolewski. Hot-electron effect in superconductors and its applications for radiation sensors. *Superconductor Science and Technology*, 15(4):R1, 2002.

[14] P. Probst, A. Semenov, M. Ries, A. Hoehl, P. Rieger, A. Scheuring, V. Judin, S. Wünsch, K. Il'in, N. Smale, Y.-L. Mathis, R. Müller, G. Ulm, G. Wüstefeld, H.-W. Hübers, J. Hänisch, B. Holzapfel, M. Siegel, and A.-S. Müller. Nonthermal response of $YBa_2Cu_3O_{7-\delta}$ thin films to picosecond THz pulses. *Physical Review B*, 85(17):174511, 2012.

[15] P. Thoma. *Ultra-fast $YBa_2Cu_3O_{7-x}$ detectors for the THz frequency range*. PhD thesis, Institut für Mikro- und Nanoelektronische Systeme, Karlsruher Institut für Technologie (KIT), 2013.

[16] M. Abo-Bakr, J. Feikes, K. Holldack, G. Wüstefeld, and H.-W. Hübers. Steady-state far-infrared coherent synchrotron radiation detected at BESSY II. *Physical Review Letters*, 88(25):254801, 2002.

[17] E. Bründermann, H.-W. Hübers, and M. F. Kimmitt. *Terahertz Techniques*, volume 151 of *Springer Series in Optical Sciences*. Springer, 2012.

[18] A. Novokhatski. Coherent synchrotron radiation: theory and simulations. *ICFA Beam Dynamics Newsletter*, 57:127–144, 2012.

[19] G. Wüstefeld. Short bunches in electron storage rings and coherent synchrotron radiation. In *Proceedings of the 11th European Particle Accelerator Conference*, pages 26–30, 2008.

[20] N. Hiller, A. Borysenko, E. Hertle, V. Judin, B. Kehrer, S. Marsching, A.-S. Müller, and M. J. Nasse. Status of single-shot EOSD measurement at ANKA. In *Proceedings of the 5th International Particle Accelerator Conference*, 2014.

[21] J. L. Steinmann, M. Brosi, E. Bründermann, M. Caselle, E. Hertle, N. Hiller, B. Kehrer, A.-S. Müller, P. Schönfeldt, M. Schuh, P. Schütze, M. Schwarz, and J. Hesler. Non-interferometric spectral analysis of synchrotron radiation in the THz regime at ANKA. In *Proceedings of the 6th International Particle Accelerator Conference*, 2015.

[22] Machine parameters of DLS. `http://www.diamond.ac.uk/Science/Machine.html`. Accessed: 2016-11-16.

[23] P. Schoenfeldt, N. Hiller, V. Judin, and A.-S. Müller. Comparison of different approaches to determine the bursting threshold at ANKA. *Verhandlungen der Deutschen Physikalischen Gesellschaft*, 2013.

[24] I. P. S. Martin, C. A. Thomas, and R. Bartolini. Modelling the steady state CSR emission in low alpha mode at the DIAMOND storage ring. *Proceedings of the 3rd International Particle Accelerator Conference*, 4:6, 2012.

[25] A. Plech, S. Casalbuoni, B. Gasharova, E. Huttel, Y. L. Mathis, A.-S. Müller, K. Sonnad, A. Bartels, and R. Weigel. Electro-optical sampling of terahertz radiation emitted by short bunches in the ANKA synchrotron. *Proceedings of the 23rd Particle Accelerator Conference*, pages 1150–1152, 2009.

[26] E. J. Jaeschke, S. Khan, J. R. Schneider, and J. Hastings. *Synchrotron Light Sources and Free-Electron Lasers: Accelerator Physics, Instrumentation and Science Applications*. Switzerland: Springer Reference, 2016.

[27] P. Ungelenk. *Generation and detection schemes for laser-induced coherent terahertz radiation at the electron storage ring DELTA*. PhD thesis, Technische Universität Dortmund, 2015.

[28] S. Bielawski, C. Evain, T. Hara, M. Hosaka, M. Katoh, S. Kimura, A. Mochihashi, M. Shimada, C. Szwaj, and T. Takahashi. Tunable narrowband terahertz emission from mastered laser–electron beam interaction. *Nature Physics*, 4(5):390–393, 2008.

[29] M. Adachi, H. Zen, T. Konomi, J. Yamazaki, K. Hayashi, and M. Katoh. Design and construction of UVSOR-III. *Journal of Physics: Conference Series*, 425(4):042013, 2013.

[30] M. Hosaka, N. Yamamoto, Y. Takashima, C. Szwaj, M. Le Parquier, C. Evain, S. Bielawski, M. Adachi, H. Zen, T. Tanikawa, S. Kimura, M. Katoh, M. Shimada, and T. Takahashi. Saturation of the laser-induced narrowband coherent synchrotron radiation process: Experimental observation at a storage ring. *Physical Review Special Topics – Accelerators and Beams*, 16(2):020701, 2013.

[31] M. Labat, M. Hosaka, A. Mochihashi, M. Shimada, M. Katoh, G. Lambert, T. Hara, Y. Takashima, and M. E. Couprie. Coherent harmonic generation on UVSOR-II storage ring. *The European Physical Journal D*, 44(1):187, 2007.

[32] Y. Takashima, M. Katoh, M. Hosaka, A. Mochihashi, S. Kimura, and T. Takahashi. Observation of intense bursts of terahertz synchrotron radiation at UVSOR-II. *Japanese Journal of Applied Physics*, 44(8L):L1131, 2005.

[33] Machine parameters of FELBE. `http://www.hzdr.de/`. Accessed: 2017-01-29.

[34] Machine parameters of TELBE. `http://www.hzdr.de/`. Accessed: 2017-01-29.

[35] G. Berden, A. F. G. van der Meer, S. P. Jamison, B. Steffen, E.-A. Knabbe, B. Schmidt, P. Schmüser, A. M. MacLeod, P. J. Phillips, and W. A. Gillespie. Time resolved single-shot measurements of transition radiation at the THz beamline of FLASH using electro-optic spectral decoding. In *Proceedings of 10th European Particle Accelerator Conference*, pages 1058–1060, 2006.

[36] D. H. Auston. Picosecond optoelectronic switching and gating in silicon. *Applied Physics Letters*, 26(3):101–103, 1975.

[37] M. Tani, M. Herrmann, and K. Sakai. Generation and detection of terahertz pulsed radiation with photoconductive antennas and its application to imaging. *Measurement Science and Technology*, 13(11):1739, 2002.

[38] E. R. Brown, F. W. Smith, and K. A. McIntosh. Coherent millimeter-wave generation by heterodyne conversion in low-temperature-grown GaAs photoconductors. *Journal of Applied Physics*, 73(3):1480–1484, 1993.

[39] S. Kono, M. Tani, P. Gu, and K. Sakai. Detection of up to 20 THz with a low-temperature-grown GaAs photoconductive antenna gated with 15 fs light pulses. *Applied Physics Letters*, 77(25):4104–4106, 2000.

[40] E. R. Brown, K. A. McIntosh, F. W. Smith, K. B. Nichols, M. J. Manfra, C. L. Dennis, and J. P. Mattia. Milliwatt output levels and superquadratic bias dependence in a low-temperature-grown GaAs photomixer. *Applied Physics Letters*, 64(24):3311–3313, 1994.

[41] R. J. Wylde. Installation and operating instructions for the TK terahertz absolute power meter system. Technical report, Tech. rep., Thomas Keating Ltd., Station Mills, Billingshurst, West Sussex, RH14 9SH, England, 2002.

[42] A. Podzorov and G. Gallot. Low-loss polymers for terahertz applications. *Applied Optics*, 47(18):3254–3257, 2008.

[43] Thomas Keating absolute Power Meter. `http://www.terahertz.co.uk/`. Accessed: 2017-01-31.

[44] Microtech Instruments Inc.: THz sensors. `http://mtinstruments.com/THz_Detectors.html`. Accessed: 2017-01-31.

[45] R. W. Whatmore. Pyroelectric devices and materials. *Reports on Progress in Physics*, 49(12):1335, 1986.

[46] D. H. Auston and A. M. Glass. Optical generation of intense picosecond electrical pulses. *Applied Physics Letters*, 20(10):398–399, 1972.

[47] Gentec-EO: Pyroelectric THz sensors. `http://gentec-eo.com/`. Accessed: 2017-01-31.

[48] A. J. Kreisler and A. Gaugue. Recent progress in high-temperature superconductor bolometric detectors: from the mid-infrared to the far-infrared (THz) range. *Superconductor Science and Technology*, 13(8):1235, 2000.

[49] H. Kraus. Superconductive bolometers and calorimeters. *Superconductor Science and Technology*, 9(10):827, 1996.

[50] P. L. Richards. Bolometers for infrared and millimeter waves. *Journal of Applied Physics*, 76(1):1–24, 1994.

[51] J. Nemarich. Microbolometer detectors for passive millimeter-wave imaging. Technical report, DTIC Document, 2005.

[52] G. L. Carr, M. Quijada, D. B. Tanner, C. J. Hirschmugl, G. P. Williams, S. Etemad, B. Dutta, F. DeRosa, A. Inam, T. Venkatesan, and X. Xi. Fast bolometric response by high T_{c} detectors measured with subnanosecond synchrotron radiation. *Applied Physics Letters*, 57(25):2725–2727, 1990.

[53] S. E. Schwarz and B. T. Ulrich. Antenna-coupled infrared detectors. *Journal of Applied Physics*, 48(5):1870–1873, 1977.

[54] D. P. Neikirk, W. W. Lam, and D. B. Rutledge. Far-infrared microbolometer detectors. *International Journal of Infrared and Millimeter Waves*, 5(3):245–278, 1984.

[55] P. W. Kruse. Physics and applications of high-T_c superconductors for infrared detectors. *Semiconductor Science and Technology*, 5(3S):S229, 1990.

[56] J. Clarke, G. I. Hoffer, P. L. Richards, and N.-H. Yeh. Superconductive bolometers for submillimeter wavelengths. *Journal of Applied Physics*, 48(12):4865–4879, 1977.

[57] N. S. Nishioka, P. L. Richards, and D. P. Woody. Composite bolometers for submillimeter wavelengths. *Applied Optics*, 17(10):1562–1567, 1978.

[58] H. T. Nguyen, J. J. Bock, P. Ringold, J. Battle, S. C. Elliott, A. D. Turner, M. Weilert, V. V. Hristov, B. Schulz, K. Ganga, L. Zhang, J. W. Beeman, P. A. R. Ade, and P.C. Hargrave. A report on the laboratory performance of the spectroscopic detector arrays for SPIRE/HSO. In *SPIE Proceedings on Millimeter and Submillimeter Detectors for Astronomy II*, volume 5498, pages 196–207. International Society for Optics and Photonics, 2004.

[59] E. H. Putley. Indium antimonide submillimeter photoconductive detectors. *Applied Optics*, 4(6):649–657, 1965.

[60] G. D. Peskett and B. V. Rollin. Energy exchange between hot carriers and the lattice in indium antimonide. *Proceedings of the Physical Society*, 82(3):467, 1963.

[61] QMC Instruments: InSb HEB. `http://www.terahertz.co.uk/`. Accessed: 2017-02-02.

[62] R. S. Nebosis, A. D. Semenov, Y. P. Gousev, and K. F. Renk. Rigorous analysis of a superconducting hot-electron bolometer mixer: Theory and comparison with experiment. In *Proceedings of the 7th International Symposium on Space Terahertz Technology*, 1996.

[63] D. E. Prober. Superconducting terahertz mixer using a transition-edge microbolometer. *Applied Physics Letters*, 62(17):2119–2121, 1993.

[64] SCONTEL: NbN HEB. `http://www.scontel.ru/terahertz/`. Accessed: 2017-02-03.

[65] A. Van Der Ziel. Infrared detection and mixing in heavily doped Schottky-barrier diodes. *Journal of Applied Physics*, 47(5):2059–2068, 1976.

[66] H. P. Röser, H. W. Hübers, E. Bründermann, and M. F. Kimmitt. Observation of mesoscopic effects in Schottky diodes at 300 K when used as mixers at THz frequencies. *Semiconductor Science and Technology*, 11(9):1328, 1996.

[67] A. J. M. Kreisler. Submillimeter wave applications of submicron Schottky diodes. In *Proceedings of SPIE*, volume 666, pages 51–63. International Society for Optics and Photonics, 1986.

[68] Infrared Instruments: Si bolometers. `http://www.infraredlaboratories.com/`. Accessed: 2017-02-02.

[69] Infrared Laboratories: InSb HEB. `http://www.infraredlaboratories.com/InSb_Hot_e_Bolometers.html`. Accessed: 2017-02-02.

[70] A. D. Semenov, O. Cojocari, H.-W. Hübers, F. Song, A. Klushin, and A.-S. Müller. Application of zero-bias quasi-optical Schottky-diode detectors for monitoring short-pulse and weak terahertz radiation. *IEEE Electron Device Letters*, 31(7):674–676, 2010.

[71] ACST GmbH: Broadband zero-biased SBDs. `http://www.acst.de/`. Accessed: 2017-02-07.

[72] Virginia Diodes, Inc.: Narrowband zero-biased SBDs. `http://vadiodes.com/`. Accessed: 2017-02-07.

[73] C. Sydlo, O. Cojocari, D. Schonherr, T. Goebel, P. Meissner, and H. L. Hartnagel. Fast THz detectors based on InGaAs Schottky diodes. *Frequenz*, 62(5-6):107–110, 2008.

[74] A. Semenov, A. Pohl, H.-W. Hübers, O. Cojocari, M. Sobornytskyy, M. Ries, G. Wüstefeld, A. Hoehl, and R. Müller. Schottky diode detectors for monitoring coherent THz synchrotron radiation pulses. In *Proceedings of the 5th International Particle Accelerator Conference*, 2014.

[75] J. L. Hesler and T. W. Crowe. NEP and responsivity of THz zero-bias Schottky diode detectors. In *2007 Joint 32nd International Conference on Infrared and Millimeter Waves and the 15th International Conference on Terahertz Electronics*, pages 844–845. IEEE, 2007.

[76] P. F. Goldsmith. *Quasioptical systems: Gaussian beam quasioptical propagation and applications*. IEEE press New York, 1998.

[77] A. B. Ruffin, J. V. Rudd, J. F. Whitaker, S. Feng, and H. G. Winful. Direct observation of the Gouy phase shift with single-cycle terahertz pulses. *Physical Review Letters*, 83(17):3410, 1999.

[78] L. G. Gouy. Sur la propagation anomale des ondes. *Comptes rendus de l'Académie des sciences*, 111:33, 1890.

[79] S. Feng and H. G. Winful. Physical origin of the Gouy phase shift. *Optics Letters*, 26(8):485–487, 2001.

[80] J. G. Bednorz and K. A. Müller. Possible high T_c superconductivity in the Ba–La–Cu–O system. *Zeitschrift für Physik B Condensed Matter*, 64(2):189–193, 1986.

[81] M.-K Wu, J. R. Ashburn, C. J. Torng, P. H. Hor, R. L. Meng, L. Gao, Z. J. Huang, Y. Q. Wang, and C. W. Chu. Superconductivity at 93 K in a new mixed-phase Y-Ba-Cu-O compound system at ambient pressure. *Physical Review Letters*, 58(9):908, 1987.

[82] J. D. Jorgensen, B. W. Veal, A. P. Paulikas, L. J. Nowicki, G. W. Crabtree, H. Claus, and W. K. Kwok. Structural properties of oxygen-deficient $YBa_2Cu_3O_{7-\delta}$. *Physical Review B*, 41(4):1863, 1990.

[83] H.-U. Habermeier. Science and technology of cuprate-based high temperature superconductor thin films, heterostructures and superlattices - the first 30 years. *Low Temperature Physics*, 42(10):840–862, 2016.

[84] H. U. Habermeier. Growth of cuprate high temperature superconductor thin films. *Iranian Journal of Physics Research*, 6(3):229–229, 2006.

[85] M. Tinkham. *Introduction to superconductivity*. Courier Corporation, 1996.

[86] T. K. Worthington, W. J. Gallagher, and T. R. Dinger. Anisotropic nature of high-temperature superconductivity in single-crystal $Y_1Ba_2Cu_3O_{7-x}$. *Physical Review Letters*, 59(10):1160, 1987.

[87] D. N. Zheng, A. M. Campbell, J. D. Johnson, J. R. Cooper, F. J. Blunt, A. Porch, and P. A. Freeman. Magnetic susceptibilities, critical fields, and critical currents of Co-and Zn-doped $YBa_2Cu_3O_7$. *Physical Review B*, 49(2):1417, 1994.

[88] K. Krishana, J. M. Harris, and N. P. Ong. Quasiparticle mean free path in $YBa_2Cu_3O_7$ measured by the thermal hall conductivity. *Physical Review Letters*, 75(19):3529, 1995.

[89] K. Kamarás, S. L. Herr, C. D. Porter, N. Tache, D. B. Tanner, S. Etemad, T. Venkatesan, E. Chase, A. Inam, X. D. Wu, M. S. Hegde, and B. Dutta. In a clean high-T_c superconductor you do not see the gap. *Physical Review Letters*, 64(1):84, 1990.

[90] T. Timusk, S. L. Herr, K. Kamarás, C. D. Porter, D. B. Tanner, D. A. Bonn, J. D. Garrett, C. V. Stager, J. E. Greedan, and M. Reedyk. Infrared studies of *ab*-plane oriented oxide superconductors. *Physical Review B*, 38(10):6683, 1988.

[91] T. Timusk and B. Statt. The pseudogap in high-temperature superconductors: an experimental survey. *Reports on Progress in Physics*, 62(1):61, 1999.

[92] D. J. Van Harlingen. Phase-sensitive tests of the symmetry of the pairing state in the high-temperature superconductors - evidence for $d_{x^2-y^2}$ symmetry. *Reviews of Modern Physics*, 67(2):515, 1995.

[93] C. C. Tsuei and J. R. Kirtley. Pairing symmetry in cuprate superconductors. *Reviews of Modern Physics*, 72(4):969, 2000.

[94] H. L. Edwards, J. T. Markert, and A. L. De Lozanne. Energy gap and surface structure of $YBa_2Cu_3O_{7-x}$ probed by scanning tunneling microscopy. *Physical Review Letters*, 69(20):2967, 1992.

[95] G. Deutscher. Andreev–saint-james reflections: A probe of cuprate superconductors. *Reviews of Modern Physics*, 77(1):109, 2005.

[96] E. Polturak, G. Koren, D. Cohen, and E. Aharoni. Measurements of the anisotropy and temperature dependence of the in-plane energy gap in $YBa_2Cu_3O_{7-\delta}$ using andreev reflections. *Physical Review B*, 47(9):5270, 1993.

[97] D. Gustafsson, D. Golubev, M. Fogelström, T. Claeson, S. Kubatkin, T. Bauch, and F. Lombardi. Fully gapped superconductivity in a nanometre-size $YBa_2Cu_3O_{7-\delta}$ island enhanced by a magnetic field. *Nature Nanotechnology*, 8(1):25–30, 2013.

[98] J. C. Loudon and P. A. Midgley. Imaging flux vortices in type II superconductors with a commercial transmission electron microscope. *Ultramicroscopy*, 109(6):700–729, 2009.

[99] A. Andronov, I. Gordion, V. Kurin, I. Nefedov, and I. Shereshevsky. Kinematic vortices and phase slip lines in the dynamics of the resistive state of narrow superconductive thin film channels. *Physica C: Superconductivity*, 213(1-2):193–199, 1993.

[100] G. R. Berdiyorov, M. V. Milošević, and F. M. Peeters. Kinematic vortex-antivortex lines in strongly driven superconducting stripes. *Physical Review B*, 79(18):184506, 2009.

[101] S. G. Doettinger, R. P. Huebener, R. Gerdemann, A. Kühle, S. Anders, T. G. Träuble, and J. C. Villegier. Electronic instability at high flux-flow velocities in high-T_c superconducting films. *Physical Review Letters*, 73(12):1691, 1994.

[102] D. Y. Vodolazov and F. M. Peeters. Rearrangement of the vortex lattice due to instabilities of vortex flow. *Physical Review B*, 76(1):014521, 2007.

[103] S. J. Pennycook, M. F. Chisholm, D. E. Jesson, R. Feenstra, S. Zhu, X. Y. Zheng, and D. J. Lowndes. Growth and relaxation mechanisms of $YBa_2Cu_3O_{7-x}$ films. *Physica C: Superconductivity*, 202(1-2):1–11, 1992.

[104] J. Ye and K. Nakamura. Systematic study of the growth-temperature dependence of structural disorder and superconductivity in $YBa_2Cu_3O_{7-\delta}$ thin films. *Physical Review B*, 50(10):7099, 1994.

[105] Q. Li, X. X. Xi, X. D. Wu, A. Inam, S. Vadlamannati, W. L. McLean, T. Venkatesan, R. Ramesh, D. M. Hwang, J. A. Martinez, and L. Nazar. Interlayer coupling effect in high-T_c superconductors probed by $YBa_2Cu_3O_{7-x}/PrBa_2Cu_3O_{7-x}$ superlattices. *Physical Review Letters*, 64(25):3086, 1990.

[106] J. Triscone, O. Fischer, O. Brunner, L. Antognazza, A. D. Kent, and M. G. Karkut. $YBa_2Cu_3O_7/PrBa_2Cu_3O_7$ superlattices: Properties of ultrathin superconducting layers separated by insulating layers. *Physical Review Letters*, 64(7), 1990.

[107] D. H. Lowndes, D. P. Norton, and J. D. Budai. Superconductivity in nonsymmetric epitaxial $YBa_2Cu_3O_{7-x}/PrBa_2Cu_3O_{7-x}$ superlattices: The superconducting behavior of Cu-O bilayers. *Physical Review Letters*, 65(9):1160, 1990.

[108] T. Frey, C. C. Chi, C. C. Tsuei, T. Shaw, and F. Bozso. Effect of atomic oxygen on the initial growth mode in thin epitaxial cuprate films. *Physical Review B*, 49(5):3483, 1994.

[109] P. R. Willmott and J. R. Huber. Pulsed laser vaporization and deposition. *Reviews of Modern Physics*, 72(1):315, 2000.

[110] G. K. Hubler and D. B. Chrisey. *Pulsed laser deposition of thin films*. New York : J. Wiley, 1994.

[111] P. J. Dobson, B. A. Joyce, J. H. Neave, and J. Zhang. Current understanding and applications of the RHEED intensity oscillation technique. *Journal of Crystal Growth*, 81(1):1–8, 1987.

[112] J. A. Venables, G. D. T. Spiller, and M. Hanbucken. Nucleation and growth of thin films. *Reports on Progress in Physics*, 47(4):399, 1984.

[113] T. Terashima, Y. Bando, K. Iijima, K. Yamamoto, K. Hirata, K. Hayashi, K. Kamigaki, and H. Terauchi. Reflection high-energy electron diffraction oscillations during epitaxial growth of high-temperature superconducting oxides. *Physical Review Letters*, 65(21):2684, 1990.

[114] I. Utke, C. Klemenz, H. J. Scheel, M. Sasaura, and S. Miyazawa. Misfit problems in epitaxy of high-T_c superconductors. *Journal of Crystal Growth*, 174(1):806–812, 1997.

[115] D. G. Schlom, D. Anselmetti, J. G. Bednorz, R. F. Broom, A. Catana, T. Frey, C. Gerber, H.-J. Güntherodt, H. P. Lang, and J. Mannhart. Screw dislocation mediated growth of sputtered and laser-ablated $YBa_2Cu_3O_{7-\delta}$ films. *Zeitschrift für Physik B Condensed Matter*, 86(2):163–175, 1992.

[116] A. Baronnet. Sur les origines des dislocations vis et des spirales de croissance dans les micas. *Journal of Crystal Growth*, 19(3):193–198, 1973.

[117] R. K. Singh, N. Biunno, and J. Narayan. Microstructural and compositional variations in laser-deposited superconducting thin films. *Applied Physics Letters*, 53(11):1013–1015, 1988.

[118] J. Schou. Physical aspects of the pulsed laser deposition technique: the stoichiometric transfer of material from target to film. *Applied Surface Science*, 255(10):5191–5198, 2009.

[119] B. Dam, J. Rector, M. F. Chang, S. Kars, D. G. De Groot, and R. Griessen. Laser ablation threshold of $YBa_2Cu_3O_{6+x}$. *Applied Physics Letters*, 65(12):1581–1583, 1994.

[120] G. Koren, A. Gupta, R. J. Baseman, M. I. Lutwyche, and R. B. Laibowitz. Laser wavelength dependent properties of $YBa_2Cu_3O_{7-\delta}$ thin films deposited by laser ablation. *Applied Physics Letters*, 55(23):2450–2452, 1989.

[121] P. E. Dyer, R. D. Greenough, and P. H. Issa, A .and Key. Spectroscopic and ion probe measurements of KrF laser ablated Y-Ba-Cu-O bulk samples. *Applied physics letters*, 53(6):534–536, 1988.

[122] R. K. Singh and J. Narayan. Pulsed-laser evaporation technique for deposition of thin films: Physics and theoretical model. *Physical Review B*, 41(13):8843, 1990.

[123] H. S. Kim and H. S. Kwok. Correlation between target-substrate distance and oxygen pressure in pulsed laser deposition of $YBa_2Cu_3O_7$. *Applied Physics Letters*, 61(18):2234–2236, 1992.

[124] D. K. Brice, J. Y. Tsao, and S. T. Picraux. Partitioning of ion-induced surface and bulk displacements. *Nuclear Instruments and Methods in Physics Research Section B: Beam Interactions with Materials and Atoms*, 44(1):68–78, 1989.

[125] D. H. A. Blank, G. Koster, G. AJHM Rijnders, E. van Setten, P. Slycke, and H. Rogalla. Epitaxial growth of oxides with pulsed laser interval deposition. *Journal of Crystal Growth*, 211(1):98–105, 2000.

[126] J. Li, W. Peng, K. Chen, Y. Zhang, L. M. Cui, Y. F. Chen, Y. R. Jin, Y. Z. Zhang, and D. N. Zheng. High pressure RHEED study on the initial structure and growth dynamics of $YBa_2Cu_3O_{7-\delta}$ thin films on $SrTiO_3$ (001). *Solid State Communications*, 152(6):478–482, 2012.

[127] D. P. Norton and D. H. Lowndes. Transport properties of ultrathin $YBa_2Cu_3O_{7-\delta}$ layers: Evidence for two-dimensional vortex fluctuations. *Physical Review B*, 48(9):6460, 1993.

[128] M. Lyatti, A. Savenko, and U. Poppe. Ultra-thin $YBa_2Cu_3O_{7-x}$ films with high critical current density. *Superconductor Science and Technology*, 29(6):065017, 2016.

[129] R. Arpaia. *$YBa_2Cu_3O_{7-\delta}$ nanowires to study nanoscale ordering in High-T_c Superdonductors*. PhD thesis, Department of Microtechnology and Nanoscience, Chalmers University of Technology, 2016.

[130] J. Gao, B. B. G. Klopman, W. A. M. Aarnink, A. E. Reitsma, G. J. Gerritsma, and H. Rogalla. Epitaxial $YBa_2Cu_3O_{7-x}$ thin films on sapphire with a $PrBa_2Cu_3O_{7-x}$ buffer layer. *Journal of Applied Physics*, 71(5):2333–2337, 1992.

[131] G. Watson, S. A. Holt, R.-P. Zhao, A. Katsaros, N. Savvides, and S. Myhra. Environmental degradation of $YBa_2Cu_3O_{7-x}$ thin films. analysis by atomic force microscopy. *Physica C: Superconductivity*, 243(1-2):123–133, 1995.

[132] R. Zhao and S. Myhra. Environmental degradation of $YBa_2Cu_3O_{7-x}$. a descriptive and predictive model. *Physica C: Superconductivity*, 230(1-2):75–81, 1994.

[133] H. Behner, K. Rührnschopf, G. Wedler, and W. Rauch. Surface reactions and long time stability of YBCO thin films. *Physica C: Superconductivity*, 208(3-4):419–424, 1993.

[134] S. E. Russek, S. C. Sanders, A. Roshko, and J. W. Ekin. Surface degradation of superconducting $YBa_2Cu_3O_{7-\delta}$ thin films. *Applied Physics Letters*, 64(26):3649–3651, 1994.

[135] H. Schneidewind, F. Schmidl, S. Linzen, and P. Seidel. The possibilities and limitations of ion-beam etching of $YBa_2Cu_3O_{7-x}$ thin films and microbridges. *Physica C: Superconductivity*, 250(1-2):191–201, 1995.

[136] H. Elsner, R. Ijsselsteijn, W. Morgenroth, H. Roth, and H.-G. Meyer. Submicrometer patterning of $YBa_2Cu_3O_{7-x}$. *Microelectronic Engineering*, 41:407–410, 1998.

[137] W. Langheinrich, B. Spangenberg, R. Barth, and H. Kurz. Superconducting submicron bridges fabricated by electron beam lithography and dry etching. *Microelectronic Engineering*, 21(1-4):479–482, 1993.

[138] C. A. J. Damen, H. J. H. Smilde, D. H. A. Blank, and H. Rogalla. Selective epitaxial growth for YBCO thin films. *Superconductor Science and Technology*, 11(5):437, 1998.

[139] N. Bergeal, J. Lesueur, G. Faini, M. Aprili, and J. P. Contour. High T_c superconducting quantum interference devices made by ion irradiation. *Applied Physics Letters*, 89(11):112515, 2006.

[140] N. Curtz, E. Koller, H. Zbinden, M. Decroux, L. Antognazza, Ø. Fischer, and N. Gisin. Patterning of ultrathin YBCO nanowires using a new focused-ion-beam process. *Superconductor Science and Technology*, 23(4):045015, 2010.

[141] C. Peroz, J. C. Villégier, A. F. Dégardin, B. Guillet, and A. J. Kreisler. High critical current densities observed in $PrBa_2Cu_3O_{7-\delta}$/$YBa_2Cu_3O_{7-\delta}$/$PrBa_2Cu_3O_{7-\delta}$ ultrathin film constrictions. *Applied Physics Letters*, 89(14):142502, 2006.

[142] C. Péroz, A. F. Degardin, J.-C. Villegier, and A. J. Kreisler. Fabrication and characterization of ultrathin PBCO/YBCO/PBCO constrictions for hot electron bolometer THz mixing application. *IEEE Transactions on Applied Superconductivity*, 17(2):637–640, 2007.

[143] C. Williams, Y. Xu, R. Adam, M. Darula, O. Harnack, J. Scherbel, M. Siegel, F. A. Hegmann, and R. Sobolewski. Ultrafast YBCO photodetector based on the kinetic-inductive process. *IEEE Transactions on Applied Superconductivity*, 11(1):578–581, 2001.

[144] M. Lindgren, M. Currie, C. A. Williams, T. Y. Hsiang, P. M. Fauchet, R. Sobolewski, S. H. Moffat, R. A. Hughes, J. S. Preston, and F. A. Hegmann. Ultrafast photoresponse in microbridges and pulse propagation in transmission lines made from high-T_c superconducting Y-Ba-Cu-O thin films. *IEEE Journal of Selected Topics in Quantum Electronics*, 2(3):668–678, 1996.

[145] O. Harnack, B. Karasik, W. McGrath, A. Kleinsasser, and J. Barner. Microwave Mixing and IF Bandwidth In Sub-Micron Long High-T_c Hot-Electron Bolometers. In *Proceedings of the 10th International Symposium on Space Terahertz Technology*, 1999.

[146] B. S. Karasik, W. R. McGrath, and M. C. Gaidis. Analysis of a high-T_c hot-electron superconducting mixer for terahertz applications. *Journal of Applied Physics*, 81(3):1581–1589, 1997.

[147] A. D. Semenov, R. S. Nebosis, Y. P. Gousev, M. A. Heusinger, and K. F. Renk. Analysis of the nonequilibrium photoresponse of superconducting films to pulsed radiation by use of a two-temperature model. *Physical Review B*, 52(1):581, 1995.

[148] A. D. Semenov. Transient photoimpedance response of $YBa_2Cu_3O_{7-\delta}$ epitaxial films in the mixed state. *Journal of Experimental and Theoretical Physics*, 89(3):552–558, 1999.

[149] R. G. Ladret, A. F. Degardin, and A. J. Kreisler. Nanopatterning and hot spot modeling of YBCO ultrathin film constrictions for THz mixers. *IEEE Transactions on Applied Superconductivity*, 23(3):2300305–2300305, 2013.

[150] R. G. Ladret, A. J. Kreisler, and A. F. Dégardin. YBCO-constriction hot spot modeling: DC and RF descriptions for HEB THz mixer noise temperature and conversion gain. *IEEE Transactions on Applied Superconductivity*, 25(3):1–5, 2015.

[151] K. S. Ilin and M. Siegel. Microwave mixing in microbridges made from $YBa_2Cu_3O_{7-x}$ thin films. *Journal of Applied Physics*, 92(1), 2002.

[152] R. S. Nebosis, M. A. Heusinger, W. Schatz, K. F. Renk, G. N. Gol'tsman, B. S. Karasik, A. D. Semenov, and G. M. Gershenzon. Ultrafast photoresponse of a structured $YBa_2Cu_3O_{7-\delta}$ thin film to ultrashort FIR laser pulses. *IEEE Transactions on Applied Superconductivity*, 3(1):2160–2162, 1993.

[153] A. D. Semenov, P. T. Lang, K. F. Renk, and I. G. Gogidze. Fast far-infrared to visible light response of a $YBa_2Cu_3O_{7-\delta}$ film measured with subnanosecond radiation pulses. *Solid State Communications*, 80(7):507–510, 1991.

[154] Z. M. Zhang and A. Frenkel. Thermal and nonequilibrium responses of superconductors for radiation detectors. *Journal of Superconductivity*, 7(6):871–884, 1994.

[155] W. Rauch, E. Gornik, G. Sölkner, A. A. Valenzuela, F. Fox, and H. Behner. Microwave properties of $YBa_2Cu_3O_{7-x}$ thin films studied with coplanar transmission line resonators. *Journal of Applied Physics*, 73(4):1866–1872, 1993.

[156] CST Microwave Studio. `http://www.cst.com/products/cstmws`. Accessed: 2017-03-10.

[157] A. Scheuring. *Ultrabreitbandige Strahlungseinkopplung in THz-Detektoren*. PhD thesis, Institut für Mikro- und Nanoelektronische Systeme, Karlsruher Institut für Technologie (KIT), 2013.

[158] E. L. Kollberg, K. S. Yngvesson, Y. Ren, W. Zhang, P. Khosropanah, and J.-R. Gao. Impedance of hot-electron bolometer mixers at terahertz frequencies. *IEEE Transactions on Terahertz Science and Technology*, 1(2):383–389, 2011.

[159] A. D. Semenov, H. Richter, H.-W. Hübers, B. Gunther, A. Smirnov, K. S. Il'in, M. Siegel, and J. P. Karamarkovic. Terahertz performance of integrated lens antennas with a hot-electron bolometer. *IEEE Transactions on Microwave Theory and Techniques*, 55(2):239–247, 2007.

[160] J. D. Kraus and R. D. Marhefka. *Antennas: For all applications*. McGraw Hill, 3 edition, 2003.

[161] J. Ye and K. Nakamura. Relaxation of crystallographic defects in $YBa_2Cu_3O_{7-\delta}$ thin films by heat treatment and its effects on t_c. *Physica C: Superconductivity*, 254(1):113–123, 1995.

[162] P. Sedlmeier. Prozessautomatisierung einer PLD mit LabVIEW. Bachelor thesis, Institut für Mikro- und Nanoelektronische Systeme, Karlsruher Institut für Technologie (KIT), 2014.

[163] E. K. Hollmann, O. G. Vendik, A. G. Zaitsev, and B. T. Melekh. Substrates for high-T_c superconductor microwave integrated circuits. *Superconductor Science and Technology*, 7(9):609, 1994.

[164] T. Konaka, M. Sato, H. Asano, and S. Kubo. Relative permittivity and dielectric loss tangent of substrate materials for high-T_c superconducting film. *Journal of Superconductivity*, 4(4):283–288, 1991.

[165] M. W. Denhoff and J. P. McCaffrey. Epitaxial $YBa_2Cu_3O_7$ thin films on CeO_2 buffer layers on sapphire substrates. *Journal of Applied Physics*, 70(7):3986–3988, 1991.

[166] S. Y. Lee. Characterization of the interface between laser ablated YBCO film and buffered sapphire substrate. *Journal of Alloys and Compounds*, 251(1):41–43, 1997.

[167] M. Maul, B. Schulte, P. Häussler, G. Frank, T. Steinborn, H. Fuess, and H. Adrian. Epitaxial CeO_2 buffer layers for $YBa_2Cu_3O_{7-\delta}$ films on sapphire. *Journal of Applied Physics*, 74(4):2942–2944, 1993.

[168] X. D. Wu, R. C. Dye, R. E. Muenchausen, S. R. Foltyn, M. Maley, A. D. Rollett, A. R. Garcia, and N. S. Nogar. Epitaxial CeO_2 films as buffer layers for high-temperature superconducting thin films. *Applied Physics Letters*, 58(19):2165–2167, 1991.

[169] M. E. Lopez-Morales, D. Rios-Jara, J Tagüea, R. Escudero, S. La Placa, A. Bezinge, V. Y. Lee, E. M. Engler, and P. M. Grant. Role of oxygen in $PrBa_2Cu_3O_{7-y}$: Effect on structural and physical properties. *Physical Review B*, 41(10):6655, 1990.

[170] E. Olsson, A. Gupta, M. D. Thouless, A. Segmüller, and D. R. Clarke. Crack formation in epitaxial [110] thin films of $YBa_2Cu_3O_{7-\delta}$ and $PrBa_2Cu_3O_{7-x}$ on [110] $SrTiO_3$ substrates. *Applied Physics Letters*, 58(15):1682–1684, 1991.

[171] S. R. Foltyn, R. C. Dye, K. C. Ott, E. Peterson, K. M. Hubbard, W. Hutchinson, R. E. Muenchausen, R. C. Estler, and X. D. Wu. Target modification in the excimer laser deposition of $YBa_2Cu_3O_{7-x}$ thin films. *Applied Physics Letters*, 59(5):594–596, 1991.

[172] J. H. Lee, W. I. Yang, H. J. Kwon, V. A. Komashko, and S. Y. Lee. Significant improvements in the surface smoothness of $YBa_2Cu_3O_{7-\delta}$ films on high-temperature annealed CeO_2-buffered r-cut sapphire. *Superconductor Science and Technology*, 13(7):989, 2000.

[173] J. C. Nie, H. Yamasaki, H. Yamada, Y. Nakagawa, and K. Develos-Bagarinao. Self-assembled CeO_2 buffer layers on R-cut sapphire for high-current-density $YBa_2Cu_3O_{7-\delta}$ films. *Superconductor Science and Technology*, 16(7):768, 2003.

[174] T. Haugan, P. N. Barnes, L. Brunke, I. Maartense, and J. Murphy. Effect of O_2 partial pressure on $YBa_2Cu_3O_{7-\delta}$ thin film growth by pulsed laser deposition. *Physica C: Superconductivity*, 397(1):47–57, 2003.

[175] T. I. Selinder, U. Helmersson, Z. Han, J.-E. Sundgren, H. Sjöström, and L. R. Wallenberg. Yttrium oxide inclusions in $YBa_2Cu_3O_x$ thin films: enhanced flux pinning and relation to copper oxide surface particles. *Physica C: Superconductivity*, 202(1-2):69–74, 1992.

[176] R. Krupke, Z. Barkay, and G. Deutscher. A systematic approach to reduce macroscopic defects in c-axis oriented YBCO films. *Physica C: Superconductivity*, 315(1):99–106, 1999.

[177] J. P. Gong, M. Kawasaki, K. Fujito, R. Tsuchiya, M. Yoshimoto, and H. Koinuma. Investigation of precipitate formation on laser-ablated $YBa_2Cu_3O_{7-\delta}$ thin films. *Physical Review B*, 50(5):3280, 1994.

[178] Z. Han, T. I. Selinder, and U. Helmersson. Formation of Cu-rich particles on the surface of $YBa_2Cu_3O_{7-x}$ thin film grown by insitu off-axis sputtering. *Journal of Applied Physics*, 75(4):2020–2025, 1994.

[179] L. Guan, D. M. Zhang, X. Li, and Z. H. Li. Role of pulse repetition rate in film growth of pulsed laser deposition. *Nuclear Instruments and Methods in Physics Research Section B: Beam Interactions with Materials and Atoms*, 266(1):57–62, 2008.

[180] H. A. Wheeler. Formulas for the skin effect. *Proceedings of the IRE*, 30(9):412–424, 1942.

[181] J. Du, S. K. H. Lam, and D. L. Tilbrook. Metallization and interconnection of HTS YBCO thin film devices and circuits. *Superconductor Science and Technology*, 14(10):820, 2001.

[182] J. W. Ekin, S. E. Russek, C. C. Clickner, and B. Jeanneret. In situ noble metal $YBa_2Cu_3O_7$ thin-film contacts. *Applied Physics Letters*, 62(4):369–371, 1993.

[183] D. R. Lide, editor. *CRC handbook of chemistry and physics*. CRC press, 90 edition, 2010.

[184] S. Amari and J. Bornemann. Lse-and lsm-mode sheet impedances of thin conductors. *IEEE Transactions on Microwave Theory and Techniques*, 44(6):967–970, 1996.

[185] R. K. Waits. Planar magnetron sputtering. *Journal of Vacuum Science and Technology*, 15(2):179–187, 1978.

[186] E. Schmiedl, P. Wissmann, and H.-U. Finzel. The electrical resistivity of ultra-thin copper films. *Zeitschrift für Naturforschung A*, 63(10-11):739–744, 2008.

[187] G. Kästle, H.-G. Boyen, A. Schröder, A. Plettl, and P. Ziemann. Size effect of the resistivity of thin epitaxial gold films. *Physical Review B*, 70(16):165414, 2004.

[188] T. A. Green. Gold etching for microfabrication. *Gold Bulletin*, 47(3):205–216, 2014.

[189] W. Eidelloth and R. L. Sandstrom. Wet etching of gold films compatible with high T_c superconducting thin films. *Applied Physics Letters*, 59(13):1632–1634, 1991.

[190] J. Raasch. Untersuchung der Detektion von Terahertzstrahlung in Submikrometer-YBCO-Strukturen. Diploma thesis, Institut für Prozessdatenverarbeitung und Elektronik, Karlsruher Institut für Technologie (KIT), 2012.

[191] Y. Xia, X.-M. Zhao, E. Kim, and G. M. Whitesides. A selective etching solution for use with patterned self-assembled monolayers of alkanethiolates on gold. *Chemistry of Materials*, 7(12):2332–2337, 1995.

[192] Z. Hu and T. Ritzdorf. Cyanide-and thiourea-free electrochemical etching of gold for microelectronics applications. *Journal of the Electrochemical Society*, 154(10):D543–D549, 2007.

[193] C. M. Melliar-Smith. Ion etching for pattern delineation. *Journal of Vacuum Science and Technology*, 13(5):1008–1022, 1976.

[194] ALLRESIST GmbH: PMMA resist and chemicals. `http://www.allresist.de/`. Accessed: 2017-03-21.

[195] MicroChemicals GmbH: photo resists and chemicals. `http://www.microchemicals.com`. Accessed: 2017-03-21.

[196] H. Darhmaoui and J. Jung. Crossover effects in the temperature dependence of the critical current in $YBa_2Cu_3O_{7-\delta}$. *Physical Review B*, 53(21):14621, 1996.

[197] J. Mannhart, P. Chaudhari, D. Dimos, C. C. Tsuei, and T. R. McGuire. Critical currents in [001] grains and across their tilt boundaries in $YBa_2Cu_3O_7$ films. *Physical Review Letters*, 61(21):2476, 1988.

[198] P. Larsson, B. Nilsson, and Z. G. Ivanov. Fabrication and transport measurements of $YBa_2Cu_3O_{7-x}$ nanostructures. *Journal of Vacuum Science & Technology B: Microelectronics and Nanometer Structures Processing, Measurement, and Phenomena*, 18(1):25–31, 2000.

[199] T. H. P. Chang. Proximity effect in electron-beam lithography. *Journal of Vacuum Science and Technology*, 12(6):1271–1275, 1975.

[200] TransMIT GmbH — Zentrum für Adaptive Kryotechnik und Sensorik. *Bedienungsanleitung: Flüssigstickstoff-Kryostat mit optischen Fenstern.*

[201] TransMIT GmbH — Zentrum für Adaptive Kryotechnik und Sensorik. *Bedienungsanleitung: Koaxialer Pulsrohrkühler PT-09b mit Polar SC7 Linearkompressor.*

[202] SHF Communication Technologies AG. `http://www.shf.de/`. Accessed: 2017-04-05.

[203] Rogers Corporation. `http://www.rogerscorp.com/`. Accessed: 2017-04-05.

[204] Keysight Technologies Inc. `http://www.keysight.com/`. Accessed: 2017-04-06.

[205] C. A. Balanis. *Antenna theory: analysis and design.* John Wiley & Sons, 2005.

[206] D. F. Filipovic, G. P. Gauthier, S. Raman, and G. M. Rebeiz. Off-axis properties of silicon and quartz dielectric lens antennas. *IEEE Transactions on Antennas and Propagation*, 45(5):760–766, 1997.

[207] N. Hiller, A. Borysenko, E. Hertle, E. Huttel, V. Judin, B. Kehrer, S. Marsching, A.-S. Müller, M. Nasse, A. Plech, M. Schuh, N. J. Smale, B. Steffen, P. Peier, and V. Schlott. Electro-optical bunch length measurements at the ANKA storage ring. In *Proceedings of the 4th International Particle Accelerator Conference*, pages 500–502, 2013.

[208] M. V. Pedyash, D. H. A. Blank, J. H. de Muijnck, and H. Rogalla. Properties of YBaCuO nanobridges and dc-SQUIDs. *IEEE Transactions on Applied Superconductivity*, 7(2):2764–2767, 1997.

[209] S. A. Kuznetsov, M. A. Astafyev, A. V. Gelfand, and A. V. Arzhannikov. Microstructured frequency selective quasi-optical components for submillimeter-wave applications. In *2014 44th European Microwave Conference*, pages 881–884. IEEE, 2014.

[210] J. E. Sonier, J. H. Brewer, R. F. Kiefl, G. D. Morris, R. I. Miller, D. A. Bonn, J Chakhalian, R. H. Heffner, W. N. Hardy, and R. Liang. Field induced reduction of the low-temperature superfluid density in $YBa_2Cu_3O_{6.95}$. *Physical Review Letters*, 83(20):4156, 1999.

[211] D. B. Tanner, F. Gao, K. Kamarás, H. L. Liu, M. A. Quijada, D. B. Romero, Y.-D. Yoon, A. Zibold, H. Berger, G. Margaritondo, L. Forro, R.J. Kelly, M. Onellion, G. Cao, J. E. Crow, O. Beom-Hoan, J. T. Markert, J. P. Rice, D. M. Ginsberg, and T. Wolf. Superfluid and normal-fluid density in the cuprate superconductors. *Ferroelectrics*, 249(1):175–184, 2001.

[212] F. A. Hegmann and J. S. Preston. Origin of the fast photoresponse of epitaxial $YBa_2Cu_3O_{7-\delta}$ thin films. *Physical Review B*, 48(21):16023, 1993.

[213] P. Probst, A. Scheuring, M. Hofherr, D. Rall, S. Wünsch, K. Ilin, M. Siegel, A. Semenov, A. Pohl, H.-W. Hübers, V. Judin, A.-S. Müller, A. Hoehl, R. Müller, and G. Ulm. $YBa_2Cu_3O_{7-\delta}$ quasioptical detectors for fast time-domain analysis of terahertz synchrotron radiation. *Applied Physics Letters*, 98(4):043504, 2011.

[214] R. C. Jones. The general theory of bolometer performance. *Journal of the Optical Society of America*, 43(1):1–14, 1953.

[215] J.-P. Maneval, K. P. Hong, and F. Chibane. On the response time of $YBa_2Cu_3O_7$ superconducting bolometer films. *Physica C: Superconductivity*, 235:3389–3390, 1994.

[216] P. Probst, A. Scheuring, M. Hofherr, S. Wünsch, K. Ilin, A. Semenov, H.-W. Hübers, V. Judin, A.-S. Müller, J. Hänisch, B. Holzapfel, and M. Siegel. Superconducting $YBa_2Cu_3O_{7-\delta}$ thin film detectors for picosecond THz pulses. *Journal of Low Temperature Physics*, 167(5-6):898–903, 2012.

[217] M. J. Nasse, M. Schuh, S. Naknaimueang, M. Schwarz, A. Plech, Y.-L. Mathis, R. Rossmanith, P. Wesolowski, E. Huttel, M. Schmelling, and A.-S. Müller. FLUTE: A versatile linac-based THz source. *Review of Scientific Instruments*, 84(2):022705, 2013.

Own Publications

[CBC^{+}14a] M. Caselle, M. Brosi, S. Chilingaryan, T. Dritschler, E. Hertle, V. Judin, A. Kopmann, A.-S. Müller, J. Raasch, M. Schleicher, N. J. Smale, J. Steinmann, M. Vogelgesang, S. Wüensch, M. Siegel, and M. Weber. Commissioning of an ultra fast data acquisition system for coherent synchrotron radiation detection. *Proceedings of the 5th International Particle Accelerator Conference*, 2014.

[CBC^{+}14b] M. Caselle, M. Brosi, S. Chilingaryan, T. Dritschler, V. Judin, A. Kopmann, A.-S. Müller, J. Raasch, N. J. Smale, J. Steinmann, M. Vogelgesang, S. Wüensch, M. Siegel, and M. Weber. An ultra-fast digitizer with picosecond sampling time for coherent synchrotron radiation. In *2014 19th IEEE-NPSS Real Time Conference*, pages 1–3. IEEE, 2014.

[MJB^{+}13] A.-S. Müller, V. Judin, M. Balzer, M. Caselle, N. Hiller, M. Hofherr, K. S. Il'in, B. Kehrer, S. Marsching, S. Naknaimueang, M.-J. Nasse, J. Raasch, A. Scheuring, M. Schuh, M. Schwarz, M. Siegel, N. J. Smale, J. Steinmann, P. Thoma, M. Weber, and S. Wünsch. Studies of bunch-bunch interactions in the ANKA storage ring with coherent synchrotron radiation using an ultra-fast terahertz detection system. In *Proceeding of the 4th International Particle Accelerator Conference*, pages 109–111, 2013.

[RES^{+}14a] E. Roussel, C. Evain, C. Szwaj, S. Bielawski, J. Raasch, P. Thoma, A. Scheuring, M. Hofherr, K. S. Ilin, S. Wünsch, M. Siegel, M. Hosaka, N. Yamamoto, Y. Takashima, H. Zen, T. Konomi, M. Adachi, S. Kimura, and M. Katoh. Microbunching instability in relativistic electron bunches: Direct observations of the microstructures using ultrafast YBCO detectors. *Physical Review Letters*, 113(9):094801, 2014.

[RES^{+}14b] E. Roussel, C. Evain, C. Szwaj, S. Bielawski, J. Raasch, P. Thoma, A. Scheuring, K. S. Ilin, M. Siegel, M. Hosaka, N. Yamamoto, Y. Takashima, H. Zen, T. Konomi, M. Adachi, S. Kimura, and M. Katoh. Numerical study of the microbunching instability at UVSOR-III: Influence of the resistive and inductive impedances. In *Pro-*

ceedings of the 5th International Particle Accelerator Conference, pages 1656–1658, 2014.

[RES+15] E. Roussel, C. Evain, C. Szwaj, S. Bielawski, J. Raasch, P. Thoma, A. Scheuring, K. S. Ilin, M. Siegel, M. Hosaka, N. Yamamoto, Y. Takashima, H. Zen, T. Konomi, M. Adachi, S. Kimura, and M. Katoh. Microbunching instability in relativistic electron bunches: Direct observations of the microstructures using ultrafast YBCO detectors. In *Proceedings of the 4th International Beam Instrumentation Conference*, pages 17–21, 2015.

[RIS+14] J. Raasch, K. S. Ilin, A. Scheuring, M. Siegel, P. Thoma, A.-S. Müeller, Y.-L. Mathis, N. J. Smale, B. Holzapfel, K. Iida, S. Bielawski, C. Evain, E. Roussel, C. Szwaj, M. Katoh, S. Kimura, T. Konomi, M. Hosaka, N. Yamamoto, and H. Zen. Electrical field sensitive high-T_c YBCO detector for real-time observation of CSR. In *Proceedings of the 5th International Particle Accelerator Conference*, pages 3533–3536, 2014.

[RKT+15] J. Raasch, A. Kuzmin, P. Thoma, K. S. Ilin, M. Arndt, S. Wünsch, M. Siegel, J. L. Steinmann, A.-S. Müller, E. Roussel, C. Evain, C. Szwaj, S. Bielawski, T. Konomi, S. Kimura, M. Katoh, M. Hosaka, N. Yamamoto, H. Zen, K. Iiida, and B. Holzapfel. Investigation of the Electrical Field Sensitivity of Sub-µm Y–Ba–Cu–O Detectors. *IEEE Transactions on Applied Superconductivity*, 25(3):1–6, 2015.

[RSK+16] J. Raasch, A. Schmid, A. Kuzmin, K. S. Ilin, M. Arndt, S. Wünsch, M. Siegel, J. L. Steinmann, A.-S. Müller, G. Cinque, M. D. Frogley, J. Hänisch, and B. Holzapfel. Single-shot THz spectroscopy for the characterization of single-bunch bursting CSR. In *Proceedings of the 6th International Beam Instrumentation Conference*, pages 778–781, 2016.

[SBB+16a] A. Schmid, M. Brosi, E. Bründermann, K. S. Ilin, B. Kehrer, A. Kuzmin, S. Kuznetsov, A.-S. Müller, J. Raasch, P. Schönfeldt, M. Schuh, M. Siegel, J. L. Steinmann, and S. Wünsch. Single-shot spectral analysis of synchrotron radiation in the THz regime at ANKA. In *Proceedings of 7th International Particle Accelerator Conference*, pages 115–117. JACOW, Geneva, Switzerland, 2016.

[SBB+16b] J. L. Steinmann, E. Blomley, M. Brosi, E. Bründermann, M. Caselle, J. L. Hesler, N. Hiller, B. Kehrer, Y.-L. Mathis, M. J. Nasse, J. Raasch, M. Schedler, P. Schönfeldt, M. Schuh, M. Schwarz, M. Siegel, N. J. Smale, M. Weber, and A.-S. Müller.

Frequency-comb spectrum of periodic-patterned signals. *Physical Review Letters*, 117(17):174802, 2016.

[SRK+16] A. Schmid, J. Raasch, A. Kuzmin, S. Wünsch, and M. Siegel. Integrated four-pixel narrow-band antenna array for picosecond THz spectroscopy. *IEEE Transactions on Applied Superconductivity*, 26(3):1800905, 2016.

[SRK+17] A. Schmid, J. Raasch, A. Kuzmin, J. L. Steinmann, S. Wuensch, M. Arndt, M. Siegel, A.-S. Müller, G. Cinque, and M. D. Frogley. An integrated planar array of ultrafast THz Y–Ba–Cu–O detectors for spectroscopic measurements. *IEEE Transactions on Applied Superconductivity*, 27(4):1–5, 2017.

[TRS+13] P. Thoma, J. Raasch, A. Scheuring, M. Hofherr, K. S. Il'in, S. Wünsch, A. D. Semenov, H.-W. Hübers, V. Judin, A.-S. Müller, N. J. Smale, J. Hänisch, B. Holzapfel, and M. Siegel. Highly responsive Y–Ba–Cu–O thin film THz detectors with picosecond time resolution. *IEEE Transactions on Applied Superconductivity*, 23(3):2400206, 2013.

[UMB+14] P. Ungelenk, C. Mai, L. G. Böttger, S. Hilbrich, M. Höner, H. Huck, M. Huck, S. Khan, A. Meyer auf der Heide, R. Molo, H. Rast, A. Schick, N. Hiller, V. Judin, J. Raasch, P. Thoma, S. Bielawski, C. Evain, C. Le Parquier, E. Roussel, and C. Szwaj. Studies of ultrashort THz pulses at DELTA. In *Proceedings of the 5th International Particle Accelerator Conference*, 2014.

Supervised Student Theses

[Feß16] Jan Feßler. Untersuchung der Einflüsse von Laserablationsparametern auf die Schichtdickenhomogenität von ultra-dünnen PBCO- und YBCO-Filmen. Bachelor thesis, Institut für Mikro- und Nanoelektronische Systeme, Karlsruher Institut für Technologie (KIT), 2016.

[Gan15] Jakob Gantenbein. Optimierung der Pufferschichten für die Herstellung sensitiver $YBa_2Cu_3O_{7-x}$-THz-Detektoren. Bachelor thesis, Institut für Mikro- und Nanoelektronische Systeme, Karlsruher Institut für Technologie (KIT), 2015.

[Kne15] Emanuel Knehr. Herstellung und Optimierung ultra-dünner Multischichtsysteme zur Anwendung in YBCO-Detektoren mittels Laserablation. Bachelor thesis, Institut für Mikro- und Nanoelektronische Systeme, Karlsruher Institut für Technologie (KIT), 2015.

[Koc14] Steffen Koch. Optimierung und Nanostrukturierung ultra-dünner YBCO Schichten zur Herstellung von SNSPDs. Master thesis, Institut für Prozessdatenverarbeitung und Elektronik, Karlsruher Institut für Technologie (KIT), 2014.

[Krä14] Martin Krämer. Strukturierung dicker YBCO-Schichten für Röntgen-SNSPDs. Bachelor thesis, Institut für Mikro- und Nanoelektronische Systeme, Karlsruher Institut für Technologie (KIT), 2014.

[Rot16] Fabian Roth. Entwicklung eines Ätzprozesses für Submikrometer-$YBa_2Cu_3O_{7-x}$-Detektoren für den THz-Frequenzbereich. Bachelor thesis, Institut für Mikro- und Nanoelektronische Systeme, Karlsruher Institut für Technologie (KIT), 2016.

International conferences and workshops

1. J. Raasch, *et al.* Zero-biased YBCO detectors for the real-time detection of coherent synchrotron radiation. *KSETA Plenary Workshop 2017*, Bad Durbach, Germany, 13-15 of February 2017.
2. J. Raasch, *et al.* Real-time observation of ultra-short THz synchrotron radiation pulses. *Invited talk at the Workshop on Detector Technologies for High Energy Physics*, CiS Forschungsinstitut für Mikrosensorik und Photovoltaik GmbH, Erfurt, Germany, 11-15 of November 2016.
3. J. Raasch, *et al.* Single-shot THz spectroscopy for the characterization of single-bunch bursting CSR. *6th International Beam Instrumentation Conference 2016*, Barcelona, Spain, 28-29 of September 2016.
4. J. Raasch, *et al.* Ultra-fast YBCO detectors for single-shot THz spectroscopy of Coherent Synchrotron Radiation. *KSETA Plenary Workshop 2016*, Bad Durbach, Germany, 22-24 of February 2016.
5. J. Raasch, *et al.* Ultra-fast THz detectors for synchrotron radiation. *Invited talk at the WE-Heraeus Seminary on Semiconductor Detectors in Astronomy, Medicine, Particle Physics and Photon Science*, Bad Honeff, Germany, 15-17 of February 2016.
6. J. Raasch, *et al.* Single-shot THz Spectroscopy with Picosecond Time Resolution. *Invited talk at the 8th International Workshop on Infrared Microscopy and Spectroscopy using Accelerator Based Sources*, Long Island, New York, US, 11-15 of October 2015.
7. J. Raasch, *et al.* Picosecond YBCO detection system for Coherent Synchrotron Radiation. *3rd Workshop on Accelerator Research and Development*, Karlsruhe, Germany, 15-17 of July 2015.
8. J. Raasch, *et al.* Ultra-fast high-T_c YBCO Detector for real-time observation of Coherent Synchrotron Radiation. *ANKA Machine Advisory Committee Meeting*, Karlsruhe, Germany, 27th of January 2015.

9. J. Raasch, *et al.* Versatile detector technologies and fast readout electronics: Ultra-fast $YBa_2Cu_3O_{7-x}$ detectors for Coherent Synchrotron Radiation. *Invited talk at the Detector Lab of the PRISMA Excellence Cluster*, Mainz, Germany, 11th of December 2014.
10. J. Raasch, *et al.* Detection of the electrical field of pulsed THz radiation by thin-film YBCO microbridges. *Invited talk at the Applied Superconductivity Conference 2014*, Charlotte, North Carolina, US, 10-15 of August 2014.
11. J. Raasch, *et al.* Fast YBCO detector for real-time resolution of picosecond THz pulses. *3rd Mini-Workshop on Longitudinal Diagnostics for Free-Electron Lasers*, Karlsruhe, Germany, 3-4 of July 2014.
12. J. Raasch, *et al.* Electrical field sensitive high-T_c YBCO detector for real-time observation of CSR. *5th International Particle Accelerator Conference 2014*, Dresden, Germany, 16-20 of June 2014.
13. J. Raasch, *et al.* Ultra-fast YBCO detector for the real-time shot-by-shot observation of the electrical field of CSR. *2nd Workshop on Accelerator Research and Development*, Dresden, Germany, 26-27 of March 2014.
14. J. Raasch, *et al.* 15 ps temporal resolution of the electric field of Coherent Synchrotron Radiation using a high-T_c $YBa_2Cu_3O_{7-x}$ real-time detection system. *7th International Workshop on Infrared Microscopy and Spectroscopy using Accelerator Based Sources*, Lorne, Victoria, Australia, 10-14 of November 2013.
15. J. Raasch, *et al.* Real-time detection system for ultra-short THz pulses using a high-T_c thin $YBa_2Cu_3O_{7-x}$-film detector. *Tagung Kryoelektronische Bauelemente 2013*, Bad Herrenalb, Germany, 6-8 of October 2013.
16. J. Raasch, *et al.* High-T_c YBCO detectors with high sensitivity and broad dynamic range for pulsed THz radiation. *11th European Conference on Applied Superconductivity*, Genova, Italy, 15-19 of September 2013.
17. J. Raasch, *et al.* High-T_c YBCO nanobridges for sensitive THz detectors. *Tagung Kryoelektronische Bauelemente 2012*, Freudenstadt-Lauterbad, Germany, 30th of September - 2nd of October 2012.